Single Molecule Particle Analysis using Nanotechnology

By Swarnagowri Vaidyanathan

B.Tech., Alagappa College of Technology, India, 2015

Submitted to the graduate degree program in Bioengineering and the Graduate Faculty of the University of Kansas in partial fulfillment of the requirements for the degree of Doctor of Philosophy.

Chair: Steven A. Soper

Robert Dunn

Sara Wilson

Elizabeth Friis

Jennifer Robinson

Date Defended: 29 April 2021

The dissertation committee for Swarnagowri Vaidyanathan certifies that this is the approved version of the following dissertation:

Single Molecule Particle Analysis using Nanotechnology

Chair: Steven A. Soper

Date Approved: 14 May 2021

Abstract

Nanotechnology is the area of science that involves creation of devices/materials or systems in the nanometer scale. The last few decades have seen an increasing demand for rapid, sensitive, and cheaper diagnostic tools in healthcare. Advances in fabrication technologies have led to more miniaturized systems that are satisfying the promise of "micro total analysis" or "lab-on-chip" systems by facilitating the integration of multiple processing steps into a single device or multiple task-specific devices into a fluidic motherboard (*i.e.*, modular microfluidics). The field of nanotechnology has the ability to revolutionize medical diagnostics by facilitating point-of-care testing with greater sensitivity even at the single molecule level. This allows for the screening of diseases at an early stage by identifying biomarkers of the diseases that are in extremely low concentrations in the blood (*i.e.*, liquid biopsy). To this realization, we have used thermoplastics as our choice of material to fabricate microfluidic/nanofluidic hybrid systems that can evaluate how well a patient responds to chemotherapy, identify single nucleotide polymorphisms that cause major life threatening diseases such as stroke and caner, and development of nanofluidic devices to enumerate SARS CoV-2 viral particles that causes the novel coronavirus of 2019. We developed a high-throughput nanofluidic circuit on which single DNA molecules can be stretched to near their full contour length in nanochannels (<100 nm). Patients with cancer undergoing chemotherapy have more oxidative damage in their DNA compared to a healthy individual, which is an indicator of their response to therapy. We tested the device using calf thymus DNA standards labelled with a bis-intercalating dye and the abasic sites were labelled with another dye. Thus, the DNA molecules that were stretched in the nanochannels were parked and visualized using a fluorescent microscope. The abasic sites that were labelled were identified with their position in the DNA and the number of abasic sites per 10^5 nucleotides identified. This technique can be effectively used on samples having mass limits (picograms range) and where PCR cannot be utilized. Higher the number of abasic sites, better the response of the patient to chemotherapy, such as doxorubicin for breast cancer patients. While this nanofluidic circuit was used only to visualize the abnormalities in DNA, the next device we developed, called the nanosensor, facilitates the integration of

multiple processes into a single device. The nanosensor was used to identify point mutations in DNA or mRNA responsible for diseases such as cancer and stroke, respectively. The device featured 8 pixel array populated with 1 µm pillars, which act as a solid support for Ligase Detection Reactions (spLDR) that can identify a single nucleotide mutation in a DNA from a large majority of wild type DNA. The spLDR can also identify mRNA transcripts from the design of spLDR primers that specifically recognize a unique transcript. The reaction is performed on the pixel arrays and the products are subsequently shuttled into nanometer flight tubes featuring two in-plane nanopores that act as resistive pulse sensors (RPS) to generate a current drop as the products pass through these pores. The time-of-flight (TOF) between the pores in series are used to distinguish between normal and mutated DNA, thus acting as a diagnostic appropriate for the precision medicine initiative. We were able to successfully fabricate the device, run COMSOL simulations to test operation using both hydrodynamic and electrokinetic flows, which were verified via experimentation to establish the functionality of the device to perform the above mentioned processes. The hydrodynamic flow operations used for spLDR was tested using Rhodamine B and the electrokinetic flow to inject the products of the spLDR into the flight tube was tested using oligonucleotides (25mer).

Further, plastic-based nanofluidic devices were extended to detect the presence of SARS-CoV-2 viral particles using a nanopore of 350 nm in effective diameter, which has called a nano-coulter Counter (nCC). Briefly, saliva samples containing the viral particles were run through a microfluidic affinity chip containing pillars with surface-immobilized aptamers specific to the SARS-CoV-2 particles. The captured viral particles were released from the microfluidic chip using a blue light and the elute containing only the SARS viral particles were sent to the nCC, which used the RPS technique to count the number of particles. We designed multiple iterations of the nCC and used COMSOL simulations to guide device development. Using the combined principle of hydrodynamic and electrokinetic flow to introduce the viral particles into the nCC, we were able to detect patients with COVID-19 as well as estimate the viral load in SARS CoV-2 standards based on the frequency of the signals generated by correlating the results to a calibration curve. Thus, this combined multi-chip process can diagnose COVID-19 in <20 min thus venturing as an in-home diagnostic kit in the future by automating the operations into a hand-held device.

Acknowledgments

I would like to express my sincere gratitude to my advisor and mentor, Professor Steven Allan Soper for his relentless support, encouragement, and kindness throughout my PhD journey. I would not have been able to come this far in my research career without his guidance. I am also thankful for to all the members of my dissertation committee, Professor Robert Dunn, Professor Elizabeth Friis, Professor Jenny Robinson, and Professor Sara Wilson for their valuable inputs and unwavering guidance towards the realization of my degree.

I would like to extend my gratitude to Dr. Maggie Witek for her extensive support and valuable suggestions to guide my research in a better direction. I would like to thank all the past members, Dr. Matt Jackson, Dr. Swathi Pullagurla, Dr. Bethany Gross and Dr. Kumuditha Ratnayake for training me effectively in their expertise fields. I would also like to thank all of the collaborators of the projects I worked on including Dr Sunggook Park, Dr. Junseo Choi and Dr. Daniel Park for all the fabrication help, Dr. Collin Mckinney and Matt Webber for helping me with setting the TIA and its analysis software and imparting knowledge on electrical measurements and most importantly for being super friendly and responsive to help me solve any issues I was stuck with.

Special thanks to Kavya Dhathatreya who helped me extensively with the designing of the nanosensor and its fabrication, Sachindra Gamage who worked with me on the nCC and the oligonucleotides, for all the hardwork and daily brain storming sessions to make this project work. I also appreciate the other lab members of the soper group: Dr. Zheng Zhao for helping with the EV and nCC work, Dr. Anishkumar Manoharan, Dr. Lulu Zhang, Thilanga Nandana, Uditha Athapattu, Chathurika Ratnayake, Ian Freed, Katie Childers and Ziyu Zhu.

Sincere thanks to the Bioengineering Program coordinator Denise Bridwell for being my go-to person to guide me through what courses to take and keeping me up to date with my graduate program and Dr. Kenneth Fischer for his guidance throughout.

Finally, I would like to thank my parents, Mr. Vaidyanathan and Ms. Sarada Vaidyanathan, my sister Ms. Sridhevi Vaidyanathan and my husband Mr. Ramkishore Swaminathan for being my pillar of strength and being there for me all through my life and as well as my research career, for constantly pushing me to achieve higher, and motivating me every single day.

Table of Contents

Abstract iii

Acknowledgments v

Table of Contents vii

List of Figures xiv

List of Tables xxxiii

List of Equations xxxiii

1. Chapter 1: Introduction, Basic Concepts, Fabrication, and Important Applications of Single Molecule Analysis in Nanofluidics 1

1.1 Introduction 1

1.2 Unique physical phenomena in confined environments with nanometer critical dimensions 8

1.2.1 Nanoslits (1D), nanochannels (2D) and nanopores (3D) 8

1.2.2 Sense-of-scale 8

1.2.3 Surface charge effects 9

1.2.4 Electroosmotic flow (EOF) and electric double layer (EDL) 9

1.2.5 Electrokinetic versus hydrodynamic pumping at the nanometer scale 11

1.2.6 Nanometer confinement and stretching of single DNA molecules 13

1.2.7. Shaping electrical fields 16

1.2.8. Concentration polarization 16

1.3 Fabrication of nanochannel devices 17

1.3.1. Fabrication techniques of nanofluidic devices 17

1.3.2 Bonding strategies for nanofluidic devices 18

1.3.3 Fabrication of Thermoplastic Nanofluidic Devices 22

1.4 Applications of Single Molecule Detection in Nanofluidic Devices 24

1.4.1 DNA stretching....24
1.4.2 Effects of channel dimensions....25
1.4.3 Effects of ionic strength....26
1.4.4 Optical mapping in nanochannels....28
1.4.5 Enzymatic labelling....29
1.4.6 Affinity labeling....31
1.4.7 DNA methylation detection using nanochannels....32
1.4.8 Genomic mapping for sequence variation maps using nanofluidic devices....35
1.5 Nanoscale electrophoresis....38
1.6 Conclusions....40
1.7 References:....41
2. Chapter 2: Thermoplastic Nanofluidic Devices for Identifying Abasic Sites in Single DNA Molecules....1
2.1 Abstract....47
2.2 Introduction....47
2.3 Experimental Methods....51
2.3.1 Materials and reagents....51
2.3.2 Fabrication of the multi-structured nanofluidic devices....52
2.3.3 Finite element analysis (COMSOL)....53
2.3.4 Current-voltage measurements....53
2.3.5 Dual color laser system (see Figure 2.2).....54
2.3.6 Labelling λ-DNA using a bis-intercalating dye....55
2.3.7 ARP-streptavidin assay....55

2.3.8 Colorimetric assay for AP site quantification 56

2.3.9 Fluorescence dyes for AP site labeling 57

2.3.10 Labeling bARP AP DNA 57

2.3.11 DNA trapping and extension in nanostructures 58

2.4 Results and Discussion 59

2.4.1 Multi-structured nanofluidic device 59

2.4.2 COMSOL analysis of the nano-trap 62

2.4.3 Translocation of dsDNA through the nanofluidic circuit 64

2.4.4 DNA stretching and detection of AP sites using the nanofluidic circuit 67

2.5 Conclusion 71

2.6 References 72

3. Chapter 3: Nanosensor: Detection and Identification of Single Molecules for Comprehensive Molecular Profiling 47

3.1 Abstract 76

3.2 Introduction 77

3.3 Materials and Methods 82

3.3.1 Fabrication of the Nanosensor 82

3.3.2 Fabrication of the nanosensor in thermoplastic using nanoimprint lithography (NIL) 82

3.3.3 Metrology of the Si master and thermoplastic substrate to ensure fidelity. 83

3.3.4 Micromilling of thermoplastic. 83

3.3.5 COMSOL. 83

3.3.6 Hydrodynamic flow. 83

3.3.7 Electrokinetic flow.....84

3.3.8 Data Analysis.....84

3.4 Results and Discussion.....85

3.4.1 Fabrication of the multi-scale nanosensor.....85

3.4.2 Fluid dynamics.....89

3.4.2.1 Passive valving in the nanosensor device.....89

3.4.2.2 COMSOL simulations.....90

3.4.2.3 Hydrodynamic pumping monitored using a fluorescent tracer dye.....95

3.4.2.4 Electrokinetic flow monitoring using fluorescently-labeled oligonucleotides.....97

3.5 Conclusions.....98

3.6 References.....99

4. Chapter 4: Tailoring Thermoplastic In-Plane Nanopore Size by Thermal Fusion Bonding.....76

4.1 Abstract.....102

4.2 Introduction.....102

4.3 Materials and Methods.....105

4.3.1 Reagents and Materials.....105

4.3.2 Device fabrication and assembly.....106

4.3.3 Atomic Force Microscopy.....107

4.3.4 Scanning Electron Microscopy.....107

4.3.5 COMSOL.....107

4.3.6 Conductance Measurements.....108

4.3.7 λ- DNA and Oligonucleotides Translocation 108

4.3.8 Statistical analysis 109

4.4 Results and discussion 109

4.4.1 Device fabrication and assembly 109

4.4.2 Nanopore Size analysis 112

4.4.3 COMSOL simulations 112

4.4.4 Conductance measurements 114

4.4.5 λ-DNA translocation through the dual in-plane nanopore 116

4.4.6 Translocation of Oligonucleotides through the Dual in-plane Nanopore 117

4.5 Conclusion 119

4.6 References 120

5. Chapter 5: Nano-coulter counter for detection of SARS CoV-2 Viral Particles 102

5.1 Abstract 124

5.2 Introduction 125

5.3 Evolution of resistive pulse sensing 128

5.4 Quantification of viral particles using different RPS techniques 131

5.4.1 Types of RPS Detectors 132

5.5 Materials and Methods 135

5.5.1 Overall experimental set up with current amplifier circuitry 135

5.5.2 COMSOL simulations 136

5.5.3 Fabrication of the nCC 136

5.5.4 Scanning Electron Microscopy 137

5.5.5 Nanoparticle tracking analysis (NTA) 138

5.5.6 Calibration curve for viral particle counting 138

5.5.7 Pressure sensing at the withdrawal end 139

5.5.8 Fluorescence measurements 140

5.6 Results and Discussion 140

5.6.1 Design Iteration 1 140

5.6.1.1 Initial Design Schematic and Operational Characteristics 140

5.6.1.2 COMSOL simulations of nCC and its fabrication 142

5.6.1.3 Calibration curve 144

5.6.2 Design Modifications: Iteration 2 145

5.6.2.1 Schematic and SEM of Iteration 2 design 145

5.6.3 Design Modifications: Iteration 3 146

5.6.3.1 Schematic and SEM images of Iteration 3 design 146

5.6.3.2 COMSOL Simulations 147

5.6.3.3 Estimation of the pressure drop at 20 µL/min withdrawal rate 149

5.6.4 Some important considerations while optimizing the results of nCC 150

5.6.4.1 Selecting the correct material for nCC 150

5.6.4.2 Testing the translocation of polystyrene beads though the COP devices 151

5.6.4.3 Selecting the correct low pass filter for electronic signals 153

5.6.5 Design Modifications: Iteration 4 154

5.6.5.1 Rationale behind choosing 5 pores in parallel 154

5.6.5.2 Design schematic and SEM images 157

5.6.5.3 COMSOL simulations 158

5.6.5.4 Estimation of pressure at outlet channel under vacuum withdrawal 160

5.6.5.5 Effect of forward flow rate on the number of current transient events ...161

5.6.5.6 Determining the event width at half-maximum and amplitude at 3 μl/min in-flow rate in -1V. 162

5.6.5.7 Determining the event width at half-maximum and amplitude at 3 μl/min in-flow rate in -5V 163

5.6.5.8 Calibration curve for viral particle counting....165

5.7 Conclusion 169

5.8 References....170

6. Chapter 6: Conclusions and Future Directions: Simulations of Single Molecule Sequencing using X-TOF 176

6.1 Conclusions....176

6.2 Future Directions....178

6.3 References....188

List of Figures

Figure 1.1 Poisson distribution probability of finding *m* molecules in a probing volume for different values of the average molecular occupancy, *K*. 3

Figure 1.2 Left – Schematic of a focused laser beam serving as the excitation source with the probe volume, P, defined by the laser beam waist size, ω_0. Right – Drawing of the probe volume assuming a cylindrical geometry, and the terms defining its volume, *P* (see equation 3). 4

Figure 1.3 Plots of the average molecule occupancy (Pm) as a function of the excitation beam waist. ($\omega 0$). The calculations used equations 5 (DOF ~0.4 μm), 4, 3 and 1. The y-axis was plotted on a log scale, while the x-axis was on a linear scale. The dashed line represents the average molecular occupancy of 0.1 so that the probability of double occupancy is 1%. 5

Figure 1.4 Model representation of the electric double layer at a solid-liquid interface at a negatively charged solid surface/channel wall. The electric potential and ionic concentration versus distance from the surface is illustrated for channel filled with A) a moderately high electrolyte concentration (and/or large channel height [$h > \lambda_D$]) and B) a relatively low electrolyte concentration (and/or small channel height [$h \leq \lambda_D$]) (Reproduced from Lyklema J., 1995 [19]) 9

Figure 1.5 Schematic of EOF in a microchannel and in a nanochannel. (a) Plug-like EOF velocity profile in a microchannel without overlap of EDL. (b) Parabolic-shaped velocity profile in a nanochannel with overlapped EDL (Reproduced from Peng, R., 2018 [27]). 10

Figure 1.6 Required pressure drop (to generate pressure driven flow) and voltage drop (to generate EOF) to transport fluid through nanochannels with different channel heights. Nanochannel length and width are 3.5 μm and 2.3 μm, respectively; zeta potential is −11 mV for 1 M NaCl solution. (Reproduced from Conlisk *et al*., 2005 [34]) Insert shows the comparison between the parabolic and plug flow profiles from the pressure-driven and electroosmotic flow, respectively. 12

Figure 1.7 Cartoon illustration of a coiled DNA in a showing its full unfolded length (*R*), persistence length (*P*), effective width (*w*) and depletion width between the wall and the DNA molecule (δ) (Reproduced from Reisner *et. al.,* 2012 [32]) 13

Figure 1.8 A representation of the physical regimes when DNA is confined in a nanochannel environment. It takes the form of isometric Flory blobs in the deGennes regime. The region between $D=D_{**}$ and $D = D_{*} = 2P$ is defined as

the extended deGennes regime where the molecule takes both the forms of ideal and Flory behavior producing anisometric Flory blobs. When the channel size decreases from D = D_* = 2P, DNA molecule takes the shape of an isolated hairpin at a transition with back bended regions until the channel length D=P. The identified classic Odijk region where D<P, the molecule completely stretches to its contour length where it makes deflection lengths with the wall denoted by λ (Reproduced from Reisner *et. al.*, 2012 [39]). 14

Figure 1.9 (a) Schematic shows a DNA molecule confined in de Gennes regime where D>>P. There is a series of self-repulsive isomeric blobs with a defined contour length L_b. (b) DNA molecule confined in Odijk regime where D<<P. Odijk length is given by λp and the average deflection angle is denoted by θ. (Reproduced from Reisner *et. al.*, 2005 [42]) 15

Figure 1.10 (A) A schematic of the design and fabrication process of a thermoplastic-based nanofluidic device. (a) Silicon master, which consists of micron-scale transport channels, nanochannels and a funnel-like inlet for the nanochannels; (b)-(d) fabrication steps to produce a protrusive polymer stamp in a UV-curable resin by imprinting from the silicon master; (e)-(g) fabrication steps to generate nanofluidic structures in PMMA by imprinting from the UV-curable resin stamp; (h) bonding step with a PMMA cover plate to build the enclosed mixed-scale polymer device with microchannels and nanochannels. (B) (a) Schematic of the protocol used for assembly of a hybrid fluidic device and the thermal press instrument. (b) Temperature-pressure process profile showing the six stages for the thermal fusion bonding cycle. See main text for a description of the 6 stages of bonding. (Reproduced from Wu *et al.*, 2011 [6] and Uba *et al.*, 2015 [6]) 19

Figure 1.11 SEMs of Si masters (a, d, g, h, i, l, m), resin stamps (b, e, j) and nanofluidic devices imprinted in PMMA (c, f, k, n). The device in a – c consists of nanoslits with a width of 1 µm and depth of 50 nm. In d – f, a device with a 120 nm × 120 nm channels are shown. In g – k, a nanofluidic device with a 40 × 40 nm channel is shown with a 40 nm thick Al layer that was deposited onto the Si master prior to using focused ion beam milling to generate the nano-structures. In l – n is shown a nanofluidic device with an approximately 20 × 20 nm channel with a 80 nm thick Al layer deposited onto the Si master prior to focused ion beam milling. In all cases, the substrate was PMMA (glass transition temperature 105°C). Figures a – f, m – n were reproduced with permission of The Royal Society of Chemistry from Uba *et al*., 2014 [71]. Figures g – k and l are previously unpublished. 21

Figure 1.12 A) Fluorescent images of T4 DNA molecules stretched in nanochannels devices. An exposure time of 10 ms was set and the electric field was turned off as the DNA entered into the channels. B) A log–log plot showing the

extension of DNA with respect of the average depth of the nanochannels. The contour length was normalized to a 64 μm when labeled with a dye. The red and blue lines indicate deGennes and Odijk regimes respectively. The black line represents the best power law fit to the DNA stretching on the nanochannel ranging from depths of 53nm to 200nm (Reproduced from Uba et al., 2015 [6]). 26

Figure 1.13 Nanochannels were fabricated on a silicon wafer with dimensions of 200 nm, 100 nm and 50 nm. λ-phage DNA dyed with YOYO-1 was driven electrophoretically or using over-pressure into the nanochannels under 0.05X, 0.2 X, 0.5 X, 2 X, 5 X TBE ionic strengths, and the signal was recorded using an iXon EMCCD camera. Fluorescence images of λ-DNA molecules obtained at different TBE concentrations (left to right, 0.05X, 0.2X , 0.5X , 2X , 5X TBE) in (a) 200 nm channels, (b) 100 nm channels, and (c) 50 nm channels (Reproduced from Reisner *et al.*, 2007 [46]). 28

Figure 1.14 Demonstration of the labelling techniques used in DNA for optical mapping. The DNA confined in nanofluidic channels is labelled and visualized under fluorescence microscope thus facilitating the study of genomic information over larger molecules. A) A nick is created by any nicking enzyme at its specific site of 4-7bp long. Following that a DNA polymerase removes the nick and adds new nucleotides in that site. By labelling any of the four deoxynucleotide triphosphates, dNTP, visualization of the nick, along with the DNA molecule is possible. B) A methyl transferase enzyme is used to transfer a methyl group that is labelled, to a specific sequence in the DNA of 4 bp, thus enabling fluorescence detection of the attached site. C) Denaturation mapping exploits the lower melting temperature of AT base pairs compared to GC regions. Hence, the DNA labelled with a bisintercalating dye emits no fluorescence from AT regions as they are melted. D) In the competitive binding mapping method, a compound such as Netrospin selective for AT regions is added along with YOYO to the DNA, such that Netrospin binds specifically to AT regions, leaving GC regions to bind YOYO. Thus, based on the difference in fluorescence emitted, one can discern the sequence of DNA (Reproduced from Muller *et al.*, 2017 [102]). 30

Figure 1.15 a) – e) Fluorescence images of concatenation of methylated and non-methylated λ-DNA stretched in nanochannels and labelled with YOYO-1 (green) and Alexa568MBD (red). The panels have each color split for convenience. Different regions of methylation have been depicted in these images (Reproduced from Lim *et al.*, 2011 [107]). 33

Figure 1.16 Contracted length of both methylated (red) and non-methylated (blue) T4 DNA as a function of time using equation (16) (Reproduced from Sun *et al.*, 2016 [108]). 34

Figure 1.17 a) Nick labelling in the DNA achieved using Nt.BspQI and DNA polymerase by cleaving the top DNA strand followed by fluorescent nucleotide insertion (red) from the 3' end, and simultaneous strand displacement. B) Stretching of DNA electrophoretically inside a 45nm channel, where the DNA unwinds in micron scale area and stretches in the nanochannels to about 85% of its contour length. C) The length of the DNA molecule and the position of nicks is represented, with a narrower peak corresponding to proper linearization of DNA. D) The DNA molecules arranged according to their nicking pattern similarity, with each BAC represented by two clusters (first and second panels) based on their orientation to determine the location of each sequence motif, represented by the histogram of peaks (GCTCTTC) in the bottom panel (Reproduced from Lam *et al*., 2012 [108]). 36

Figure 1.18 (A) Elongation of dsDNA standards labeled with biotin-ARP (b-ARP) that contained 20 AP-sites per 100 Kbp. The standards were incubated with streptavidin containing 2-3 dye molecules (Alexa 594). The DNA are "parked" in the non-pillared region in this fluorescence micrograph (5 s integration time). (B) The DNA was stretched in PMMA nanochannels (100 x 60 nm, w x d) that were 100 μm in length with pre-stretching pillars (C). The DNA fragment shown in (B) was ~20 Kbp and 2 AP sites were detected. 37

Figure 1.19 Representative frames of fluorescently stained λ-DNA molecules translocating through a 100 nm × 100 nm oxygen plasma modified PMMA nanochannel and imaged in (a) 0.5X and (b) 2X TBE buffer at 80 V cm^{-1} and 120 V cm^{-1}, respectively. The time between frames is approximately 20 ms and scale bars are 10 μm. (c) Apparent mobility against the electric field strength for DNA translocation through the single nanochannel filled with 0.5X (black markers) and 2X(red markers) TBE buffer. The error bars represent the standard deviation of the measurements (n=10). (Reproduced from Uba *et al.*, 2014 [5])..... 38

Figure 1.20 (a, b) Histogram of apparent mobility of ATTO-532 labeled deoxynucleotide monophosphate in 100 nm deep and 100nm wide nanochannels at a filed strength of 342V/cm and background electrolyte concentration was 44.5 mM TBE at pH 10.3 and 8.3 respectively. c) Relative apparent mobility of the ATTO 532-labeled dNMPs with respect to carrier electrolyte pH and apparent mobilities have been normalized to the highest observed apparent mobility for pH 8.3, 9.3 and 10.3. d) Histogram of apparent mobility of ATTO-532 labeled deoxynucleotide monophosphate in 100 nm deep and 100 nm wide nanochannels at a filed strength of 342V/cm and background electrolyte concentration was 0.45 mM TBE. (Reproduced from O'Neil *et al.*, 2018 [110]). 40

Figure 2.1 Schematic showing the top down fabrication process used to make the plastic nanofluidic devices used in these studies. (**A**) First, photolithography on Si wafer using AZ1518 resist was performed followed by wet etching to

achieve the desired depth of the microfluidic channels. As a final step, FIB was performed to fabricate the nanodimensional features on the Si master. (**B**) The NIL steps are shown here. Briefly, the features from the Si master were transferred to a resin stamp using UV light. They were then thermally imprinted using NIL into a PMMA substrate. Finally, thermal fusion bonding was performed to seal the fluidic network with a COC cover plate. 53

Figure 2.2 Schematic of the dual-color microscope system for single-molecule tracking and imaging. The nanofluidic device was placed on a translational stage associated with the inverted microscope and Pt electrodes were placed within specific reservoirs of the chip to supply the driving electric field to the chip using a DC power supply, which was earth grounded. Switching between the two lasers was controlled manually with a 1 s switching delay using a filter cube resident within the microscope. All images were acquired using an EMCCD camera and Metamorph software. 54

Figure 2.3 ROS inducing a loss of a nucleotide base (AP site) in dsDNA followed by ring opening, which generates an aldehyde group that is available for conjugation to an aldehyde reactive probe (ARP). ARP reacts with an active aldehyde group in the ring-opened form of the AP site. The biotin group in the ARP (bARP) has a strong affinity toward streptavidin, which allows for the generation of fluorescence at each AP site due to streptavidin being labeled with Alexa Fluor 647.[1]..... 56

Figure 2.4 (**A**) SEM images of the multi-structured nanofluidic circuit comprised of a 3D funnel, nano-trap, and a stretching nanochannel. Its equivalent circuit diagram with resistors including an adjustable resistor for the nano-trap (variable resistance is predicated on changing the trap size) is also shown. (**B**) Array of multi-structured nanofluidic circuits for high throughput processing of single DNA molecules to search for AP sites. (**C**) Entrance funnel used to extend the electric field into the adjoining microchannel for assisting in loading single DNA molecules into the nanofluidic circuit from access microchannels. (**D**) SEM image of a 400 nm nano-trap (diameter and depth). The device shown was made from PMMA using thermal NIL from a resin stamp produced via UV-NIL from a Si master. 59

Figure 2.5 (A) SEMs of two input types used to interface the nanofluidic network to the access microchannels. In these SEMs are shown the Funnel and Groove inputs. The white scale bars represent 500 nm. The nanochannel shown on the left is 100 nm x 80 nm (width x depth). (B) Relative injection efficiency (%) of λ-DNA (48.5 Kbp) into the nanofluidic circuit for three types of nanochannel/microchannel interfaces. For the Blunt input type, the access

microchannel of the device was directly connected to the nanofluidic channel. All data were normalized with respect to the Funnel input event frequency. 61

Figure 2.6 (A) Vector plots showing the electric fields across the 400 nm and 600 nm diameter nano-traps and one without a nano-trap. (**B**) Line plots showing the change in electric field strength across the nano-traps. (**C**) Current-voltage (I/V) curves for the multi-structured nanofluidic circuit with no nano-trap (black), 400 nm (red) and 600 nm diameter (blue) nano-traps measured with 1 M KCl added to 1X TBE buffer (pH = 8.0). Each data point represents the mean ±standard deviation from five different measurements. One M KCl was spiked into the buffer to increase the current flowing through the device. 63

Figure 2.7 (**A**) Representative frames showing the translocation of stained λ-DNA through the multi-structured nanofluidic circuit. The frames were divided into 4 sections; (i) 'Enter the funnel,' where the DNA enters the funnel from the microfluidic channel and into the nanofluidic circuit. (ii) 'From the funnel to trap,' where the DNA leaves the funnel, stretches briefly in the short nanochannel section and enters into the nano-trap. (iii) 'Escape from trap,' where the DNA resides in the trap for a period of time and subsequently ejected from the nano-trap and inserted into the stretching nanochannel. (iv) "Stretching of dsDNA" in the stretching nanochannel to near its full contour length and is parked so as to detect the AP sites. For these experiments, the driving voltage was 0.1 V DC and the buffer used was 1× TBE (pH = 8.0). The scale bar (5 μm) is shown in Section 4, image (viii) at the top right corner of the image. Box plots showing (**B**) trapping and (**C**) translocation times of λ-DNA electrokinetically transported through the multi-structured nanofluidic circuit under a 0.1 V driving voltage having a 400 nm or 600 nm trap. The average trapping time for the 400 nm trap was ~138 ms, while for the 600 nm trap it was 225 ms. The average translocation time through the nanofluidic circuit with a 400 nm trap was 660 ms, while for the 600 nm trap it was 1847 ms. All measurements were performed using 1X TBE buffer (pH = 7.9). Events were captured at 10 ms exposure times resulting in a frame rate of 90 fps and 1 × 1 binning for the EMCCD. The *p value* calculated between the 400 and 600 nm traps for the trapping and translocation times (Wilcoxon signed rank test) were statistically different at the 95% confidence interval ($p<0.05$). 65

Figure 2.8 (**A**) Background image to evaluate the noise and speckle pattern imaged from a COC cover plate**.** (**B**) Line plot showing background intensity gray values. (**C**) Images of streptavidin Alexa Fluor 647 conjugates deposited on a COC cover plate. Excitation was provided by the 641 nm red laser with the fluorescence collected using a 100X (1.49 N/A) microscope objective. (**D**) Histograms showing the number of occurrences (frequency) for integrated

intensity of all current voxels for single fluorescently labeled streptavidin molecules. (**E**) The bleaching of a streptavidin molecule at various time points and the corresponding intensity gray values. The sharp intensity drop at around 45.03 s corresponds to a single-molecule bleaching event. 67

Figure 2.9 Images of λ-DNA confined in 100 nm × 80 nm stretching nanochannels. (**A**) Raw images of λ-DNAs' backbones labeled with YOYO-1 intercalating dye (green) in the multi-structured device having 20 stretching nanochannels. (**B**) Examples of unprocessed raw images, where the AP sites were labeled with Alexa Fluor 647 streptavidin (red) with AP sites identified within the dsDNA molecules. (**C**) Processed composite image showing the AP sites co-localized in the DNA strand (yellow). Three specific strands are shown, 1 AP site was identified in 8.9 μm strand, 2 AP sites were identified in a 14 μm length strand and 3 AP sites were identified in a 16.2 μm length DNA strand. The images were processed in Fiji and images of DNA and the AP sites were imaged separately and merged. A scale bar of 5 μm is represented in the images unless otherwise indicated. 68

Figure 2.10 Tape station data for abasic site labeled Calf-thymus DNA from the Dojindo abasic site quantification kit. According to the data, there are various lengths of DNA strands present in the sample. 69

Figure 2.11 (**A**) Calibration curve for a colorimetric assay for measuring AP sites in dsDNA. The data was collected by measuring absorbance at 650 nm in a 96-well plate reader. Data points were obtained using 3 duplicate measurements and fitted to a linear calibration curve, which yielded a correlation coefficient of 0.997. (**B**) Calibration data points using the colorimetric assay based on a 96-well plate for different concentrations of dsDNA. Controls with no abasic DNA are shown in black and different concentrations of abasic dsDNA are shown in red (0.025 ng/μL), blue (0.075 ng/μL), and pink (0.300 ng/μL) with respect to the number of AP sites per unit length of dsDNA. 70

Figure 3.1 A) Schematic of the Nanosensor is shown above. The nanosensor is placed between two-micron access channels. The device comprises of three main features; 20 Baffles of 7 μm x 7 μm each to distribute the reagents; 8-pixel arrays containing 268 pillars/array to simultaneously perform spLDR reaction; 8 flight tubes of 50 nm X 50 nm X 50 μm (w x d xl) each to analyse the products of spLDR reaction. B) The workflow process of the hydrodynamic flow is utilized to pump the reagents at a flow rate of 1 nL/s required for the LDR into the chip (1). During this process, the target DNA which have the mutations are immobilized on to the pixel array (2). The spLDR is performed and the waste products at the end of the reaction are rinsed using the hydrodynamic flow (3). C) The electrokinetic flow is performed at the end of the spLDR, where the products are formed in the pixel array (1). They are electrokinetically driven into the flight tube by applying a DC bias and placing the electrodes to one end of the microchannel and earth

ground to the ends of the flight tube (2). Once the products enter the flight tube, they are detected for the presence of mutation by monitoring the current amplitude and the TOF generated by the products (3)..... 78

Figure 3.2 A) Schematic representation of the activation of a polymer substrate, PMMA in this case, followed by subsequent modification of the surface. UV/O_3 treatment of the polymer surface induces oxygen containing groups followed by EDC (1-Ethyl-3-(3-dimethylaminopropyl) carbodiimide), NHS (N-hydroxyl succinimide) treatment to allow streptavidin and one of its primary amines to bind to the surface –COOH group. Streptavidin strongly binds to biotin in the DNA allowing immobilization of the target DNA. COC and COP can be activated in a similar fashion. B) The process of spLDR is depicted for both normal and mutated KRAS gene occurring in codon 12 at position 34 (C.34 G>A, where the guanine is replaced by adenine, and hence the amino acid coded is converted from Glycine to Serine for the mutated DNA) in the schematic. The DNA that is immobilized on the pillar arrays is denatured to form a single stranded DNA. To the ssDNA immobilized, a common primer, a discriminating primer and thermostable ligase are added to the reaction mixture. Ligase covalently bonds discriminating primer and phosphorylated common primer together. If there is a mutation, then ligation happens. If there is no mutation, ligation does not happen. The products formed are of different lengths, with mutated LDR product having a longer length. 80

Figure 3.3 A) Schematic showing the process of fabrication of the Si master; positive photolithography using AZ9260 resist is performed in 3 main steps : Spin coating, where AZ9260 resist is spun on to the Si wafer, followed by exposure via dark field mask to UV light at 365 nm. After exposure, the resist is developed in MIF 300 developer and visualized under microscope. This step is followed by DRIE, where the Si master is etched to a depth of ~6-7 μm. Finally the FIB process to fabricate the nanochannels is performed where Ga ions are rastered onto the Si master to fabricate the pixel arrays and the flight tubes which are in the nanometer range; B) SEM images showing the images of Si master after photolithography but before the DRIE, where the all the micron scale features are successfully. The pillars and flight tube are not seen after Photolithography as they are fabricated using FIB. C) SEM images of the final Si master after DRIE and FIB, where the desired depth in the device is achieved and both the pixel arrays (ii) and the flight tubes are clearly visible (iii)..... 85

Figure 3.4 A) Schematic of Nanosensor in the Keyence profilometer showing the depth of the Si master after DRIE. B) The first graph shows the depth across the baffle area which is estimated to be ~7.3 μm. The second graph shows the depth across the microchannel channels that follow the flight tubes. The depth in this region is estimated to be ~6.9 μm..... 87

Figure 3.5 Process of NIL: A) Schematic showing the process of nanoimprint lithography is described in 3 steps; Step 1 is the process of using PUA resin to create polymeric stamps from the Si master by UV treating them at 365 nm for 2.5 mins; Step 2 is followed by thermal imprinting of the stamps on a PMMA substrate at 135°C, 300 psi for 5 mins to transfer the patterns from the stamps into the PMMA device.~~,~~ Step 3: Thermal fusion bonding is performed by using a COC cover plate to seal the features at 70°C, 120 psi for 15 mins. ; B) SEM images showing the images of UV resin stamp where the structures are formed in the direction opposite to the Si master. The pixel arrays (a), the pillars (b) in them and the flight tube (c) are transferred. C) SEM images of the final PMMA device after thermal imprinting that has structure similar to the original Si master. The final device with the pixel arrays (a), the side profile of the pillars (b), the funnel entrance to the flight tubes (c) and the flight tubes (d) are replicated with high fidelity. 88

Figure 3.6 . A) COMSOL simulation of hydrodynamic flow of 1X TBE through the nanosensor device at a flow rate of 1 nL/s. The entrance of the nanosensor (25 μm) is placed as the inlet of the liquid. The flow entering the nanosensor is distributed uniformly across the baffles such that all the 8 pixel arrays get a uniform distribution of the fluid. The colors correspond to the scale bar in the graph. B) Hydrodynamic flow across the pixel array is magnified (maroon color in the scale bar). The graph shows the average velocity across the 8-pixel array, which is about 3.7 mm/s. The velocity across the 8 pixel arrays are very uniform with a standard deviation of 6 μm/s between the arrays. C) The flow across the 8 flight tubes in region in the nanosensor is negligible. This is empirically represented in the line graph that is drawn across the flight tubes, where the velocity at the entrance of the flight tubes drops rapidly as seen by the drop in velocity (to ~0 mm/s). D) The pressure drop across the pixel array is seen. The average current drop among the 8 arrays are similar. E) The pressure drop across the 8 nanochannels show a negligible drop in pressure (30 Pa to 0 Pa) compared to the pixel array. 90

Figure 3.7 Schematic of pixel arrays set up in COMSOL. Each chamber measures 20 μm x 20 μm and contains 8 pixels with 268 pillars per pixel array. A) The flow across two rows in one pixel array in the horizontal direction is represented, which are all nearly similar (~ 5.7 mm/s). B) The pixel array flow rate profile across two rows in a single pixel array in vertical direction which again shows uniform velocity (~5.7 mm/s) throughout array. 91

Figure 3.8 COMSOL simulation of electrokinetic flow through the nanosensor; A) Field strength across the nanosensor is represented. A potential of 10 V is applied in the inlet of the nanosensor and each of the flight tubes are placed at earth ground in their individual reservoirs. The areas of the nanosensor having the smallest dimensions have the higher field strengths. B) Line plot of the field strength across the 8 flight tubes as represented in the figure. The

field strength gradually increases from the entrance of the flight tube through its length. There is a uniform field strength observed across the 8 flight tubes, which is 1650 V/cm. C) The current density plot (at a potential of 10 V) showing one pixel array and the flight tube with arrows representing the direction of the fluid movement and the magnitude of arrows representing areas of higher field strength. D) The line graph showing an increase of current density upto 0.1 A/m^2 in the entrance of the flight tube and a drop in current density of 0.0015 A/m^2 in the regions away from the channel. E) Particle tracing representative of ssDNA is simulated showing 10 particles simulated in the pixel array (t=0). The time scale of movement is shown where the particles are observed moving to the entrance of the funnel inlet (2.25 s), eventually moving into the flight tube and more particles entering into the funnel (t=2.9 s), and all of them translocating into the flight tubes (t=6). Those particles that are not in the funnel, but still in the radius of the current density are also drawn into the flight tube (t=7.3 s). The transmission efficiency of 80% is observed. 92

Figure 3.9 COMSOL simulation of electrokinetic potential drop through the nanosensor device. A) The electrical potential across the nanosensor is represented. A potential of 10 V is applied across the nanosensor device. The arrows depict the potential at each section of the device. B) Most of the potential drop occurs across the nanometer flight tubes as represented in the schematic. The line graph shows the drop in potential from the inlet of the nanosensor to the ends of the nanochannel which is kept at earth ground. The 10 V is applied in the entrance of the nanosensor, where it drops to 9.5V after the pixel array. There is an 8.5V drop in potential across the flight tube. This represents the transport of spLDR products into the nanochannel during the experiment. 94

Figure 3.10 Experimental results of the hydrodynamic flow across the nanosensor. This is observed to evaluate the performance of how similar the flow is among each pixel array. A) The figure represents how the nanosensor device looks like after pumping Rhodamine-B as the tracer pumped at a flow rate of 1nL/s. The dye is distributed across the baffles to the pixel arrays and to the areas surrounding the flight tubes. No visible fluorescence is seen in the flight tubes B) Fluorescence intensities across the 8 pixels are evaluated showing similar levels of intensities ranging from 800-1000. The intensities are represented as grey values and they correspond to the liquid flow C) Correspondingly, the intensity in the flight tubes are evaluated, and a significant drop is seen in the 8 flight tubes in a similar fashion. The areas having dye have a grey value of 800 or more, while the intensity in the nanochannels are ~300. The measurements are taken from 5 different experiments calculated with mean and sd evaluated. No statistical significance was seen between the intensity of the pixel arrays at $p<0.01$ at 95% CI. A scale bar of 20 μm is represented in the images. 96

Figure 3.11 A) Schematic of the application of the DC bias is represented. The potential is applied to the entrance of the microchannel, while the ends of the nanochannel are placed at earth ground. Fluorescent images showing the accumulation of DNA from the pixel array to the end of each of the flight tubes are represented; B) The intensity of the fluorescence accumulation is represented using a line graph. The areas of DNA accumulation show higher intensity grey values (300-500). The conditions of the experiment are given in the table. C) The flight tubes are magnified at a higher exposure (3500 ms) with ROI's 1 and 2 showing the DNA molecules parked in the flight tube when the voltage is turned off. The corresponding line plots show an increase of fluorescence to a grey value of 2000 (1) and 1000(2) confirms the movement of analytes into the flight tube in a DC field. The parameters used for the experiment are given in the table. A scale bar of 20 μm is represented in the images. 97

Figure 4.1 Dual in-plane nanopore device. (**A**) SEM image of the Si mold master. The two in-plane nanopores are 5 μm apart from each other. AFM scans of the (**B**) TPGDA resin stamp and (**C**) imprinted PMMA substrate. Tapping mode AFM scans (Shimadzu SPM) were acquired at 0.5 Hz scanning frequency using a high aspect ratio tip with a radius <2 nm. (**C**) Schematic representation of experimental procedure for determining depth and width of dual in-plane nanopores. (**D**) Schematic representation of device assembly for DNA translocation studies. 110

Figure 4.2 Nanopore depth and width with varying thermal fusion bonding pressure. (**A**) AFM scans of PMMA devices at 110 psi and 170 psi bonding pressures. (**B**) SEM image of PMMA device at 200 psi bonding pressure. A 2 nm thin conductive Iridium layer was sputter coated onto the PMMA device using an EMS 150ES sputter coater before SEM Imaging. (**C**) Change in the depth of the in-plane nanopores with bonding pressure. (**D**) Relative width of the in-plane nanopores after bonding at different pressures relative to the width of the nanopore before bonding (0 psi). There was no statistical difference in relative width from 130-200 psi at the 95% confidence interval ($p > 0.05$). (**E**) Cross sectional area of the in-plane nanopore with thermal fusion bonding pressure. 111

Figure 4.3 Simulated and experimental analysis of the electrical behavior of the dual in-plane nanopores connected by a 5 μm length flight tube at different bonding pressures. (A) The 2D design of the dual in-plane nanopores used for COMSOL simulations. The pore and intervening 5 μm long nanochannel were assumed to be cylindrical. In order to understand if a change of in-plane nanopore size (diameter) would cause an increase in conductance, the pore diameter was varied from 10-50 nm while the length was kept constant at 30 nm. (B) The electric potential data from COMSOL simulations shows that the majority of the potential drop appears across the two nanopores and the nanochannel implying that the overall conductance is contributed by the two nanopores and the nanochannel. (C) The current

density was plotted from which the current and the subsequent conductance was calculated (I/V). (D) Conductance (nS) calculated from COMSOL for varying pore size in 1 M KCl. There is a linear increase in conductance with increasing pore width. (E) Variation of measured conductance through the dual in plane nanopore PMMA and COP devices at different bonding conditions using an electrolyte of 1M KCl ($n \geq 3$). There was a decrease in conductance with increase in bonding pressure, but with no statistical differences at pressures above 130 psi ($p>0.05$). The conductance results agree with the pore size determined using AFM and SEM correlated to the results from COMSOL. The y-axis scales of graphs for figures D and E are adjusted according to their corresponding x-axis and hence the range might be different..... 113

Figure 4.4 λ-DNA translocation through the dual in-plane PMMA nanopores and the ramifications of the size of the nanopore on peak amplitude. **(A)** Schematic of the λ-DNA translocation through the in plane dual nanopore device that gives rise to a negative peak as the DNA enters the first pore. Since the contour length of the DNA is longer than both the pores, there is a second subsequent peak when the DNA co-resides in both the pores. The DNA then leaves the pores very quickly which makes the current return to the baseline. **(B)** A detected current transient trace typically observed in a time interval of 400 s as a result of λ-DNA translocation and magnified images of individual peak shapes at various translocation stages of the DNA through the dual nanopore at 110 and 170 psi pressure respectively. **(C)** Distribution of peak amplitudes of λ-DNA at 110, 170 and 200 psi bonding pressures. The average peak amplitude increases with the increasing bonding pressure. p values calculated between each bonding pressure condition (Wilcoxon signed rank test) show statistically significant difference at 95% confidence interval ($p < 0.05$). 115

Figure 4.5 A) Different in time of flights between oligo 50 and oligo 70 as they translocate through the PMMA device. The mean TOF of the oligo 50 is 0.43 ms, while for oligo 70 the TOF is higher, i.e 1.48 ms. B) Representative traces of oligo 70 showing two peaks as they pass through the two nanopores placed in series, having TOF of 0.88 ms and 0.67 ms. C) The pulse amplitudes comparison of oligo 70 of peak 1 corresponding to the oligos as they pass through pore 1 and peak 2 corresponding to pore 2 show that there are no statistically significant differences between the amplitudes..... 118

Figure 5.1 Hypothetical viral load as a function of disease progression and different testing strategies. Taken from Ref. (18)..... 126

Figure 5.2 The evolution of the RPS development through the years is described. The RPS technology started off with detecting microparticles, eventually leading to single molecule detection. Biological nanopores such as α-hemolysin

nanopores to detect ssDNA. Synthetic nanopores having a fixed pore size were used to detect nanoparticles and estimate the concentration, size and even the charge. Microfluidic sensors offer electrical, hydrodynamic focusing to detect particles. Elastic nanopores offer tunable pores that can be stretched to suit the detection conditions [1]..... 129

Figure 5.3 A) The steps depicting the process of positive photolithography and wet etching used to fabricate micron scale features are shown; briefly 4 major steps are involved where the Si wafter is spin coated (1) with AZ1518 resist, exposed to UV for 4 s via chrome coated masks that has the features (2). The features were developed using MIF 300 for 20 s (3) and wet etching on Si is performed using 40% KOH to achieve the required depths. The nanoscale features were fabricated using FIB milling using Ga^+ ions rastered on to the Si substrate. B) The features from the Si substate were transferred to the COP/PMMA substrate using NIL. A polymeric resin stamp was made by applying PUA resin on the Si substate and placing PET sheet over it and exposing it to UV for 365 mins (1). The patterns on the stamp are imprinted on the COP/PMMA substrate (2) and finally bonded using a COC 8007 coverplate to seal the devices (3). 137

Figure 5.4 Overall concept of RPS and experimental set up of nCC for detecting viral particles. A) The concept of RPS where two access microchannels are connected by a nanopore, which is connected to an electrical circuit. When the viral particles are in microchannel, there is a constant current produced expressed by region 1 in the trace. When the particle moves into the nCC, a drop in current is generated due to the blockage of current produced by viral particle (region 2). The current resumes to the baseline when the viral particle moves from the nCC to the microchannel (region 3). B) The experimental setup is performed in 3 stages; stage 1, where one microchannel is filled with the sample and the other one with the buffer. A ferrule is fixed to connect the syringe pump that withdraws at 20 µl/min on the buffer side, while the other end of the buffer is sealed. The setup is connected to an electrical circuit to measure the current. 141

Figure 5.5 A) The overall schematic of the first design of the nCC is shown. The two microchannels (~6 µm deep) is connected to a nanochannel of 500 nm in width and depth, having a nanopore in the center of the channel of 200 nm X 200 nm width and depth and 100 nm long. B) The SEM images of the microchannels, the nanochannel having the nanopore is shown. The distance between the two microchannels is 15 µm. C) The magnified SEM image of the nCC is shown where the actual dimensions of the pore and the nanochannel are shown. 142

Figure 5.6 Nanopores for resistive pulse sensing of VPs**.** A) SEM image of the nCC (200 nm effective diameter. B) Equivalent sensing circuit for the nano-coulter counter, where Rmc is the resistance of the microchannel, Rnc is the

resistance of nanochannel, R_{np} is the resistance of the in-plane nanopore, and R_{np} is the resistance of the nanoparticle. C) Simulations of nanopore-based VPs sensing showing the relation between the size of the particle and the size of the pore and the current drop that is expected D) COMSOL simulations of the voltage potential drop across the nanochannel. E) The plot of potential drop vs. distance of nanochannel. The potential drop across the nanopore is only 4% in the 2D dimension. By involving the depth to the 3D factor, the nanopore only shares the potential by 10%. F) Electric field strength profile showing the nCC having a higher field strength extending out to the nanochannel. G) The 50% of full strength was taken as the effective nanopore length, which is 224.7 nm. 143

Figure 5.7 Representative traces of the Calibration curve that are background subtracted and filtered built for SARS CoV-2 VPs. A) The blank of 1X PBS showing no peaks that are observed above the discriminator threshold. B) The SARS stock having a concentration of 3 x 10^8 particles/mL showing 371 particles/µL. C) 100 fold dilution of SARS CoV-2 showing only 21 particles/µL. A 30 s time trace is shown for all the three data sets. D) Calibration curve built for 6 different concentrations (represented in the table 5.1) showing a LOD in the range of 6 x 10^5 particles mL^{-1} for a 600 s counting interval..... 144

Figure 5.8 A) Schematic of a single nanochannel with nCC in the second iteration. B) SEM images of the nCC device showing the overall view of the 5 nanochannels with the nCC. C-D) Magnified image of a single nanochannel with nCC in the 5 channel design. The dimensions of the individual nCC and the connecting nanochannels have been fabricated similar to iteration. 146

Figure 5.9 A) Overall Schematic showing the modified design having the connecting nanochannel increased from 200 nm to 2 µm. B) Overall SEM image showing the 5 channels. C-D) Magnified image of the modified nanochannel and the nCC, showing the depth profiles. The size of the nanochannel has been increased 20 fold, but the size of the nCC nanopores have been retained similar to previous iterations. 147

Figure 5.10 COMSOL simulation of iteration 3 design. A) The velocity profile with the inlets set to atmospheric pressure on both the same inlets and the outlets set to the pressure 97000 Pa (estimated from the pressure sensor set to 20 µL/min. The fluid from the inlet side are seen entering the outlet side due to the difference in pressure drop. The magnified image showing the higher velocity in the nCC. B) The pressure profile and the line graph showing a sharp decrease in the pressure at the pore region. It is evident the pressure drop does not occur in the access microchannels. C) The potential drop profile and the line graph showing the voltage drop at the pore (0.2 V) with the rest of the voltage drop across the nanochannel. D) The current density profile plotted from the voltage profile to estimate the

effective length of the pore at FWHM, which is ~407 nm. This happens due to the field strength extending out of the pore and into the nanochannel contributing to the current drop. 148

Figure 5.11 The experimental setup modified from iteration 1 to have a pressure sensor fixed before the withdrawal pump to estimate the pressure drop at the buffer side at a flow rate of 20 μL/min. B) The pressure drop across the sample and the buffer side at this flow rate was evaluated across the nCC for a period of 12 mins. The purple line represents the atmospheric pressure (101325 Pa) in the absence of any flow rate. The orange and green lines represent the pressure at buffer side from 2 different trails averaging to approximately 97000 Pa. The differential pressure drop across the nCC is about 4000 Pa. 149

Figure 5.12 A) Polystyrene beads stuck on the microchannel walls on the PMMA device, represented by red circles. B) COP device showing no beads stuck on the microchannel wall and some beads are observed moving across the nCC from the sample to the buffer side. 151

Figure 5.13 A) Fluorescence image of the nCC device which is filled with Rhodamine-B, showing the fluorescence in the microchannel and the 3 nCC that is in the field of view. B) The line plot showing the fluorescence intensity values in the 3 nCC compared to the background. C) 40 and 100 nm Polystyrene beads mixed that were filled on the sample side of the nCC and were drawn into the nCC using 20 μL/min withdrawal rate. The 5 nCC shown in the field of view have beads in the nCC region. C) The magnified image of the beads in one of the nCC shows that there are single molecules occupying a 3X3 pixel array D) A 3D plot of a single molecule shows the intensity spread across the 3X3 pixel array..... 152

Figure 5.14 The baseline noise levels at three different low pass filters : 5,10 and 100 kHz. The data was recorded at 5 kHz, subsequently increased to 10 and 100 kHz, followed by gradually reducing the frequencies, all acquired in a time duration of ~278 s. A voltage of 1V was applied and an open pore current of 22.2 nA in 1X PBS was recorded on multiple pore nCC device. The data shown above is baseline subtracted and filtered using a 400 Hz high pass filter. The sampling frequency was set to 100 kHz..... 154

Figure 5.15 COMSOL simulations of the 1.75 μm pore ; A) Electric potential (-5V) applied in the microchannel inlet showing a drop in potential through the nCC and the connecting nanochannels. A magnified image of the nCC and the corresponding line plot showing the drop from 5V to the ground is shown. B) The current density corresponding to the potential drop is shown with the regions in the nCC having a higher current density. A magnified image of the nCC with the corresponding line plot showing the current density across the microchannels, nCC and the connecting

nanochannels. The current density in the nCC reaches the highest of 600000 A/m^2, giving rise to an effective length of 18.65 µm. 156

Figure 5.16 A) Gray-scale diagram of a single in-plane nanopore associated with the final nCC iteration. The nCC in this design was placed adjacent to the access microchannel and the funnel structure near the pore was increased to 4 µm and the nanochannels to 2 µm to have a higher injection efficiency of the VPs into the nCC. B) SEM of the 5 in-plane nanopores FIB milled in the Si wafer. The width of the access microchannels on the sample side was reduced from 25 µm to 10 µm only in the region having the nCC pores. C) SEM showing the bridge channels flanking the access microchannels. D) The final nCC dimensions after FIB milling was 350 nm X 336 nm (w x d). 157

Figure 5.17 COMSOL simulation of iteration 4 design. A) The velocity profile with the inlets set to atmospheric pressure on one side of the inlet and the other side at a flow rate of 3 µL/min. The outlets were set to a pressure 50000 Pa (estimated from the pressure sensor). The fluid from the inlet side are seen entering the outlet side due to the difference in pressure drop. B) The magnified image showing the higher velocity in the nCC and the line graph shows the velocity profiles across all the 5 nCCs. C) Pressure drops across the 5 in-plane nCC; i) The pressure drop in the inlet microchannel showing a small pressure drop of 3500 Pa; ii) The pressure drop across the nCC showing the majority of the pressure drop occurring across the nCC. D) Potential drop across the 5 nCC in-plane nanopore sensors. A 2-dimensional line plot of potential drop versus distance across one of the nCC in-plane nanopore sensors. The potential drop across the nCC represents 10% of the total voltage drop across the sensor (5.0 V). E) The current density profile plotted from the voltage profile to estimate the effective length of the pore at FWHM, which is ~667 nm for a pore width of 350 nm..... 159

Figure 5.18 A) Final design experimental setup that features a forward flow for the sample to be injected at ~ 3 µL/min. The buffer ends are connected to a vacuum pump to increase the pressure drop across the nCC. The pressure sensor is inserted to quantitatively measure the increase in pressure drop. B) The pressure sensor was connected to the buffer ends using a T shaped connector and reading was recorded for 12 min with the pump on. The pressure drop reportedly increased from ~4000 Pa to ~60,000 Pa for the time the pump was on. Once the vacuum was disconnected the pressure increased to the atmospheric level for the next 8 min of the recorded time interval..... 160

Figure 5.19 Graph showing the effect of varying the forward flow to the number of peaks obtained. The device was set up to simultaneously have a withdrawal using a vacuum pump. The data was recorded for a period of 300 s... 161

Figure 5.20 A) Representative data trace showing the SARS stock diluted 100 X times. The events are shown as peaks showing a drop in the current amplitude. The threshold is set to 65 pA, beyond which the peaks are considered as events. Two random events (a) and (b) are magnified showing the peak amplitudes of 250 and 300 pA respectively. B) The peak amplitude histogram showing the distribution of the event amplitudes is shown. The amplitudes range from 66 pA to 1000 pA, with an average amplitude of 204 pA. C) The half-width of the peaks showing the width at FWHM corresponding to the events obtained in the peak amplitude graph. The half-width in ms ranges from 0.02 to 3 ms, with an average half-width of 0.6 ms. 163

Figure 5.21 A) Processed representative data trace of dilution A (520,000 VPs/mL) with events spanned over a 30 s time interval. The peak shape of one event in magnified that shows a peak amplitude of 264 pA and a half-width of 0.02 ms. B) Histogram showing the distribution of peak amplitudes with an average peak amplitude of 307 pA. The SD threshold was set to 224 pA, only beyond which the peaks were counted as events. C) The half width distribution of the events is shown with events ranging from 0.02 ms to 0.10 ms, having an average half-width of 0.031 ms... 164

Figure 5.22 A) NTA results of SARS CoV-2 VPs diluted 30X showing the size distribution of the particles (average ~43 nm) and the concentration, from which he concentration of the original stock is estimated to be 7.8×10^9 particles/mL. B) The dilution ID with the corresponding concentration of VPs/mL used for the calibration curve. C) Results of the calibration curve calculated from nCC showing the VPs concentration/mL and the events detected in a 30 s time interval for various dilutions. 166

Figure 5.23 A) Processed data showing the negative control, blank 1X PBS for a period of 100 s, with no apparent events crossing the threshold. The magnified image of the 1X PBS for a duration of 0.01 s is correspondingly shown. B) Representative data trace of dilution A (52,000 VPs/mL) with events spanned over the same 100 s time interval. (a) The peak shape of a negative event is magnified that shows a peak amplitude of 255 pA and a half-width of 0.02 ms. (b) shows a negative event with a positive shoulder (biphasic pulse) having an amplitude of 420 pA and a half-width of 0.02 ms. (c) shows a negative and positive event occurring in a close interval (0.29 ms). Magnified images of the event are shown where the positive pulse has an amplitude of 229 pA and a half-width of 0.03 ms, followed by the negative event having an amplitude of 230 pA and a half-width of 0.02 ms..... 168

Figure 6.1 Commonly used sample processing techniques used for NGS. Steps 1 and 2 remains common for most NGS techniques, while step 3 shows steps specific for each type of NGS technique chosen. The figure explains

sequencing by synthesis, pyrosequencing, and sequencing by ligation. **Adapted from https://www.abmgood.com/marketing/knowledge_base/next_generation_sequencing_introduction.php** 179

Figure 6.2 A) Schematic showing the overall X-TOF sensor that features the nanotrap for storing the nucleic acids, the solid phase bioreactor for immobilizing the target, and the TOF nanochannel that features two in-plane pores. B-C) The entire process of the SM sequencing in X-TOF takes place in 5 steps and is represented in a flow chart in (B) and a schematic in (C); 1) The XRN1 enzyme is immobilized to the bioreactor; 2) The DNA/RNA molecule is driven for immobilization in the bioreactor containing the XRN1 enzyme. 3) The Mg^{2+} cofactor is added to activate the enzyme. 4) The XRNI that is activated, starts clipping the nucleotides one by one. 5) The clipped nucleotides are electrokinetically driven into the flight tube and is identified by the current drop and the TOF. 181

Figure 6.3 A) COMSOL simulations of the electric field strength profiles of the 3 inlet designs (i,ii,iii) is represented with their corresponding line graphs (B). A-B) The design (i) inlet has an abrupt increase in field strength right at the entrance of the nanochannel. The design (ii) has a narrower inlet where the entrance to the nanochannel is more gradual and the electric field is seen extending out of the nanochannel. The design (iii) has pillars that only helps to unravel the DNA/RNA molecules before entering, but also helps in reducing the entropic barrier. The field strength extends further towards the pillars, which shows a step wise increase in field strength. 183

Figure 6.4 A) The schematics of the different offset percentages and how the position of the inlet/outlet microchannel varies with respect to the bioreactor. B) The velocity profiles of the different offset conditions show the areas in the bioreactor that would be accessible to the DNA that is introduced. As the offset percentage is increased, the accessibility area decreases. C) The corresponding electric field strength profile showing the field strength in the areas of the bioreactor corresponding to the offset conditions. 184

Figure 6.5 Effects of voltage on DMD RNA translocation velocity. A) The velocity of the translocating nucleic acids was evaluated a voltage of 1V. It takes 12.96 ms for the DMD RNA to reach the bioreactor; B) At 3V, the RNA translocates much faster, where it takes only 4.32 ms for the reactor. A higher velocity is seen from the scale bar. C) At 5V, RNA translocates even faster, where it takes only 2.6 ms to reach the bioreactor. D) The simulated particles at different regions in the X-TOF device is shown. The table below corresponds to the time it takes for the particles to reach the designated region at the given voltages. 185

Figure 6.6 Effect of voltage to control the velocity and field strength of introducing Mg^{2+} to the bioreactor. A) The effect of voltages on the velocity of cofactor injection. At higher voltages, there is a significant increase in the velocity

at which the Mg^{2+} is introduced. The increase in velocity at higher voltages can be seen in the scale bar. The arrows are proportional to the velocity. At 5V velocity, the arrows are much larger than those at 3V and 1V. The direction of arrows indicates the direction of injection. B) The corresponding increase in field strengths at higher voltages (1,3 and 5V) is seen. The field strength is highly restricted to the bioreactor indicating the possibility of the cofactor to bleed outside. Refer the scale bar for the absolute values corresponding to the scale..... 186

Figure 6.7 Effect of voltage on translocation of rAMP from the bioreactor after it has been cleaved by the XRN1 enzyme. They are driven into the flight tube electrokinetically by applying voltage. A) At 1V, the rAMP molecule simulated takes about 2.1 ms to reach the first pore and 5.92 ms to reach the second pore (see the table). B) At 3V, they take only 0.72 ms to reach the first pore and a 2.04 ms to the second pore, giving a TOF of 1.32 ms. C) At 5V, it takes 0.44 ms and 1.2 ms to reach the first and second pore thus giving a TOF of 0.76 ms. D) The particle tracing results showing the position of the particles at various positions on the device: 1- Bioreactor, 2- When they start moving into the flight tube, 3- first pore, 4-second pore. The time at which the simulated rAMP molecules reach the designated regions at different voltages is given in the table. 187

List of Tables

Table 1.1. Scaling laws for detection volumes, considered for an aqueous solution of a rhodamine dye (D = 2.8×10^{-10} m^2 s^{-1}, concentration = 1.7 nM) (Reproduced from Liu *et al.*, 2011 [2]). 1

Table 5.1 Figures-of-merit for RPS sensors for the detection of nanoparticles, including virus particles. 134

Table 5.2 Dilution factors of the SARS CoV-2 stock solution used for the calibration curve **(Iteration 1)** 138

Table 5.3 The dilution factors of the SARS CoV-2 stock solution with clinically relevant concentration based on the results from NTA **(Iteration 4)** 139

List of Equations

Equation 1.1. $Pv = CNAP$ 2

Equation 1.2. $Pm = Km\exp - Km!$ 2

Equation 1.3. $P = \pi\omega022z$ 3

Equation 1.4. $\omega0 = 2\lambda f\pi d$ 4

Equation 1.5. $DOF = \lambda\, nNA2$ 4

Equation 1.6. $vEOF = -\varepsilon0\varepsilon r\zeta w\eta E$ 10

Equation 1.7. $kd - 1 = \lambda D = \varepsilon0\varepsilon rkBT2ni\infty ze2$ 11

Equation 1.8. $\lambda D = 3.04zM \times 10 - 10\, m$ 11

Equation 1.9. $Rg \cong R6 = P * w15L35$ 14

Equation 1.10. $rdeGennes = LcwPDavg213$ 15

Equation 1.11. $rOdijk = Lc\cos\theta = Lc1 - 0.361DavgP23$ 16

Equation 1.12. $cy = cbulk.e - ze\psi ykBT$ 16

Equation 1.13. $P = Po + ¼k2lb = Po + 0.0324MI\, nm$ 27

Equation 1.14. $lt = le + lo - le \exp(-5\text{kB}TD138\pi\eta L2pw23t)$ 34

Equation 4.1. $\mu app = v_{app}/E$ 117

Equation 4.2. $v_{app} = l/\Delta t$ 117

Equation 5.1 Infinitely small diameter particle: $\Delta RR = d3D2L$ 132

Equation 5.2 Small diameter: $\Delta RR = d3D2L[D22L2 + 1\sqrt{(1 + DL2)}]\, F(d3D3)$ 132

Equation 5.3 Medium diameter: $\Delta RR = d3D2L.1\,1 - 0.8dD3$ 132

Equation 5.4 Large diameter: $\Delta RR = DL[\arcsin dD\sqrt{(1 - dD2)} - dD]$ 132

Chapter 1: Introduction, Basic Concepts, Fabrication, and Important Applications of Single Molecule Analysis in Nanofluidics

1.1 Introduction

Micrometer and nanometer channels reduce sampling volumes and at the same time, reduce analysis times allowing for near real time measurements, even at the single-molecule level [1]. The reduced sampling volume also increases the chances of detecting single molecules as the signal-to-noise ratio increases (Table 1). The requirement to use smaller sampling volumes has led to the development of nanofluidic platforms, including one dimensional (1D) structures such as nanoslits, two-dimensional (2D) structures such as nanochannels, and 3D structures such as nanopores. Table 1 shows the number of molecules resident within a sampling volume when the dimensions of the sampling volume decreases (d = probe volume single dimension). The fluorescent signal of a single molecule is independent of the dimensions of the detection volume and remains constant (see Table 1). In contrast, the background signal generated by impurities, Rayleigh and Raman scattering decreases with decreasing detection volume. This enhances the signal-to-noise ratio and facilitates the detection of single fluorophore molecules residing within the detection volume. Confinement in a smaller volume increases the observation time for a single molecule, allowing for more exacting measurements [2].

Table 1.1. Scaling laws for detection volumes, considered for an aqueous solution of a rhodamine dye (D = 2.8×10^{-10} m^2 s^{-1}, concentration = 1.7 nM) (Reproduced from Liu *et al.*, 2011 [2]).

Dimension (d)	100 µm	10 µm	1 µm	100 nm	10 nm
Volume d^3	1 nL	1 pL	1 fL	1 aL	1 zL
Number of molecules	10^6	10^3	1	10^{-3}	10^{-6}
Fluorescence signal per molecule	1 a.u.	1 a.u.	1 a.u.	1 a.u.	1 a.u.

Fluorescence signal per molecule/background signal	10^3 a.u.	10^6 a.u.	10^9 a.u.	10^{12} a.u.	10^{15} a.u.
Diffusion time of a molecule over *d*	1.8×10^4 ms	1.8×10^2 ms	1.8 ms	1.8×10^{-2} ms	1.8×10^{-4} ms

For the detection of single molecules, the probability of occupancy within the probe volume should be smaller than unity. The probability (P_v) of a mean number of molecules occupying the probe volume can be calculated from;

Equation 1.1. $$P_v = CN_AP$$

where C is the molecular concentration (mol L^{-1}), N_A is Avogadro's number, and P is the probe volume size (L) [3]. Instantaneous occupational probabilities of molecules within the probe volume can also be calculated from the Poisson distribution [4];

Equation 1.2. $$P(m) = \frac{K^m \exp(-K)}{m!}$$

where K is the mean number of molecules per probe volume (*see equation 1*), and m represents the instantaneous number of molecules within the probe volume (*e.g.*, $P(1)$ represents the probability of one molecule existing in the probe volume, $P(2)$ represents the probability of double occupancy).

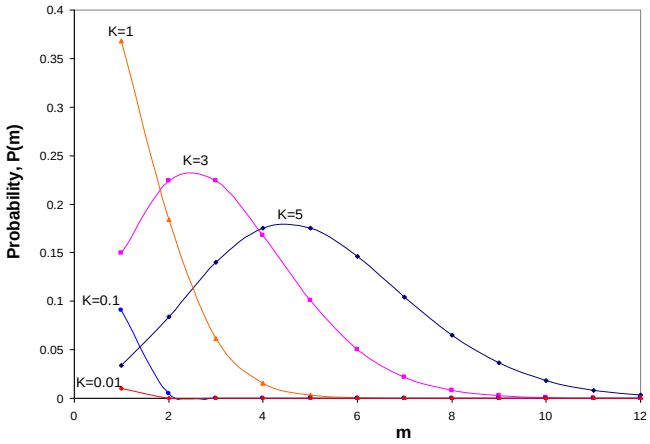

Figure 1.1 Poisson distribution probability of finding *m* molecules in a probing volume for different values of the average molecular occupancy, K.

Figure 1.1 shows the Poisson probability distributions for different values of K. We can see in this figure that when the average molecular occupancy K = 1, the probability of detecting multiple molecules dominates. When K decreases to 0.1, the probability of detecting one molecule $P(1)$ is reduced to 0.09, while the probability of detecting two molecules $P(2)$ is reduced to 0.0045, giving a $P(1)$ to $P(2)$ ratio of 20, which suggests that among 20 detected single molecule events, there is about one event resulting from 2 molecules. When K further decreases to 0.01, $P(1)$ is reduced to 0.01 and $P(2)$ is reduced to 5 x 10^{-5}, giving a $P(1)$ to $P(2)$ ratio of 200, which suggests that >99% of the events recorded arise from single molecules. Thus, a molecular occupancy of 0.01 is usually selected as the criteria when performing single molecule detection experiments.

From equation 1, there are two methods to assure that single molecule experiments are carried out under conditions where K < 0.01; reduce the analyte concentration or reduce the probe volume size, P. For the probe volume size, optical monitoring for the detection of single molecule events, P, is defined by the excitation laser beam size ($1/e^2$ intensity), ω_0, and is given by

Equation 1.3. $$P = (\pi\omega_0^2)(2z)$$

where the symbols are defined in Figure 1.2.

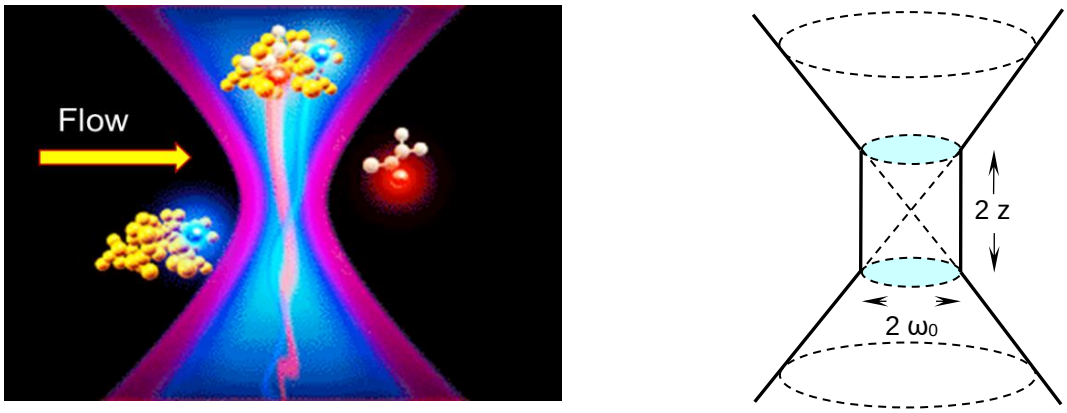

Figure 1.2 Left – Schematic of a focused laser beam serving as the excitation source with the probe volume, P, defined by the laser beam waist size, ω_0. Right – Drawing of the probe volume assuming a cylindrical geometry, and the terms defining its volume, P (see equation 3).

The beam waist and thus the probe volume size is typically determined by the diffraction-limited focusing of the excitation beam, which can be approximated from the wavelength of the excitation light (λ), and the properties of the focusing optic (NA – numerical objective or focal length, f):

Equation 1.4. $$\omega_0 = \frac{2\lambda f}{\pi d}$$

where f is the focal length of the relay optic and d is the diameter of the beam before the relay optic (this is based on epi-illumination in which the focusing optic is also used for collecting the resulting optical signal). Assuming an excitation wavelength of 532 nm, ω_0 would be 10.6 µm. To determine z (see equation 3) to calculate the probe volume size, we can assume z is determined by the relay optic's depth of focus (DOF) (see equation 5; assumes that the detector spatial resolution is small).

Equation 1.5. $$DOF = {\lambda n}/{NA^2}$$

Assuming an air-immersion objective (n = 1.00), 532 nm excitation, and a 100X objective with a NA = 1.1, inserting these values into equation 5 produces a DOF of ~0.4 µm. Using the DOF of 0.4 µm and a beam waist of 10.6 µm would produce a probe volume of 35 μm^3 (35 fL). In Figure 1.3 is plotted the average single molecule occupancy for different beam waist sizes assuming a DOF as noted above. As can be seen, to keep the double occupancy probability below 1% at all probe volume sizes will require a molecular concentration less than 1 pM (beam waist < 70 µm).

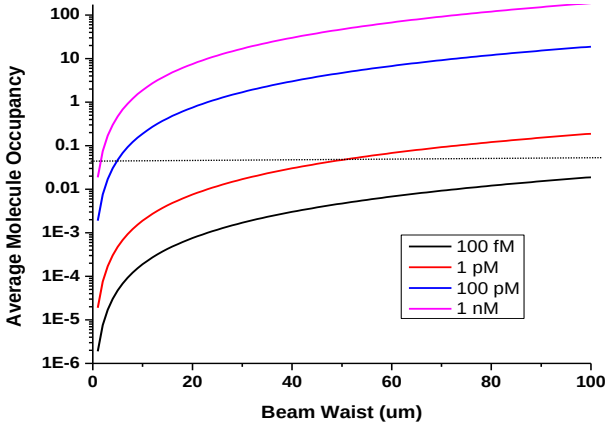

Figure 1.3 Plots of the average molecule occupancy (P_m) as a function of the excitation beam waist. (ω_0). The calculations used equations 5 (DOF ~0.4 µm), 4, 3 and 1. The y-axis was plotted on a log scale, while the x-axis was on a linear scale. The dashed line represents the average molecular occupancy of 0.1 so that the probability of double occupancy is 1%.

The challenge with using diffraction limited probe volumes required when using optical monitoring of single molecule events is that the concentrations required are relatively small and as such, challenges can result when biological systems must be studied. For example, in the case of biological enzymes studied at the single molecule level to obviate issues with ensemble averaging, the low concentration requirements to assure the monitoring of single molecules in the probing volume can generate issues with mechanistic pathways due to the relatively high Michaelis-Menten constants (mM - µM) requiring high ligand concentrations. Therefore, it is advantageous to consider alternative methods to restrict the probe volume besides diffraction-limited probe volumes.

Nanofluidics is a field of research in which synthetic boundaries are imposed on the probing volume, with the dimensions typically being below the diffraction limit. These sub-diffraction boundaries can be produced by nanostructures that can range in size from <10 nm to ~100 nm. For example, it is not uncommon in the area of nanofluidics to create channels with dimensions that are 50 nm x 50 nm (width x depth). For epi-illumination using a laser beam with a waist of 10 µm, the probing volume here would be 2.5×10^7 nm^3 (25 aL). At this probe volume size, a concentration of 6.7 nM could be employed in the single molecule experiment to generate an average occupancy of 0.1.

Several techniques have been reported for producing nanostructures. These include photolithography, electron beam lithography (EBL), focused ion beam (FIB) milling, and nano-imprint lithography (NIL). Different substrates ranging from silica (Si), glass (SiO_2), polydimethyl-siloxane (PDMS), and thermoplastics have been used with the appropriate fabrication methods [3]. Some examples of nanochannel fabrication include the use of NIL with mold fabrication to achieve uniform channels in the range of 11- 50 nm [5]. FIB and EBL were mainly done on materials like Si, SiO_2 to achieve 2D structures up to 50 nm, while NIL combined with reactive ion etching (RIE) can be used to achieve dimensions close to 10 nm. Although nanochannels with 10-nm dimensions are achievable, higher cost of production, low throughput and pattern limitations are drawbacks.

Craighead *et al.* were able to fabricate 20-nm channels using size-reduced electrospun nanofibers [5], but the method was limited by the lack of precise control of the nanochannel dimensions [5]. Hence, thermoplastics have been used to build nanostructures via NIL, which provides dimensional flexibility while offering low cost and high throughput generation of devices. This was demonstrated by Wu *et al.*, who fabricated poly(methyl methacrylate), PMMA, devices imprinted from a polymer stamp using NIL [5]. A hybrid microfluidic-nanofluidic device with structures of 20 nm depth were achievable at low cost [5]. Subsequently, Uba and co-workers [6] investigated the use of thermoplastic devices to study about DNA translocation and further exploited the use of cyclic olefin copolymer (COC) and PMMA to produce nanofluidic devices that were useful for fluorescence imaging at high signal-to-noise ratios [7]. Recently,

Weerakoon-Ratnayake *et al.* [1] discussed the use of thermoplastics like PMMA, COC, and PC for nanofluidic devices and their applications in single molecule DNA translocation measurements.

Confinement of nucleic acids, such as double-stranded (ds) DNAs, in nanometer domains allows the dsDNA to undergo a conformational change from its natural coiled structure to a "rod-like" structure with stretching to different percentages with respect to its full contour length depending on the nanochannel geometry. This becomes important and useful as many potential applications use DNA linearization in nano-dimensional devices to interrogate to allow structural interrogations, such as single base mutations. Longer nanochannels have also been used to separate DNA and SDS-protein complexes based on their molecular weights [1]. Electrokinetic separation has been used to separate fluorescently-labelled dsDNA by analyzing the order of their migration through nanochannel devices [1]. Enzymatic reactions using restriction endonucleases have been exploited for restriction mapping of DNA in nanochannels with dimensions ranging from 100 – 200 nm [1]. Optical barcodes with fluorescently labelled sequence motifs obtained from stretched DNA were acquired to study bacterial artificial chromosome (BAC) clones [1]. In addition, single-molecule detection (SMD) has been used to identify methylation patterns in stretched dsDNA to identify specific diseased genes, to investigate DNA-protein interactions, single molecule DNA sequencing, and to analyze DNA damage [8].

In this chapter, we will review important single molecule phenomena that occurs within restricted domains with dimensions less than 150 nm, the fabrication methods used to develop those nano-dimensional devices, the required instrumentation necessary to obtain single molecule readouts using nanofluidic platforms, and applications of single-molecule analysis in nanochannels.

1.2 Unique physical phenomena in confined environments with nanometer critical dimensions

Here we consider a critical dimension of less than 150 nm as the relevant length scale for nano-structures. In the context of lengths less than 150 nm, several unique phenomena occur. In this restricted domain, single molecules can be monitored to investigate unique molecular characteristics or for simple detection.

1.2.1 Nanoslits (1D), nanochannels (2D) and nanopores (3D)

We will define here structures with <150 nm can be classified as nanoslits (1D), nanochannels (2D), or nanopores (3D). As the number of dimensions associated with the nanostructure increases (1D – 3D), the complexity of device fabrication increases. As such, distinct observations for single molecules in a nanometer device arises from a range of surface forces acting on the molecule [9]. Nanoslits have one dimension at the nanoscale, usually the depth of the channel. Nanochannels have their width and depth in the nanometer dimension, and hence form a more restricted environment due to boundary conditions. Compared to 1D and 2D nanodevices, nanopores have a 3rd dimension at the nanoscale, thus creating higher resistance for the liquid passing through a region where surface charges and physical barrier forces dominate. At this level, it has been observed that fluid-particle behavior deviates from normal expectations observed in bulk fluids [10-11].

1.2.2 Sense-of-scale

Within the nanodomain, the physics of the flowing liquid changes as the surface-to-volume ratio increases. Because of this, overall flow dynamics become dependent on surface roughness and surface chemistry [11-17]. Although Poisson-Boltzmann equations can be used to describe electrokinetic flow in microchannels, this approach is not completely valid for electrokinetic flows in nanochannels because co-ions and counterions are not equally distributed [18]. Although, it can be used to get an approximation. This partly due to electrical double layer (EDL) overlap. EDL in nanochannels is usually generated due to the charged groups on the surface attracting counter ions from the surface (this will be explained in detail later

in the chapter). Therefore, theories applicable to micron or larger scales cannot be directly applied to nanofluidics.

1.2.3 Surface charge effects

Surface charge originates from surface groups present on the nanochannels. Figure 1.4 shows the charge distribution from co-ions and counterions at the surface. Surface groups repel co-ions and attract counterions to build a net charge distribution. This surface charge is mainly defined by the zeta potential, which is the potential at the shear plane. The boundary where the compact Stern layer ends is defined as the shear plane. The zeta potential is the difference in potential between the Stern layer (the compact, immobile layer at the channel surface) and the mobile, diffuse layer.

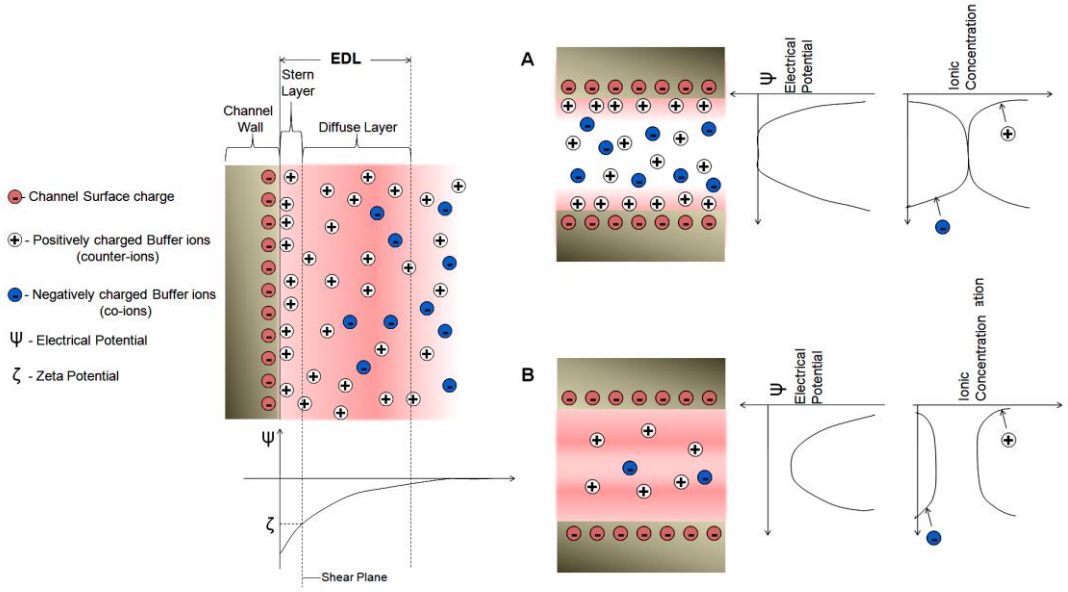

Figure 1.4 Model representation of the electric double layer at a solid-liquid interface at a negatively charged solid surface/channel wall. The electric potential and ionic concentration versus distance from the surface is illustrated for channel filled with A) a moderately high electrolyte concentration (and/or large channel height [$h > \lambda_D$]) and B) a relatively low electrolyte concentration (and/or small channel height [$h \leq \lambda_D$]) (Reproduced from Lyklema J., 1995 [19])

1.2.4 Electroosmotic flow (EOF) and electric double layer (EDL)

Electroosmotic flow (EOF) and EDL are two critical parameters associated with nanoscale fluid dynamics. EOF was first observed by Reuss [20] and Wiedemann [21]. Theories of the EDL and electrokinetic transport phenomena were developed by researchers such as Helmholtz [13] and Smoluchowski [22]. Existing theories of the EDL such as those of Helmholtz [23], Gouy [22], Chapman [24], and Stern [25], provide an

understanding of the EDL. Gouy-Chapman introduced a model for the diffuse layer, and Stern modified it and combined it with the model introduced by Helmholtz in the Gouy-Chapman-Stern (GCS) model [26]. This model states that the EDL consists of two main layers; a compact layer called the Stern layer and the other being a mobile, diffuse layer. The outer boundary of the Stern layer was named the Outer Helmholtz Plane (OHP). Figure 1.4 represents the two layers discussed and the potential drop across the layers.

A fluid in contact with the channel surface spontaneously acquires an EDL near the channel surface. Co-ions, which have the same charge as surface ions, are repelled from the surface, whereas counterions, which have the opposite charge, are attracted to the channel surface. This results in a net charge near the channel surface (diffuse layer) characterized by the zeta potential. The net charge generated in the diffuse layer moves along the channel wall. This flow, dominated by viscous drag, is called the EOF. The double layer is in the nanometer range and thus, negligible when considering fluid flow in microchannels (see Figure 1.5). However, in the case of nanochannels, the EDL plays a role in fluid transport because the EDLs from opposite channel walls overlap, as discussed below.

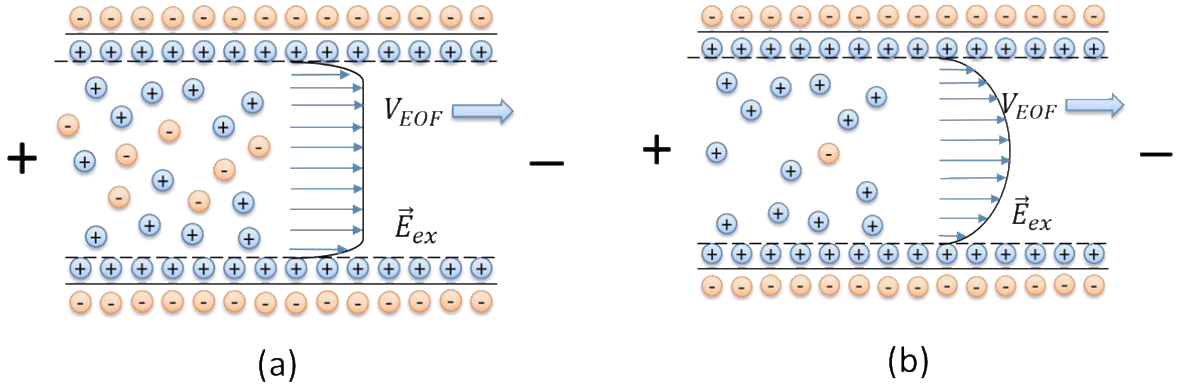

Figure 1.5 Schematic of EOF in a microchannel and in a nanochannel. (a) Plug-like EOF velocity profile in a microchannel without overlap of EDL. (b) Parabolic-shaped velocity profile in a nanochannel with overlapped EDL (Reproduced from Peng, R., 2018 [27]).

The Helmholtz-Smoluchowski equation derived to calculate the EOF in microchannels is [13, 28];

Equation 1.6. $$v_{EOF} = -\frac{\varepsilon_0 \varepsilon_r \zeta_w}{\eta} E$$

where ζ_w is the zeta potential, η is the viscosity of the electrolyte, and E is the external electric field applied.

An electric field applied in a channel filled with ionic fluids will generate a bulk flow called the EOF. Here, the ions in the mobile layer with co-ions start to travel towards an electrode. A positive EOF is generated when the bulk flow is moving from anode to cathode and the reverse for a negative EOF (see Figure 1.5). For example, when the walls are negatively charged, positive counter ions will be attracted towards the wall creating a strong compact Stern layer. The excess cations close to the channel walls at the bulk solution move towards the cathode and generate a positive EOF from anode to cathode. EOF is mainly dependent on the charge of the channel walls, the applied electric field, and the ionic solution with which the channels are filled [10, 22-23, 29].

In nanometer domains, electrokinetic theories combined with the Boltzmann distribution and Poisson-Boltzmann equations are not directly applicable. The EDL generated by the co- and counterions usually have a thickness of a few nanometers. In the case of nanochannel domains, the two layers generated at opposite walls can partially overlap. EDL overlap restricts the use of electrokinetic theories and force us to develop new theories to describe EDLs in the nanoscale.

The EDL thickness is characterized by the Debye length, which can be calculated by [29-32]:

Equation 1.7. $$k_d^{-1} = \lambda_D = \sqrt{\frac{\varepsilon_0 \varepsilon_r k_B T}{2 n_{i\infty} (ze)^2}}$$

The Stern layer extends to around 3-5 times the Debye length. For a symmetric monovalent electrolyte, the equation can be modified as;

Equation 1.8. $$\lambda_D = \frac{3.04}{z\sqrt{M}} \times 10^{-10}\ (m)$$

where M is the molarity of the electrolyte solution. The EDL when overlapped, which can occur in nanometer structures, can generate Poiseuille-like flow because of partial overlap in the EDLs. This results in analytes spending more time migrating with the EDL (Figure 1.5-B) compared to analytes in microchannels (Figure 1.5-A), and this in turn affects separation in nanochannels [33].

1.2.5 Electrokinetic versus hydrodynamic pumping at the nanometer scale

In a length-scale <150 nm, distinct and unique forces dominate the fluidic properties. These forces include electrostatic, van der Waals, and steric interface forces. Not only does the dominating forces change

when approaching the nanoscale, but the driving forces of fluid/particle and wall/particle interaction physics changes completely as well.

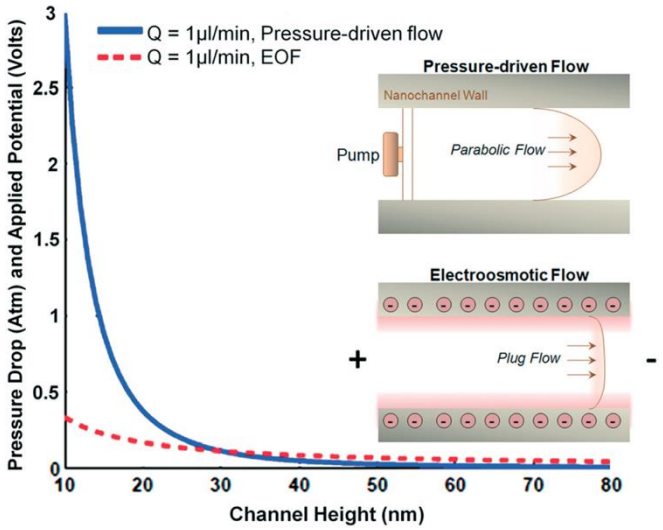

Figure 1.6 Required pressure drop (to generate pressure driven flow) and voltage drop (to generate EOF) to transport fluid through nanochannels with different channel heights. Nanochannel length and width are 3.5 µm and 2.3 µm, respectively; zeta potential is −11 mV for 1 M NaCl solution. (Reproduced from Conlisk *et al*., 2005 [34]) Insert shows the comparison between the parabolic and plug flow profiles from the pressure-driven and electroosmotic flow, respectively.

The phenomena discussed above leads to unique transport characteristics on the nanoscale deriving from the increased surface-to-volume ratio. Figure 1.6 shows the nanochannel height versus the pressure drop and applied potential drop across the nanochannel [7]. It is understood that dominant forces in microscale flow, such as pressure, gravity, viscosity, and inertia are replaced on the nanoscale by the more dominant interfacial forces such as surface tension and capillary forces. As can be seen from the figure, at lower nanochannel heights such as 10 nm it will be impossible to transport fluids through nanochannel via pressure driven flow. Compared to a ~500-fold increase in pressure (from 0.006 to 3 atm), when the channel size is reduced from 80 nm to a 10 nm, the required ~5.6-fold increase in the voltage drop across the channel is easier to handle at this scale. Thus, electrokinetic flow alone is used to fill the nanochannels and transport biomolecules through the nanochannels.

1.2.6 Nanometer confinement and stretching of single DNA molecules

DNA is the most common biopolymer that has been studied in nanochannels because of its unique physical conformation and stretching when it is confined to nanoscale domains. Recently, it has been reported that a DNA molecule in a nanochannel will stretch along the channel axis to near its full contour length [7]. Confinement elongation of long DNA fragments has several advantages over alternative techniques for extending DNA, such as flow stretching and/or stretching relying on a tethered molecule. Confinement elongation does not require the presence of a known external force because a molecule in a nanochannel will remain stretched in its equilibrium configuration, and hence, the mechanism is in equilibrium with the degree of stretching dependent on the channel dimensions (width and depth). It also allows for continuous measurement of length [7]. Single DNA confinement, dynamics, and conformations were extensively studied by Reisner and coworkers [7]. The physical geometry of double-stranded DNA is explained by three main parameters; the contour length L_c, the persistence length P, and the effective width w (see Figure 1.7). The total length of the DNA when it is stretched to its full length is its contour length. The local rigidity of the double helical structure is described by the persistence length [35-37]. When the DNA molecule is confined to a length scale less than P, it will act as a rigid rod, while it is flexible at lengths higher than P. Manning *et al.* [34] reported a persistence length P of ~50 nm and an effective width w ~2 nm for a dsDNA in 0.1 M aqueous NaCl solution.

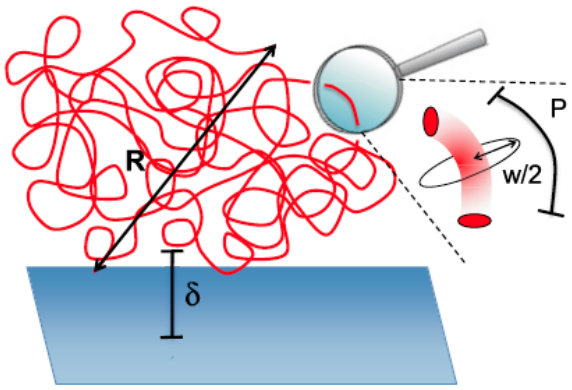

Figure 1.7 Cartoon illustration of a coiled DNA in a showing its full unfolded length (R), persistence length (P), effective width (w) and depletion width between the wall and the DNA molecule (δ) (Reproduced from Reisner *et. al.*, 2012 [32])

Flory *et al.* [34] introduced the concept of self-avoidance of a biopolymer such as a dsDNA confined in a finite volume. As DNA is negatively charged, when it is in solution it will occupy a finite space repelling any other molecules trying to occupy the same space by the steric hindrance [33, 38]. Schaefer *et al.* [32] extended the theory to the semi-flexible case. The resulting Flory-Pincus equation for the radius of gyration (R_g) of a self-avoiding polymer is;

Equation 1.9. $$R_g \cong \frac{R}{\sqrt{6}} = (P * w)^{\frac{1}{5}} L^{\frac{3}{5}}$$

where R is the end-to-end length. For most common DNAs, such as lambda DNA (48.5 kbp) and T4 DNA (169 kbp), the calculated R_g is ~560 nm and ~1140 nm, respectively.

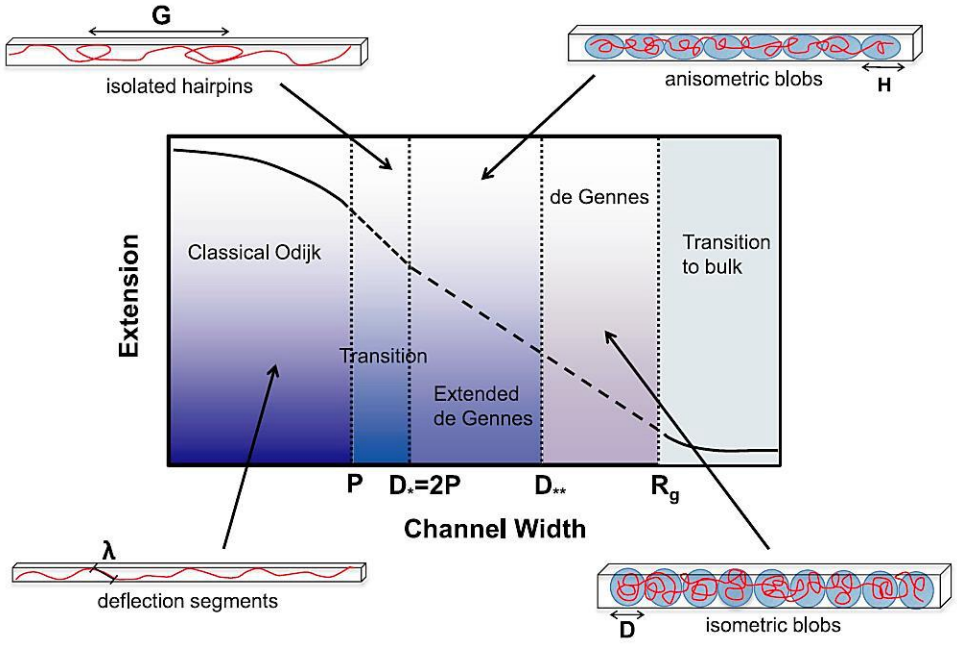

Figure 1.8 A representation of the physical regimes when DNA is confined in a nanochannel environment. It takes the form of isometric Flory blobs in the deGennes regime. The region between D=D** and D = D* = 2P is defined as the extended deGennes regime where the molecule takes both the forms of ideal and Flory behavior producing anisometric Flory blobs. When the channel size decreases from D = D* = 2P, DNA molecule takes the shape of an isolated hairpin at a transition with back bended regions until the channel length D=P. The identified classic Odijk region where D<P, the molecule completely stretches to its contour length where it makes deflection lengths with the wall denoted by λ (Reproduced from Reisner *et. al.*, 2012 [39]).

In solution where there exists a large volume of space (compared to R_g), DNA takes a coiled form called a "Pincus blob" [40]. When it is confined in to a nano-domain, DNA stretches to a fraction of L_c along the

channel axis. Nano-domain size is defined by the geometric average depth from the two confined dimensions; $D = \sqrt{d \times h}$. A Pincus blob can be separated into separate blobs called isometric blobs when D is larger than P. These blobs repel each other, causing the DNA stretch inside the nanochannel in a manner characteristic of the de Gennes regime (Figure 1.8) [33]. The de Gennes regime extends down to D = D**, below which the geometry of the blobs is perturbed resulting in different shapes. These shapes in the extended nano-region are called anisometric blobs [32, 41].

Confinement forces are weak as they help to keep the blobs apart while keeping its original form of the polymer. The length of extension (r) in the de Gennes regime can be calculated using the equation;

Equation 1.10. $$r_{(deGennes)} = L_c \left(\frac{wP}{D_{avg}^2}\right)^{\frac{1}{3}}$$

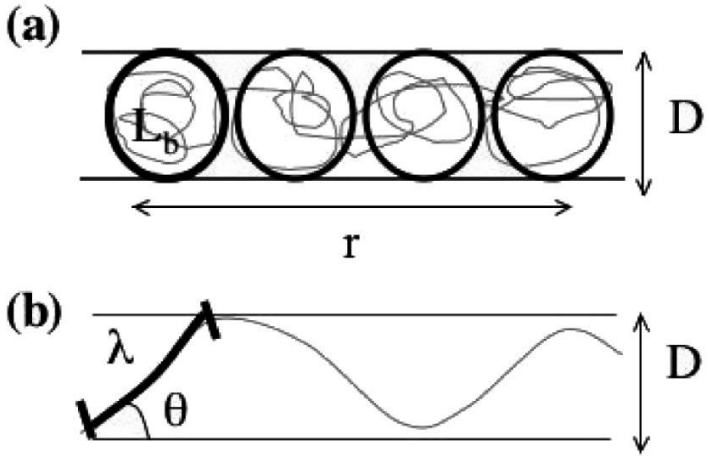

Figure 1.9 (a) Schematic shows a DNA molecule confined in de Gennes regime where D>>P. There is a series of self-repulsive isomeric blobs with a defined contour length L_b. (b) DNA molecule confined in Odijk regime where D<<P. Odijk length is given by λ_p and the average deflection angle is denoted by θ. (Reproduced from Reisner *et. al.*, 2005 [42])

The regime in which $D < P$ is called the Odijk regime (Figure 1.9). When D is decreased below P, stretching is based on the elasticity of the DNA molecule and the confinement, which prevents formation of loops inside the nanochannel. The energy barrier becomes too high for back-folding to occur. Thus, the molecule stretches along the channel wall as a result of deflection. The average deflection length on the Odijk length scale is given by $\lambda \cong (D^2 P)^{1/3}$. The average stretching in the Odijk regime is given by [41, 43]:

Equation 1.11. $$r_{(Odijk)} = L_c \cos\theta = L_c \left[1 - 0.361 \left(\frac{D_{avg}}{P}\right)^{\frac{2}{3}}\right]$$

Reports show that, apart from these two main regions identified for stretching, there are other segmented regimes such as extended de Gennes region (up to $D = 2P$) and transition regions ($P < D < 2P$) where the DNA molecule takes different forms such as isolated hairpin [44-45].

1.2.7. Shaping electrical fields

One important factor to affect single molecules motion through nanochannels by shaping the electric field applied across the nanochannels. By shaping the electric field, it is possible to control translocation events of single molecules within the nanodomain [8, 10]. However, shaping the electrical fields in combination with different sized channels, researchers have been able to control the physical characteristics of single DNA molecules such as relaxation properties [10].

1.2.8. Concentration polarization

As discussed, the EDL is governed by the ion concentration in the nanochannel. As a result of the formed EDL, the ionic concentration near the wall and in the middle of the channel are different compared to the bulk concentration of the electrolyte. Thus, there are excess co-ions in the middle of channel compared to near the nanochannel walls [46-47]. We can use Boltzmann equation to understand these phenomena:

Equation 1.12. $$c(y) = c_{bulk}.e^{(-ze\psi(y)/k_BT)}$$

where c is the concentration, z is the ionic charge, e is the unit charge, k_BT is the thermal energy, y is the coordinate perpendicular to wall and ψ is the electrical potential compared to the bulk [48].

This imbalance of ions of the solution inside the nanochannels creates non-uniformity in the bulk electrolyte within the nanochannel. Thus, in the presence of an applied transverse electric field it generates Poiseuille-like flow. This flow results in trapping of analytes in solution, which leads to a transverse concentration gradients generated by the equilibrium between transverse electromigration and diffusion [49]. These analytes spend much more time migrating through the EDL and the charge of these analytes tends to play a critical role here.

A solution with divalent counterions was found to contain higher ionic concentrations in nanochannels compared to a monovalent solution with the same ionic strength (under the assumption that there is no significant ionic adsorption on the nanochannel walls). In a case of where there is ionic absorption, the EOF in nanochannels will be lower due to the reduced zeta potential as more counterions tend to immobilize near the channel walls [50].

The above discussed phenomena will result in ion-enriched and ion-depleted zones in nanochannels, especially near intersections. The ion flux is thought to be higher due to amplified transport through the EDL and this creates zones with imbalanced ion flux. This phenomenon is explained as concentration polarization, which is most common near inlets and outlets of the channels both in microchannels and nanochannels. But, in the nanodomain at low ionic strengths, the EDL will be thicker, preventing entities from entering the nanochannel and thus acting as a gate These polarization forces create anisotropic diffusivity, which also changes the rate of interaction of ions with the channel walls [51].

1.3 Fabrication of nanochannel devices

There are many published articles on fabricating nanochannel devices using high resolution techniques [7]. Here we briefly discuss selected fabrication techniques most commonly used for nanodevice fabrication. Many organic and inorganic materials are available for nanochannel devices. Inorganic materials include glass, silicon, and silicon nitride, and fused silica. Organic materials include thermoplastics, and elastomers. The fabrication technique chosen depends mainly on the material of choice and the required dimensions of the nanofluidic device.

1.3.1. Fabrication techniques of nanofluidic devices

There have been many reports about the efforts to use standard lithography techniques to fabricate nanochannels [52]. But with standard lithography, it is extremely difficult to fabricate nanochannels with 2 dimensions <100 nm. Photolithography techniques can achieve structures with near nanometer domains by tuning the properties of the photomask and the wavelength of the incident light. With 365-nm ultraviolet light, a size resolution as small as 200 nm can be achieved [53-54]. Deep UV lithography and X-ray lithography

with shorter wavelengths and higher energy have been reported to create features in the 100 nm range [41, 55-56]. In 2013, features of sub-25 nm were reported using X-ray lithography [57].

The two prominent techniques used for nanofabrication are electron beam lithography (EBL) and focused ion beam (FIB) milling. EBL is a widely used technique to fabricate masks containing nanochannel/nanopore structures. Electron beams with energies ranging from 1 KeV to 200 KeV are capable of achieving nanometer spot sizes [58-59]. In theory, using a higher energy e-beam generates a smaller feature size. The smallest nano-feature size achieved by EBL is on the order of 2 nm [60], although it is an expensive technique preventing its use for nanostructure fabrication for larger areas [61]. One drawback of EBL is proximity effects caused by backscattering, which limits its use for producing high-resolution nanofeatures.

Compared to EBL, FIB milling uses an ion beam to produce high-quality, high-resolution nanostructures. FIB has four main functionalities; milling, implanting, ion-induced milling, and ion-induced deposition. It is capable of working with a wide variety of substrates including conductive material [4, 62] (aluminum, gold) and non-conductive materials [63-65] (silicon, silicon nitride, polymer). The main ion source for FIB is a high-energy gallium (Ga^+) ion beam that can displace molecules on the surface allowing for direct milling down to 5 nm. FIB induced deposition (FIB-ID), also known as chemical vapor deposition (FIB-CVD), is another technique to create nanostructures by localizing the chemical vapor. FIB is a powerful nanofabrication technique but suffers from slow scan speeds and it is expensive.

1.3.2 Bonding strategies for nanofluidic devices

The aforementioned techniques for producing nanostructures employ a top-down approach and, as such, require an assembly step to enclose the fluidic network. This consists of bonding a cover plate to the substrate possessing the fluidic network, a process that typically involves heating the cover plate and substrate to a temperature near the glass transition temperature T_g of the material for bonding of materials such as Si, glass, and thermoplastics. This assembly step can involve thermal- or solvent-assisted fusion bonding [66]. Thermal fusion bonding is achieved by either heating the substrate and cover plate to a

temperature slightly above the T_g of the material under constant pressure and time, or bonding at a temperature lower than the T_g coupled with UV/O_3 or O_2 plasma treatment of the surfaces prior to assembly[61, 65, 67-69]. The former approach has been known to result in significant nanochannel deformation while the latter results in devices with weak bond strength. Some polymers such as PDMS and SU-8 photoresist use direct bonding after O_2 plasma [4, 6, 70] or UV treatments [6]. Similarly, solvent-assisted bonding frequently result in dimensional instability due to material embrittlement or dissolution [6]. Unfortunately, these assembly issues can generate low process yield rates, typically <40%. (The process yield rate is the percentage of devices that possess dimensions comparable to design parameters.) The Anodic bonding method (for Si-SiO_2 bonding) uses high electric fields and temperatures [6], while some methods use adhesive layers (water, glue, benzo cyclobutene, glue) to maximize the bonding strength.

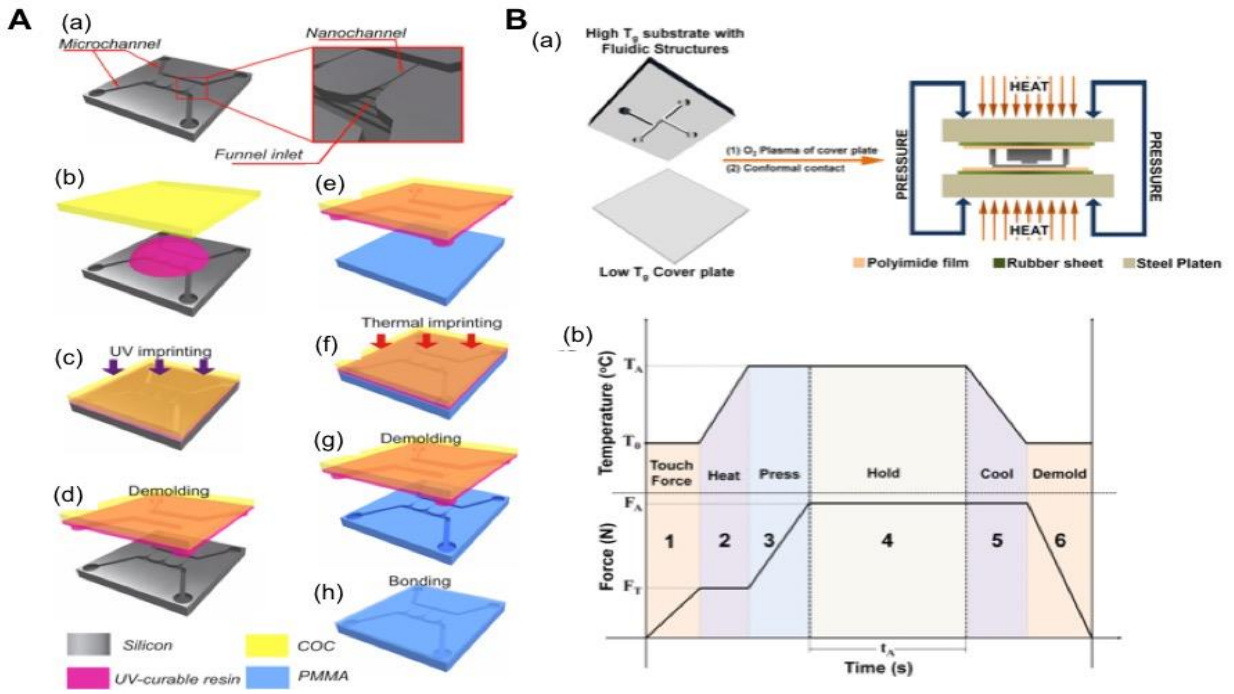

Figure 1.10 (A) A schematic of the design and fabrication process of a thermoplastic-based nanofluidic device. (a) Silicon master, which consists of micron-scale transport channels, nanochannels and a funnel-like inlet for the nanochannels; (b)-(d) fabrication steps to produce a protrusive polymer stamp in a UV-curable resin by imprinting from the silicon master; (e)-(g) fabrication steps to generate nanofluidic structures in PMMA by imprinting from the UV-curable resin stamp; (h) bonding step with a PMMA cover plate to build the enclosed mixed-scale polymer device with microchannels and nanochannels. (B) (a) Schematic of the protocol used for assembly of a hybrid fluidic device and the thermal press instrument. (b) Temperature-pressure process profile showing the six stages for the thermal fusion bonding cycle. See main text for a description of the 6 stages of bonding. (Reproduced from Wu *et al.*, 2011 [6] and Uba *et al.*, 2015 [6])

In a recent report (see Figure 1.10), functional thermoplastic nanofluidic devices were developed at process yield rates >90% using a robust assembly scheme in which a thermoplastic substrate with high T_g was thermally fusion-bonded to a cover plate with a T_g lower than that of the substrate [5]. Device assembly was achieved by bonding a plasma treated cover plate to an untreated substrate at a temperature ~5°C lower than the T_g of the cover plate using a total processing time of 16 min. COC (T_g = 75°C) was used as the cover plate for a PMMA substrate due to its excellent optical transmissivity, low autofluorescence [5], low moisture uptake (< 0.01%), high temperature tolerance, and chemical resistance. Examples of nanofluidic devices made from thermoplastics and assembled using this method are shown in Figure 1.11.

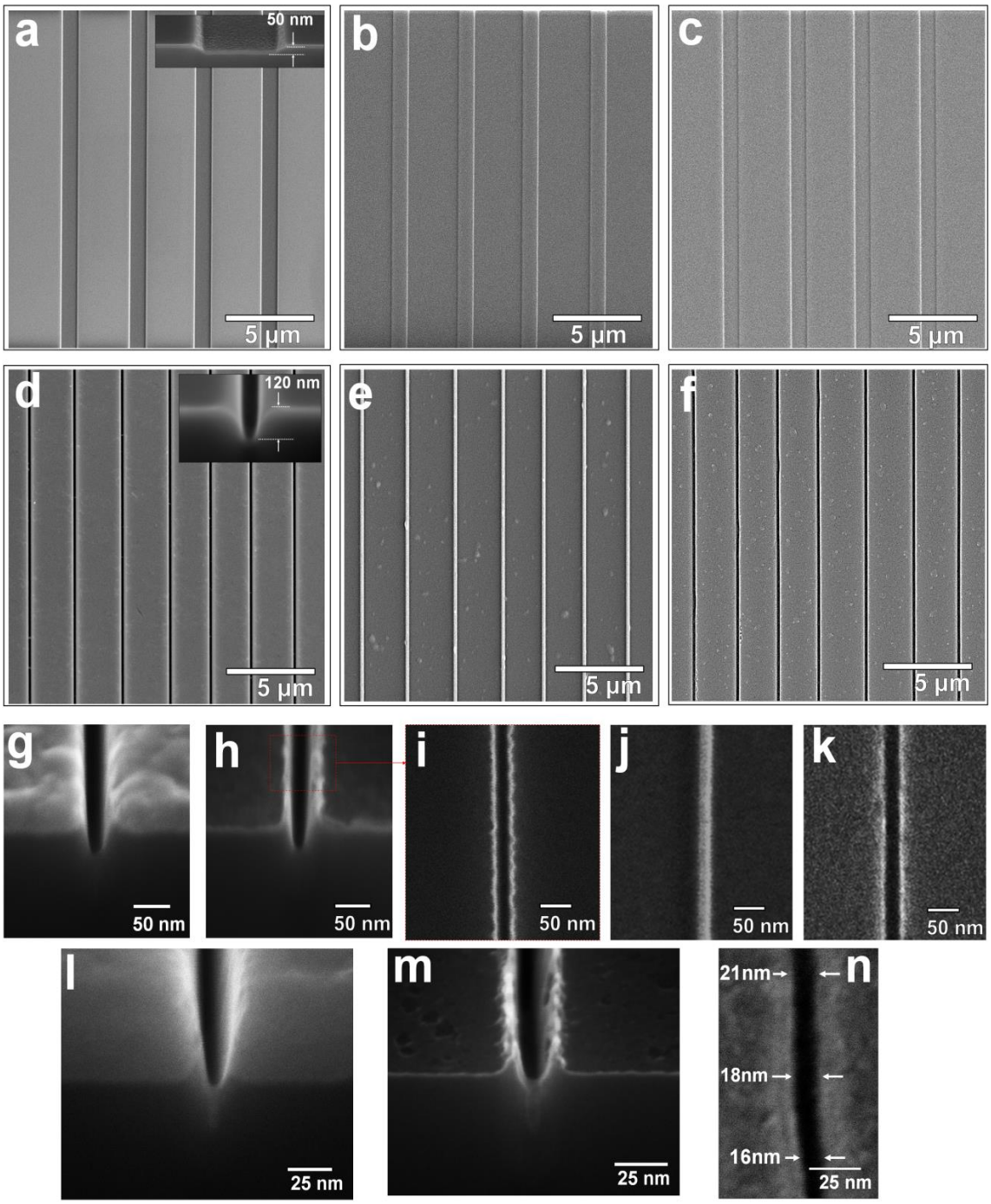

Figure 1.11 SEMs of Si masters (a, d, g, h, i, l, m), resin stamps (b, e, j) and nanofluidic devices imprinted in PMMA (c, f, k, n). The device in a – c consists of nanoslits with a width of 1 µm and depth of 50 nm. In d – f, a device with a 120 nm × 120 nm channels are shown. In g – k, a nanofluidic device with a 40 × 40 nm channel is shown with a 40 nm thick Al layer that was deposited onto the Si master prior to using focused ion beam milling to generate the nano-structures. In l – n is shown a nanofluidic device with an approximately 20 × 20 nm channel with a 80 nm thick Al layer deposited onto the Si master prior to focused ion beam milling. In all cases, the substrate was PMMA (glass transition temperature 105°C). Figures a – f, m – n were reproduced with permission of The Royal Society of Chemistry from Uba *et al*., 2014 [71]. Figures g – k and l are previously unpublished.

1.3.3 Fabrication of Thermoplastic Nanofluidic Devices

Inorganic substrates have been widely used as substrates for the fabrication of nanofluidic devices due to their established surface chemistry, excellent optical properties and well-entrenched fabrication techniques [72]. As noted previously, fabrication of nanochannels in inorganic substrates utilize a top-down approach with direct writing via EBL followed by dry etching or FIB milling. Over the years, several research groups have utilized EBL and/or FIB to develop nanofluidic devices in inorganic substrates for the analysis of biomolecules or evaluating transport properties in nanofluidic channels [6, 73-76].

Other techniques for making nanofluidic devices in inorganic substrates include the use of nanowires as sacrificial templates [6], conventional machining by etching a sacrificial strip separating a substrate and the capping layer [6] and self-enclosure of nanochannels using a UV laser pulse [6]. A relatively new technique for the direct writing of sub-10 nm structures into Si or other inorganic substrates is He ion beam writing [6]. In this case, low atomic mass He ions are used instead of gallium with concomitantly less scattering of He ions compared to Ga ions, resulting in the ability to form nanostructures with much smaller dimensions.

The challenge with using inorganic substrates is the fact that EBL or FIB must be used in many cases, making use of these nanofluidic devices prohibitive for most applications based on accessibility of the patterning equipment and the cost of producing the device. While a commercial entity does market glass-based nanofluidic devices fabricated by deep UV lithography, the structure size is limited to >100 nm and the cost is still high (see www.bionanogenomics.com). Thus, alternative fabrication strategies must be considered to realize better accessibility of nanofluidic devices into the general research and commercial sectors, especially in the diagnostic regime where disposable devices are required due to issues arising from cross-contamination giving rise to false negative results.

Thermoplastics are high molecular weight, linear or branched polymers with a lower Young's modulus compared to inorganic material and a wider range of physicochemical properties. The deformability of thermoplastics makes them useful substrates for the fabrication of microfluidic channels via hot embossing, injection molding, compression molding, thermal forming or casting techniques. Typical

thermoplastics, including PMMA, polycarbonate (PC), COC and polyethylene terephthalate (PET), possess glass transition temperatures that are significantly lower than that of glass, allowing for the fabrication of nanostructures at high production rates, low cost and high-fidelity using techniques such as NIL. Furthermore, copolymers can be used as a substrate for nanofluidic devices that have a range of *p*hysiochemical properties arising from differences in the ratio of monomers used in the polymer [77].

NIL is an effective technique to produce low-cost nanostructures with high resolution. This technique was first developed in the 1990's [77-78]. NIL uses fabricated micro/nanostructure patterned into, for example, Si via EBL or FIB to create a mold master from which structures can be imprinted [77]. Structures down to ~5 nm are possible to produce using this technique, and it can be used with a wide range of polymer substrates. Hence, it is a highly adaptable technique, but still suffers from depending on expensive instruments to create the initial master mold [78-80]. The main advantage of NIL is the ability to build multi-scale patterns in a single imprinting step. Further details on NIL are presented in a recent review by Chantiwas *et al.* [81]. Additional techniques for the fabrication of nanochannels in thermoplastics includes direct proton beam writing [82], thermomechanical deformation [83], compression of microchannels [4], sidewall lithography and hot embossing [49], UV-lithography/O_2 plasma etching [84], hot embossing with PMMA molds [85], refill of polymer microchannels [86], and the use of silica nanowire as templates [46].

The process of NIL-based fabrication of nanofluidic devices begins by patterning microchannels in a Si substrate using conventional optical lithography (Figure 1.10-A) [86]. This is followed by FIB writing of nanochannels into the same Si substrate containing the microchannels. The Si wafer is used as a mold master and has the same polarity as the desired finished thermoplastic device. Once the Si mold master is produced, UV-NIL is undertaken to produce resin stamps with the reverse polarity relative to the Si master. These resin stamps are then used in a thermal-NIL step to generate the finished thermoplastic device. The advantage of this production process is that a number of nanofluidic devices (>100) can be produced from the same Si mold master without requiring returning to the optical lithography and EBL/FIB patterning tools, significantly reducing the cost of generating nanofluidic devices.

1.4 Applications of Single Molecule Detection in Nanofluidic Devices

1.4.1 DNA stretching

Nucleic acids undergo conformational changes such as bending, compression and twisting, which contribute to the structural aspects of transcription and replication. Both the static and dynamic properties of DNA molecules vary in a bulk environment versus confined space. In bulk solution, DNA is typically randomly coiled, making it difficult to determine the nucleotide composition of the intact DNA molecule. In order to allow for direct reading of single or multiple nucleotide variations within DNA molecules, a plethora of techniques such as optical tweezers, hydrodynamic fluid flow and more recently nanoconfinement, have been realized to study the composition and even mechanical properties of DNA. Nano-dimensional confinement is a method of restricting single DNA or RNA molecules in a structure where its critical dimension is similar to the persistence length of the molecule being interrogated, thus stretching the DNA and lowering its entropy [86]. This characteristic of DNA has been exploited by driving DNA polymers into a nano-dimensional space using pressure to induce the bio-polymer to interact with the nanostructure [87]. Stretching of DNA on surfaces is useful for some applications, but fixation of the polymers to surfaces is poorly controlled and not reproducible [84]. For precise DNA elongation, confinement in spaces with dimensions in the range of the persistence length (50 nm for dsDNA and around 10 nm for ssDNA – single stranded DNA) is ideal, so that DNA can be stretched to near its contour length. Confinement of DNA in nanochannels are promising because they can be used for optical mapping to detect genomic variations, DNA methylation and so on. Stretching via confinement to near a DNA molecule's contour length (a 48.5 Kbp DNA can have a contour length of ~16.5 μm) can be extremely important for direct labeling and reading of the aforementioned sequence variations. In bulk solution, the location of these variations cannot be determined nor the number of the variations. For example, by labeling the sequence variations, such as the methylation sites, along with DNA staining via intercalating dyes, can allow for reading the contour length of the DNA as well as determining the frequency and location of the sequence variations.

Early experiments involved stretching of DNA by end-attaching them to beads in a microfluidic device where the DNA was stretched under hydrodynamic flow, and the extent of stretching was monitored under a tunable force. With the evolution of fabrication techniques, nano-dimensional structures could be assembled that facilitate the confinement of DNA in near persistence-length dimensions. Their use has become widespread as they restrict Brownian motion of DNA by limiting the degree of freedom, especially in 2D nanochannels. They are also beneficial for biochemical analysis due to their reduced sample volume requirements and faster analysis time [88]. Surface functionalization helps to increase the specificity for nucleic acids as well [88]. The use of intercalating dyes for DNA provides high fluorescence signal because of their high QE when bound to DNA, thus facilitating single-molecule imaging [6]. Intact DNA molecules are labelled with a fluorescent dye, stretched and finally imaged with a fluorescence microscope. Information from hundreds of Kilobase pairs (Kbp) can be acquired from one single image due to the unvaried stretching that occurs in the nano-dimensional regime [6]. DNA barcoding is one of the recent techniques where DNA is fluorescently labelled with probes that adhere to specific sites in the backbone, which helps in measuring the distance between the labelled sites when the molecule is fully stretched [6].

1.4.2 Effects of channel dimensions

The behavior of DNA under confinement in different dimensional regimes will depend on the contour length, and persistence length of the DNA, and the width/depth of the nanochannel. Consequently, stretching in nanochannels of appropriate dimensions is necessary to achieve stretching to near the contour length. Guo *et al.* fabricated three different nanochannel dimensions namely, 300 nm x 700 nm, 300 nm x 500 nm and 75 nm on a PMMA device [6]. T5 bacteriophage DNA (103 Kb) was stained with YOYO-1 bis-intercalating dye and transported to the nanochannels by capillary force. An EMCCD camera mounted on a fluorescence microscope with a 63X oil immersion objective was used for capturing the images of the DNA. When the nanochannel dimension was 700 nm, the length of the DNA measured was 6.2 ±1.3 μm, which is approximately 15% of its contour length (35 μm). As the channel dimension was decreased, the measured length increased. For a 300 nm x 500 nm channel, the measured length was 12.7 ± 4.5 um (30% of contour), and when the dimensions were 75 nm × 120 nm, the length measured was 39.8 ± 7.7 um (95%

contour). Staining of the DNA backbone with the fluorescent dye accounts for a 20% increase in the contour length [6].

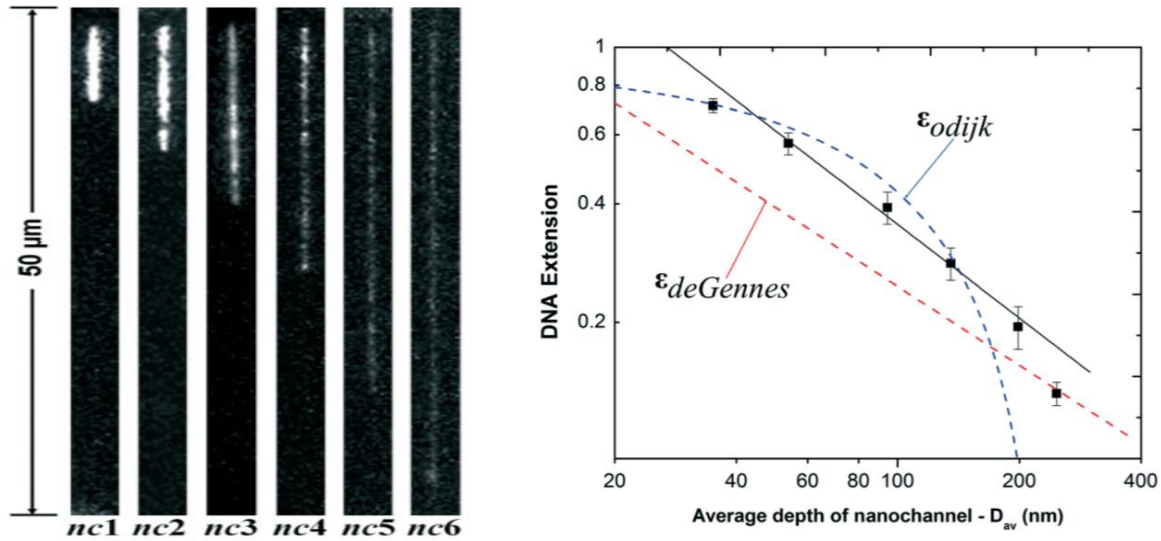

Figure 1.12 A) Fluorescent images of T4 DNA molecules stretched in nanochannels devices. An exposure time of 10 ms was set and the electric field was turned off as the DNA entered into the channels. B) A log–log plot showing the extension of DNA with respect of the average depth of the nanochannels. The contour length was normalized to a 64 µm when labeled with a dye. The red and blue lines indicate deGennes and Odijk regimes respectively. The black line represents the best power law fit to the DNA stretching on the nanochannel ranging from depths of 53nm to 200nm (Reproduced from Uba et al., 2015 [6]).

Six different nanochannels with different dimensions were fabricated in PMMA using NIL. T4 DNA was stretched in these nanochannels, which contained the following dimensions: nc1 = 300 × 200 nm, nc2 = 250 × 155 nm, nc3 = 190 × 95 nm, nc4 = 150 × 60 nm, nc5 = 110 × 25 nm and nc6 = 35 × 35 nm. From the results, it was observed that the DNA stretches to its maximum contour length in the lowest dimension channel, *i.e.* nc6 = 35 × 35 nm, with decreased stretching for larger channel dimensions (Figure 1.12). Ideally, only the nc6 falls in the Odijk regime. Stretching of DNA in dimensions of the channel >200 nm fall in the De-Gennes regime, whereas stretching in nc3-nc5 fall in-between De-Gennes and Odijk regime. Hence, it can be concluded that stretching of DNA depends on the nanochannel dimensions [5, 33].

1.4.3 Effects of ionic strength

Reiner *et al.* [89-91] evaluated the dependence of DNA conformation on ionic strength. Variation in ionic strength of the electrolyte modulates the interaction between the base pairs, which carry charges on the phosphate backbone that are screened at lengths above the Debye length (equations 9 and 10). Two

types of electrostatic interactions dominate the DNA stretching: local charges that produce repulsive interactions that increase persistence length, and other charges that prevent back-looping of DNA, causing an increase in the effective width.

Based on the above-mentioned factors, Odijk-Skolnick-Fixman (OSF) came up with a formula that describes the persistence length [92];

Equation 1.13. $$P = Po + ¼k2lb = Po + \frac{0.0324M}{I}\ nm$$

where P is the persistence length (see Figure 1.7), P_0 is the persistence length (~50 nm) at high salt concentration, k is the Debye length and l_b is the Bjerrum length (~0.7 nm at room temperature in aqueous solution). For salt concentrations above 10 mM, P equals P_0. For concentrations in the range of 1 mM to 10 mM, the value of P can increase up to 80 nm.

The effective width of DNA is approximately equal to (1/k) with some additional pre-factors that can be determined by light scattering or sedimentation techniques. The extension of the DNA in the De-Gennes and Odijk regime is also highly dependent on the ionic strength.

In a study of the measured extension lengths as a function of ionic strength, it was observed that the extension decreased with increasing ionic strength: 0.05X > 0.2 X > 0.5 X > 2 X > 5 X Tris Borate EDTA (TBE) buffer for channel dimensions of 200 nm, 100 nm and 50 nm (Figure 1.13) [87]. This led to the conclusion that DNA stretching can be altered by changing the ionic strengths in the range of 10-100 mM, which provides a highly stable environment for most enzymatic reactions with DNA.

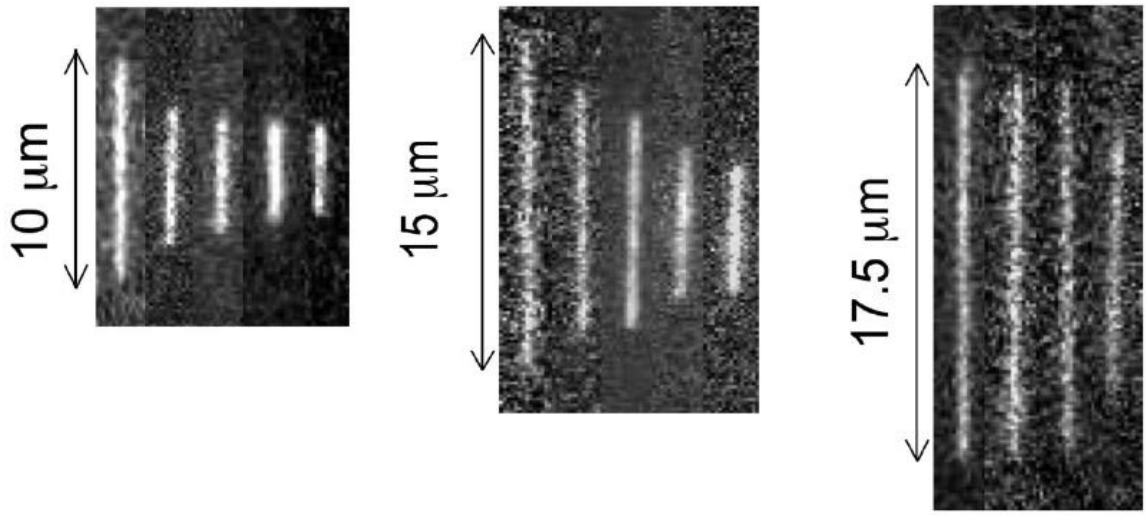

Figure 1.13 Nanochannels were fabricated on a silicon wafer with dimensions of 200 nm, 100 nm and 50 nm. λ-phage DNA dyed with YOYO-1 was driven electrophoretically or using over-pressure into the nanochannels under 0.05X, 0.2 X, 0.5 X, 2 X, 5 X TBE ionic strengths, and the signal was recorded using an iXon EMCCD camera. Fluorescence images of λ-DNA molecules obtained at different TBE concentrations (left to right, 0.05X, 0.2X , 0.5X , 2X , 5X TBE) in (a) 200 nm channels, (b) 100 nm channels, and (c) 50 nm channels (Reproduced from Reisner *et al.*, 2007 [46]).

1.4.4 Optical mapping in nanochannels

Optical mapping is a single molecule approach to construct well-ordered restriction maps of single DNA molecules from genomic DNA of high molecular weight whose sequence is unknown. This generates a unique barcode of the DNA, which provides insights into the structure of the mapped DNA [90]. The overall aim of optical mapping is to analyze sequences from a single DNA molecule typically ranging from 50 kb to a few megabases in length. This way, *de novo* templates can be analyzed for sequence variations. Optical mapping has been mainly used for identifying different bacterial species and strains [87].

Optical DNA mapping in nanochannels is the stretching of DNA linearly to near its full contour length in order to correlate the position in DNA with the underlying sequence. This was demonstrated in some early work by Riehn *et al.*, where DNA was confined inside nanochannels of dimensions 100-200 nm and restriction mapping was performed on DNA using endonucleases. The position of restriction sites were identified with a resolution of 1.5 kbp within 1 min by single molecule DNA detection [87]. One example is the optical mapping of GFP-LacI repressor protein bound to λ-DNA, which was analyzed by confining the

DNA in nanochannels so that the number of proteins bound could be quantified [86]. For optical mapping to be performed, the DNA must be labelled to reveal sequence-dependent information. Two types of labelling techniques have been adopted: enzyme-based labelling, where fluorescent dyes are covalently attached to specific sites within the DNA molecule, and affinity-based labelling, which reveals the AT-GC content in the DNA molecule.

1.4.5 Enzymatic labelling

Enzymatic labelling is a commonly used technique, which is also referred to as nick labelling. Nicking endonucleases are used to create single strand breaks at site specific sequences. DNA polymerases are then used to synthesize a new strand starting from the nicking site while simultaneously incorporating fluorescently labelled deoxynucleotide triphosphates (dNTP; see Figure 1.14). This will enable visualization of the nicking sites using fluorescence microscopy. Finally, DNA ligases are employed to seal the strand. It is important to make sure that the DNA strand has no pre-existing nicks, as the nicks labelled with fluorescent probes should be due to the nicking enzyme and not other sources [93-95]. The entire DNA strand is typically stained with a bisintercalating dye, such as YOYO-1 and fluorescence from the nicks (labelled with a different dye that binds only to the nicks only) is located to create a map to show their location.

Initially, optical mapping was performed on a glass slide, but DNA on glass does not stretch completely, affecting the distance between the nicks. Better resolution can be acquired if the DNA is completely stretched. This can be achieved by confining the DNA in nanochannels of 100 nm or less [96]. The first optical mapping was performed by labelling the entire DNA with an intercalating dye and inducing nicks at specific locations using endonucleases and imaging the position of nicks by Förster resonance energy transfer [87, 96-97]. The technique was extended by Das *et al.* [98] who used nick-flap labeling, in which short single-strand flaps were created at each nicking site using a polymerase that does not have 5'→3' exonuclease activity. These single stranded flaps are then used as binding sites to attach a labelled oligonucleotide. Thus, either the nicks or flaps or both are labelled and can be fluorescently identified by

stretching them in nanochannels. The nicking enzymes used were able to induce a nick (4-7 bp) that was too small to discern the gene of interest and it was highly improbable to recognize longer sequences. Later, McCaffrey *et al.* [98] used CRISPR/Cas9 to induce nicks of 23 bp, which was long enough to identify specific genes. Enzyme labelling was extended to the use of methyl transferase to label a specific TCGA sequence with fluorophores [99]. Each molecule of DNA could be identified based on the fluorescence with this type of labelling. An intercalating dye was not used in this case.

Other enzymes have also been used for optical mapping of DNA. One such enzyme is methyl transferase (M. TaqI), which has been used to transfer a fluorescent dye molecule to a particular sequence of the DNA as demonstrated by Grunwald *et al.* [100] in T7 and λ phages. In this method, short DNA sequences

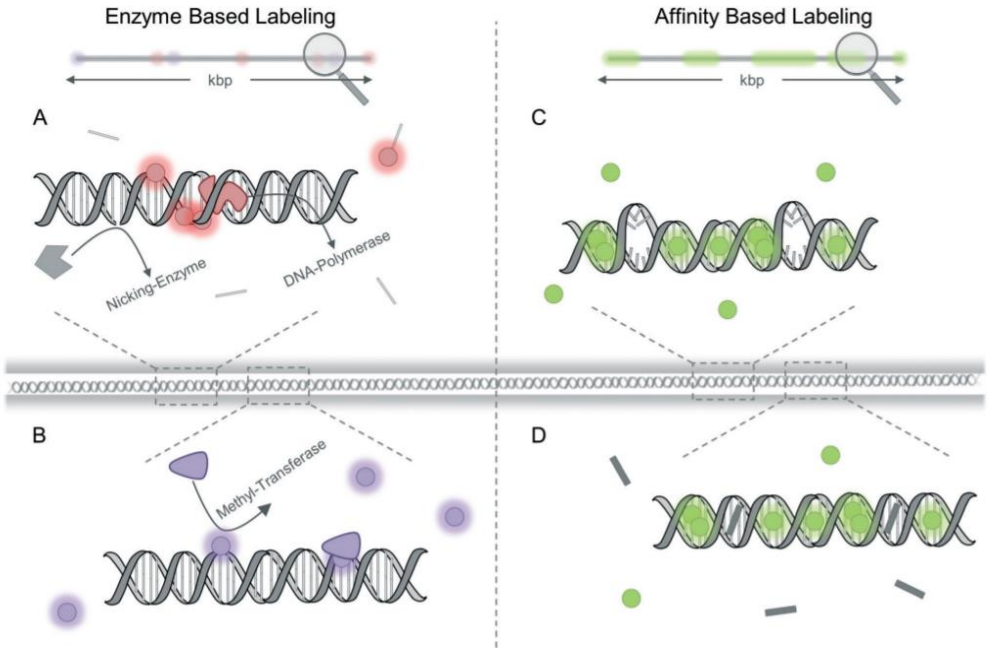

Figure 1.14 Demonstration of the labelling techniques used in DNA for optical mapping. The DNA confined in nanofluidic channels is labelled and visualized under fluorescence microscope thus facilitating the study of genomic information over larger molecules. A) A nick is created by any nicking enzyme at its specific site of 4-7bp long. Following that a DNA polymerase removes the nick and adds new nucleotides in that site. By labelling any of the four deoxynucleotide triphosphates, dNTP, visualization of the nick, along with the DNA molecule is possible. B) A methyl transferase enzyme is used to transfer a methyl group that is labelled, to a specific sequence in the DNA of 4 bp, thus enabling fluorescence detection of the attached site. C) Denaturation mapping exploits the lower melting temperature of AT base pairs compared to GC regions. Hence, the DNA labelled with a bisintercalating dye emits no fluorescence from AT regions as they are melted. D) In the competitive binding mapping method, a compound such as Netrospin selective for AT regions is added along with YOYO to the DNA, such that Netrospin binds specifically to AT regions, leaving GC regions to bind YOYO. Thus, based on the difference in fluorescence emitted, one can discern the sequence of DNA (Reproduced from Muller *et al.*, 2017 [102]).

were used where the entire sequence was labelled with a dye by methyl transferase and hence, an "amplitude modulation profile" was produced that obviates the need for a bisintercalating dye. This facilitates "dense labelling" with each DNA strand having its own fluorescent profile [101].

1.4.6 Affinity labeling

This method relies on the principle of measuring the localized AT/GC content and forming optical maps based on non-covalent interactions. Affinity labelling is performed using two approaches: denaturation mapping or competitive binding. As with enzymatic labelling, the amount of information that can be inferred from the DNA depends on the degree of stretching. The more stretched the DNA, the fewer bases are accommodated in each imaging pixel improving the resolution of the optical barcoding (see Figure 1.13). In denatured mapping, DNA is melted on chip or before loading on to the nanofluidic device. Adenine and thymine associate by two hydrogen bonds, while guanine and cytosine form three hydrogen bonds making them thermodynamically more stable. When partial melting the DNA, A/T bonds denature at a lower temperature than G/C bonds. As A/T regions denature, bisintercalating dyes that are already bound to dsDNA dissociates from the AT regions leading to a difference in the fluorescence intensity observed in the DNA, with GC regions significantly brighter than AT regions. Denaturation mapping was demonstrated on different DNA sequences such as λ phage, T4GT7, T4 and BAC- RP11-125C7 in nanofluidic channels [103]. Genomic maps were obtained from nanofluidic channels and compared to the reference maps to obtain a barcode [101]. Following this, individual maps of DNA fragments were obtained in 120 nm nanochannels in a fluidic device for *Saccharomyces cerevisiae*, where lengths up to 360 Kbp were detected and compared to computational results [102].

In the competitive binding technique, two DNA adhering molecules, a fluorescent dye and a non-fluorescent molecule that is specific to AT or GC regions are chosen. A difference in intensity is observed due to the preferential binding of the non-fluorescent molecules to certain locations in the DNA fragment, thus blocking the site for fluorescent dye intercalation. Netrospin is one such molecule that is used in the competitive binding method that binds to AT rich regions of the DNA molecule.

Competitive binding has been used to study bacterial plasmids that are the reason for antibacterial resistance. In work by Nyberg *et al.*, different genes that were the basis for antibiotic resistance were explored and compared to theoretical barcodes to confirm that optical mapping in nanofluidic channels is reliable to identify plasmids [104].

1.4.7 DNA methylation detection using nanochannels

DNA methylation is a form of epigenetic modification in DNA and RNA [105]. Researchers have shown that methylation of DNA in eukaryotic cells can lead to the silencing of tumor suppressor genes, which ultimately leads to the progression of cancer [101]. Because DNA methylation is preserved during the replication process, it leads to inheritance of methylated sites [101]. Methylation at 5-cytosine is one of the most common mechanisms for suppressing gene activity. A CpG or CG site is a region where a cytosine nucleotide is followed by a guanine nucleotide in the 5'-3' direction, and a high frequency of CpG sites forms CpG islands, where the C in the CpG undergoes methylation. This contributes to various biological processes such as aging, cell differentiation/replication, X-chromosomal inactivation and cancer [101]. Methylation sites have been identified in the tumor suppressor genes of patients with breast, lung, cervical, and colorectal cancers with an increase in methylated cytosines in patients with breast cancer [101]. Hence, single-molecule detection of methylated sites in DNA has been used to detect various types of early-stage cancers as a promising tool for tumor diagnosis and for determining the efficacy of anticancer treatment regimens.

Traditionally, DNA methylation has been identified by the bisulfite method, which was introduced by Shigematsu, *et al*. [102] and Cokus *et al.* [102] in which bisulfite modified DNA is amplified by PCR and the methylation detected by sequencing techniques. Hybridization assays and methylation-sensitive single-nucleotide primer extension (Ms-SNuPE) are other ensemble detection techniques that have been used to detect methylated sites. However, these ensemble methods are extremely time consuming and require large sample volumes. The use of nanofluidic devices to optically detect methylated sites in DNA at the single molecule level have emerged as a powerful technique to analyze CpG domains for cytosine methylation [102].

Methylation affects the physical properties of DNA, causing the methylated DNA to stretch more than the non-methylated one. Lim *et al.* [106] showed that it is possible to stretch DNA in nanochannels and visualize the methylated sites in DNA by labelling them specifically with fluorescent dyes (Figure 1.15). Briefly, a 5 mC modified λ-DNA and a non-modified DNA were concatenated and labeled with the bisintercalating dye YOYO-1. A fluorescently labeled vector methyl-binding-domain (MBD), Alexa568-MBD, was subsequently added to the DNA. The DNA molecules were then driven into nanochannels of 250 X 200 nm (width and depth) by an electric field to facilitate stretching of DNA. It was found that the methylated regions of the DNA co-localized with YOYO-1 dye (green) and Alexa 568 MDB (red) as opposed to the non-methylated regions, which did not have bound MDB. The MDB fluorescence appeared in a stretch of sequence due to the high frequency of CpG sites (about 3000 nucleotides). The position was based on the position of the concatenation of the methylated DNA to the non-methylated DNA. Hence, the researchers concluded that the binding of MDB labelled with a fluorophore identified 5-methyl cytosine clusters in genomic length DNA at a resolution of about 10 Kbp. This resolution is appropriate as it's approximately the size of a human gene [106].

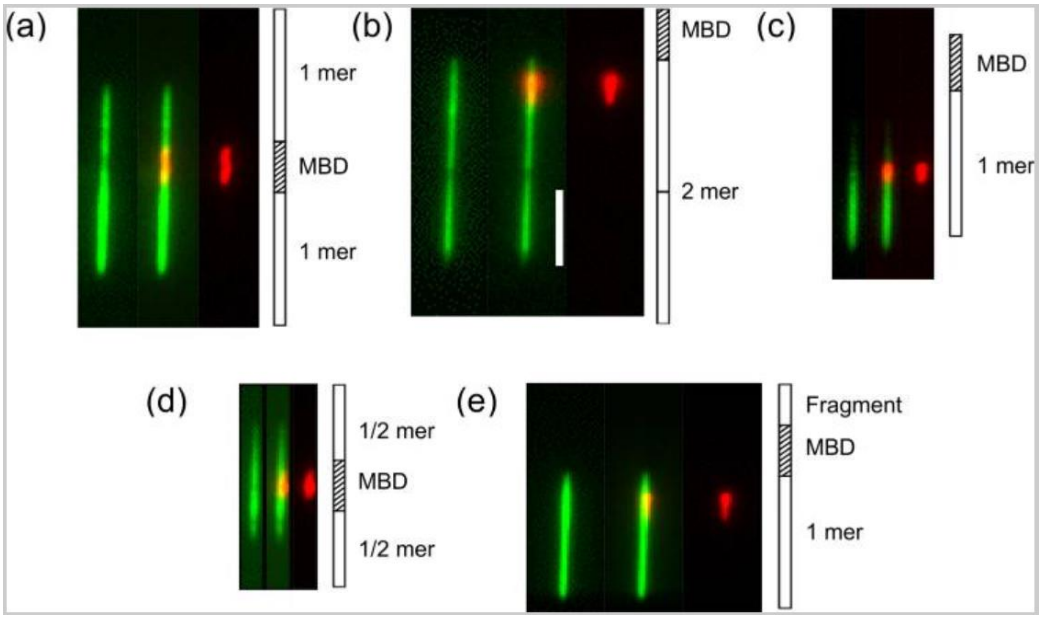

Figure 1.15 a) – e) Fluorescence images of concatenation of methylated and non-methylated λ-DNA stretched in nanochannels and labelled with YOYO-1 (green) and Alexa568MBD (red). The panels have each color split for convenience. Different regions of methylation have been depicted in these images (Reproduced from Lim *et al.*, 2011 [107]).

Sun *et al.* [107] proposed an interesting methodology based on the fact that methylated sites in DNA are much stiffer and hence have a longer contracted length and a slower contraction rate compared to nonmethylated DNA. This difference can be used to identify CpG sites at the single molecule level. They induced methylation of a T4 DNA using restriction enzymes, labeled the DNA with YOYO-1, and drove the DNA into 300 X 300 nm nanochannels electrophoretically. They compared the contraction of single DNA molecules that were methylated to non-methylated DNA and reported that the contraction values after a 7-s relaxation time were 13.58 μm and 11.06 μm, respectively. The difference in the process of contraction of the methylated and non-methylated DNA were calculated using the following equation;

Equation 1.14. $$l(t) = l_e + (l_o - l_e)\exp\left(\frac{-5k_B T D^{\frac{1}{3}}}{8\pi\eta L^2 (pw)^{\frac{2}{3}}} t\right)$$

where l_e is the equilibrium length, l_0 is the initial length in the nanochannel, η is the viscosity of the solvent, L is the contour length, P is the persistence length, w is the width of DNA, and D is the channel diameter. Further, an increase in persistence length of 23% for the methylated DNA was observed from the calculated and fitted length. However, because the contraction of DNA depends on the methylation, a difference in fluorescence intensity occurs that can more accurately reveal the site of the methylation. Therefore, the importance of detecting the increase of methylation in DNA for cancer diagnosis was delineated by this mechanism [107] (Figure 1.16).

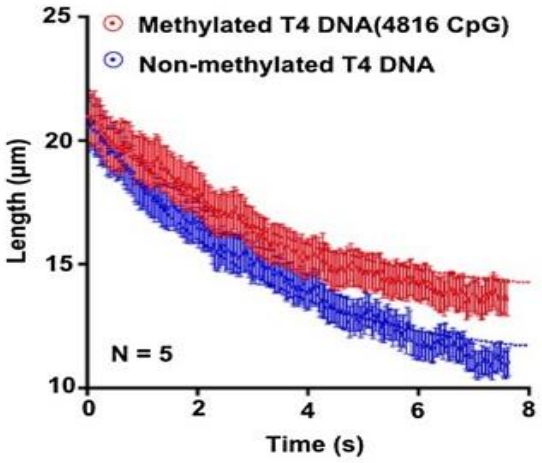

Figure 1.16 Contracted length of both methylated (red) and non-methylated (blue) T4 DNA as a function of time using equation (16) (Reproduced from Sun *et al.*, 2016 [108]).

Later, Michal-levy *et al.* [108] demonstrated SMD of 5 hydroxymethylcytosine (5hmC), an oxidized version of 5 mC, by covalently labelling a chemical to the damaged base. T4 β-glucosyltransferase was used to attach an azido-modified glucose to 5hmC incorporated into λ DNA. The azide group could then be labeled with an Alexa Fluor dye. The DNA was labelled with YOYO-1 and the 5hmC sites were fluorescently detected. This technique can be combined by monitoring other information such as protein-binding sites, thus giving optical mapping an advantage of examining the chromosomes and genes based on their co-operative binding patterns, which cannot be obtained in bulk assays such as DNA sequencing [108].

1.4.8 Genomic mapping for sequence variation maps using nanofluidic devices

Genome mapping, like optical mapping, relies on inducing sequence-specific labelling followed by labelling the DNA molecules and imaging them using a fluorescence microscope. Ernest *et al.* [108] illustrated the process in a 183-Kbp bacterial artificial chromosome (BAC) clone, where a nicking endonuclease was used to introduce a nick in one of the strands of the dsDNA at specific sequence regions. Nucleotides incorporated with a fluorescent dye, Alexa 546 dUTP, were added to the single strand break site using a Vent exopolymerase. The DNA was subsequently stained with YOYO-1 and loaded electrophoretically into a nanochannel array device with 45 nm channels (width and depth). As the molecule stretches inside the nanochannel, the DNA (blue) along with the nick site (green) are visible. The measured stretched length was 50.5 μm, which is about 85% of its contour length. Based on the location of the fluorescent labels, nicks could be recognized at the site of the specific sequence that was labelled. Subsequently, a consensus map was constructed based on the comparison of different DNA molecules followed by grouping them together. Because the BAC enters the nanochannel from one of two orientations (5’ → 3’ or 3’→ 5’), every BAC was represented by two clusters, both of which were combined to acquire a histogram of the DNA with the labelled nicks of the specific sequence (GCTCTTC) and accurately determine the location of nicks from each other [108](Figure 1.17).

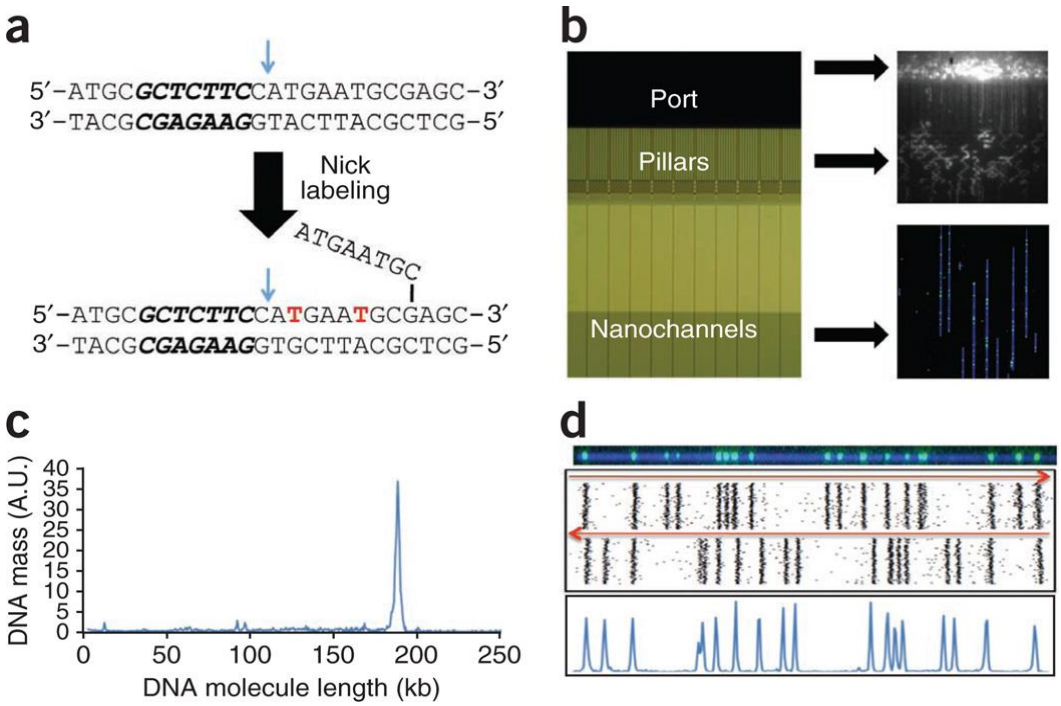

Figure 1.17 a) Nick labelling in the DNA achieved using Nt.BspQI and DNA polymerase by cleaving the top DNA strand followed by fluorescent nucleotide insertion (red) from the 3' end, and simultaneous strand displacement. B) Stretching of DNA electrophoretically inside a 45nm channel, where the DNA unwinds in micron scale area and stretches in the nanochannels to about 85% of its contour length. C) The length of the DNA molecule and the position of nicks is represented, with a narrower peak corresponding to proper linearization of DNA. D) The DNA molecules arranged according to their nicking pattern similarity, with each BAC represented by two clusters (first and second panels) based on their orientation to determine the location of each sequence motif, represented by the histogram of peaks (GCTCTTC) in the bottom panel (Reproduced from Lam *et al*., 2012 [108]).

Similar labelling techniques can be used to detect damaged sites such as abasic sites in the DNA of patients undergoing chemotherapy. Patients undergoing cancer have a significantly higher percentage of unrepaired abasic sites in their DNA as compared to a healthy individual. Because chemotherapy works by damaging the DNA, effective identification of abasic sites in cancer patients can help the physicians determine the effectiveness of therapy as well as act as a biomarker of cancer diagnosis. Abasic sites (missing purine or a pyrimidine) have an aldehyde open ring group to which a biotinylated aldehyde reactive probe can be attached, which in turn can be covalently bound to a fluorescently labelled streptavidin [6]. The DNA labelled with a bisintercalating dye can be electrophoretically introduced into a nanochannel with

dimensions less than its persistence length. The fluorescence from the DNA and the abasic sites can be read optically at the single molecule level to determine the response of the patient to cancer chemotherapy.

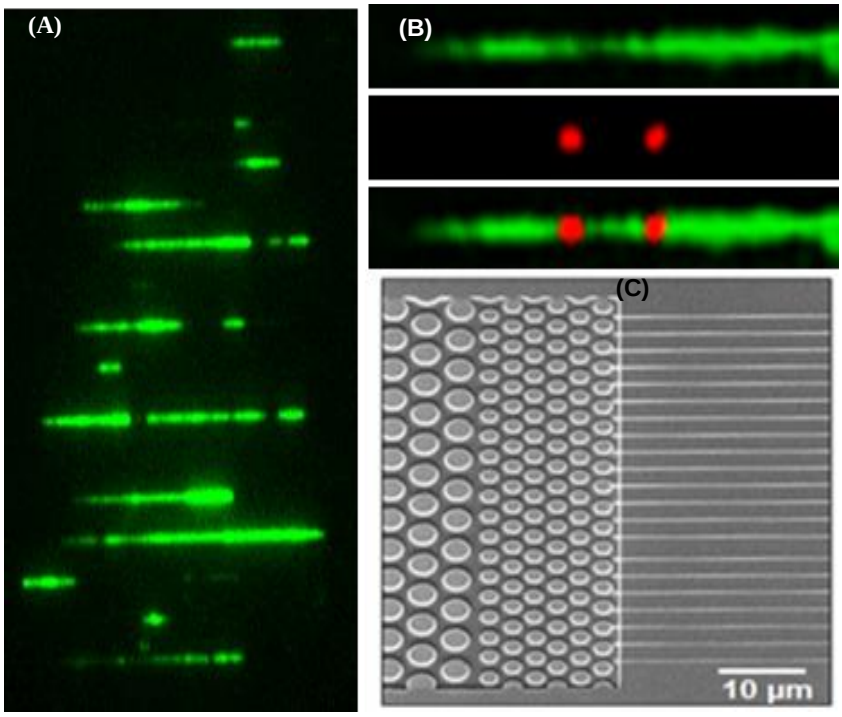

Figure 1.18 (A) Elongation of dsDNA standards labeled with biotin-ARP (b-ARP) that contained 20 AP-sites per 100 Kbp. The standards were incubated with streptavidin containing 2-3 dye molecules (Alexa 594). The DNA are "parked" in the non-pillared region in this fluorescence micrograph (5 s integration time). (B) The DNA was stretched in PMMA nanochannels (100 x 60 nm, w x d) that were 100 µm in length with pre-stretching pillars (C). The DNA fragment shown in (B) was ~20 Kbp and 2 AP sites were detected.

Figure 1.18 C shows a nanochannel device a fabricated in a plastic using nanoimprint lithography using previous work [5-6]. This device was made in PMMA (glass transition temperature, T_g = 105 ^oC) and sealed with a COC cover plate (T_g = 76 ^oC); a higher T_g substrate is thermally bonded to a lower T_g cover plate to minimize structural deformation during assembly with yield rates >90% [6]. Figure 1.18 A-B shows λ-DNA stained with YOYO-1 resident within this device. It has been demonstrated that nanochannels as small as 18 nm (width × depth) can be made in plastic, which will allow for extension of dsDNA to near its full contour length simplifying fluorescence readout of the abasic sites as well as their quantification [7, 109]. As shown in Figure 1.18-C, input structures were used (pillar array) to enhance the sampling efficiency of DNA loading into the nanochannels by extending the electric field into adjoining microchannels.

1.5 Nanoscale electrophoresis

Nanochannels offer great flexibility in terms of shape and size with increased robustness and surface properties, which can be modified based on the required function [109]. The unique nanophenomena observed in nanoconfined environments introduce unique separation modalities that are not found in microscale electrophoresis. Nanoscale electrophoresis is applicable to the determination of wide variety of compounds such as DNA, nucleotide monophosphates [5].

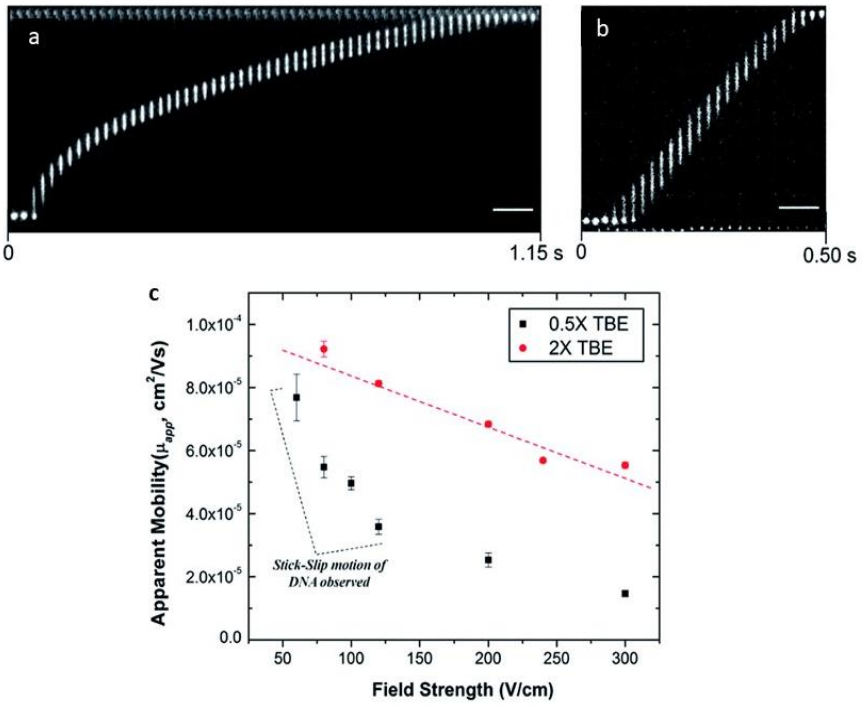

Figure 1.19 Representative frames of fluorescently stained λ-DNA molecules translocating through a 100 nm × 100 nm oxygen plasma modified PMMA nanochannel and imaged in (a) 0.5X and (b) 2X TBE buffer at 80 V cm^{-1} and 120 V cm^{-1}, respectively. The time between frames is approximately 20 ms and scale bars are 10 μm. (c) Apparent mobility against the electric field strength for DNA translocation through the single nanochannel filled with 0.5X (black markers) and 2X(red markers) TBE buffer. The error bars represent the standard deviation of the measurements (n=10). (Reproduced from Uba *et al.*, 2014 [5]).

In 2014, Uba *et al.* [109] has demonstrated the electrophoretic mobility of single λ-DNA molecules through thermoplastic nanochannels made with PMMA that are 50 μm long 100 nm x 100 nm in depth and width made by nanoimprinting lithography. A laser induced fluorescence microscope equipped with an EMCCD camera was used to detect the fluorescently labeled λ-DNA single molecules migrating through

nanochannels electrokinetically. λ-DNA was labeled with the intercalating dye YOYO-1 to see the fluorescence of DNA. A 0.75-pM concentration of labeled DNA was used to achieve single molecule occupancy inside the nanochannel. The frames in Figure 1.19 a-b represent movement of DNA through nanochannel. The apparent mobility reported here is the sum of the electrophoretic mobility of DNA and the electroosmotic flow mobility. In their study, the authors observed a lower apparent mobility when using 0.5X TBE (trisborate EDTA) buffer vs 2X TBE buffer. With low ionic strength buffer (0.5X), the thickness of the EDL and the electroosmotic flow both increased compared to the high ionic strength buffer, leading to lower the apparent mobility. In addition, the authors observed a dependence of the apparent mobility on field strength for DNA seeded with 0.5X TBE buffer due to intermittent (stick–slip) motion of DNA. The increased surface area to volume ratio increase interactions with the channel wall leading to intermittent motion of DNA in these nanochannels (Figure 1.19-c).

O'Neil *et al.* [109] in 2018 showed the separation of deoxynucleotide monophosphates (dNMPs) in 100 nm x 100 nm (depth and width) nanochannels fabricated in thermoplastic nanochannels (PMMA and cyclic olefin copolymer). The detection was done by using wide field epifluorescence microscope with an EMCCD camera. Because of the low probe volume in nanochannels ($1.07 \times 10^{-22}\ m^3$), 64 molecules would be passing the laser beam illuminating the entire nanochannel at any given time in all of the experiments they performed. The electrophoresis separation of dNMPs was done in a microscale channel as a comparison to nanoscale channels. The authors showed that the separation was not achieved for all four nucleotides in the microscale channel. In contrast to this, they observed separation of all the dNMPs in nanoscale electrophoresis at pH 8.3 and pH 10.3. The authors investigated the effect of pH on the separation and on the EDL overlap. Separation resolution values ranging from 0.84-4.84 was achieved at pH 10.3, showed an increase in the resolution compared to pH 8.3 (Figure 1.20 a-b). Moreover, the experiments were done in a lower ionic strength buffer to investigate the EDL overlap effects for nanoscale separation. As seen in Figure 1.20-d there is more peak overlap at low ionic strength buffer than at high ionic strength. The authors claim that the EDL overlap leads to a more parabolic flow profile and creates a larger variance in the apparent mobility depending on the position of the analyte in the flow profile, leading to poor

resolution. In addition to the electrophoretic separation, authors suggest that a chromatographic-like separation occurs in the nanoscale channels due to increased surface interactions in nanoscale, creating wall adsorption and desorption of dNMP molecules depending on their hydrophilicity.

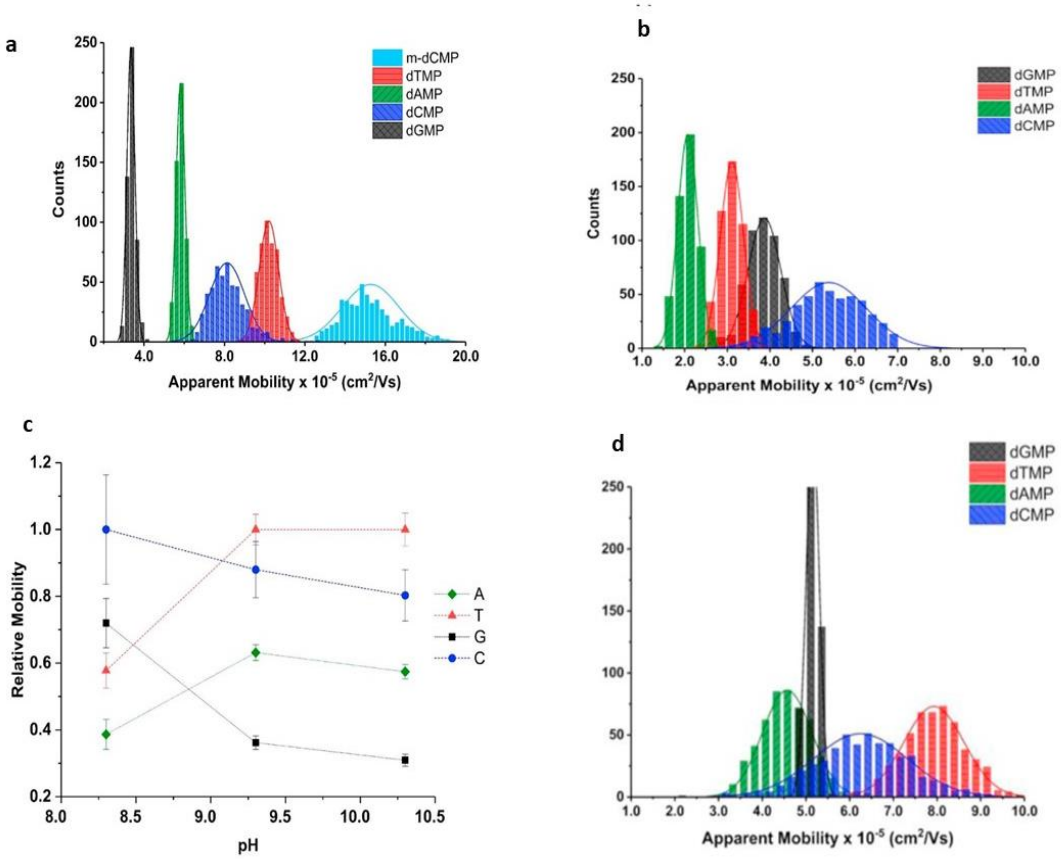

Figure 1.20 (a, b) Histogram of apparent mobility of ATTO-532 labeled deoxynucleotide monophosphate in 100 nm deep and 100nm wide nanochannels at a filed strength of 342V/cm and background electrolyte concentration was 44.5 mM TBE at pH 10.3 and 8.3 respectively. c) Relative apparent mobility of the ATTO 532-labeled dNMPs with respect to carrier electrolyte pH and apparent mobilities have been normalized to the highest observed apparent mobility for pH 8.3, 9.3 and 10.3. d) Histogram of apparent mobility of ATTO-532 labeled deoxynucleotide monophosphate in 100 nm deep and 100 nm wide nanochannels at a filed strength of 342V/cm and background electrolyte concentration was 0.45 mM TBE. (Reproduced from O'Neil *et al.*, 2018 [110]).

1.6 Conclusions

As an emerging field, nanofluidics offers some interesting unique phenomena compared to well-established microscale devices. Most importantly, it gives an opportunity to investigate molecules closely in their single molecule level. Distinctive capabilities such as stretching the DNA to identify their single sequence variations, optical mapping of the whole human genome, distinctive separation and

electrophoresis phenomena to separate small biopolymers, DNA/RNA sequencing are with such high-importance which enables us to realize the translation of these methods in to commercialization. Thermoplastic nanofluidics may increasingly be popular due to their low cost and suitability for in-vitro diagnostic applications compared to expensive glass based and Si based devices. Nevertheless, clinical translation of these in-vitro diagnostic devices and including these in production pipelines in commercial sector with a high-scale production rate would definitely be an invaluable investment in future research and development.

1.7 References:

1. Liu, C.; Qu, Y.; Luo, Y.; Fang, N., Recent advances in single-molecule detection on micro- and nano-fluidic devices. *Electrophoresis* **2011,** *32* (23), 3308-18.
2. Hoang, H. T.; Segers-Nolten, I. M.; Berenschot, J. W.; Boer, M. J. d.; Tas, N. R.; Haneveld, J.; Elwenspoek, M. C., Fabrication and interfacing of nanochannel devices for single-molecule studies. *Journal of Micromechanics and Microengineering* **2009,** *19* (6), 065017.
3. Wu, J.; Chantiwas, R.; Soper, S. C.; Park, S., Nanofluidic Channel Based Single Molecular Sensors in Polymer Substrate Fabricated by Novel Nanoimprinting Processes. **2010,** *2*, 4.
4. Wu, J.; Chantiwas, R.; Amirsadeghi, A.; Soper, S. A.; Park, S., Complete plastic nanofluidic devices for DNA analysis via direct imprinting with polymer stamps. *Lab on a Chip* **2011,** *11* (17), 2984-2989.
5. Uba, F. I.; Pullagurla, S.; Sirasunthorn, N.; Wu, J.; Park, S.; Chantiwas, R.; Cho, Y.-K.; Shin, H.; Soper, S. A., Surface charge, electroosmotic flow and DNA extension in chemically modified thermoplastic nanoslits and nanochannels. *Analyst* **2014,** *139*.
6. Uba, F. I.; Hu, B.; Weerakoon-Ratnayake, K.; Oliver-Calixte, N.; Soper, S. A., High process yield rates of thermoplastic nanofluidic devices using a hybrid thermal assembly technique. *Lab on a Chip* **2015,** *15* (4), 1038-1049.
7. Weerakoon-Ratnayake, K. M.; O'Neil, C. E.; Uba, F. I.; Soper, S. A., Thermoplastic nanofluidic devices for biomedical applications. *Lab on a Chip* **2017,** *17* (3), 362-381.
8. Yuan, Z.; Garcia, A. L.; Lopez, G. P.; Petsev, D. N., Electrokinetic transport and separations in fluidic nanochannels. *Electrophoresis* **2007,** *28* (4), 595-610.
9. Pennathur, S.; Santiago, J. G., Electrokinetic transport in nanochannels. 1. Theory. *Analytical chemistry* **2005,** *77* (21), 6772-6781.
10. Baldessari, F.; Santiago, J. G., Electrophoresis in nanochannels: brief review and speculation. *Journal of Nanobiotechnology* **2006,** *4* (1), 12.
11. Movahed, S.; Li, D., Electrokinetic transport through nanochannels. *Electrophoresis* **2011,** *32* (11), 1259-1267.
12. Xuan, X.; Li, D., Electrokinetic transport of charged solutes in micro-and nanochannels: The influence of transverse electromigration. *Electrophoresis* **2006,** *27* (24), 5020-5031.
13. Lyklema, J., Fundamentals of interface and colloid science Solid-Liquid Interfaces vol 2 (San Diego, CA: Academic). **1995**.
14. Reuss, F. F., Charge-induced flow. *Proceedings of the Imperial Society of Naturalists of Moscow, 1809* **1809,** *3*, 327-344.
15. Wiedemann, G., First Quantitative Study of Electrical Endosmose. *Pogg. Ann.* **1852,** *87*, 321.

16. Von Helmholtz, H. L. F., Studies of electric boundary layers. *Wied. Ann* **1879,** *7*, 337-382.
17. Smoluchowski, M., Krak. Anz: 1903.
18. Helmholtz, H. v., Ueber einige Gesetze der Vertheilung elektrischer Ströme in körperlichen Leitern, mit Anwendung auf die thierisch-elektrischen Versuche (Schluss.). *Annalen der Physik* **1853,** *165* (7), 353-377.
19. Guoy, G., Constitution of the electric charge at the surface of an electrolyte. *J Physique* **1910,** *9*, 457-67.
20. Chapman, D. L., LI. A contribution to the theory of electrocapillarity. *The London, Edinburgh, and Dublin philosophical magazine and journal of science* **1913,** *25* (148), 475-481.
21. Stern, O., The theory of the electrolytic double-layer. *Z. Elektrochem* **1924,** *30* (508), 1014-1020.
22. Peng, R., Electrokinetic Transport Phenomena in Nanochannels and Applications of Nanochannel-based Devices in Nanoparticle Detection and Molecule Sensing. **2018**.
23. Li, D., *Electrokinetics in microfluidics*. Elsevier: 2004; Vol. 2.
24. Jorgenson, J. W.; Lukacs, K. D., Capillary zone electrophoresis. *Science* **1983,** *222*, 266-274.
25. Rice, C. L.; Whitehead, R., Electrokinetic flow in a narrow cylindrical capillary. *The Journal of Physical Chemistry* **1965,** *69* (11), 4017-4024.
26. Altria, K. D., *Capillary electrophoresis guidebook: principles, operation, and applications*. Springer Science & Business Media: 1996; Vol. 52.
27. Paul, P. H.; Garguilo, M. G.; Rakestraw, D. J., Imaging of pressure-and electrokinetically driven flows through open capillaries. *Analytical Chemistry* **1998,** *70* (13), 2459-2467.
28. Russel, W. B.; Saville, D. A.; Schowalter, W. R., Colloidal dispersions, Cambridge monographs on mechanics and applied mathematics. Cambridge University Press, Cambridge: 1989.
29. Conlisk, A. T., The Debye-Hückel approximation: Its use in describing electroosmotic flow in micro-and nanochannels. *Electrophoresis* **2005,** *26* (10), 1896-1912.
30. Reisner, W.; Beech, J. P.; Larsen, N. B.; Flyvbjerg, H.; Kristensen, A.; Tegenfeldt, J. O., Nanoconfinement-enhanced conformational response of single DNA molecules to changes in ionic environment. *Physical review letters* **2007,** *99* (5).
31. Tegenfeldt, J. O.; Prinz, C.; Cao, H.; Chou, S.; Reisner, W. W.; Riehn, R.; Wang, Y. M.; Cox, E. C.; Sturm, J. C.; Silberzan, P.; Austin, R. H., The dynamics of genomic-length DNA molecules in 100-nm channels. *Proceedings of the National Academy of Sciences of the United States of America* **2004,** *101* (30), 10979-10983.
32. Reisner, W.; Morton, K. J.; Riehn, R.; Wang, Y. M.; Yu, Z.; Rosen, M.; Sturm, J. C.; Chou, S. Y.; Frey, E.; Austin, R. H., Statics and dynamics of single DNA molecules confined in nanochannels. *Physical Review Letters* **2005,** *94* (19), 196101.
33. Reisner, W.; Beech, J. P.; Larsen, N. B.; Flyvbjerg, H.; Kristensen, A.; Tegenfeldt, J. O., Nanoconfinement-enhanced conformational response of single DNA molecules to changes in ionic environment. *Physical review letters* **2007,** *99* (5), 058302.
34. Reisner, W.; Pedersen, J. N.; Austin, R. H., DNA confinement in nanochannels: physics and biological applications. *Reports on Progress in Physics* **2012,** *75* (10), 106601.
35. Orland, H., Flory theory revisited. *Journal de Physique I* **1994,** *4* (1), 101-114.
36. Baumgärtner, A., Excluded volume effect on polymer films. *Polymer* **1982,** *23* (3), 334-335.
37. Schaefer, D. W.; Joanny, J. F.; Pincus, P., Dynamics of semiflexible polymers in solution. *Macromolecules* **1980,** *13* (5), 1280-1289.
38. Tegenfeldt, J. O.; Prinz, C.; Cao, H.; Chou, S.; Reisner, W. W.; Riehn, R.; Wang, Y. M.; Cox, E. C.; Sturm, J. C.; Silberzan, P., The dynamics of genomic-length DNA molecules in 100-nm channels. *Proceedings of the National Academy of Sciences* **2004,** *101* (30), 10979-10983.

39. Odijk, T., The statistics and dynamics of confined or entangled stiff polymers. *Macromolecules* **1983,** *16* (8), 1340-1344.
40. Odijk, T., DNA confined in nanochannels: Hairpin tightening by entropic depletion. *The Journal of chemical physics* **2006,** *125* (20), 204904.
41. Han, J.; Craighead, H. G., Separation of Long DNA Molecules in a Microfabricated Entropic Trap Array. *Science* **2000,** *288* (5468), 1026-1029.
42. Han, J.; Craighead, H. G., Characterization and optimization of an entropic trap for DNA separation. *Analytical chemistry* **2002,** *74* (2), 394-401.
43. Plecis, A.; Schoch, R. B.; Renaud, P., Ionic transport phenomena in nanofluidics: experimental and theoretical study of the exclusion-enrichment effect on a chip. *Nano letters* **2005,** *5* (6), 1147-1155.
44. Karnik, R.; Fan, R.; Yue, M.; Li, D.; Yang, P.; Majumdar, A., Electrostatic control of ions and molecules in nanofluidic transistors. *Nano letters* **2005,** *5* (5), 943-948.
45. Napoli, M.; Eijkel, J. C. T.; Pennathur, S., Nanofluidic technology for biomolecule applications: a critical review. *Lab on a Chip* **2010,** *10* (8), 957-985.
46. Xia, D.; Yan, J.; Hou, S., Fabrication of Nanofluidic Biochips with Nanochannels for Applications in DNA Analysis. *Small* **2012,** *8* (18), 2787-2801.
47. de la Escosura-Muñiz, A.; Merkoçi, A., Nanochannels Preparation and Application in Biosensing. *ACS Nano* **2012,** *6* (9), 7556-7583.
48. Chantiwas, R.; Park, S.; Soper, S. A.; Kim, B. C.; Takayama, S.; Sunkara, V.; Hwang, H.; Cho, Y.-K., Flexible fabrication and applications of polymer nanochannels and nanoslits. *Chemical Society Reviews* **2011,** *40* (7), 3677-3702.
49. Douville, N.; Huh, D.; Takayama, S., DNA linearization through confinement in nanofluidic channels. *Anal Bioanal Chem* **2008,** *391* (7), 2395-2409.
50. Mijatovic, D.; Eijkel, J. C. T.; van den Berg, A., Technologies for nanofluidic systems: top-down vs. bottom-up-a review. *Lab on a Chip* **2005,** *5* (5), 492-500.
51. Duan, C.; Wang, W.; Xie, Q., Review article: Fabrication of nanofluidic devices. *Biomicrofluidics* **2013,** *7* (2), -.
52. Leontowich, A. F. G.; Hitchcock, A. P.; Watts, B.; Raabe, J., Sub-25 nm direct write (maskless) X-ray nanolithography. *Microelectronic Engineering* **2013,** *108*, 5-7.
53. Kim, S.; Marelli, B.; Brenckle, M. A.; Mitropoulos, A. N.; Gil, E.-S.; Tsioris, K.; Tao, H.; Kaplan, D. L.; Omenetto, F. G., All-water-based electron-beam lithography using silk as a resist. *Nature nanotechnology* **2014,** *9* (4), 306.
54. Tseng, A. A.; Chen, K.; Chen, C. D.; Ma, K. J., Electron beam lithography in nanoscale fabrication: recent development. *IEEE Transactions on electronics packaging manufacturing* **2003,** *26* (2), 141-149.
55. Manfrinato, V. R.; Zhang, L.; Su, D.; Duan, H.; Hobbs, R. G.; Stach, E. A.; Berggren, K. K., Resolution limits of electron-beam lithography toward the atomic scale. *Nano letters* **2013,** *13* (4), 1555-1558.
56. Liu, C. Y.; Datta, A.; Wang, Y. L., Ordered anodic alumina nanochannels on focused-ion-beam-prepatterned aluminum surfaces. *Applied Physics Letters* **2001,** *78* (1), 120-122.
57. Tseng, A. A.; Insua, I. A.; Park, J. S.; Li, B.; Vakanas, G. P., Milling of submicron channels on gold layer using double charged arsenic ion beam. *Journal of Vacuum Science & Technology B: Microelectronics and Nanometer Structures Processing, Measurement, and Phenomena* **2004,** *22* (1), 82-89.
58. Li, H.-W.; Kang, D.-J.; Blamire, M. G.; Huck, W. T. S., Focused ion beam fabrication of silicon print masters. *Nanotechnology* **2003,** *14* (2), 220.
59. Tong, H. D.; Jansen, H. V.; Gadgil, V. J.; Bostan, C. G.; Berenschot, E.; van Rijn, C. J. M.; Elwenspoek, M., Silicon nitride nanosieve membrane. *Nano letters* **2004,** *4* (2), 283-287.

60. Cannon Jr, D. M.; Flachsbart, B. R.; Shannon, M. A.; Sweedler, J. V.; Bohn, P. W., Fabrication of single nanofluidic channels in poly (methylmethacrylate) films via focused-ion beam milling for use as molecular gates. *Applied Physics Letters* **2004,** *85* (7), 1241-1243.
61. Cho, Y. H.; Park, J.; Park, H.; Cheng, X.; Kim, B. J.; Han, A., Fabrication of high-aspect-ratio polymer nanochannels using a novel Si nanoimprint mold and solvent-assisted sealing. *Microfluid Nanofluid* **2010,** *9* (2-3), 163-170.
62. Chantiwas, R.; Hupert, M. L.; Pullagurla, S. R.; Balamurugan, S.; Tamarit-Lopez, J.; Park, S.; Datta, P.; Goettert, J.; Cho, Y.-K.; Soper, S. A., Simple replication methods for producing nanoslits in thermoplastics and the transport dynamics of double-stranded DNA through these slits. *Lab on a Chip* **2010,** *10* (23), 3255-3264.
63. Lasse, H. T.; Anna, K.; Anders, K., Stretching DNA in polymer nanochannels fabricated by thermal imprint in PMMA. *Nanotechnology* **2008,** *19* (12), 125301.
64. Abgrall, P.; Low, L.-N.; Nguyen, N.-T., Fabrication of planar nanofluidic channels in a thermoplastic by hot-embossing and thermal bonding. *Lab on a Chip* **2007,** *7* (4), 520-522.
65. Hu, X.; He, Q.; Zhang, X.; Chen, H., Fabrication of fluidic chips with 1-D nanochannels on PMMA substrates by photoresist-free UV-lithography and UV-assisted low-temperature bonding. *Microfluid Nanofluid* **2011,** *10* (6), 1223-1232.
66. Xu, Y.; Wang, C.; Dong, Y.; Li, L.; Jang, K.; Mawatari, K.; Suga, T.; Kitamori, T., Low-temperature direct bonding of glass nanofluidic chips using a two-step plasma surface activation process. *Anal Bioanal Chem* **2012,** *402* (3), 1011-1018.
67. Kim, S. H.; Cui, Y.; Lee, M. J.; Nam, S.-W.; Oh, D.; Kang, S. H.; Kim, Y. S.; Park, S., Simple fabrication of hydrophilic nanochannels using the chemical bonding between activated ultrathin PDMS layer and cover glass by oxygen plasma. *Lab on a Chip* **2011,** *11* (2), 348-353.
68. Gu, J.; Gupta, R.; Chou, C.-F.; Wei, Q.; Zenhausern, F., A simple polysilsesquioxane sealing of nanofluidic channels below 10 nm at room temperature. *Lab on a Chip* **2007,** *7* (9), 1198-1201.
69. Mao, P.; Han, J., Fabrication and characterization of 20 nm planar nanofluidic channels by glass–glass and glass–silicon bonding. *Lab on a Chip* **2005,** *5* (8), 837-844.
70. Garcia, A. L.; Ista, L. K.; Petsev, D. N.; O'Brien, M. J.; Bisong, P.; Mammoli, A. A.; Brueck, S. R.; López, G. P., Electrokinetic molecular separation in nanoscale fluidic channels. *Lab on a Chip* **2005,** *5* (11), 1271-1276.
71. Cabodi, M.; Turner, S. W. P.; Craighead, H. G., Entropic Recoil Separation of Long DNA Molecules. *Analytical Chemistry* **2002,** *74* (20), 5169-5174.
72. Kyo Seon, C.; Seungwook, K.; Haegeun, C.; Joon-Ho, O.; Tae-Yeon, S.; Boo Hyun, A.; Young Keun, K.; Jae Hyoung, P.; Young Rag, D.; Woong, K., Fabrication of monolithic polymer nanofluidic channels using nanowires as sacrificial templates. *Nanotechnology* **2010,** *21* (42), 425302.
73. Tas, N. R.; Berenschot, J. W.; Mela, P.; Jansen, H. V.; Elwenspoek, M.; van den Berg, A., 2D-Confined Nanochannels Fabricated by Conventional Micromachining. *Nano Letters* **2002,** *2* (9), 1031-1032.
74. Xia, Q.; Morton, K. J.; Austin, R. H.; Chou, S. Y., Sub-10 nm Self-Enclosed Self-Limited Nanofluidic Channel Arrays. *Nano Letters* **2008,** *8* (11), 3830-3833.
75. Tan, S.; Klein, K.; Shima, D.; Livengood, R.; Mutunga, E.; Vladar, A., Mechanism and applications of helium transmission milling in thin membranes. *Journal of Vacuum Science & Technology B* **2014,** *32*, 06FA01.
76. Yang, J.; Ferranti, D. C.; Stern, L. A.; Sanford, C. A.; Huang, J.; Ren, Z.; Qin, L.-C.; Hall, A. R., Rapid and precise scanning helium ion microscope milling of solid-state nanopores for biomolecule detection. *Nanotechnology* **2011,** *22*, 285310.
77. Chou, S. Y.; Krauss, P. R.; Renstrom, P. J., Imprint of sub-25 nm vias and trenches in polymers. *Applied Physics Letters* **1995,** *67* (21), 3114-3116.

78. Chou, S. Y.; Krauss, P. R.; Renstrom, P. J., Nanoimprint lithography. *Journal of Vacuum Science & Technology B* **1996,** *14* (6), 4129-4133.
79. Chou, S. Y.; Krauss, P. R., Imprint lithography with sub-10 nm feature size and high throughput. *Microelectronic Engineering* **1997,** *35* (1–4), 237-240.
80. Junshan, L.; Hongchao, Q.; Zheng, X.; Chong, L.; Junyao, W.; Liqun, D.; Xi, Z.; Liding, W., Fabrication of planar nanofluidic channels in thermoplastic polymers by O₂ plasma etching. *Micro & Nano Letters, IET* **2012,** *7* (2), 159-162.
81. Liu, J.; Jin, X.; Sun, T.; Xu, Z.; Liu, C.; Wang, J.; Chen, L.; Wang, L., Hot embossing of polymer nanochannels using PMMA moulds. *Microsyst Technol* **2013,** *19* (4), 629-634.
82. Li, J.-m.; Liu, C.; Ke, X.; Xu, Z.; Duan, Y.-j.; Fan, Y.; Li, M.; Zhang, K.-p.; Wang, L.-d., Microchannel refill: a new method for fabricating 2D nanochannels in polymer substrates. *Lab on a Chip* **2012,** *12* (20), 4059-4062.
83. Zhang, L.; Gu, F.; Tong, L.; Yin, X., Simple and cost-effective fabrication of two-dimensional plastic nanochannels from silica nanowire templates. *Microfluid Nanofluid* **2008,** *5* (6), 727-732.
84. Manneschi, C.; Fanzio, P.; Ala-Nissila, T.; Angeli, E.; Repetto, L.; Firpo, G.; Valbusa, U., Stretching of DNA confined in nanochannels with charged walls. *Biomicrofluidics* **2014,** *8* (6).
85. Kim, Y.; Kim, K. S.; Kounovsky, K. L.; Chang, R.; Jung, G. Y.; de Pablo, J. J.; Jo, K.; Schwartz, D. C., Nanochannel Confinement: DNA Stretch Approaching Full Contour Length. *Lab on a chip* **2011,** *11* (10), 1721-1729.
86. Marie, R.; Kristensen, A., Nanofluidic devices towards single DNA molecule sequence mapping. *Journal of Biophotonics* **2012,** *5* (8-9), 673-686.
87. Müller, V.; Westerlund, F., Optical DNA mapping in nanofluidic devices: principles and applications. *Lab on a Chip* **2017,** *17* (4), 579-590.
88. Guo, L. J.; Cheng, X.; Chou, C.-F., Fabrication of Size-Controllable Nanofluidic Channels by Nanoimprinting and Its Application for DNA Stretching. *Nano Letters* **2004,** *4* (1), 69-73.
89. Ravindran, P.; Gupta, A., Image processing for optical mapping. *GigaScience* **2015,** *4*, 57-57.
90. Neely, R. K.; Deen, J.; Hofkens, J., Optical mapping of DNA: Single-molecule-based methods for mapping genomes. *Biopolymers* **2011,** *95* (5), 298-311.
91. Riehn, R.; Lu, M.; Wang, Y.-M.; Lim, S. F.; Cox, E. C.; Austin, R. H., Restriction mapping in nanofluidic devices. *Proceedings of the National Academy of Sciences of the United States of America* **2005,** *102* (29), 10012-10016.
92. Wang, Y. M.; Tegenfeldt, J. O.; Reisner, W.; Riehn, R.; Guan, X.-J.; Guo, L.; Golding, I.; Cox, E. C.; Sturm, J.; Austin, R. H., Single-molecule studies of repressor–DNA interactions show long-range interactions. *Proceedings of the National Academy of Sciences of the United States of America* **2005,** *102* (28), 9796-9801.
93. Jo, K.; Dhingra, D. M.; Odijk, T.; de Pablo, J. J.; Graham, M. D.; Runnheim, R.; Forrest, D.; Schwartz, D. C., A single-molecule barcoding system using nanoslits for DNA analysis. *Proceedings of the National Academy of Sciences of the United States of America* **2007,** *104* (8), 2673-2678.
94. Das, S. K.; Austin, M. D.; Akana, M. C.; Deshpande, P.; Cao, H.; Xiao, M., Single molecule linear analysis of DNA in nano-channel labeled with sequence specific fluorescent probes. *Nucleic acids research* **2010,** *38* (18), e177-e177.
95. Jinek, M.; Chylinski, K.; Fonfara, I.; Hauer, M.; Doudna, J. A.; Charpentier, E., A Programmable Dual-RNA–Guided DNA Endonuclease in Adaptive Bacterial Immunity. *Science* **2012,** *337* (6096), 816-821.
96. Grunwald, A.; Dahan, M.; Giesbertz, A.; Nilsson, A.; Nyberg, L. K.; Weinhold, E.; Ambjornsson, T.; Westerlund, F.; Ebenstein, Y., Bacteriophage strain typing by rapid single molecule analysis. *Nucleic Acids Res* **2015,** *43* (18), e117.

97. Grunwald, A.; Dahan, M.; Giesbertz, A.; Nilsson, A.; Nyberg, L. K.; Weinhold, E.; Ambjörnsson, T.; Westerlund, F.; Ebenstein, Y., Bacteriophage strain typing by rapid single molecule analysis. *Nucleic acids research* **2015,** *43* (18), e117-e117.
98. Reisner, W.; Larsen, N. B.; Silahtaroglu, A.; Kristensen, A.; Tommerup, N.; Tegenfeldt, J. O.; Flyvbjerg, H., Single-molecule denaturation mapping of DNA in nanofluidic channels. *Proceedings of the National Academy of Sciences of the United States of America* **2010,** *107* (30), 13294-13299.
99. Welch, R. L.; Sladek, R.; Dewar, K.; Reisner, W. W., Denaturation mapping of Saccharomyces cerevisiae. *Lab on a Chip* **2012,** *12* (18), 3314-3321.
100. Nyberg, L. K.; Quaderi, S.; Emilsson, G.; Karami, N.; Lagerstedt, E.; Müller, V.; Noble, C.; Hammarberg, S.; Nilsson, A. N.; Sjöberg, F.; Fritzsche, J.; Kristiansson, E.; Sandegren, L.; Ambjörnsson, T.; Westerlund, F., Rapid identification of intact bacterial resistance plasmids via optical mapping of single DNA molecules. *Scientific Reports* **2016,** *6*, 30410.
101. Lim, S. F.; Karpusenko, A.; Sakon, J. J.; Hook, J. A.; Lamar, T. A.; Riehn, R., DNA methylation profiling in nanochannels. *Biomicrofluidics* **2011,** *5* (3), 34106-341068.
102. Sun, X.; Yasui, T.; Yanagida, T.; Kaji, N.; Rahong, S.; Kanai, M.; Nagashima, K.; Kawai, T.; Baba, Y., Identifying DNA methylation in a nanochannel. *Science and technology of advanced materials* **2016,** *17* (1), 644-649.
103. Nagase, H.; Ghosh, S., Epigenetics: differential DNA methylation in mammalian somatic tissues. *The FEBS Journal* **2008,** *275* (8), 1617-1623.
104. Shigematsu, H.; Suzuki, M.; Takahashi, T.; Miyajima, K.; Toyooka, S.; Shivapurkar, N.; Tomlinson, G. E.; Mastrangelo, D.; Pass, H. I.; Brambilla, E.; Sathyanarayana, U. G.; Czerniak, B.; Fujisawa, T.; Shimizu, N.; Gazdar, A. F., Aberrant methylation of HIN-1 (high in normal-1) is a frequent event in many human malignancies. *International Journal of Cancer* **2005,** *113* (4), 600-604.
105. Cokus, S. J.; Feng, S.; Zhang, X.; Chen, Z.; Merriman, B.; Haudenschild, C. D.; Pradhan, S.; Nelson, S. F.; Pellegrini, M.; Jacobsen, S. E., Shotgun bisulphite sequencing of the Arabidopsis genome reveals DNA methylation patterning. *Nature* **2008,** *452* (7184), 215-219.
106. Levy-Sakin, M.; Grunwald, A.; Kim, S.; Gassman, N. R.; Gottfried, A.; Antelman, J.; Kim, Y.; Ho, S. O.; Samuel, R.; Michalet, X.; Lin, R. R.; Dertinger, T.; Kim, A. S.; Chung, S.; Colyer, R. A.; Weinhold, E.; Weiss, S.; Ebenstein, Y., Toward Single-Molecule Optical Mapping of the Epigenome. *ACS Nano* **2014,** *8* (1), 14-26.
107. Lam, E. T.; Hastie, A.; Lin, C.; Ehrlich, D.; Das, S. K.; Austin, M. D.; Deshpande, P.; Cao, H.; Nagarajan, N.; Xiao, M.; Kwok, P.-Y., Genome mapping on nanochannel arrays for structural variation analysis and sequence assembly. *Nat Biotech* **2012,** *30* (8), 771-776.
108. Wang, Y.; Liu, L.; Wu, C.; Bulgar, A.; Somoza, E.; Zhu, W.; Gerson, S. L., Direct detection and quantification of abasic sites for in vivo studies of DNA damage and repair. *Nuclear medicine and biology* **2009,** *36* (8), 975-983.
109. O'Neil, C.; Amarasekara, C. A.; Weerakoon-Ratnayake, K. M.; Gross, B.; Jia, Z.; Singh, V.; Park, S.; Soper, S. A., Electrokinetic transport properties of deoxynucleotide monophosphates (dNMPs) through thermoplastic nanochannels. *Analytica Chimica Acta* **2018,** *1027*, 67-75.
110. Weerakoon Ratnayake, K., Single Molecule Electrophoresis and Optical Detection Using Thermoplastic Nanofluidic Devices: An Experimental and Simulation Study. *LSU Doctoral Dissertations* **2015**.

Chapter 2: Thermoplastic Nanofluidic Devices for Identifying Abasic Sites in Single DNA Molecules

2.1 Abstract

DNA damage can take many forms such as double-strand breaks and/or the formation of abasic (apurinic/apyrimidinic; AP) sites. The presence of AP sites can be used to determine therapeutic efficacy of many drugs, such as doxorubicin. While there are different assays to search for DNA damage, they are fraught with limitations, such as the need for large amounts of DNA secured from millions of cells. This is challenging due to the growing importance of using liquid biopsies as a source of biomarkers for many *in vitro* diagnostic assays. To accommodate the mass limits imposed by the use of liquid biopsies, we report a single-molecule DNA damage assay that uses plastic nanofluidic chips to stretch DNA to near its full contour length when the channel dimensions (width and depth) are near the persistence length (~50 nm) of double-stranded (ds) DNA. The nanofluidic chip consisted of input funnels for high loading efficiency of single DNA molecules, entropic traps to store the DNA and simultaneous load a series of nanochannels for high throughput processing, and an array of stretching nanochannels to read the AP sites. Single dsDNA molecules, which were labeled with an intercalating dye and a biotinylated aldehyde reactive probe (bARP), could be parked in the stretching nanochannels, where the AP sites were read directly using a dual-color fluorescence microscope equipped with an EMCCD camera. One color of the microscope was used to read the DNA length and the second color detected the AP sites. The nanofluidic chip was made from thermoplastics via nanoimprint lithography, which obviated the need for direct writing the devices in glass or quartz using focused ion beam milling. We show that we can read the frequency of AP sites in single dsDNA molecules with the frequency of AP sites determined by associating fluorescently-labeled streptavidin with bARP through a biotin/streptavidin complex.

2.2 Introduction

Cellular DNA is constantly subjected to various exogenous and endogenous reactive species that result in DNA damage. DNA damage can generate a loss of a nucleotide base, usually from spontaneous

hydrolysis of N-glycosylic bonds leading to the formation of apurinic/apyrimidinic (AP) sites, commonly referred to as abasic sites.[2] Exogenous factors such as ultraviolet radiation, X-rays, tobacco smoke, and endogenous factors such as metabolic processes that produce reactive oxygen species (ROS) can generate AP sites in DNA.[3] These factors can alter the bases in several ways including methylation or oxidation of guanine bases producing N^7-methylguanine (N^7-meG) or 8-oxo-7,8-dihydroguanine (8-oxoG), respectively.[4]

These damaged bases can be repaired through a variety of *in vivo* mechanisms but the predominant repair mechanism is the base excision repair (BER) pathway. BER repairs single bases with modifications[3-4] by removal of the damaged bases via DNA glycosylases resulting in AP sites that are intermediates of the BER pathway.[5]

Many therapies for cancer depend on DNA damaging agents that cause cytotoxicity and cell death, which impeded tumor growth and spreading. Thus, increase in the number of AP sites often serve as biomarkers of a patient's response to therapy.[6] Most AP sites in healthy individuals are repaired, while the excess number of AP sites produced in cancer patients receiving chemotherapy are higher in abundance than those not receiving DNA damaging chemotherapeutic agents. An example of a damaging chemotherapeutic agent is Doxorubicin (DOX), an anthracycline antibiotic that is used for treating breast cancer patients,[7] and is a potent exogenous agent that causes extensive production of ROS.[8] DOX works by interfering with topoisomerase II enzyme action in addition to the formation of several ROS and H_2O_2.

Several methods to quantify AP sites have been reported. One method uses capillary electrophoresis with laser-induced fluorescence (CE-LIF), where the DNA possessing AP sites are labelled with a fluorescent aldehyde reactive probe (FARP).[9] Robert *et al.* developed a chromatographic/tandem mass spectrometry method for the detection of AP sites pre-labelled with O-4-nitrobenzylhydroxylamine.[5] Wang *et al.* used Positron Emission Tomography, where a positron emitting carbon-11 was integrated into methoxyamine that identified AP sites by forming covalent bonds with them. Some of the above-mentioned methods are expensive and/or labor intensive and as such, are clinically incompatible. [10-11]

The use of a biotin containing aldehyde reactive probe (bARP) to quantify AP sites[12] was initially developed by Kubo *et al.*[13] In this method, the aldehyde group in the deoxyribose sugar of the open ring form of the AP site reacts with the alkoxyamine in bARP forming an oxime. The bARP binds to dye-labelled streptavidin to allow securing an optical signature indicative of an AP site. [12, 14-15]

Commercially available benchtop techniques to detect AP sites include a microtiter method, where bARP binds specifically to the aldehyde groups in the AP sites followed by ELISA, where alkaline phosphatase reacts with bARP and absorbance is measured at 650 nm.[16] However, because this is a colorimetric assay, it can only determine the number of AP sites, but cannot deduce the position of AP sites within the DNA molecule. In addition, the concentration of DNA has to be above a certain limit for the benchtop method to detect the AP sites. Unfortunately, this technique requires large quantities of DNA, which is not achievable when analyzing DNA secured from liquid biopsy markers. For example, circulating tumor cells (CTCs) recovered from liquid biopsies typically yield only 2-200 cells per mL with the number recovered depending on the cancer type and stage. [17-18] This small number of cells corresponds to a DNA mass in the range of picograms, which is well below the lower limit of sample required for the colorimetric method (see SI for more information).

Another method to detect AP sites is based on PCR. But the issue with this method is when amplifying the DNA containing AP sites, the DNA polymerase results in mis-incorporation of nucleotides leading to mutations or stalling of the PCR at the 3' hydroxyl end of the missing nucleobase. Sikorsky *et al.* suggested that the presence of AP sites leads to the DNA polymerase during PCR to preferentially incorporate dATP and inducing n-1 deletions opposite the AP sites.[19] As such, researchers have been investigating methods to quantify AP sites using techniques that require smaller amounts of input DNA.

Single-molecule imaging can process small amounts of DNA. Detection of AP sites on a 250 bp DNA with 2 AP sites was performed using atomic force microscopy.[20] A method to directly visualize AP sites on λ-DNA stretched on a glass slide[21] used scanning near-field optical microscopy.[22] Chastain and coworkers mapped the frequency of AP sites in DNA by optically interrogating single DNA molecules spread on a

glass slide.[23] These methods suffered from several shortcomings, such as time consuming optical scanning, and the need for complicated sample preparation workflows.[24]

The ability to detect smaller masses of DNA, even single molecules, has led to the development of nanofluidics, which includes 1D structures like nano-slits, 2D structures like nanochannels, and 3D structures like nanopores.[1] Nano-confined environments, for example nanochannels, overcome the static and dynamic motions of nucleic acids by confining and stretching them in a space smaller than their persistence length, which is approximately 50 nm for double stranded (ds) DNA. Nanometer channels also reduce the sample volume requirements and analysis time.[25] One approach for visualizing single molecule in a high throughput format is DNA curtain technology developed by Greene *et al.*, where DNA is anchored to one end of a lipid bilayer membrane and is pushed using hydrodynamic forces to the other end. The DNA molecules were aligned and stretched simultaneously along these barriers. But, the bottleneck of this approach is the requirement of a lipid barrier in the absence of which the DNA would not align.[26] In addition, the technique uses electron beam lithography (EBL) of fused silica glass, which makes the fabrication process both complicated and expensive.[27] Recently, a DNA-skybridge (3D-structure) was reported, which used the same principles for stretching DNA molecules and imaging them in a high throughput format using light sheet microscopy.[28]As with the aforementioned techniques, hydrodynamic forces are required to stretch the DNA and the DNA must be functionalized with a biotin molecule on both ends to anchor the DNA to a surface.

Here we present a high throughput, novel sensing platform for the direct reading of AP sites with optical quantification by the controlled stretching of single dsDNA molecules to near their full contour length using a nanochannel array imprinted into a thermoplastic. Our nanostructures were fabricated in poly(methyl methacrylate), PMMA, using nanoimprint lithography (NIL), where the structures from a Si master were transferred into the PMMA polymer using a three-step process. The first step consisted of the transfer of nanoscale features into a UV resin. The second step used the UV resin stamp to transfer the structures into another polymer (PMMA) under certain pressure and temperature depending on the glass transition temperature (Tg) of the polymer. Finally, the nano-features were covered with a cyclic olefin copolymer

(COC) plate using thermal fusion bonding according to a previously published method from our group. [29-31]

Imprinted channels were ≤100 nm (width and depth) to allow stretching of single dsDNA molecules close to their contour length. The device consisted of an array of nanochannels with each channel possessing a funnel entrance capable of efficient loading of single DNA molecules and connected to an entropic nano-trap for storing the DNA that enters the nanofluidic circuit randomly. The stored DNA could then be loaded simultaneously into an array of stretching nanochannels, where they were parked for direct reading of the AP sites using single-molecule imaging. AP sites were labeled with bARP, which associated to a fluorescently-labeled streptavidin molecule (red fluorescent label). The dsDNA molecule was also labeled with an intercalating dye (green fluorescence intercalating dye) to read DNA length. After loading into the nanochannels, fluorescently-labeled AP sites were optically visualized using wide-field epi-illumination microscopy with dual color laser excitation and direct quantification of AP sites by analyzing optical signatures of the stretched DNA.

2.3 Experimental Methods

2.3.1 Materials and reagents

Silicon (Si) <100> wafers were secured from University Wafers (Boston, MA). PMMA (T_g = 105°C) sheets were purchased from Good Fellow (Berwyn, PA) and cyclic olefin copolymer (COC 8007, T_g = 78°C) cover plates were purchased from TOPAS Advanced Polymers (Florence, KY). The anti-adhesion coating material, (tridecafluoro–1,1,2,2-tetrahydrooctyl) trichlorosilane (T-silane), was secured from Gelest, Inc. (Morrisville, PA). Tripropylene glycol diacrylate (TPGDA), trimethylolpropane triacrylate (TMPTA), Irgacure 651 (photo-initiator), sodium citrate buffer (pH = 5.0), and β-mercaptoethanol were obtained from Sigma-Aldrich (St Louis, MO). λ-DNA, 48.5 Kbp (New England BioLabs, Ipswich MA) and T4 DNA, 166 Kbp (Wako Chemicals USA, Inc. Richmond VA) were used as received. The DNA damage quantification kit was purchased from Dojindo Molecular Technologies, Inc. Rockville MD. Aldehyde Reactive Probe with biotin (bARP), streptavidin/Alexa Fluor® 594 conjugate,

streptavidin/Alexa Fluor® 647 conjugate, and YOYO-1 were all purchased from Life Technologies (Carlsbad, NY). Chroma spin TE-1000 columns were obtained from Clontech Laboratories, Inc. (San Francisco CA). Aqueous citrate buffer and Tris-Borate-EDTA (TBE, 89 mM Tris, 89 mM Borate, 2 mM EDTA) buffer were secured from Fisher Scientific® (Philadelphia, PA). All dilutions of reagents and model samples were made using 18 MΩ/cm milliQ water (Millipore). Solutions were filtered through 0.2 μm filters (Thermo Scientific® Nalgene syringe filters) prior to use.

2.3.2 Fabrication of the multi-structured nanofluidic devices

Nanofluidic devices were fabricated using our published procedures (see Figure 2.1).[22, 32] Briefly, microstructures were fabricated into a Si substrate using photolithography and wet-etching. Photolithography was done using AZ1518 photoresist, spin coated on oxide coated wafers at 3000 rpm for 60 s. The wafers were baked at 100°C for 2 mins and exposed to UV light for 4 s and the features were developed using MIF-300 developer. Subsequently, they are wet-etched using 40% KOH until the Si is etched for a depth of 6-7 μm. Nanochannels were milled into the Si substrate by FIB milling (FEI Helios 600 Nanolab Dual Beam System). A multi-structure device with an array of nanochannels (100 nm x 80 nm) possessing a 3D tapered funnel with/without a nano-trap (400 nm and 600 nm diameter) were fabricated by FIB milling. The Si master was first replicated into a UV-resin consisting of 70% TPGDA, 28% TMPTA, and 2% Igacure 651 via UV-NIL to produce a UV-resin stamp. The patterns in the UV-resin stamp were then transferred into a PMMA substrate by thermal NIL at 130°C for 120 s under 1910 kN/m^2 (HEX03, JenOptik). The structures were enclosed with a low T_g COC 8007 cover plate by thermal fusion bonding at 70°C under a pressure of 680 kN/m^2 for 900 s.

2.3.3 Finite element analysis (COMSOL)

The nano-trap structure was simulated using a 2D model in COMSOL to explore the electric field drop across nano-traps of different sizes (400 nm and 600 nm) for λ-DNA (48.5 Kbp). The electric field was simulated with a driving potential of 0.1 V at a temperature of 293 K. A line plot across the nano-trap was created and the drop in electric field strength across the corresponding nano-trap was determined from the simulation.

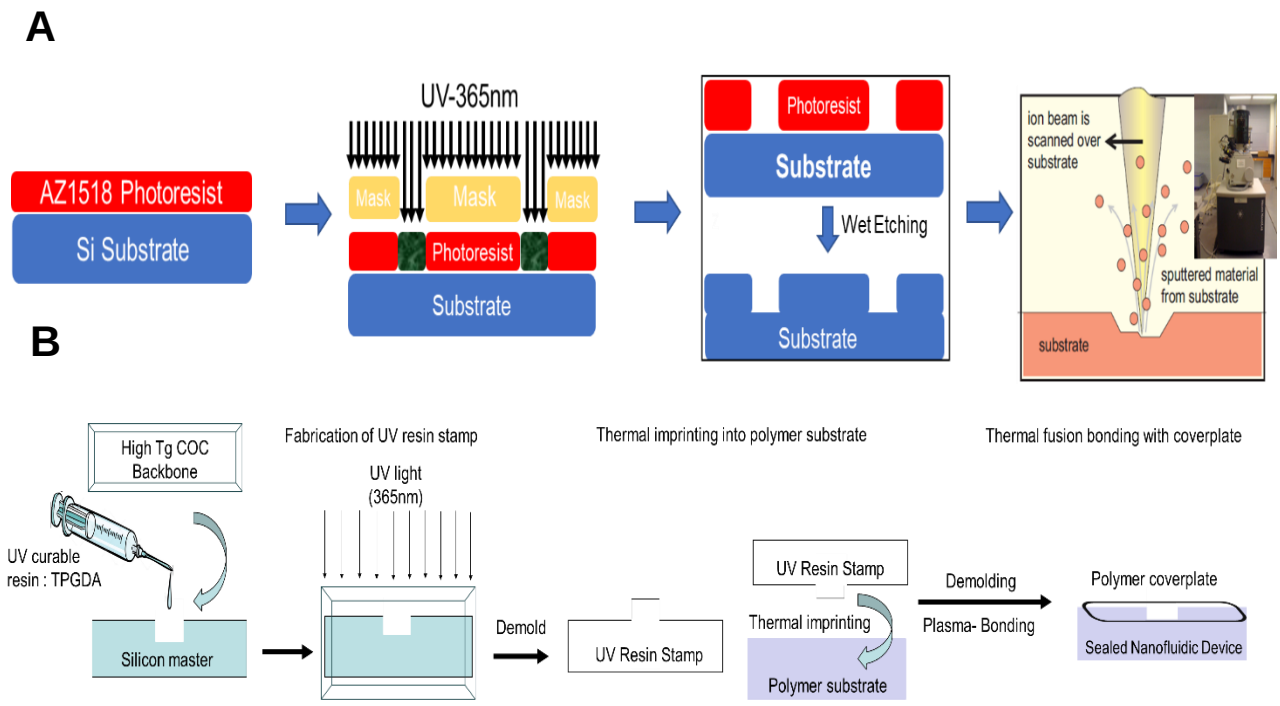

Figure 2.1 Schematic showing the top down fabrication process used to make the plastic nanofluidic devices used in these studies. (**A**) First, photolithography on Si wafer using AZ1518 resist was performed followed by wet etching to achieve the desired depth of the microfluidic channels. As a final step, FIB was performed to fabricate the nanodimensional features on the Si master. (**B**) The NIL steps are shown here. Briefly, the features from the Si master were transferred to a resin stamp using UV light. They were then thermally imprinted using NIL into a PMMA substrate. Finally, thermal fusion bonding was performed to seal the fluidic network with a COC cover plate.

2.3.4 Current-voltage measurements

The current across the multi-structured nanofluidic device with no nano-trap, 400 nm X 400 nm (dia X depth), and 600 nm X 600 nm (dia X depth) nano-traps were measured using an Axopatch 200B. Devices were initially filled with 50% methanol (v/v) to facilitate easy filling with aqueous buffers, followed by filling with a 1 M KCl solution in TBE buffer. The Pt electrodes were placed at each end of

the fluidic circuit equipped with large reservoirs to make ohmic contact and the device was placed inside a Faraday cage. Then, different voltages and the corresponding currents were recorded. Each data point represented the mean ±standard deviation from five different measurements.

2.3.5 Dual color laser system (see Figure 2.2).

The Gaussian beam from a 488 nm laser (λ_{ex} = 488 nm; P = 2000 mW; 2 mm beam diameter) was passed through a short pass dichroic filter (DF1) and expanded 10 times with a Galilean beam expander (focal lengths were -25 mm and 250 mm for L3 and L4 plano-concave and plano-convex lenses, respectively). The 641 nm laser beam (λ_{ex} = 641 nm; P = 140 mW; 0.7 mm beam diameter) was expanded 5 times with a Galilean beam expander (focal lengths were -25 mm and 125 mm for L1 and L2 plano-concave and plano-convex lenses, respectively). Then, it was passed through an iris used to knock off the wings of the beam and was reflected by DF1. Both laser beams were directed into the microscope to ensure

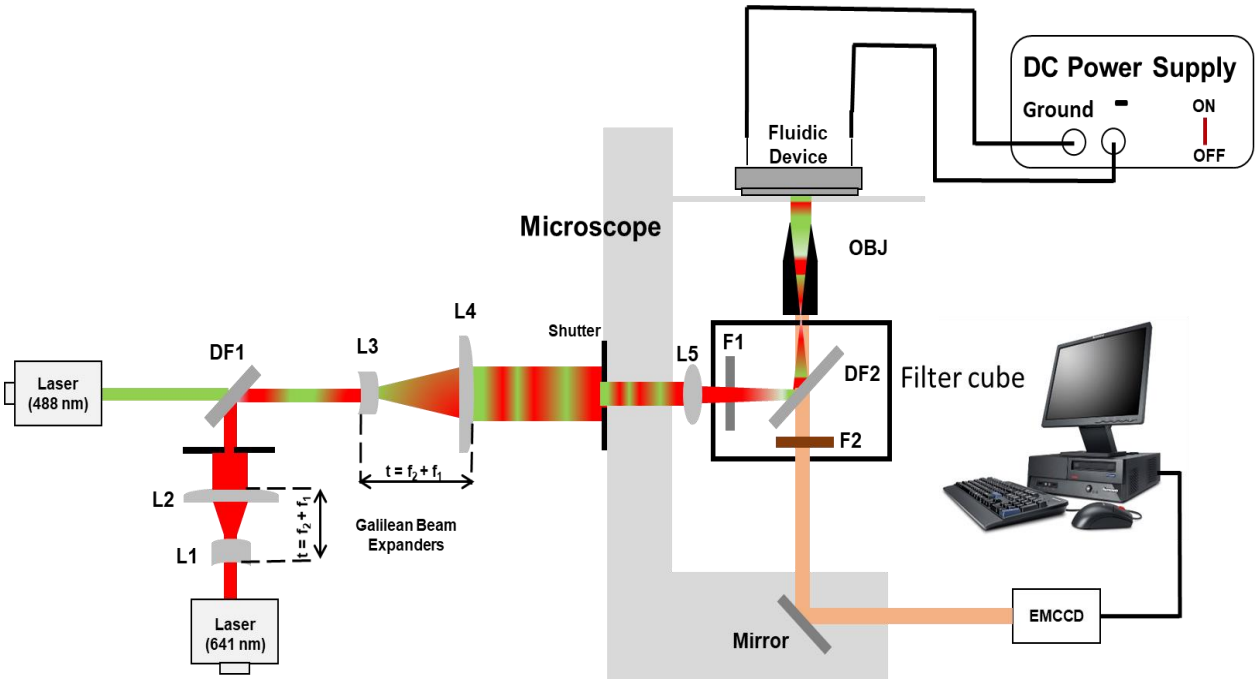

Figure 2.2 Schematic of the dual-color microscope system for single-molecule tracking and imaging. The nanofluidic device was placed on a translational stage associated with the inverted microscope and Pt electrodes were placed within specific reservoirs of the chip to supply the driving electric field to the chip using a DC power supply, which was earth grounded. Switching between the two lasers was controlled manually with a 1 s switching delay using a filter cube resident within the microscope. All images were acquired using an EMCCD camera and Metamorph software.

uniform laser intensity in the field-of-view and complete back-filling of the microscope objective (OBJ). The beam was passed through an iris into the back of a 100x oil immersion objective lens (1.25 NA) using lens L5 after passing through a laser line filter (F1) and reflected by a dichroic filter (DF2). A collimated laser beam impinged upon the nanofluidic device. Fluorescence emission was collected by the objective and passed through DF2 and spectrally selected using a long pass filter (F2). A mirror was used to steer the fluorescence onto an EMCCD camera. The videos and data were collected at ~150 fps using a Hamamatsu EMCCD C9100-13 digital camera with an EM gain and subsequently captured using Metamorph software. Faster frame rates (up to 405 fps) could be achieved using a smaller ROI and a binning option of the EMCCD camera.

2.3.6 Labelling λ-DNA using a bis-intercalating dye

λ-DNA (NEB) was stained with a bis-intercalating dye, YOYO-1 (Molecular Probes, Eugene, OR) in a 5:1 base-pair/dye ratio in 1X TBE (89 mM Tris, 89 mM Borate, 2 mM EDTA) buffer solution. The TBE solution also contained 4% v/v β-mercaptoethanol as an anti-photobleaching agent to reduce photo-induced damage by acting as a radical scavenger.

2.3.7 ARP-streptavidin assay

Genomic DNA in biological cells can be damaged due to reactive oxygen species (ROS) present in the cell. ROS inside the cell can be generated by radiation, chlorinated compounds, ultraviolet light, metal ions, peroxide compounds, or chemotherapeutic drugs.[14] Generated AP sites in a DNA reside in equilibrium with a ring opened and a ring closed structure (see Figure 2.3).

It has been reported that under native conditions, 5% of AP sites are in the ring-opened form containing an active aldehyde group.[14] Through the use of molar excess of reactive species or a probe with the aldehyde group, it is possible to convert all of the closed AP sites into the open-ring form.[14] A biotinylated hydroxylamine, called “aldehyde reactive probe” (bARP), readily conjugates to the active aldehyde group in the ring-opened form and attaches strongly through an imine bond (Figure 3). After labeling with bARP,

it is possible to produce an association complex with streptavidin. Horseradish peroxidase assays[20] and Alexa Fluor labeled streptavidin assays[21, 30] can then be used to produce biotin-streptavidin complexes.

2.3.8 Colorimetric assay for AP site quantification

DNA damage quantification kit was purchased from Dojindo Molecular Technologies, Inc. Standard AP DNA with a known number of AP sites was labeled with ARP. It included calf-thymus DNA (0.5 μg/mL) with 0, 2.5, 5, 10, 20, and 40 ARP-labeled AP sites per molecule, DNA binding solution, substrate solution, HRP-streptavidin, TE buffer, and washing buffer. Calibration curves were obtained using the standard protocol provided by the manufacturer.

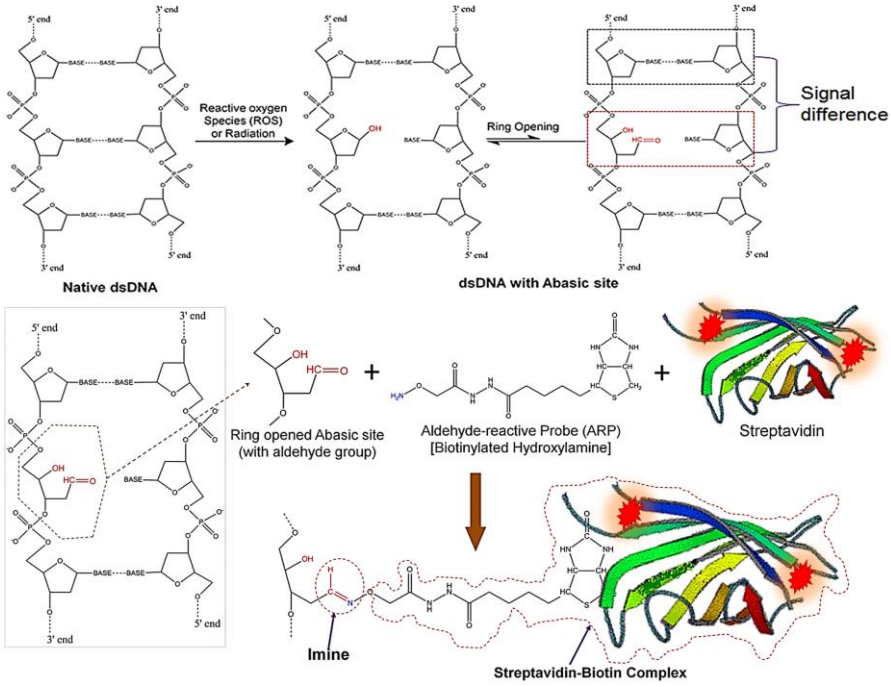

Figure 2.3 ROS inducing a loss of a nucleotide base (AP site) in dsDNA followed by ring opening, which generates an aldehyde group that is available for conjugation to an aldehyde reactive probe (ARP). ARP reacts with an active aldehyde group in the ring-opened form of the AP site. The biotin group in the ARP (bARP) has a strong affinity toward streptavidin, which allows for the generation of fluorescence at each AP site due to streptavidin being labeled with Alexa Fluor 647.[1]

To prepare the colorimetric assay using DNA standards in a 96 well plate, 60 μL of each standard ARP-DNA was added in 3 wells for each sample. Then, 100 μL of DNA binding solution was mixed by pipetting into each well followed by overnight incubation at room temperature. The next day, 1/4000 diluted HRP-

streptavidin solution was freshly prepared by mixing 10 µL of HRP-streptavidin in 40 mL of washing buffer (due to its instability, this solution was freshly prepared every time). Binding solutions were discarded, and the wells were washed with washing buffer 5 times. After washing, 150 µL of diluted HRP-streptavidin was added to each well and incubated at 37°C for 1 h. After incubation, the washing step was repeated. Then, 100 µL of substrate solution was added to each well and incubated at 37°C for another 1 h. The optical density (OD) was recorded using a 96-well plate reader (SpectraMax M5 Multimode Plate Reader, Molecular Devices, LLC).

2.3.9 Fluorescence dyes for AP site labeling

Suitable dyes for direct imaging of the AP sites were selected prior to the experiment and the feasibility of imaging with YOYO-1 was evaluated (YOYO-1 is an intercalating dye and is used to measure the DNA length to normalize the AP site frequency with respect to DNA length). We selected Alexa Fluor 647 for scoring the presence of AP sites (Alexa Fluor 647 was covalently attached to streptavidin and carried from 1-3 dyes per molecule) due to its deep red fluorescence, which showed minimal amounts of spectral overlap with the YOYO-1 intercalating dye. In addition, both YOYO-1 and Alexa Fluor 647 could be excited with both lasers found in our imaging system.

2.3.10 Labeling bARP AP DNA

bARP AP DNA was tagged with streptavidin covalently labeled with Alexa Fluor 647. The corresponding streptavidin molecule reacts with the biotin group present in bARP to produce Alexa Fluor labeled AP sites in the dsDNA. Figure 1 shows the amine group of the bARP probe reacting with an aldehyde group of the open-ringed form to produce an imine bond. Alexa Fluor labeled streptavidin solution was diluted by volume of 1 to 5,000. Ten µL of the diluted streptavidin solution was mixed with 10 µL of bARP AP DNA and the mixture was incubated at 37°C for 1 h. Following this step, gel filtration was performed to remove the excess Alexa Fluor labeled streptavidin from the solution. Finally, the DNA backbone was labeled with YOYO-1 at 5:1 bp/dye ratio in 1X TBE including 4% v/v β-mercaptoethanol as an anti-photobleaching agent.

2.3.11 DNA trapping and extension in nanostructures

Labeled DNA samples were directed towards the multi-structured nanochannel by an applied electric potential. Single DNA molecules entered through the funnel entrance and were injected towards the nano-trap where it was stored. The electric field was then adjusted to eject the single DNA molecules into the array of nanochannels, where they were elongated to near their full contour length. When the DNA entered the stretching nanochannels, the electric field was turned off such that the DNA would be confined and extended inside the nanochannels so that they could be imaged to detect the AP sites. DNA molecules were allowed to relax before imaging. Fluorescence images were acquired using the dual color microscope system described previously. Image acquisition was performed using a Hamamatsu EMCCD camera (digital mode, 1024 ×1024 pixels, high-resolution) with Metamorph software.

2.4 Results and Discussion

2.4.1 Multi-structured nanofluidic device

We have discussed in our previous publications the use of thermoplastics as substrates for nanofluidic devices. [28-29, 33] These materials, which can be linear or branched polymers, have different physiochemical properties such as glass transition temperatures (T_g), hardness, and chemical composition, which allows for the selection of a material best suited for a particular application. In addition, the surface properties of thermoplastics can be modified using techniques such as UV/O_3 irradiation or O_2 plasma treatment.[31] For example, PMMA has a water contact angle of 69° and following exposure to UV/O_3 light, the water contact angle is reduced to 36° making the nanochannel more receptive to wetting reducing bubble formation, which can cause device failure when requiring aqueous buffers. COC is actually a copolymer consisting of ethylene and norbornene monomers with the mole fraction of each monomer in the COC grade

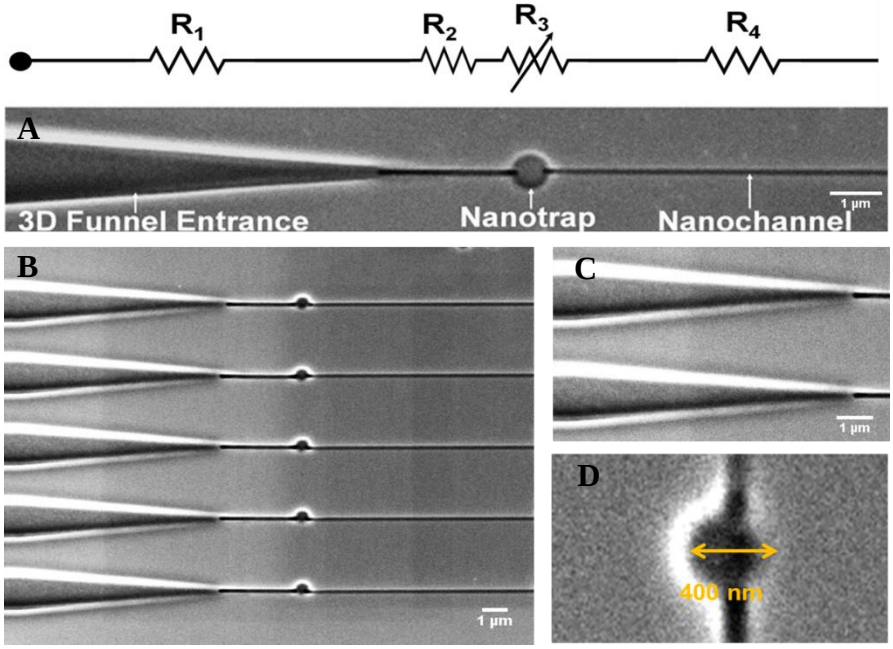

Figure 2.4 (**A**) SEM images of the multi-structured nanofluidic circuit comprised of a 3D funnel, nano-trap, and a stretching nanochannel. Its equivalent circuit diagram with resistors including an adjustable resistor for the nano-trap (variable resistance is predicated on changing the trap size) is also shown. (**B**) Array of multi-structured nanofluidic circuits for high throughput processing of single DNA molecules to search for AP sites. (**C**) Entrance funnel used to extend the electric field into the adjoining microchannel for assisting in loading single DNA molecules into the nanofluidic circuit from access microchannels. (**D**) SEM image of a 400 nm nano-trap (diameter and depth). The device shown was made from PMMA using thermal NIL from a resin stamp produced via UV-NIL from a Si master.

affecting its physiochemical properties such as the T_g and has excellent optical clarity with low background autofluorescence. The PMMA substrate with COC cover plate was selected here due to the high optical clarity of the COC cover plate to allow for single-molecule detection of the AP sites, the fact that PMMA can be used with NIL to provide high replication fidelity for nanometer structures, and finally the lower T_g of COC compared to PMMA allowed for the ability to thermally fusion bond the COC cover plate to the PMMA substrate to minimize nanostructure deformation in the PMMA substrate.[34]

The deformability of thermoplastics due to their relatively low T_g and melting temperature makes them useful for the fabrication of micro- and nanofluidic channels via hot embossing, injection molding, compression molding, thermal forming, and casting techniques. A method for the fabrication of nanochannels in thermoplastics is NIL, which is a variant of hot embossing. Since its first report in the 1990s by Steven Chou and co-workers, [35-37] NIL has become an extensively used tool for the fabrication of nanostructures even with sub-10 nm sizes. The main advantage of NIL is the ability to build multi-scale patterns in a single imprinting step with high reproducibility. Thus, higher rates of production of nanofluidic devices at lower cost can be realized using NIL compared to direct writing of devices using electron beam or focused ion beam milling.[38] In this paper, our mixed-scale nanofluidic devices were made via NIL. However, we note that nanofluidic devices can also be made using injection compression molding at even higher rates of production and lower device cost compared to NIL.[30]

The detailed procedure of nanofluidic device fabrication has been described elsewhere, but a schematic of this process can be found in Figure 2.1. [28-29, 39] Figure 2.4-A shows SEM images of the PMMA nanofluidic circuit investigated herein, which consisted of 3 main components: (i) A tapered 3D funnel that facilitates the entry of dsDNA into the nanofluidic circuit; (ii) a nano-trap (600 μm) that stores the dsDNA entropically during the loading stage of operation. DNA molecules randomly enter the funnel and placing a trap in the fluidic circuit stores them until they are simultaneously ejected into the stretching nanochannel array simultaneously so they can be stretched and parked for analysis in a high throughput format; and (iii) a

stretching nanochannel that stretches the molecule to assist in visualizing the AP sites within a single dsDNA molecule.[40]

The DNA molecule entering into the nanofluidic circuit must overcome the free energy barrier created as a result of the reduction in the conformational entropy associated with the confined molecule when resident within a nanochannel. [41-43] The effect of inlet structures connecting a microchannel to nanochannel influences the rate of DNA entry into a nanofluidic network.[43] DNA molecules can be efficiently introduced into nanochannels by using a 3D funnel structure. This funnel is shaped to increase electrostatic and hydrodynamic forces so that they are greater than the repelling entropic force. As the funnel tapers towards the nanochannel, there is a gradual increase in confinement of the DNA molecule.[44] The funnel entrance also increases the probability of dsDNA molecules entering into the nanochannel by increasing the effective electric field penetration depth into the adjoining microchannel. As can be seen from Figure 2.5A-B, we found that the injection efficiency of single λ-DNA molecules into the nanofluidic circuit increased nearly 6-fold compared to a blunt interface between the microfluidic network and nanofluidic circuit. We also tested a groove-type input and found that it was not as efficient as the 3D funnel (Figure 2.5-B).

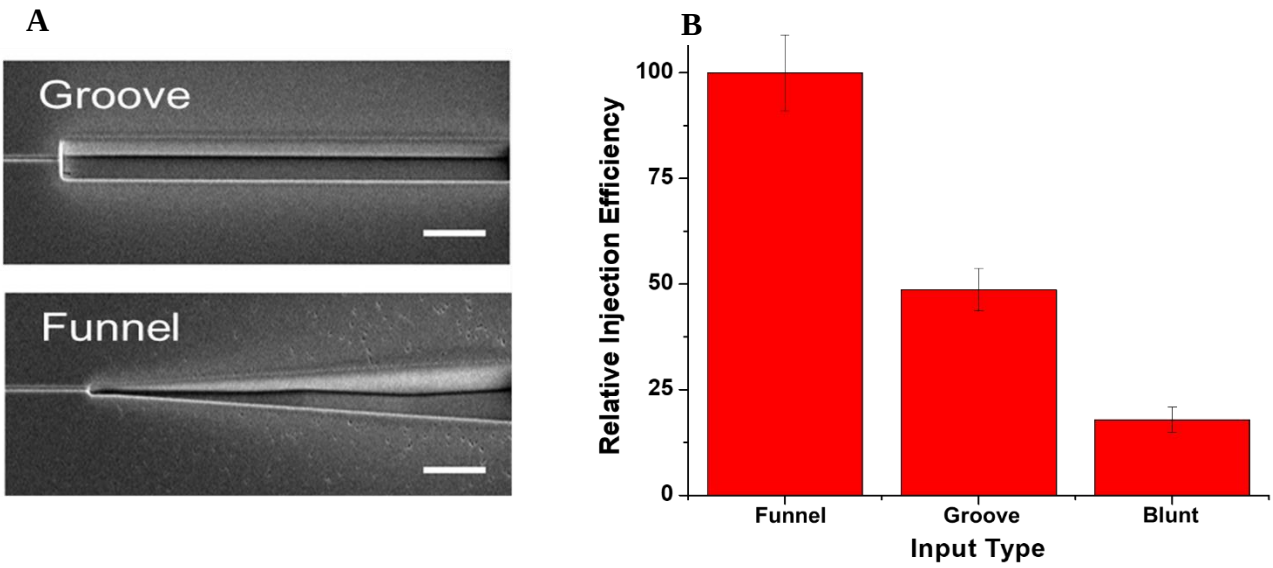

Figure 2.5 (A) SEMs of two input types used to interface the nanofluidic network to the access microchannels. In these SEMs are shown the Funnel and Groove inputs. The white scale bars represent 500 nm. The nanochannel shown on the left is 100 nm x 80 nm (width x depth). (B) Relative injection efficiency (%) of λ-DNA (48.5 Kbp) into the nanofluidic circuit for three types of nanochannel/microchannel interfaces. For the Blunt input type, the access microchannel of the device was directly connected to the nanofluidic channel. All data were normalized with respect to the Funnel input event frequency.

Following the 3D funnel, there was placed a nano-trap (Figure 2.4-B) in the circuit that served to "store" the dsDNA molecules entering into the device. Craighead *et al.* used entropic traps, which consisted of expansion chambers, to separate DNA molecules based on entropic considerations the effects of which were dependent on the DNA length (*i.e.*, longer DNA molecules moved out of the expansion chamber faster than shorter DNAs and thus, had a shorter trapping time).[32, 45-47] In this paper, we used a similar structure, but as a storage unit during loading so that dsDNA molecules could be uniformly introduced into a parallel array of stretching nanochannels so that multiple molecules could be parked and imaging in stretching nanochannels. Two different nano-traps sizes were evaluated, a 400 (diameter and depth) and 600 nm (diameter and depth) trap. The region following the nano-trap leads to the stretching nanochannel, which was 100 x 80 nm (width x depth; the length was 80 μm to allow the accommodation of dsDNA molecules with relatively large contour lengths; Figure 2.4-C) to allow for detection of the AP sites. Figure 2.4-B shows the array of nanofluidic circuits, which facilitated high throughput processing of DNA molecules. Figure 2.4-C and 2.4-D show high resolution SEMs of the 3D funnel and the nano-trap, respectively. Furthermore, COMSOL simulations were performed to evaluate the electric field strength distributions across the nano-traps of 400 nm and 600 nm. This assisted in determining the approximate driving voltage required to trap the DNA molecules and then, subsequently inject them into the stretching nanochannel array (Figure 2.6).

2.4.2 COMSOL analysis of the nano-trap

COMSOL simulations were performed to investigate the effects of trap size on the electric field distribution and on the translocation rate of dsDNA. When a voltage of 0.1 V was applied to the nanofluidic circuit, dsDNA entered into the 3D funnel from the microchannel and then into the nano-trap. We speculated that the trap size would influence the trapping and translocation rates of dsDNA molecules. Figure 2.6-A shows COMSOL simulation results for the electric field strength distribution within two different sized nano-traps (assumed a cylindrical geometry). The 600 nm trap had a field drop of ~70 V/cm from the feeding nanochannel to the center of the nano-trap (see Figure 2.6-B), whereas the smaller 400 nm

trap showed a drop of ~55 V/cm. Thus, it would be expected that the effective field strength influencing the DNA molecules inside the nano-trap was higher in the smaller nano-trap (400 nm) and thus, would require less driving voltage to eject a molecule from this trap compared to the larger nano-trap. Typically, concentration polarization is exhibited in channel dimensions less than <50 nm when a low ionic strength buffer is used and because of this, the field distribution may be different from what is shown in Figure 6

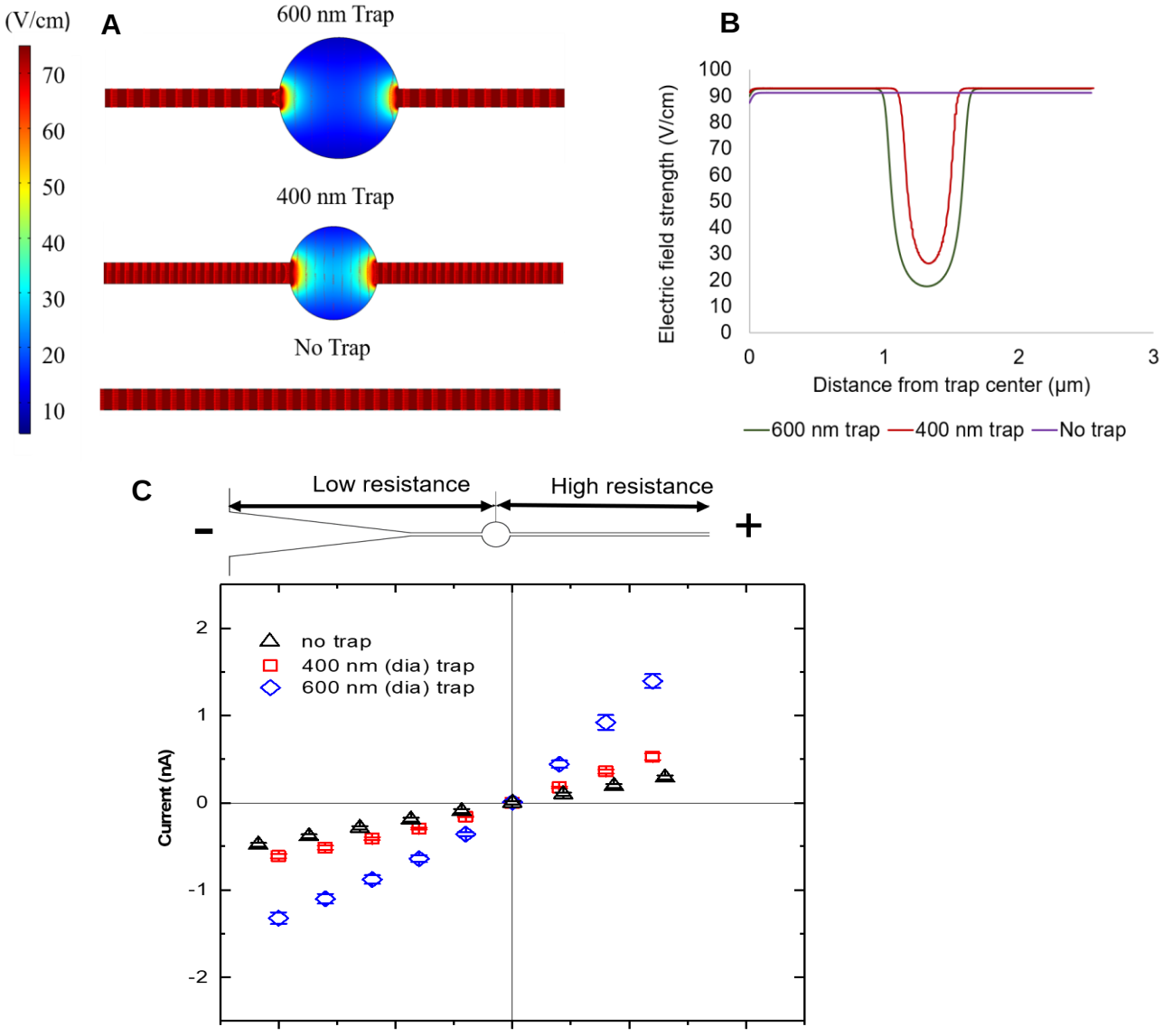

Figure 2.6 (A) Vector plots showing the electric fields across the 400 nm and 600 nm diameter nano-traps and one without a nano-trap. (**B**) Line plots showing the change in electric field strength across the nano-traps. (**C**) Current-voltage (I/V) curves for the multi-structured nanofluidic circuit with no nano-trap (black), 400 nm (red) and 600 nm diameter (blue) nano-traps measured with 1 M KCl added to 1X TBE buffer (pH = 8.0). Each data point represents the mean ±standard deviation from five different measurements. One M KCl was spiked into the buffer to increase the current flowing through the device.

due to changes in the zeta potential. However, concentration polarization requires significant overlap in the electrical double layer, EDL. [32] In our experiments and simulations, we did not experience significant EDL overlap as the buffer used was 1X TBE (89 mM Tris, 89 mM borate, 2 mM EDTA), generated an EDL thickness of 1.3 nm,[32] and the smallest channels used in our nanofluidic circuit was 80 x 110 nm, which indicated that EDL overlap was <2%.

The current voltage (I/V) characteristics were measured for devices without and with nano-traps of different sizes. From Figure 6C for the same applied voltage, different I/V curves were obtained for devices with different trap sizes. Two main factors contribute to the rectification of the ionic current in the nanofluidic circuit, which were due to asymmetry in either the geometry of the channel network or surface charge.[32] Here, we treated the entire device with an O_2 plasma to facilitate thermal fusion bonding, and hence, the surface charge was assumed to be symmetric throughout the circuit (for a fully deprotonated PMMA nanochannel, the surface charge is -40.5 mC/m^2).[29] However, the presence of the inlet funnel and the nano-trap followed by the stretching nanochannels made the nanofluidic circuit geometry asymmetric. Hence, the presence of a larger nano-trap increased the ion selectivity ratio between the nanochannel (shallow region) and the nano-trap (deep region), which increased the rectification and thus, a more non-linear IV plot. [29]

2.4.3 Translocation of dsDNA through the nanofluidic circuit

λ-DNA stained with YOYO-1 in 1X TBE buffer was introduced into the nanofluidic circuit under the influence of an applied potential of 0.1 V. The electrodes (Pt) made electrical contact to the fluidic circuit as they were placed at each end of the circuit in large reservoirs to accommodate large amounts of buffer so as to not shift the pH during the measurements. The dsDNA was loaded into the nanofluidic circuit with a negative voltage applied to the funnel side of the circuit and the opposite size was kept at earth ground. Therefore, the electrophoretic mobility of the stained dsDNA was higher than the electroosmotic flow of the device and drove the translocation process through the circuit. [22, 28, 30]

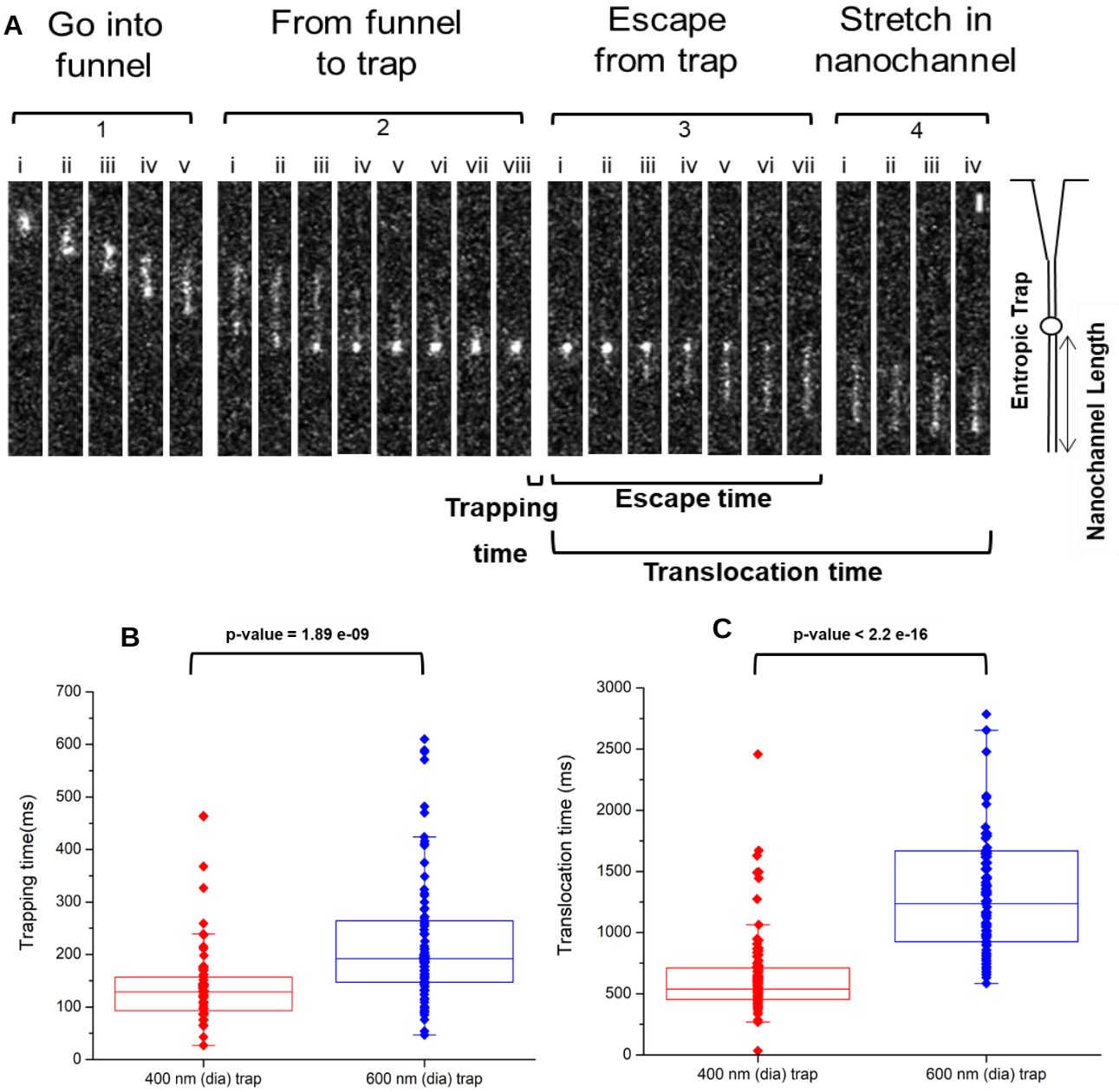

Figure 2.7 (**A**) Representative frames showing the translocation of stained λ-DNA through the multi-structured nanofluidic circuit. The frames were divided into 4 sections; (i) 'Enter the funnel,' where the DNA enters the funnel from the microfluidic channel and into the nanofluidic circuit. (ii) 'From the funnel to trap,' where the DNA leaves the funnel, stretches briefly in the short nanochannel section and enters into the nano-trap. (iii) 'Escape from trap,' where the DNA resides in the trap for a period of time and subsequently ejected from the nano-trap and inserted into the stretching nanochannel. (iv) "Stretching of dsDNA" in the stretching nanochannel to near its full contour length and is parked so as to detect the AP sites. For these experiments, the driving voltage was 0.1 V DC and the buffer used was 1× TBE (pH = 8.0). The scale bar (5 μm) is shown in Section 4, image (viii) at the top right corner of the image. Box plots showing (**B**) trapping and (**C**) translocation times of λ-DNA electrokinetically transported through the multi-structured nanofluidic circuit under a 0.1 V driving voltage having a 400 nm or 600 nm trap. The average trapping time for the 400 nm trap was ~138 ms, while for the 600 nm trap it was 225 ms. The average translocation time through the nanofluidic circuit with a 400 nm trap was 660 ms, while for the 600 nm trap it was 1847 ms. All measurements were performed using 1X TBE buffer (pH = 7.9). Events were captured at 10 ms exposure times resulting in a frame rate of 90 fps and 1 × 1 binning for the EMCCD. The *p value* calculated between the 400 and 600 nm traps for the trapping and translocation times (Wilcoxon signed rank test) were statistically different at the 95% confidence interval ($p<0.05$).

Fluorescence measurements were collected using the dual-color, single-molecule microscope (see Figure 2.2). Representative images are shown in Figure 2.7 as a single λ-DNA molecule translocated through the circuit. These experiments were performed for both trap sizes and DNA entered through the funnel and moved to the trap, where it coiled inside the nano-trap (trapping) and was then subsequently ejected from the trap and into the stretching nanochannel (translocation time). Complete trapping was observed in Figure 3, panel 2, image (viii) where the molecule was observed to form a blob. In addition, we could manipulate the applied voltage to control the storage/trapping time. At voltages <0.1 V, the molecule was found to remain in the trap until a higher voltage was applied (data not shown). We should note that at the voltage (0.1 V) used in these experiments, the λ-DNA molecules were found to transiently remain in the nano-trap. We note as well that using the 600 nm trap and T4 DNA, which has a length of 160 Kbp, we were unable to even intermittently trap this DNA molecule using the 600 nm trap (data not shown).

The effect of different trap sizes were evaluated. We considered these sets of experiments to be important as we are using a high throughput approach to increase the number of DNA strands that can be effectively analyzed simultaneously. When multiple channels are used, the stochastic nature of DNA entering into the circuit could lead to some molecules exiting the channels while other molecules are imaged. We should note as well that the dsDNA molecules must be parked in the stretching nanochannels to provide sufficient time to image the single molecule. Figure 2.7-A shows the trapping time of λ-DNA in the nano-traps under the influence of 0.1 V DC. The average trapping time of λ-DNA (contour length ≈16 μm) in the 400 nm trap was ~138 ms, which was shorter than the trapping time in the 600 nm trap (225 ms). The experimental results agree to the observations from our simulations (Figure 2.6). Figure 2.7-B shows boxplots of the translocation times of λ-DNA through the nanofluidic circuit. The translocation time for a circuit with the 400 nm trap ranged from 400 to 800 ms, while for a 600 nm trap, the translocation times ranged from 700 to 1900 ms. We should note that in the present case, we were using λ-DNA as the

model, which has a fixed length defined by the base composition of this DNA molecule, which is 48.5 Kbp in length.

2.4.4 DNA stretching and detection of AP sites using the nanofluidic circuit

Before we embarked upon the detection of AP sites using single streptavidin molecules labeled with Alex Fluor 647 through association with the bARP (see Figure 2.3), we investigated the ability to detect single dye-labeled streptavidin molecules by dispensing a dilute solution on a COC cover slip (12 pM; 2 µL volume deposited on a glass slide; see Figure 2.8 A-E). We were able to detect single streptavidin molecules with at an average SNR of 15. The fluorescence intensity of single dye-labeled streptavidin molecules was calculated using Image J as a function of gray scale value. The average fluorescence intensity

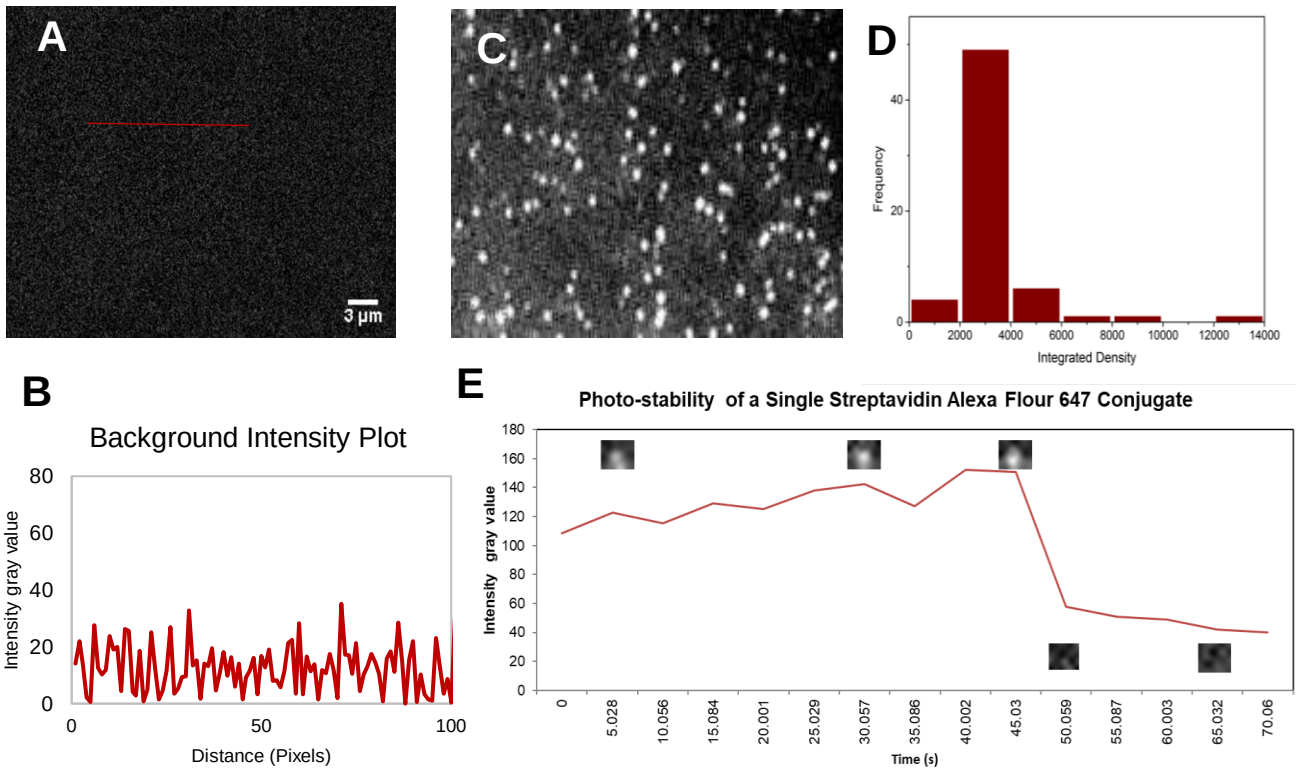

Figure 2.8 (**A**) Background image to evaluate the noise and speckle pattern imaged from a COC cover plate**.** (**B**) Line plot showing background intensity gray values. (**C**) Images of streptavidin Alexa Fluor 647 conjugates deposited on a COC cover plate. Excitation was provided by the 641 nm red laser with the fluorescence collected using a 100X (1.49 N/A) microscope objective. (**D**) Histograms showing the number of occurrences (frequency) for integrated intensity of all current voxels for single fluorescently labeled streptavidin molecules. (**E**) The bleaching of a streptavidin molecule at various time points and the corresponding intensity gray values. The sharp intensity drop at around 45.03 s corresponds to a single-molecule bleaching event.

of a single streptavidin molecule was found to be 2,000 – 4,000 arbitrary units. A few streptavidin molecules had an intensity of ~14,000 and this could have been due to those streptavidin molecules being multiply labeled. To assure that we were indeed detecting single streptavidin molecules, the fluorescence image was tracked over time with the intensity of a single spot measured (see Figure 2.8-E). As can be seen from this intensity plot, there was an abrupt cessation of fluorescence observed at that spot indicative of a single bleaching event.

Single dsDNA molecules have been stretched on a glass slide via electrostatic interactions between the DNA and the glass slide with AP sites analyzed using fluorescence.[31] The challenge with this approach was the non-controlled stretching of dsDNA, which made it difficult to determine quantitatively the frequency of AP sites (reported as number of AP sites per 10^5 nucleotides). As we have shown from our previous work, stretching of dsDNA molecules in thermoplastic nanochannels is highly reproducible with the degree of stretching dependent on the nanochannel cross-sectional area.[31]

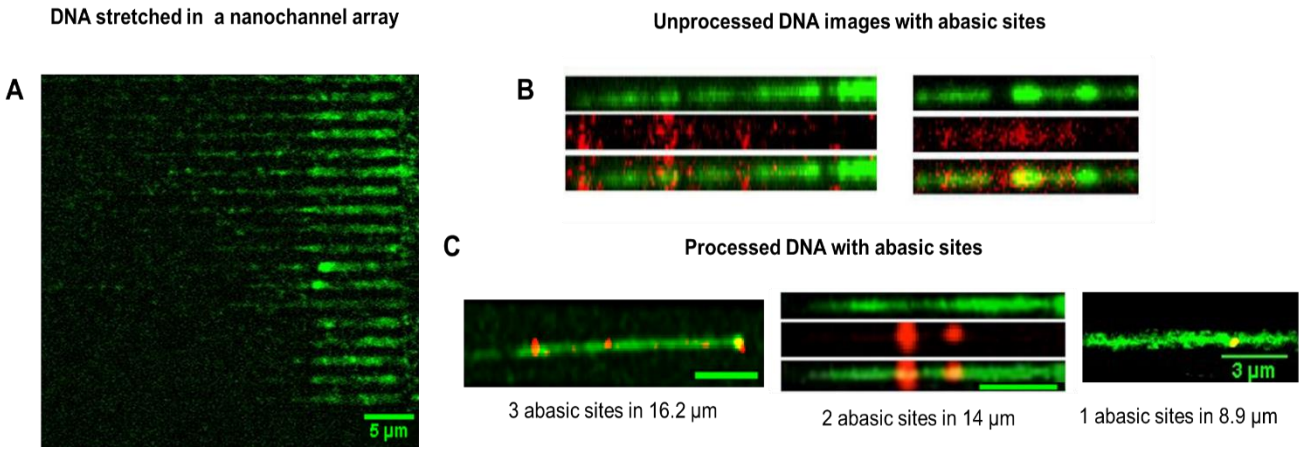

Figure 2.9 Images of λ-DNA confined in 100 nm × 80 nm stretching nanochannels. (**A**) Raw images of λ-DNAs' backbones labeled with YOYO-1 intercalating dye (green) in the multi-structured device having 20 stretching nanochannels. (**B**) Examples of unprocessed raw images, where the AP sites were labeled with Alexa Fluor 647 streptavidin (red) with AP sites identified within the dsDNA molecules. (**C**) Processed composite image showing the AP sites co-localized in the DNA strand (yellow). Three specific strands are shown, 1 AP site was identified in 8.9 µm strand, 2 AP sites were identified in a 14 µm length strand and 3 AP sites were identified in a 16.2 µm length DNA strand. The images were processed in Fiji and images of DNA and the AP sites were imaged separately and merged. A scale bar of 5 µm is represented in the images unless otherwise indicated.

For analyzing the AP sites herein, calf thymus DNA with a standard number of AP sites per unit length was used. On application of the appropriate DC voltage (>0.1 V), the DNA was ejected from the nano-trap

and moved into the stretching nanochannel where it could be parked (*i.e.*, removal of electric field) for reading AP sites as well as the length of DNA strands by staining with YOYO-1.

The dimension of the stretching nanochannel (100 x 80 nm) falls under the regime between the classic Odijk (50 nm) and extended de Gennes (100 nm) regimes. For a stretching nanochannel that was 100 nm x 80 nm, D_{ave} = 89, and from our previous work using a PMMA/COC nanofluidic devices, the DNA extension here was determined to be 60%.[48] Figure 2.9-A shows single DNA molecules parked in the stretching nanochannels. Towards the left of the image is where the trap and funnel would be located There were 20 stretching nanochannels in the device and the image shows single DNA molecules stretched in 18 of them.

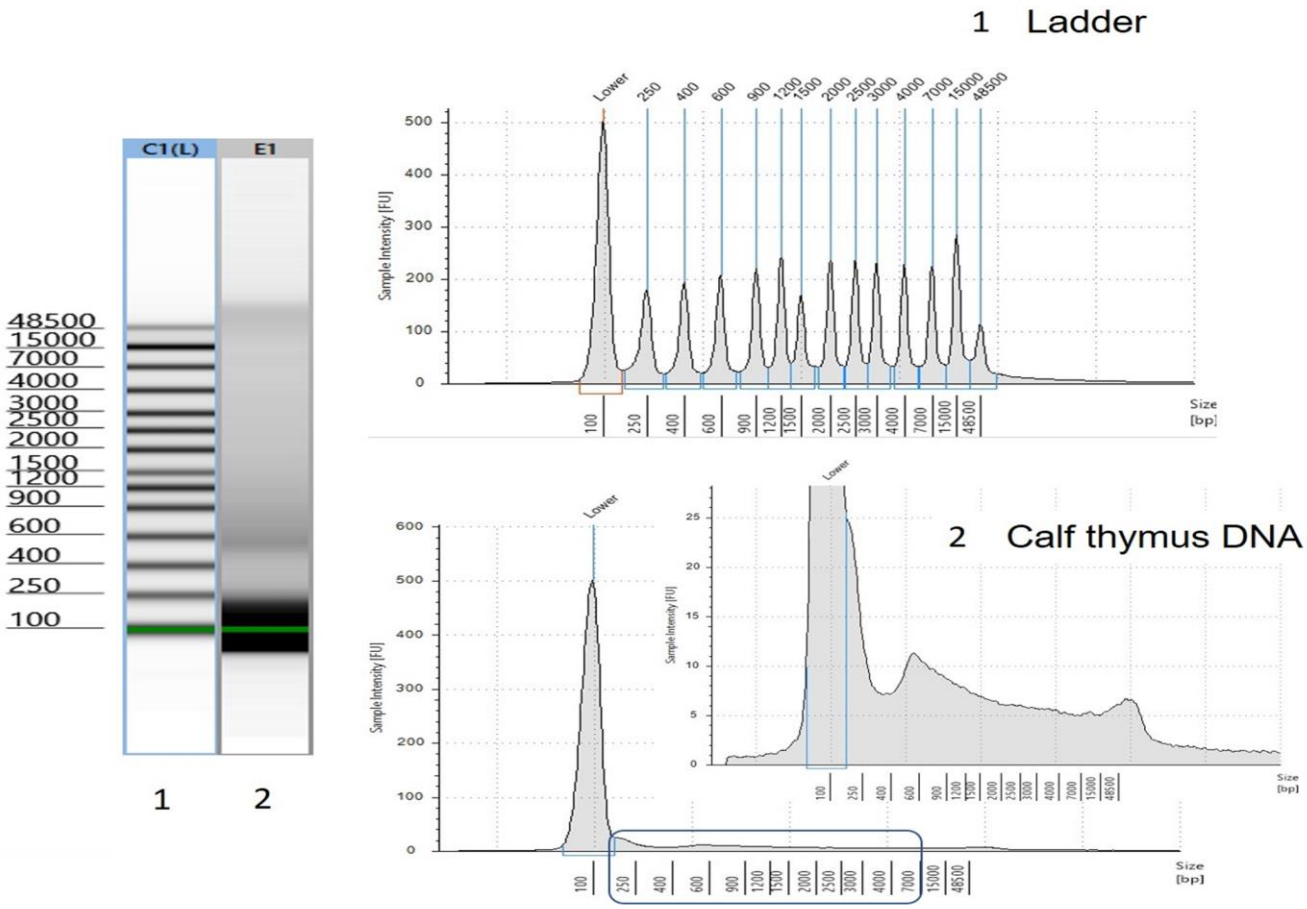

Figure 2.10 Tape station data for abasic site labeled Calf-thymus DNA from the Dojindo abasic site quantification kit. According to the data, there are various lengths of DNA strands present in the sample.

The purpose of using multiple channels was to increase the throughput of the AP site determinations.[49] The DNA molecules shown here are of different lengths as the mixture contains calf-thymus DNA, which has

variable lengths (see Figure 2.10). As the DNA molecules entered the stretching nanochannels from the trap, the electric field was turned off to park the DNA. The 488 nm laser line was used to image the DNA backbone labelled with YOYO-1 first. The AP sites labelled with streptavidin molecules were then imaged using the 647 nm laser. Once both images were acquired, they were merged for colocalization of the DNA strand (YOYO-1 image) and the AP sites (Alexa Fluor 647 image), which also assisted to discriminate between true AP sites and speckles generated from the background in the fluorescence image (see Figure 2.8-C).

Figure 2.9-B shows two unprocessed images with three rows for each image (only one stretching nanochannel is shown). The first row in the image is the DNA molecule imaged with the 488 nm laser stained with YOYO-1 that allowed determining the DNA molecule's length. For imaging AP sites (second row), the filter cube on the fluorescence microscope was changed to the 647 nm laser and red fluorescence was correspondingly imaged. The DNA with their AP sites was merged (third row) with the dsDNA back

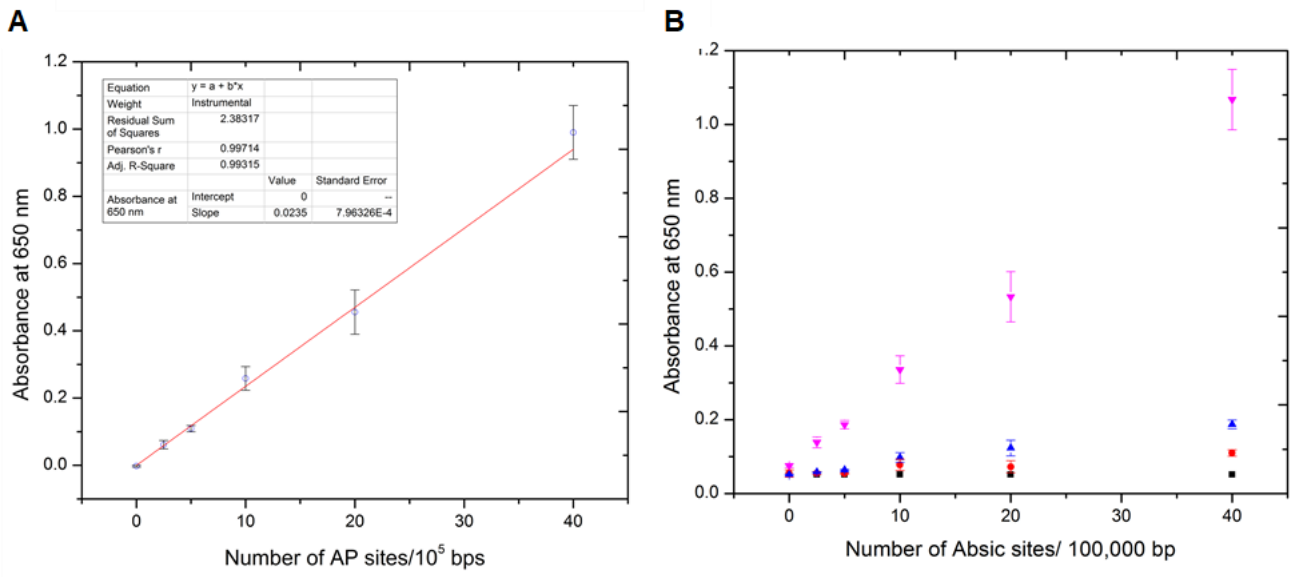

Figure 2.11 (**A**) Calibration curve for a colorimetric assay for measuring AP sites in dsDNA. The data was collected by measuring absorbance at 650 nm in a 96-well plate reader. Data points were obtained using 3 duplicate measurements and fitted to a linear calibration curve, which yielded a correlation coefficient of 0.997. (**B**) Calibration data points using the colorimetric assay based on a 96-well plate for different concentrations of dsDNA. Controls with no abasic DNA are shown in black and different concentrations of abasic dsDNA are shown in red (0.025 ng/µL), blue (0.075 ng/µL), and pink (0.300 ng/µL) with respect to the number of AP sites per unit length of dsDNA.

bone to find the number of AP sites/10^5 nucleotides. While the calorimetric assay determined the number of AP sites based on absorbance (see Figure 2.11),[50] we determined the number and position of AP sites at

the single-molecule level. The distance between nucleotides is 0.34 nm, so the corresponding length of 10^5 nucleotides is 34 μm. The standard DNAs from calf thymus had 0, 2.5, 5, 10, 20, 40 AP sites in a 34 μm length of dsDNA. As can be seen from Figure 2.11, we could produce calibration plots for AP sites spectrophotometrically, but this required high concentrations of DNA standards (0.5 ng/μL).

DNA lengths were measured from the fluorescence images using Image J based on 8.44 pixels equivalent to 1 μm. Figure 2.9-C shows three representative images where the lengths of the single dsDNA molecules were measured to be 8.9, 14 and 16.2 μm having 1, 2 and 3 AP sites (red spots colocalized with the DNA green strand), respectively. The AP sites were quantified using the intensity profile observed when imaging single streptavidin molecules. The intensity observed over the integrated intensity of 1,000 arbitrary units were counted as a single AP site and for values that exceeded 6,000 arbitrary units, two AP sites were scored. Twenty calf thymus DNA strands were analyzed and the average AP site frequency was found to be $6.0/10^5 \pm 1.8/10^5$, which was close to the $5.0/10^5$ nucleotide AP site standard used here. We should note that for these AP site standards, the length of DNA fragments was highly variable and ranged from 250 to ~48,500 bp based on gel electrophoresis data; see Figure 2.10 (average M_w of calf-thymus DNA is 8,580,000).[31] The negative control for these experiments were measured using λ-DNA molecules that did not contain AP sites, and no streptavidin molecules were found to be colocalized with the YOYO-1 stained DNA strand.

2.5 Conclusion

We report a nanofluidic device made from thermoplastics via NIL for measuring AP sites in single DNA molecules. The use of NIL provided reasonable production rates at modest costs to allow implementing the device for *in vitro* diagnostics that requires one-time use to minimize false positive results from possible sample carryover artifacts. Following NIL of the fluidic substrate, the device could be sealed with a cover plate using thermal fusion bonding of a plastic with a lower T_g than that of the substrate to minimize deformation of the underlying structures, especially the nanostructures.[22] The fluidic device possessed three components: (i) Input tapered funnel to increase loading rates of DNA into the nanofluidic

circuit; (ii) entropic nano-trap for DNA storage to allow simultaneous loading of DNAs into nanochannel arrays; and (iii) stretching nanochannels for extending the dsDNA to near its contour length to read AP sites with high spatial resolution. In microscale channels, the DNA would be randomly coiled and thus, hard to read individual AP sites nonetheless determine DNA length to arrive at AP site frequency.

The ability to analyze the position of AP sites within a DNA strand are important as studies have shown preferential formation of AP sites in areas undergoing replication.[51] The ability of detecting AP sites in DNA will have important applications to cancer chemotherapy, where the frequency of AP sites can be used to track their response to therapy. The nanofluidic assay reported herein will allow for the quantification of the number of AP sites even from single molecules. The nanofluidic circuit was able to efficiently capture single DNA molecules, store them in nano-traps, and subsequently eject them into stretching nanochannels to read the AP sites directly.

One of the advantages of the AP site detection method employed herein is its ability to detect AP sites in single molecules as shown in Figure 2.9. Spectrophotometric kits require large amounts of DNA to get viable results. For example, the spectrophotometric kit for detecting AP sites required ≥0.5 ng/μL of DNA to provide quantitative data (see Figure 2.11). This will become extremely important when considering sourcing the DNA for AP frequency determinations from circulating tumor cells, CTCs. For example, in a single CTC 6 pg of DNA are found and even 100 CTCs (600 pg) may not provide sufficient amounts of DNA for the spectrophotometric assay. Also, amplification of the DNA via PCR to accommodate the mass limits associated with the commercial kit is not feasible, because polymerization through the AP site can incorporate any nucleotide and thus, create errors in the analysis. Our assay can work directly on non-amplified DNA.

2.6 References

1. Fijen, C.; Fontana, M.; Lemay, S. G.; Mathwig, K.; Hohlbein, J., Simple nanofluidic devices for high-throughput, non-equilibrium studies at the single-molecule level. *bioRxiv* **2017**, 201079.
2. Bhattacharyya, A.; Chattopadhyay, R.; Mitra, S.; Crowe, S. E., Oxidative stress: an essential factor in the pathogenesis of gastrointestinal mucosal diseases. *Physiological reviews* **2014,** *94* (2), 329-354.

3. Boiteux, S.; Guillet, M., Abasic sites in DNA: repair and biological consequences in Saccharomyces cerevisiae. *DNA Repair* **2004,** *3* (1), 1-12.
4. COOKE, M. S.; EVANS, M. D.; DIZDAROGLU, M.; LUNEC, J., Oxidative DNA damage: mechanisms, mutation, and disease. *The FASEB Journal* **2003,** *17* (10), 1195-1214.
5. Wang, Y.; Liu, L.; Wu, C.; Bulgar, A.; Somoza, E.; Zhu, W.; Gerson, S. L., Direct detection and quantification of abasic sites for in vivo studies of DNA damage and repair. *Nuclear medicine and biology* **2009,** *36* (8), 975-983.
6. Ozcelikkale, A.; Shin, K.; Noe-Kim, V.; Elzey, B. D.; Dong, Z.; Zhang, J.-T.; Kim, K.; Kwon, I. C.; Park, K.; Han, B., Differential response to doxorubicin in breast cancer subtypes simulated by a microfluidic tumor model. *Journal of controlled release : official journal of the Controlled Release Society* **2017,** *266*, 129-139.
7. Asensio-López, M. C.; Soler, F.; Pascual-Figal, D.; Fernández-Belda, F.; Lax, A., Doxorubicin-induced oxidative stress: The protective effect of nicorandil on HL-1 cardiomyocytes. *PloS one* **2017,** *12* (2), e0172803-e0172803.
8. Fundador, E.; Rusling, J., Detection of labeled abasic sites in damaged DNA by capillary electrophoresis with laser-induced fluorescence. *Anal Bioanal Chem* **2007,** *387* (5), 1883-1890.
9. Roberts, K. P.; Sobrino, J. A.; Payton, J.; Mason, L. B.; Turesky, R. J., Determination of Apurinic/Apyrimidinic Lesions in DNA with High-Performance Liquid Chromatography and Tandem Mass Spectrometry. *Chemical Research in Toxicology* **2006,** *19* (2), 300-309.
10. Zhou, X.; Liberman, R. G.; Skipper, P. L.; Margolin, Y.; Tannenbaum, S. R.; Dedon, P. C., Quantification of DNA strand breaks and abasic sites by oxime derivatization and accelerator mass spectrometry: Application to γ-radiation and peroxynitrite. *Analytical Biochemistry* **2005,** *343* (1), 84-92.
11. Atamna, H.; Cheung, I.; Ames, B. N., A method for detecting abasic sites in living cells: age-dependent changes in base excision repair. *Proceedings of the National Academy of Sciences of the United States of America* **2000,** *97* (2), 686-691.
12. Kubo, K.; Ide, H.; Wallace, S. S.; Kow, Y. W., A novel, sensitive, and specific assay for abasic sites, the most commonly produced DNA lesion. *Biochemistry* **1992,** *31* (14), 3703-8.
13. Ide, H.; Akamatsu, K.; Kimura, Y.; Michiue, K.; Makino, K.; Asaeda, A.; Takamori, Y.; Kubo, K., Synthesis and damage specificity of a novel probe for the detection of abasic sites in DNA. *Biochemistry* **1993,** *32* (32), 8276-8283.
14. Kow, Y. W.; Dare, A., Detection of Abasic Sites and Oxidative DNA Base Damage Using an ELISA-like Assay. *Methods* **2000,** *22* (2), 164-169.
15. Shalhout, S.; Haddad, D.; Sosin, A.; Holland, T. C.; Al-Katib, A.; Martin, A.; Bhagwat, A. S., Genomic uracil homeostasis during normal B cell maturation and loss of this balance during B cell cancer development. *Molecular and cellular biology* **2014,** *34* (21), 4019-4032.
16. Allard, W. J.; Matera, J.; Miller, M. C.; Repollet, M.; Connelly, M. C.; Rao, C.; Tibbe, A. G. J.; Uhr, J. W., Tumor Cells Circulate in the Peripheral Blood of All Major Carcinomas but not in Healthy Subjects or Patients With Nonmalignant Diseases. 9.
17. He, W.; Kularatne, S. A.; Kalli, K. R.; Prendergast, F. G.; Amato, R. J.; Klee, G. G.; Hartmann, L. C.; Low, P. S., Quantitation of circulating tumor cells in blood samples from ovarian and prostate cancer patients using tumor-specific fluorescent ligands. *International journal of cancer* **2008,** *123* (8), 1968-1973.
18. Sikorsky, J. A.; Primerano, D. A.; Fenger, T. W.; Denvir, J., DNA damage reduces Taq DNA polymerase fidelity and PCR amplification efficiency. *Biochemical and biophysical research communications* **2007,** *355* (2), 431-7.
19. Sun, H. B.; Qian, L.; Yokota, H., Detection of Abasic Sites on Individual DNA Molecules Using Atomic Force Microscopy. *Analytical Chemistry* **2001,** *73* (10), 2229-2232.
20. Hirose, T.; Ohtani, T.; Muramatsu, H.; Tanaka, A., Direct Visualization of Abasic Sites on a Single DNA Molecule Using Fluorescence Microscopy¶. *Photochemistry and Photobiology* **2002,** *76* (2), 123-126.

21. Kim, J.; Muramatsu, H.; Lee, H.; Kawai, T., Near-field optical imaging of abasic sites on a single DNA molecule. *FEBS letters* **2003,** *555* (3), 611-615.
22. Chastain, P. D.; Nakamura, J.; Rao, S.; Chu, H.; Ibrahim, J. G.; Swenberg, J. A.; Kaufman, D. G., Abasic sites preferentially form at regions undergoing DNA replication. *The FASEB Journal* **2010,** *24* (10), 3674-3680.
23. Chan, T.-F.; Ha, C.; Phong, A.; Cai, D.; Wan, E.; Leung, L.; Kwok, P.-Y.; Xiao, M., A simple DNA stretching method for fluorescence imaging of single DNA molecules. *Nucleic acids research* **2006,** *34* (17), e113-e113.
24. Liu, C.; Qu, Y.; Luo, Y.; Fang, N., Recent advances in single-molecule detection on micro- and nano-fluidic devices. *Electrophoresis* **2011,** *32* (23), 3308-18.
25. Gibb, B.; Silverstein, T. D.; Finkelstein, I. J.; Greene, E. C., Single-Stranded DNA Curtains for Real-Time Single-Molecule Visualization of Protein–Nucleic Acid Interactions. *Analytical Chemistry* **2012,** *84* (18), 7607-7612.
26. Collins, B. E.; Ye, L. F.; Duzdevich, D.; Greene, E. C., Chapter 12 - DNA curtains: Novel tools for imaging protein–nucleic acid interactions at the single-molecule level. In *Methods in Cell Biology*, Waters, J. C.; Wittman, T., Eds. Academic Press: 2014; Vol. 123, pp 217-234.
27. Kim, D.; Rashid, F.; Cho, Y.; Zaher, M. S.; IIHwanCho; Hamdan, S. r.; Jeong, C.; Lee, J.-B., DNA skybridge: 3D structure producing a light sheetfor high-throughput single-molecule imaging. *Nucleic Acids Research* **2019,** *47*, e107.
28. I. Uba, F.; Hu, B.; Weerakoon-Ratnayake, K.; Oliver-Calixte, N.; A. Soper, S., High process yield rates of thermoplastic nanofluidic devices using a hybrid thermal assembly technique. *Lab on a Chip* **2015,** *15* (4), 1038-1049.
29. Uba, F. I.; Pullagurla, S. R.; Sirasunthorn, N.; Wu, J.; Park, S.; Chantiwas, R.; Cho, Y. K.; Shin, H.; Soper, S. A., Surface charge, electroosmotic flow and DNA extension in chemically modified thermoplastic nanoslits and nanochannels. *The Analyst* **2015,** *140* (1), 113-26.
30. Weerakoon-Ratnayake, K. M.; O'Neil, C. E.; Uba, F. I.; Soper, S. A., Thermoplastic nanofluidic devices for biomedical applications. *Lab on a Chip* **2017,** *17* (3), 362-381.
31. Uba, F. I.; Hu, B.; Weerakoon-Ratnayake, K.; Oliver-Calixte, N.; Soper, S. A., High process yield rates of thermoplastic nanofluidic devices using a hybrid thermal assembly technique. *Lab on a Chip* **2015,** *15* (4), 1038-1049.
32. Uba, F. I.; Pullagurla, S.; Sirasunthorn, N.; Wu, J.; Park, S.; Chantiwas, R.; Cho, Y.-K.; Shin, H.; Soper, S. A., Surface charge, electroosmotic flow and DNA extension in chemically modified thermoplastic nanoslits and nanochannels. *Analyst* **2014,** *139*.
33. O'Neil, C.; Amarasekara, C. A.; Weerakoon-Ratnayake, K. M.; Gross, B.; Jia, Z.; Singh, V.; Park, S.; Soper, S. A., Electrokinetic transport properties of deoxynucleotide monophosphates (dNMPs) through thermoplastic nanochannels. *Analytica Chimica Acta* **2018,** *1027*, 67-75.
34. Chou, S. Y.; Krauss, P. R.; Renstrom, P. J., Imprint of sub-25 nm vias and trenches in polymers. *Applied Physics Letters* **1995,** *67* (21), 3114-3116.
35. Chou, S. Y.; Krauss, P. R.; Renstrom, P. J., Nanoimprint lithography. *Journal of Vacuum Science & Technology B* **1996,** *14* (6), 4129-4133.
36. Chou, S. Y.; Krauss, P. R., Imprint lithography with sub-10 nm feature size and high throughput. *Microelectronic Engineering* **1997,** *35* (1–4), 237-240.
37. Duan, C.; Wang, W.; Xie, Q., Review article: Fabrication of nanofluidic devices. *Biomicrofluidics* **2013,** *7* (2), 026501.
38. Utko, P.; Persson, F.; Kristensen, A.; Larsen, N. B., Injection molded nanofluidic chips: Fabrication method and functional tests using single-molecule DNA experiments. *Lab on a Chip* **2011,** *11* (2), 303-308.
39. Lin, J.; Qi, R.; Aston, C.; Jing, J.; Anantharaman, T. S.; Mishra, B.; White, O.; Daly, M. J.; Minton, K. W.; Venter, J. C.; Schwartz, D. C., Whole-Genome Shotgun Optical Mapping of Deinococcus radiodurans. *Science* **1999,** *285* (5433), 1558-1562.

40. Hsieh, S.-F.; Wei, H.-H., Entropic trap, surface-mediated combing, and assembly of DNA molecules within submicrometer interfacial confinement. *Phys. Rev. E* **2009,** *79* (2), 021901.
41. Klotz, A. R., Statics and Dynamics of DNA in a Network of Nanofluidic Entropic Traps. 92.
42. Austin, R., The art of sucking spaghetti. *Nature Materials* **2003,** *2* (9), 567-568.
43. Zhou, J.; Wang, Y.; Menard, L. D.; Panyukov, S.; Rubinstein, M.; Ramsey, J. M., Enhanced nanochannel translocation and localization of genomic DNA molecules using three-dimensional nanofunnels. *Nature Communications* **2017,** *8* (1), 807.
44. Turner, S. W. P.; Cabodi, M.; Craighead, H. G., Confinement-Induced Entropic Recoil of Single DNA Molecules in a Nanofluidic Structure. *Physical Review Letters* **2002,** *88*, 128103.
45. Han, J.; Turner, S. W.; Craighead, H. G., Entropic Trapping and Escape of Long DNA Molecules at Submicron Size Constriction. *Physical Review Letters* **1999,** *83* (8), 1688-1691.
46. Hana, J.; Craighead, H. G., Entropic trapping and sieving of long DNA molecules in a nanofluidic channel. *J. Vac. Sci. Technol.* **1999,** *17*, 2142-2147.
47. Han, J.; Craighead, H. G., Separation of Long DNA Molecules in a Microfabricated Entropic Trap Array. *Science* **2000,** *288*, 1026-1029.
48. Weerakoon-Ratnayake, K. M.; Vaidyanathan, S.; Amarasekara, C. A.; Johnson, C. K.; Soper, S. A., Chapter 7 - Single molecule analysis in nanofluidic devices. In *Spectroscopy and Dynamics of Single Molecules*, Johnson, C. K., Ed. Elsevier: 2019; pp 335-377.
49. Masyuk, A. I.; Masyuk, T. V.; Larusso, N. F., Exosomes in the pathogenesis, diagnostics and therapeutics of liver diseases. *J Hepatol* **2013,** *59* (3), 621-5.
50. Porsch, B.; Laga, R.; Horsky, J.;́Konak, C.; Ulbrihc, K., NotesMolecular Weight and Polydispersity of Calf-Thymus DNA: Static Light-Scattering andSize-Exclusion Chromatography with DualDetection. *Biomacromolecules* **2009,** *10*, 3148-3150.
51. Current and Future Challenges in Point-of-Care Technologies: A Paradigm-Shift in Affordable Global Healthcare With Personalized and Preventive Medicine. *IEEE J Transl Eng Health Med* **2015,** *3*.

Chapter 3: Nanosensor: Detection and Identification of Single Molecules for Comprehensive Molecular Profiling

3.1 Abstract

The importance of molecular diagnostic tests are growing immensely due in part to the Precision Medicine Initiative, which seeks to match appropriate therapies to the molecular composition of a patient's disease. Unfortunately, the majority of these tests are expensive, involve slow turnaround times from centralized laboratories, and require highly specialized equipment with seasoned technicians to carry out the assay. An ideal platform for rapid diagnosis of diseases even at the point-of-care (POC) would be a technology that could interrogate relevant biomarkers found in a liquid biopsy. To facilitate the realization of precision medicine potentially at the POC, we have developed a mixed-scale nanosensor featuring high surface area pillar arrays where solid-phase ligase detection reactions (spLDRs) can be performed to detect and identify nucleic acid targets found in a diseased patient even when the mass of the marker is low (<1 ng). Successfully formed spLDR products can be identified using a molecular-dependent time-of-flight (TOF) through a polymer nanofluidic channel featuring two in-plane nanopores. To guide delivery of this platform, in this paper we discuss the operation of various components of the device and it's functions, the simulations (COMSOL) that were used to guide the design, and to determine the loading efficiency and transport patterns of spLDR products by evaluating parameters such as pixel loading, hydrodynamic, and electrokinetic flows. Further, the fabrication of the nanosensor is performed on a silicon (Si) master patterned using a combination of focused ion beam (FIB) milling and photolithography with inductively coupled plasma reactive ion etching (ICP-RIE). The patterns were transferred to a thermoplastic via nanoimprint lithography (NIL), which facilitates low-cost diagnosis of these leading death-causing diseases thus making it easily accessible to a broad patient population. The results from COMSOL were experimentally proved in hydrodynamic flows using Rhodamine B and electrokinetic flow using oligo 25 nucleotides which proved that this device can be used to perform spLDR and subsequently identify mutations in the single molecule level.

3.2 Introduction

US health care expenditures are estimated to be $3.68 trillion or 17.9% of the gross domestic product and are expected to continue to grow at a cumulative annual growth rate of ~3.9% over the next few years (from National Health Expenditure Accounts). The aforementioned numbers were generated pre-COVID-19 pandemic and these figures are expected to expand tremendously as a result of the pandemic. In addition, the face of healthcare must change due to the need for social distancing and quarantines, such as the evolution of telemedicine.

New technologies that address health care needs without sacrificing the quality and quantity of clinical information secured from them can be highly desirable. One area that is addressing health care needs are *in vitro* diagnostics (IVD), which are performed on clinical samples taken from a patient to help manage his/her disease. Reasons for this attribute include: (i) They can potentially be done at the Point-of-Care (PoC) eliminating the need for extended hospital stays or visits to support a growing trend of telemedicine; (ii) if engineered properly, the test can be carried out by novice users in a fully automated fashion; (iii) acquisition of samples for testing can be secured in a minimally invasive manner (e.g., liquid biopsy markers); and (iv) reduce the complexity and cost of instrumentation used for carrying out the test. The importance of *in vitro* diagnostics is growing immensely due not only as a result of the pandemic, but also in part to the Precision Medicine Initiative, which seeks to match appropriate therapies to the molecular composition of a patient's disease.

Timely disease diagnosis and prognosis pose a major challenge of disease management, particularly if management decisions are time sensitive, thus require PoC testing. For example, patients with ischemic stroke require treatment within an effective time window (<4.5 h) to be eligible for administration of the thrombolytic treatment, recombinant tissue plasminogen activator, rt-PA; currently <7% of eligible patients receive therapy due to failures at the diagnostic level.[1] Current diagnostics are based on CT or MRI that do not provide timely clinical decisions to address the time constraints associated with rt-PA therapy.[2] However, it has been shown that mRNA from specific white blood cells and the associated gene expression

they render can be used as biomarkers for diagnosis of stroke.[3] This opens the possibility of using a liquid biopsy to secure biomarkers for potential PoC testing to provide timely results.[4]

As another example of the importance of PoC testing for disease management, the 2020 COVID-19 pandemic, which is a highly contagious viral infection, has used IVD tests to manage this disease, especially those equipped to do PoC testing. Since its discovery in late 2019, COVID-19 has resulted in >59 M cases globally (daily reporting rate of new cases ~809 in January 27, 2020 and ~671,885 on November 27, 2020) and ~1.5 M deaths in a span of 12 months (https://coronavirus.jhu.edu/map.html). Testing, especially those that can be performed at the PoC, have been viewed as an important tool for the control of disease spreading. A common test for COVID-19 is RT-qPCR, which interrogate the RNA genome of SARS-CoV-2, and requires RNA extraction and purification, reverse transcription (RT) to generate complementary DNA

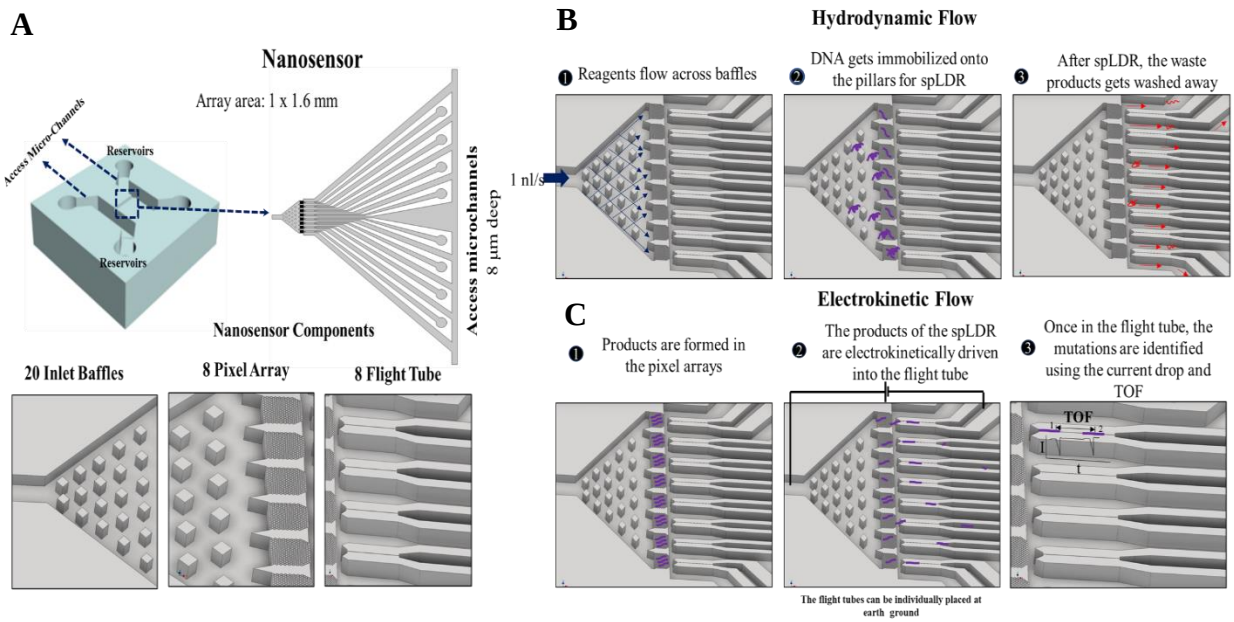

Figure 3.1 A) Schematic of the Nanosensor is shown above. The nanosensor is placed between two-micron access channels. The device comprises of three main features; 20 Baffles of 7 µm x 7 µm each to distribute the reagents; 8-pixel arrays containing 268 pillars/array to simultaneously perform spLDR reaction; 8 flight tubes of 50 nm X 50 nm X 50 µm (w x d xl) each to analyse the products of spLDR reaction. B) The workflow process of the hydrodynamic flow is utilized to pump the reagents at a flow rate of 1 nL/s required for the LDR into the chip (1). During this process, the target DNA which have the mutations are immobilized on to the pixel array (2). The spLDR is performed and the waste products at the end of the reaction are rinsed using the hydrodynamic flow (3). C) The electrokinetic flow is performed at the end of the spLDR, where the products are formed in the pixel array (1). They are electrokinetically driven into the flight tube by applying a DC bias and placing the electrodes to one end of the microchannel and earth ground to the ends of the flight tube (2). Once the products enter the flight tube, they are detected for the presence of mutation by monitoring the current amplitude and the TOF generated by the products (3).

(cDNA) from target genes (viral N, E, and S with human RNA dependent RNA polymerase (RdRp) as a control), amplification by the polymerase chain reaction (PCR), and reading a fluorescent signal.

PoC tests that use microfluidics or nanofluidics allows for rapid disease assessment with attributes of affordability and timely results to improve patient outcome.[5] In addition, PoC tests using microfluidics can reduce the costs associated with diagnosis and make even sophisticated tests more accessible to people with low socio-economic status.[6] The challenges with translating PoC tests into the field include designing the instruments with the appropriate hardware that possesses a small footprint, designing assays that are easily carried out in the field by untrained operators, and being able to produce them successfully at low-cost.[7-8] Initially, inorganic substrates such as glass, silica, or fused silica have been used to fabricate micro- and nanofluidic devices due to established manufacturing methods, and the hydrophilic surfaces that favours efficient wetting conditions.[9-10] But, the main challenges include high fabrication costs, and the inability to scale-up for inexpensive mass production.[10]We have developed a nanosensor (Figure 3.1-A) made of thermoplastics that not only enables high-scale production, but also allows for integration of a number of processing steps directly onto the mixed-scale chip to facilitate PoC testing scenarios. The nanosensor is situated between two micron-sized access channels with a common inlet. The device possesses 8-pixel arrays, where mutation detection or sequence identification assays can be performed on a solid support. Genomic DNA or RNA (following reverse transcription into cDNA) can be immobilized onto the surfaces of the pillars comprising each pixel array allowing for carrying out solid-phase ligase detection reactions (spLDR). spLDRs facilitate the detection of point mutations or identification of mRNAs through their unique sequences.[11-12] Our group has previously demonstrated that LDR can analyze oncogenic mutations in *KRAS* genes to diagnose colorectal cancer.[13-14] The mutant: wild-type ratio on the order of 1:100 from markers secured from a liquid biopsy has been analyzed using a high fidelity ligase enzyme.[15] Extremely high sensitivity of LDR combined with the flexibility of primers designed for different mutations has allowed for performing multiplexed detection of a panel of mutations.[16] In addition,

we have shown that LDR can be used with single-molecule fluorescence detection to search for point mutations in genomic DNA and do so in near real-time.[17] Finally, we have also shown that LDR can

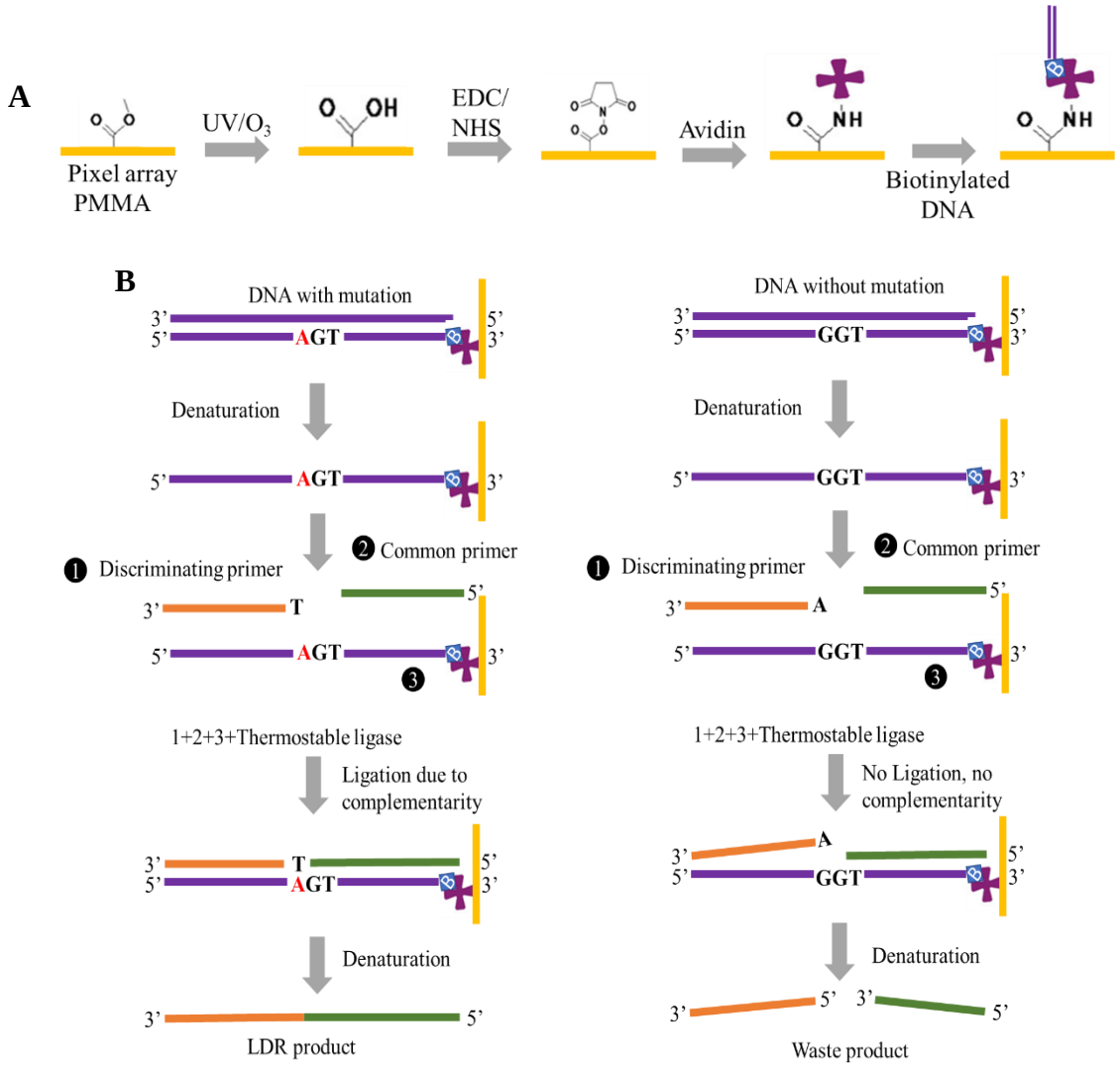

Figure 3.2 A) Schematic representation of the activation of a polymer substrate, PMMA in this case, followed by subsequent modification of the surface. UV/O_3 treatment of the polymer surface induces oxygen containing groups followed by EDC (1-Ethyl-3-(3-dimethylaminopropyl) carbodiimide), NHS (N-hydroxyl succinimide) treatment to allow streptavidin and one of its primary amines to bind to the surface –COOH group. Streptavidin strongly binds to biotin in the DNA allowing immobilization of the target DNA. COC and COP can be activated in a similar fashion. B) The process of spLDR is depicted for both normal and mutated KRAS gene occurring in codon 12 at position 34 (C.34 G>A, where the guanine is replaced by adenine, and hence the amino acid coded is converted from Glycine to Serine for the mutated DNA) in the schematic. The DNA that is immobilized on the pillar arrays is denatured to form a single stranded DNA. To the ssDNA immobilized, a common primer, a discriminating primer and thermostable ligase are added to the reaction mixture. Ligase covalently bonds discriminating primer and phosphorylated common primer together. If there is a mutation, then ligation happens. If there is no mutation, ligation does not happen. The products formed are of different lengths, with mutated LDR product having a longer length.

be used to identify mRNA transcripts using reverse molecular beacons with rapid and highly sensitive detection.[18]

The process of immobilizing the target nucleic acid to the pillars comprising the pixel array and the process of spLDR are described in Figure 3.2. Unique to this nanosensor is the ability to perform sample preparation steps, which includes a solid-phase LDR (spLDR) on-chip followed by label-free readout of the spLDR products using a flight tube situated near each pixel. The flight tube allows for single-molecule detection and identification via nanoscale electrophoresis[19-23] in conjunction with resistive pulse sensing – single-stranded DNA with a unique size ascribed to a particular spLDR product.[24]

The two main operations are performed on the nanosensor: the hydrodynamic flow and the electrokinetic flow. The hydrodynamic flow is performed for the injection of the reagents into the nanosensor for the spLDR using a forward flow. This includes treating the pixel array with streptavidin, introducing the agents required for the spLDR and introducing the target DNA that is biotinylated, so it binds to the streptavidin coated pillars. The spLDR is performed and at the end of the reaction, the waste products are removed using the hydrodynamic flow mechanism (Figure 3.1-B). The electrokinetic flow is where, the products of the spLDR are driven into the flight tubes for analysis. The spLDR product that is generated is electrokinetically driven into the flight tube that possesses two-in-plane pores placed on either end of the flight tube. When the spLDR product translocates through the first pore, it generates a current drop and a subsequent current drop at the second pore with the time difference between the sequential current drops related to the time-of-flight (ToF) or electrophoretic mobility (Figure 3.1-C). This is done by applying a DC bias in the entrance of the nanosensor and placing the ends of the flight tube at earth ground. The products generated are ssDNA have a charge and they respond to the electric field.

In this paper, we discuss the design of this nanosensor that features mixed-scale fluidic channels to carry out various functions and the operation of which uses a combination of hydrodynamic and electrokinetic flow with passive valving to facilitate operation. The valving is based on the use of fluidic resistance in nanochannels in operation when using hydrodynamic pumping and the selective field drops in nanochannels when using electrokinetic pumping. We will discuss the operational characteristics of the

device using COMSOL simulations to understand performance and fortify those observations with experimental results. The hydrodynamic flow was used for injecting reagents for the spLDR and subsequent washing steps (Figure 3.1-B). The electrokinetic flow was used for shuttling the spLDR products specifically into the flight tube where they were identified based on their size using their molecular dependent TOF (Figure 3.1-C). The results of COMSOL were experimentally verified using a fluorescent tracer for monitoring the hydrodynamic flow and labelled oligonucleotides for monitoring the electrokinetic flow.

3.3 Materials and Methods

3.3.1 Fabrication of the Nanosensor

A nanosensor mold is made in silicon (Si) containing both micro- and nanoscale features. The microscale features are fabricated using a positive resist and photolithography followed by etching the Si master to ensure appropriate pattern transfer. For positive photolithography, AZ9260 resist is spin coated onto a Si wafer at a thickness of 8 μm and exposed to UV light (365 nm). After developing the resist, deep reactive ion etching (DRIE) is performed to etch the Si to the desired depth (7-8 um) with the AZ9260 resist as the mask for the DRIE process. Further, the nano-dimensional region of the nanosensor (pixel array region containing 1 μm pillars, 250 nm spacing in between them and the flight tube of 50 nm x 50 nm) was fabricated by focused ion beam (FIB) milling using Ga ions into the Si wafer. Structures were milled with 48 pA beam current and 1 μs dwell time. The milling conditions are optimized by iterations and validated with metrology.

3.3.2 Fabrication of the nanosensor in thermoplastic using nanoimprint lithography (NIL)

Once the Si master is fabricated using the above processes, patterns are transferred to cyclic co-olefin (COC) polymer by adding 20 μl of UV resin (poly-urethane acrylate) on the Si and placing the COC over it and exposing the assembly to the UV light (365 nm) for 2.5 min for curing. Once the COC backbone is peeled, the structures from Si are transferred and metrology is performed to confirm the dimensions. This is followed by thermal-NIL, where nanosensor patterns will be transferred from the resin stamps to a

polymethyl methacrylate (PMMA) thermoplastic at 135°C, 300 psi, 5 min. The cover plate COC 8007 is then treated with O2 plasma at a power of 50 W at 1 min assembled with the imprinted device at 70°C, 120 psi, 15 min.

3.3.3 Metrology of the Si master and thermoplastic substrate to ensure fidelity.

After the fabrication and NIL process, the Si master, 6015 stamps, and the final thermoplastic device before bonding are interrogated using SEM. The dimensions at every step can be confirmed to ensure faithful replication of structures using Keyence VX-200

3.3.4 Micromilling of thermoplastic.

The nanosensor possess 8 flight tubes corresponding to each pixel array. The nano-flight tubes extend as microchannels and end in reservoirs of 60 μm in diameter. These reservoirs will be drilled using a micro-milling technique as a through hole in the thermoplastic. A Pt electrode connection is placed in each of reservoir, which in turn is suitable for the application of a DC voltage to perform electrokinetic flow measurements.

3.3.5 COMSOL.

We built a 2D nanosensor model design in AutoCAD and tested the flow patterns using finite element analysis simulations (COMSOL 5.5). The electrolyte used for the simulations was 1X TBE, at a flow rate of 1 nL/s. The Model physics used was Laminar flow for hydrodynamic flow and Electrostatics and Transport of dilute species from the AC/DC for electrokinetic flow. A no-slip condition was used for the boundary conditions as the Knudsen number was well below 0.01 (Continuum flow).

3.3.6 Hydrodynamic flow.

Rhodamine B, a neutral dye and soluble in water, has excitation and emission wavelengths at 534/570 will serve as the tracer to track fluidic operation of the nanosensor. 1 μM concentrations of Rhodamine B are pumped at a flow rate of 1 nL/s using a syringe pump. The fluorescence from the dye flowing into the nanosensor will be captured using a sCMOS camera at an exposure of 10 ms using a 60X objective. The images will be collected, and the intensity quantified as line plots. The mean intensity of

each pixel (calculated from 5 different experiments using the same concentration of the dye and the same laser power with mean and sd calculated) array will be calculated corresponding to the results seen in the COMSOL simulations.

3.3.7 Electrokinetic flow

Oligo 25 nucleotides labelled with Cy3, has a wavelength of 534/570 nm were used as representative products of spLDR reaction. A 10 V DC potential was applied to the inlet and and the ends of the flight tubes that lead to individual microchannels (60 μm dia) were placed at earth ground. Live fluorescence tracking was done and the electric field was turned off as the nucleotides started accumulating at the end of the flight tubes. The images were captured at 10 ms using a 100X 1.4 NA oil immersion objective connected to sCMOS camera.

3.3.8 Data Analysis

The fluorescence images that will be collected from the camera as a TIFF file, which will be analyzed using Image J software. The fluorescence signal can be represented quantitatively as line plots, which displays grey values of the area selected with respect to the distance in pixels. The area across the flight tube and outside the flight tube will be fluorescence intensity plots. The difference in grey values will clearly depict the fluorescence intensity between different areas. The experiment will be repeated 5 different times for each concentration and the same area will be selected and fluorescence intensity plots generated. The difference in fluorescence intensity between subsequent trials compared and statistical significance obtained using a p-test.

3.4 Results and Discussion

3.4.1 Fabrication of the multi-scale nanosensor.

The nanosensor is a multi-scale device containing both micro- and nanoscale structures. The footprint of the nanosensor is 1 x 1.6 mm, which facilitates placing multiple units onto a single chip to perform high-

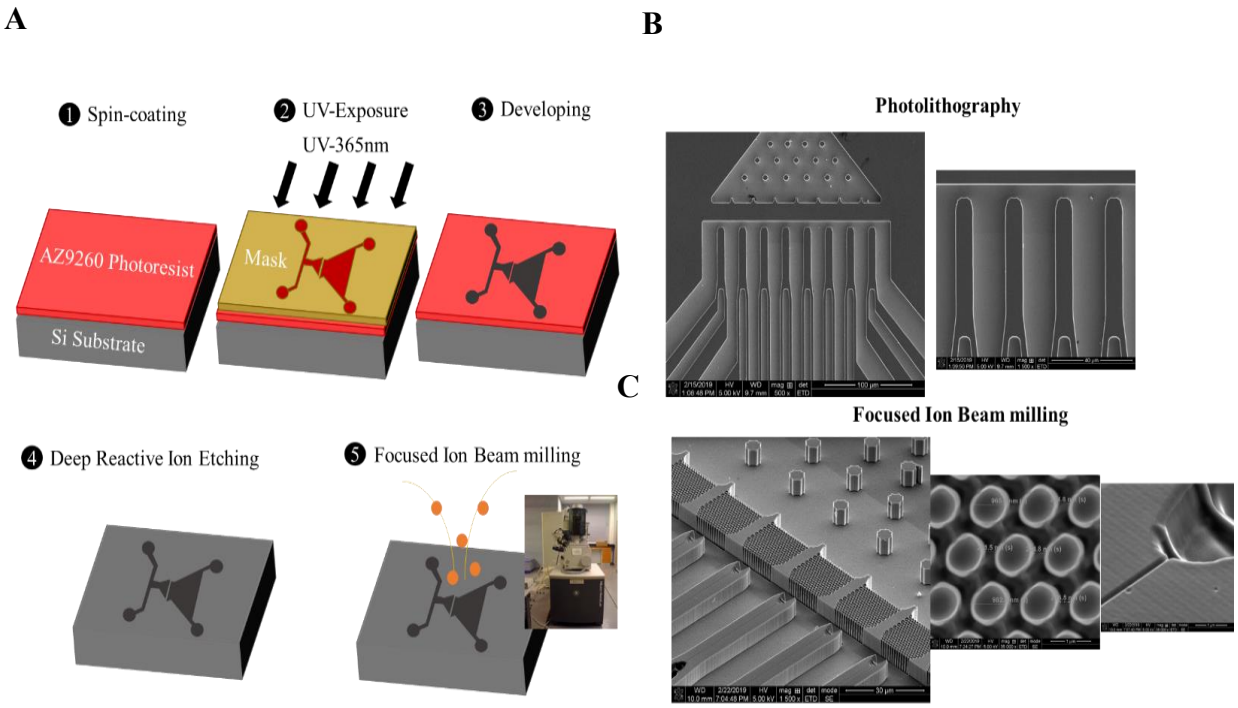

Figure 3.3 A) Schematic showing the process of fabrication of the Si master; positive photolithography using AZ9260 resist is performed in 3 main steps : Spin coating, where AZ9260 resist is spun on to the Si wafer, followed by exposure via dark field mask to UV light at 365 nm. After exposure, the resist is developed in MIF 300 developer and visualized under microscope. This step is followed by DRIE, where the Si master is etched to a depth of ~6-7 µm. Finally the-FIB process to fabricate the nanochannels is performed where Ga ions are rastered onto the Si master to fabricate the pixel arrays and the flight tubes which are in the nanometer range; B) SEM images showing the images of Si master after photolithography but before the DRIE, where the all the micron scale features are successfully. The pillars and flight tube are not seen after Photolithography as they are fabricated using FIB. C) SEM images of the final Si master after DRIE and FIB, where the desired depth in the device is achieved and both the pixel arrays (ii) and the flight tubes are clearly visible (iii).

throughput processing. The device features 20 baffles (7 µm x 7 µm) at the entrance of the device and used to uniformly distribute the input to 8-pixel arrays, with each array of 20 µm X 20 µm containing 268 pillars per array. Each pillar has a diameter of 1 µm with a spacing of 250 nm between the pillars. These pillars act as the solid phase where spLDRs take place. The pillar number and small spacing were selected to provide high surface area to increase the load of surface immobilized targets and increase capture efficiency

of targets when flowing dynamically through the pillar array, respectively. For example, at a volume flow of 1 nL/s, the capture efficiency of targets as deduced from simulation was determined to be ~80%.

Adjacent to each pixel array is a nanoscale flight tube that is 50 nm x 50 nm (w x d) and 50 μm in length, which is used to carry out the nanoscale electrophoresis for identifying spLDR products. Each flight tube has two in-plane nanopores of ~10 nm effective diameter and spaced by ~10 μm. The in-plane nanopores are used to determine the ToF via resistive pulse sensing. In this preliminary design to understand the fluidic operation of the nanosensor, the flight tube was designed with no in-plane nanopores so as to serve as a prototype to test the device in terms of successfully carrying out the fluidic operational steps associated with this device.

We used a top-down fabrication approach to produce the thermoplastic nanochannel device, which used nanoimprint lithography (NIL) as a major mode of fabrication.[25-26] The advantage of using thermoplastics as opposed to inorganic substrates such as silicon or glass is that they possess a smaller electroosmotic flow (EOF) due to their reduced zeta potential; the zeta potential is controlled by the dose of UV/O_3 exposure to the plastic, which generates surface carboxylic acid groups.[27-29] In addition, NIL is used to fabricate the device in a medium-scale production mode as opposed to direct write using electron beam lithography or focused ion beam milling as is typically done for inorganic substrate. [26] Also, the use of a thermoplastic with a high glass transition temperature (Tg) allows high aspect-ratio structures to be replicated with high fidelity.[30] The imprinted substrate can be sealed with a lower Tg cover plate via thermal fusion bonding, which prevents the structures from collapse.[31] Our group has used NIL for fabricating nanofluidic devices.[32-34] Basically, this process involves the fabrication of a Si master from which is produced resin stamps via UV-NIL followed by the production of the final device in a thermoplastic via thermal NIL.

Figure 2A represents the process schematic involved in the fabrication of the Si master; photolithography is used for the fabrication of the micron scale channels (>2 μm). The inlet baffles (7 μm x 7 μm) and microchannels are fabricated using this method. Following photolithography (Figure 3.3-B), the Si wafers were etched using DRIE producing a feature depth of 6-7 μm (Figure 3.4). Following DRIE, FIB was performed on the 8-pixel arrays (each array consisting of 268 pillars) and the flight tubes. with. The

dimensions of the pillars were set to 1 μm in diameter with a spacing of 250 nm. This design offered each pixel array with a high surface area to perform the spLDR (1242 μm^2/array). Figure 2C shows an SEM image of the Si master featuring the pixel array and the flight tubes. The average size of the pillars in the Si master were 974±8 nm with a spacing of 227±12 nm (Figure 3.3-C ii). The flight tubes (original dimensions of 50 nm X 50 nm (w x d)) were used for the nanoscale electrophoresis of the spLDR products (Figure 3.3-C iii) and they were milled right after the pixel arrays. The average dimensions of the flight tubes were 66±12 nm. The ends of flight tubes were connected to microchannels having individual reservoirs (60 μm in diameter). This design was facilitated so that a DC voltage could be applied by placing electrodes within these reservoirs for the electrophoresis.

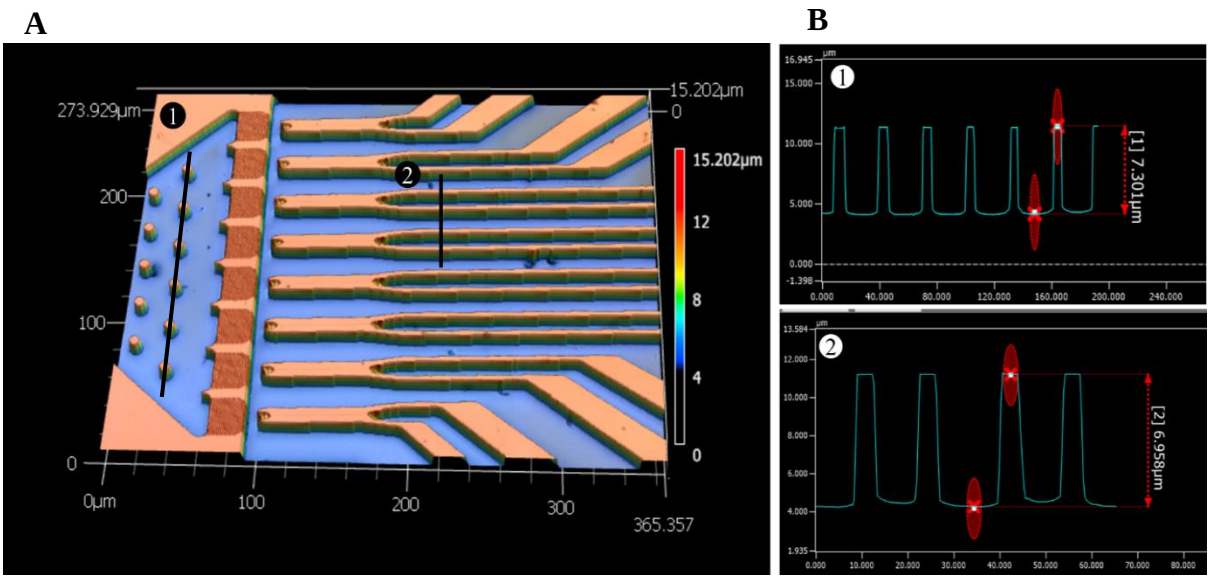

Figure 3.4 A) Schematic of Nanosensor in the Keyence profilometer showing the depth of the Si master after DRIE. B) The first graph shows the depth across the baffle area which is estimated to be ~7.3 μm. The second graph shows the depth across the microchannel channels that follow the flight tubes. The depth in this region is estimated to be ~6.9 μm.

After the pattern was successfully transferred to the Si master, the master was silanized using trichloro(1H,1H,2H,2H-perfluorooctyl) silane to make the surface hydrophobic for UV-NIL. The pattern from the Si master was then transferred to a thermoplastic polymer using NIL (this is a two-step process)

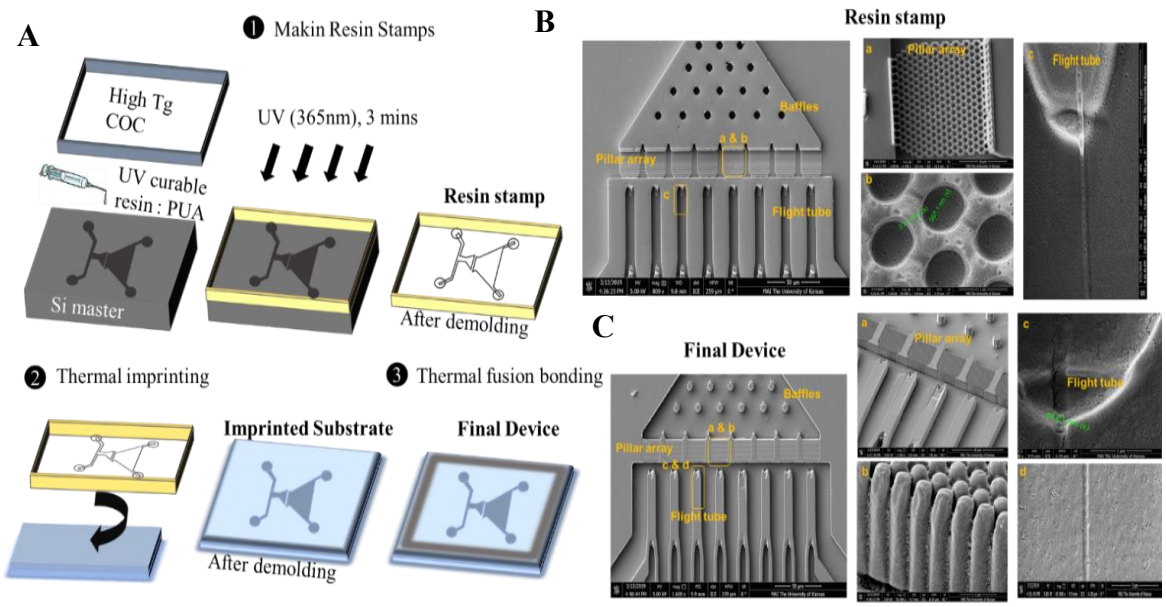

Figure 3.5 Process of NIL: A) Schematic showing the process of nanoimprint lithography is described in 3 steps; Step 1 is the process of using PUA resin to create polymeric stamps from the Si master by UV treating them at 365 nm for 2.5 mins; Step 2 is followed by thermal imprinting of the stamps on a PMMA substrate at 135°C, 300 psi for 5 mins to transfer the patterns from the stamps into the PMMA device.~~,~~ Step 3: Thermal fusion bonding is performed by using a COC cover plate to seal the features at 70°C, 120 psi for 15 mins. ; B) SEM images showing the images of UV resin stamp where the structures are formed in the direction opposite to the Si master. The pixel arrays (a), the pillars (b) in them and the flight tube (c) are transferred. C) SEM images of the final PMMA device after thermal imprinting that has structure similar to the original Si master. The final device with the pixel arrays (a), the side profile of the pillars (b), the funnel entrance to the flight tubes (c) and the flight tubes (d) are replicated with high fidelity.

thermal fusion bonding is performed for enclosing the fluidic network using a cover plate (Figure 3.5-A). The patterns were initially transferred from the Si master to a COC backbone covered with a resin that was crosslinked via UV NIL. Figure 3B shows SEM images of the resin stamp. The device is seen to have the baffles, pixel arrays as well as the flight tubes. In the stamp, the dimensions of the pillars were measured to be 1088±27 nm in diameter with a spacing of 273±77 nm between. The dimensions of the flight tubes were 118±17 nm. Following thermal NIL, the features were successfully transferred to the PMMA substrate. From Figure 3.5-C, it can be seen that the baffles, pixel arrays, and flight tubes were successfully transferred to the PMMA substrate. The average width of the pillars in the pixel array were 931±58 μm, with a spacing of 263±19 nm between them. The width of the flight tubes were 56±12 nm. The PMMA device was finally sealed using thermal fusion bonding and a COC 8007 cover plate.

3.4.2 Fluid dynamics

3.4.2.1 Passive valving in the nanosensor device.

Proper fluidic operation of the nanosensor can be achieved by using two different types of flow pumping through the device, namely hydrodynamic and electrokinetic pumping. Hydrodynamic pumping was used to perform the following operations: 1) Effective loading of the target nucleic acids for querying their mutational status (*i.e.*, DNA) or expression (*i.e.*, mRNA) and spLDR reagents through a common input, and uniformly distribute these materials into the 8 pixel arrays; 2) efficient capture of biotinylated DNA or cDNA (*i.e.*, target) to the streptavidin decorated pillars (i.e., the target is anchored to the surface of the pillars using the high association of the biotin/streptavidin couple); 3) none of these reagents enter into the flight tube. When using electrokinetic pumping, the following steps are carried out: 1) Specific entrance of the spLDR products into the flight tube; 2) high current density to direct the spLDR products into the flight tubes with an optimal transmission efficiency. By evaluating the hydrodynamic and electrokinetic flow, we can passively control the fluid dynamics in the nanosensor for performing the spLDR and successful detection and identification of those products via nanoscale electrophoresis.

Unique to this nanosensor device is the ability to control fluid direction using passive valving, which is affected by the judicious choice in the dimensions of the fluidic network and the use of both hydrodynamic and electrokinetic pumping, which will obviate the need for mechanical valves. In addition, the nanosensor not only performs detection, but also carries out sample preparation as well, which in this case is that the spLDRs are carried out on arrays of micropillars, which generates oligonucleotides of a particular size. The detection and size determination of the oligonucleotide spLDR product is transduced using nanoscale electrophoresis equipped with in-plane nanopores that obviates the need for labelling of the products and simplifies the measurement hardware. In the sections that follow, both experiments and simulation results will be provided to verify proper fluidic operation.

3.4.2.2 COMSOL simulations.

A model nanosensor design was built in AutoCAD and flow patterns were tested using finite element analysis simulations (COMSOL). The device operation was simulated with 1X TBE. This was chosen because it is a commonly used buffer for LDRs and consists of Tris Borate EDTA (TBE). TBE buffer contains ions, which makes it highly suitable for nanoscale electrophoresis. For fluid flow driven hydrodynamically at a flow rate of 1 nL/s, the placement of 20 diamond shaped chevron baffles in the entrance of the nanosensor (25 µm wide) facilitated distribution of fluid across the 8 pixel arrays. A uniform distribution is necessary to ensure that the reagents and the target DNA reaches all the 8 pixel arrays for both a homogeneous and a thorough spLDR reaction. Each array is 20 µm X 20 µm spaced 5 µm from each other. The laminar flow module governed by the Navier-Stoke's equation was used to model the flow of fluid under the influence of hydrodynamic pumping. For the electrokinetic pumping, the electrostatics

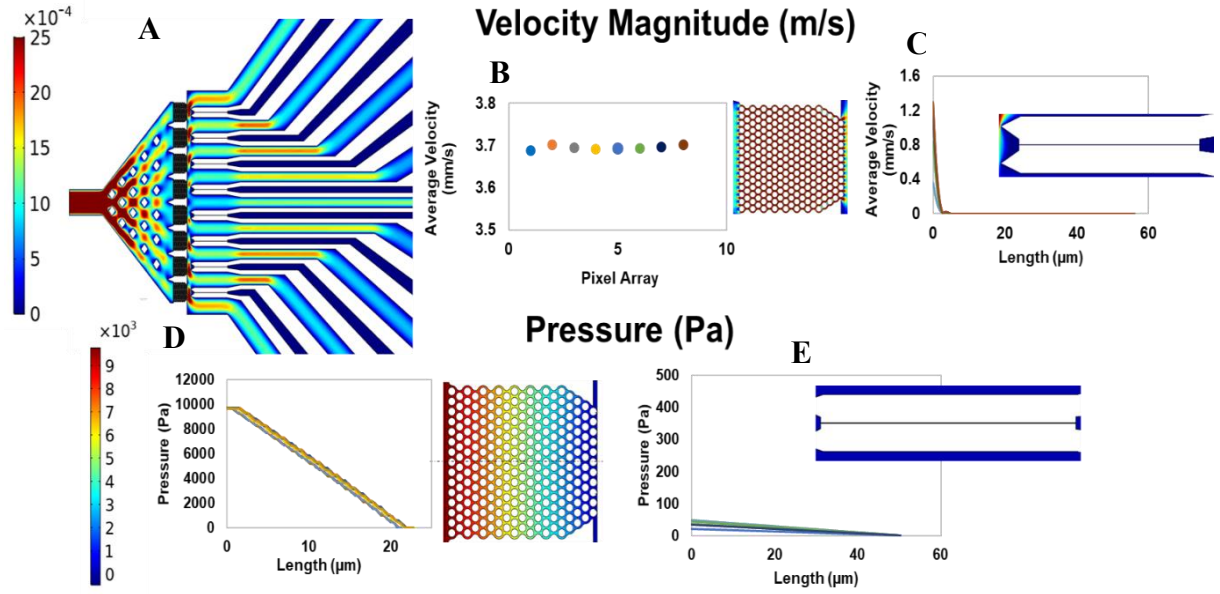

Figure 3.6 . A) COMSOL simulation of hydrodynamic flow of 1X TBE through the nanosensor device at a flow rate of 1 nL/s. The entrance of the nanosensor (25 µm) is placed as the inlet of the liquid. The flow entering the nanosensor is distributed uniformly across the baffles such that all the 8 pixel arrays get a uniform distribution of the fluid. The colors correspond to the scale bar in the graph. B) Hydrodynamic flow across the pixel array is magnified (maroon color in the scale bar). The graph shows the average velocity across the 8-pixel array, which is about 3.7 mm/s. The velocity across the 8 pixel arrays are very uniform with a standard deviation of 6 µm/s between the arrays. C) The flow across the 8 flight tubes in region in the nanosensor is negligible. This is empirically represented in the line graph that is drawn across the flight tubes, where the velocity at the entrance of the flight tubes drops rapidly as seen by the drop in velocity (to ~0 mm/s). D) The pressure drop across the pixel array is seen. The average current drop among the 8 arrays are similar. E) The pressure drop across the 8 nanochannels show a negligible drop in pressure (30 Pa to 0 Pa) compared to the pixel array.

module (AC/DC physics) governed by the Poisson's and Maxwell's equation was chosen to model the electric field in the nanosensor by application of a potential of 10 V in the common input and placing earth ground at the outlet end of each flight tube. Figure 3.6-A shows the overall hydrodynamic profile of the COMSOL simulated hydrodynamic flow. It can be seen that the flow entering through a common input was equally distributed by the baffles and entered the pixel arrays. The flow in the entrance of the nanosensor is high (~2.5 mm/s) due to a narrow entrance and gets distributed in between the baffles as represented by the scale bar (Figure 3.6-A). This is the step where the reagents are loaded into the pixel arrays for the LDR. The flow profile of how the fluid leaves the nanosensor is also seen. The fluid leaving the pixel arrays enter the areas surrounding flight tubes (the red, orange areas); this is essential for washing the waste products after LDR. A second round of hydrodynamic pumping using 1X PBS or nuclease free water would wash away the waste products of LDR in the areas surrounding the flight tubes, which would reach the access microchannels and eventually exit out of the device. The magnified image of a single pixel array is shown in the Figure 3.6-B. There is a higher velocity in the spacing between the pillars (250 nm) as represented by the red color.

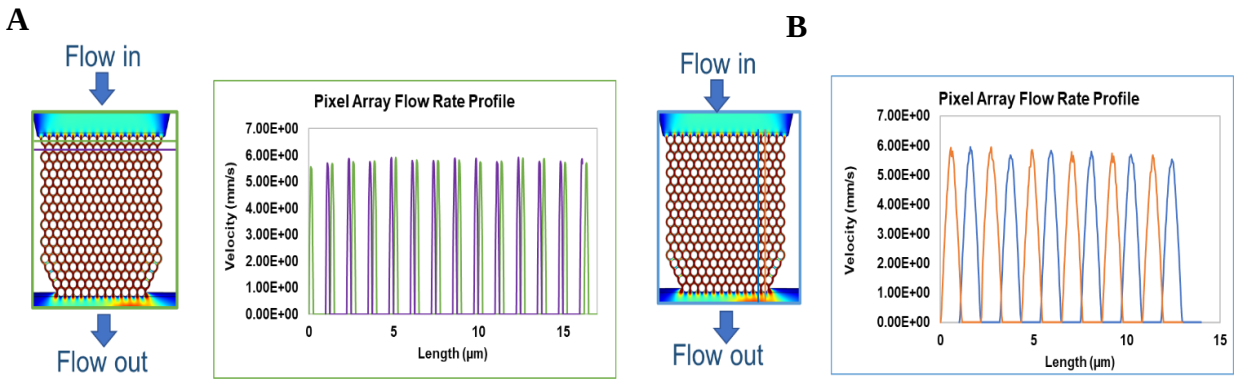

Figure 3.7 Schematic of pixel arrays set up in COMSOL. Each chamber measures 20 µm x 20 µm and contains 8 pixels with 268 pillars per pixel array. A) The flow across two rows in one pixel array in the horizontal direction is represented, which are all nearly similar (~ 5.7 mm/s). B) The pixel array flow rate profile across two rows in a single pixel array in vertical direction which again shows uniform velocity (~5.7 mm/s) throughout array.

The average velocity across the entire array in the 8 pillar arrays (Figure 3.6-B) suggested that they were similar (3.7 mm/s) between them indicating uniform access of the input fluid. This will ensure uniformity

in reagents loadings; i.e, how uniformly streptavidin can be attached to the pillars. The figure 3.7 shows a vertical and horizontal line profile of how the fluid is accessed across a single two lines of pillars in a single pixel array. There is uniformity of the flow in the pillars (5.7 mm/s) in both the horizontal (Figure 3.7-A) and vertical (Figure 3.7-B) directions which also ensures how biotinylated DNA binds to the pillars that are already immobilized with the streptavidin across all the 8 arrays. The magnified image of the flow profile (Figure 3.6-C) in the one flight tube showed that there was negligible flow (dark blue color) in these flight tubes during hydrodynamic pumping. There is drop of velocity from 1.2 mm/s in the entrance to to 0 mm/s

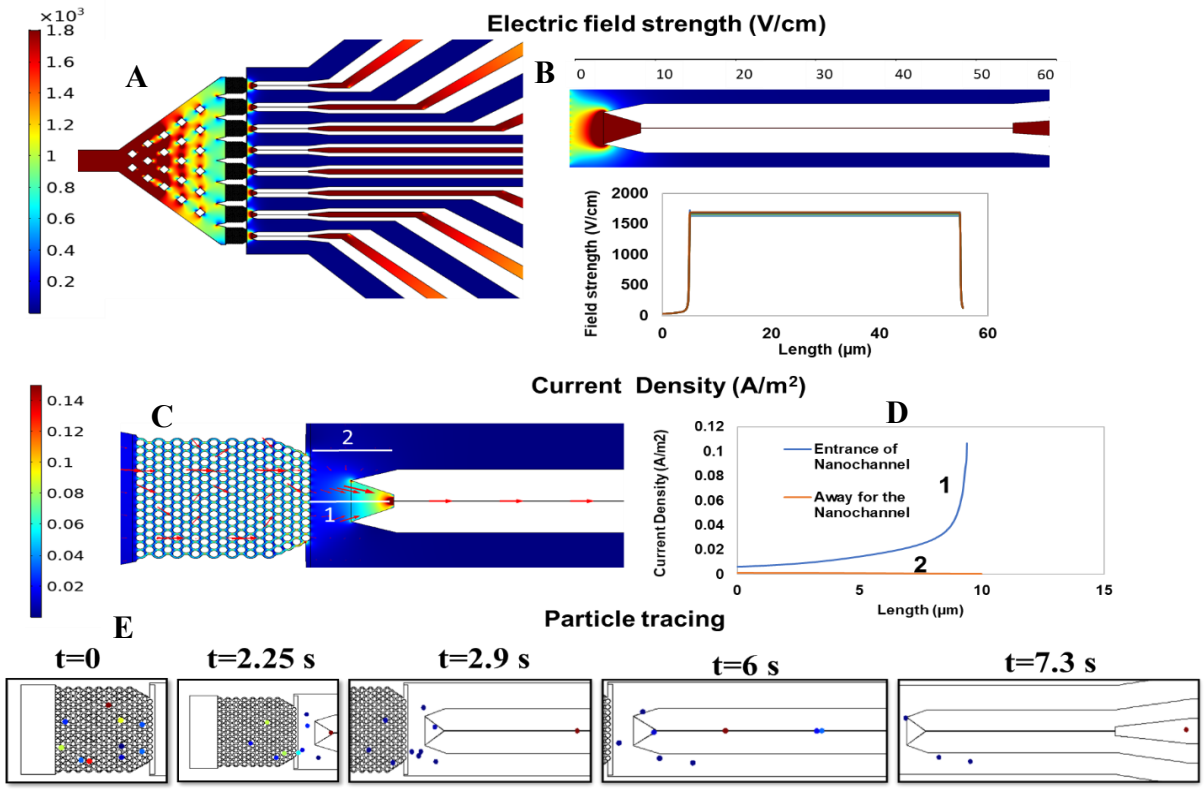

Figure 3.8 COMSOL simulation of electrokinetic flow through the nanosensor; A) Field strength across the nanosensor is represented. A potential of 10 V is applied in the inlet of the nanosensor and each of the flight tubes are placed at earth ground in their individual reservoirs. The areas of the nanosensor having the smallest dimensions have the higher field strengths. B) Line plot of the field strength across the 8 flight tubes as represented in the figure. The field strength gradually increases from the entrance of the flight tube through its length. There is a uniform field strength observed across the 8 flight tubes, which is 1650 V/cm. C) The current density plot (at a potential of 10 V) showing one pixel array and the flight tube with arrows representing the direction of the fluid movement and the magnitude of arrows representing areas of higher field strength. D) The line graph showing an increase of current density upto 0.1 A/m^2 in the entrance of the flight tube and a drop in current density of 0.0015 A/m^2 in the regions away from the channel. E) Particle tracing representative of ssDNA is simulated showing 10 particles simulated in the pixel array (t=0). The time scale of movement is shown where the particles are observed moving to the entrance of the funnel inlet (2.25 s), eventually moving into the flight tube and more particles entering into the funnel (t=2.9 s), and all of them translocating into the flight tubes (t=6). Those particles that are not in the funnel, but still in the radius of the current density are also drawn into the flight tube (t=7.3 s). The transmission efficiency of 80% is observed.

through the length of the channel for all flight tubes. This result was due to the high fluidic resistance in the nanometer flight tubes with respect to the interstitial space between these flight tubes. The pressure profiles represented in the figure bolster the conclusions made above. A larger pressure drop gradient is required for the fluid to flow across the device. The majority of the pressure drop (9500 Pa to 30 Pa) occurs across the pixel array (Figure 3.6-D), which is uniform across the 8 of them. This is essential as a higher pressure drop signifies a higher flow of fluid through the pixel arrays and a similar pressure drop among them would indicate the uniformity in how the reagents would flow and how efficiently the target DNA would attach to the streptavidin coated pillars. Figure 3.6-E shows the pressure drop across the flight tubes. There is a negligible amount of pressure drop (~30 Pa to 0 Pa) across the flight tubes compared to the pixel arrays. Since the pressure drop is extremely small, there would not be any fluid entering into the flight tube after the LDR.

In the case of electrokinetic pumping, the goal is to drive the products generated from spLDR into the flight tubes for analysis. A potential of 10 V was applied across the nanosensor by placing the inlet at the common access microchannel and the ends of the individual flight tube were placed at earth ground. The field strength across the entire nanosensor is shown in Figure 3.8-A. The areas of the sensor having a higher field strength are shown, namely the entrance of the nanosensor, the pixel arrays and the flight tubes (represented by the maroon color). Since the electrokinetic flow focuses on the movement of the analyte on to the flight tube, the field strength of 1680 V/cm (*i.e.*, potential drop of ~8.5 V is observed in each the flight tube, see Figure 3.9) across the flight tubes was observed (Figure 3.8-B) with the remaining drop predominantly occurring across the pillar arrays (0.5 V) and the baffle region (Figure 3.9-A). The magnified image of the flight tube shows a higher field strength in the entrance of the flight tube continued to the length of it. There is also a uniform field strength profile across all the 8 flight tubes thus ensuring there is equal access to all of them.

This result is supported by the current density profile to ensure the direction of the analyte movement the pixel array to the flight tube (size of the arrows represents the magnitude of the current density, Figure 3.8-C). The line graph of the current density graph with arrows showing a higher current density (0.1 A/m^2) at the entrance of the flight tubes (Figure 3.8 C-D, line 1) . A line graph at an area away from the entrance of the nanometer tubes indicated that there is an extremely small current density of 0.0015 A/m^2 eventually decaying to 0 at regions farther away from the entrance of the flight tube (Figure 3.8 C-D, line 2). This signifies that, apart from the products of LDR entering into the flight tube, they have a very minimal probability of escaping outside. Particle tracing studies with particles representing the ssDNA products were simulated, that showed that 8/10 particles enter into the flight tube under the application of a 10 V DC bias (Figure 3.8-E). The time scale of the particle movement being driven at a DC bias of 10V is represented: i) At t=0, when the particles are in the pixel array; ii) At t=2.25 s, where the first particle is in the funnel of the flight tube entering into the flight tube; iii) At t=2.9 s, where the particle is inside the flight tube; iv) At t=6 s, where more particles are seen entering into the flight tube. Some particles away

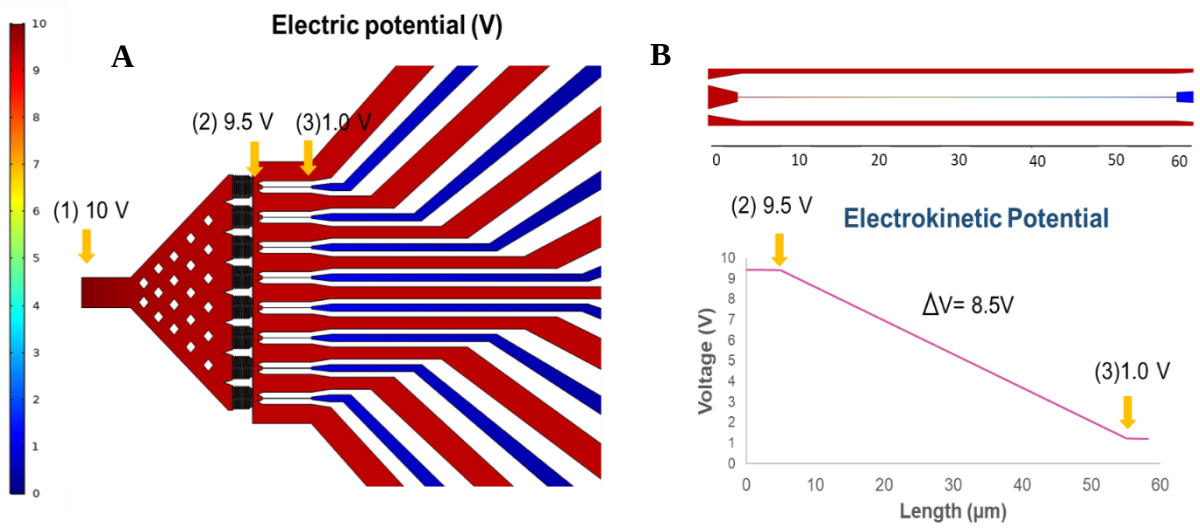

Figure 3.9 COMSOL simulation of electrokinetic potential drop through the nanosensor device. A) The electrical potential across the nanosensor is represented. A potential of 10 V is applied across the nanosensor device. The arrows depict the potential at each section of the device. B) Most of the potential drop occurs across the nanometer flight tubes as represented in the schematic. The line graph shows the drop in potential from the inlet of the nanosensor to the ends of the nanochannel which is kept at earth ground. The 10 V is applied in the entrance of the nanosensor, where it drops to 9.5V after the pixel array. There is an 8.5V drop in potential across the flight tube. This represents the transport of spLDR products into the nanochannel during the experiment.

from the entrance are seen escaping, but the ones close to the entrance of the funnel are being drawn into the flight tube due to the higher current density; v) at t=7.3 s, where 8 out of the 10 particles are seen to enter into the flight tube. The inlet of the flight tubes have a funnel shaped entrance (see Figure 3.3-C, subfigure c, showing the entrance of the flight tube) tapering in width and depth leading to the flight tube, so that there is a reduced entropic barrier, while having a larger capture area for the products that are released from the pixel arrays [35]. The field strength profile (Figure 3.8-B) also shows that the area surrounding the funnel entrance has a small radius that has higher field strength. From our particle tracing simulations, we saw that even though some particles moved away from the entrance of the funnel but stayed in the radius were drawn electrokinetically into the flight tube.

3.4.2.3 Hydrodynamic pumping monitored using a fluorescent tracer dye.

We verified the results deduced from the simulations for hydrodynamic pumping by using a fluorescent tracer and fluorescence microscopy. Rhodamine B, a neutral dye, with excitation and emission wavelength maxima of 534/570 nm was used as the tracer for monitoring hydrodynamic flow to track fluidic operation of the nanosensor. The volume flow rate used was 1 nL/s and was supplied using a syringe pump. The fluorescence was captured using a sCMOS camera at an exposure time of 10 ms with the fluorescence collected using a 100X oil immersion objective. An example image is shown in Figure 3.10-A, which shows the distribution of the fluid within the nanosensor at steady state. The dye front was traced for this flow, which showed that the dye moved through the baffle arrays and simultaneously entered the pixel array. Subsequently, the dye moved around the flight tubes and gradually entered the access microchannels. We could not observe the movement of dye into the flight tubes. The flow across the pixel arrays were quantified in terms of the fluorescence intensity which is representative of the mass flow when using the label-less reagents. The mean intensity of each pixel of the image (calculated from 5 different experiments and using the same laser power) were very similar and agreed nicely with the results seen in the COMSOL simulations (Figure 3.10-B). The intensity was represented as grey values, that ranged from (800-1000) for all the pixel arrays. However, the dramatic drop in fluorescence intensity seen in the 8 flight

tubes were also represented by the line graph shown in Figure 3.10-C and indicate minimal if any flow into the 8 flight tubes when pumping was accomplished using hydrodynamics due to the large fluidic resistance and an extremely small pressure gradient in these small diameter tubes. However, contrary to the COMSOL simulations, there was some residual fluorescence seen in the graph, which could be attributed to diffusional effects. The grey values ranged from 200-250, which is almost 4 times lower than the fluorescence intensity observed in the pixel array. A ROI was taken for each flight tube measurement to avoid the residual fluorescence if any, being masked by the surrounding areas having a much higher intensity. The images were scaled in the exact same way to avoid discrepancies. Therefore, in terms of operation of the nanosensor, during loading of biotinylated-targets to the streptavidin coated pillars of the pixel array there is equal accessibility of fluid across the arrays (demonstrated through both COMSOL simulations and

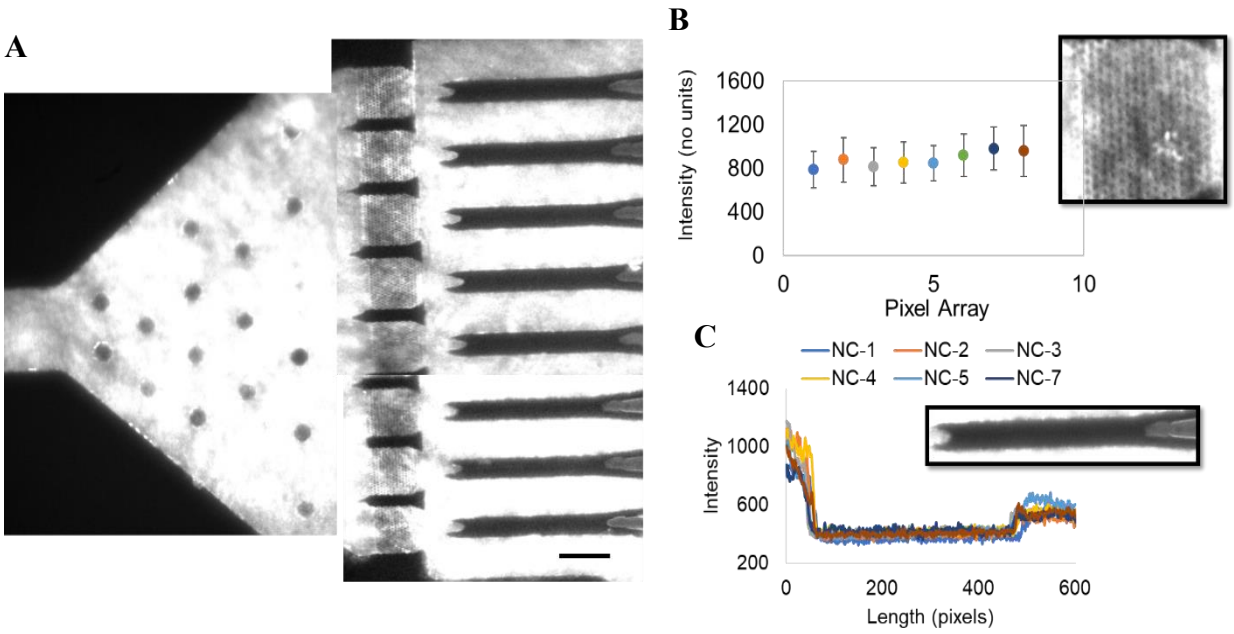

Figure 3.10 Experimental results of the hydrodynamic flow across the nanosensor. This is observed to evaluate the performance of how similar the flow is among each pixel array. A) The figure represents how the nanosensor device looks like after pumping Rhodamine-B as the tracer pumped at a flow rate of 1nL/s. The dye is distributed across the baffles to the pixel arrays and to the areas surrounding the flight tubes. No visible fluorescence is seen in the flight tubes B) Fluorescence intensities across the 8 pixels are evaluated showing similar levels of intensities ranging from 800-1000. The intensities are represented as grey values and they correspond to the liquid flow C) Correspondingly, the intensity in the flight tubes are evaluated, and a significant drop is seen in the 8 flight tubes in a similar fashion. The areas having dye have a grey value of 800 or more, while the intensity in the nanochannels are ~300. The measurements are taken from 5 different experiments calculated with mean and sd evaluated. No statistical significance was seen between the intensity of the pixel arrays at $p<0.01$ at 95% CI. A scale bar of 20 µm is represented in the images.

experimentation) and subsequent spLDR, the materials required to carry out these steps are not swept into the nanometer-flight tubes when fluidic pumping is carried out using hydrodynamics. There is a distinct movement of the materials outside of the flight tubes.

3.4.2.4 Electrokinetic flow monitoring using fluorescently-labeled oligonucleotides.

In the case of electrokinetic pumping, single-stranded DNA oligonucleotides were injected into the flight tubes so that they could be tracked using single-molecule fluorescence microscopy. Here we used Cy3-labelled 25mer oligonucleotides (random sequence) with the electrokinetic flow driven with 10 V bias voltage. Once the potential was applied, the dye-labelled oligonucleotides were observed to move towards

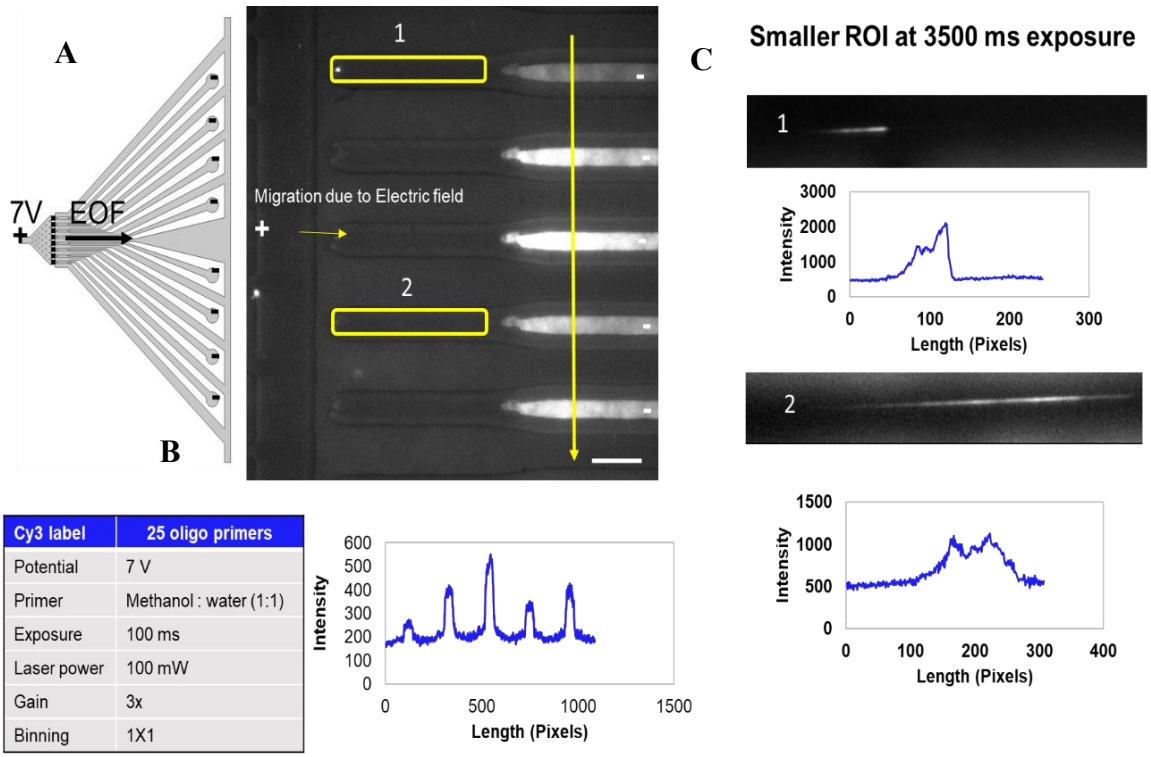

Cy3 label	25 oligo primers
Potential	7 V
Primer	Methanol : water (1:1)
Exposure	100 ms
Laser power	100 mW
Gain	3x
Binning	1X1

Figure 3.11 A) Schematic of the application of the DC bias is represented. The potential is applied to the entrance of the microchannel, while the ends of the nanochannel are placed at earth ground. Fluorescent images showing the accumulation of DNA from the pixel array to the end of each of the flight tubes are represented; B) The intensity of the fluorescence accumulation is represented using a line graph. The areas of DNA accumulation show higher intensity grey values (300-500). The conditions of the experiment are given in the table. C) The flight tubes are magnified at a higher exposure (3500 ms) with ROI's 1 and 2 showing the DNA molecules parked in the flight tube when the voltage is turned off. The corresponding line plots show an increase of fluorescence to a grey value of 2000 (1) and 1000(2) confirms the movement of analytes into the flight tube in a DC field. The parameters used for the experiment are given in the table. A scale bar of 20 μm is represented in the images.

the cathode (see Figure 3.11) due to the high electroosmotic flow (2.2 x10^{-4} cm^2/Vs)[24] associated with the O_2 plasma treated plastic due to the generation of surface –COOH groups (surface charge is -40.5 mC/m^2).[28] We also observed that there was no fluorescence seen in the pixel array, rather they were in the ends of the flight tube. Figure 3.11-B shows the intensity profiles confirming the presence of oligonucleotides. There are 5 intensity peaks ranging from grey scale values of 300 to 550 compared to the background intensity value 200. This shows that in the end of the spLDR, the products would not get stuck in the pixel arrays, but rather enter into the flight tube. Once we observed the movement of analyte, the DC field was turned off to park the DNA oligonucleotides in the flight tube and the images were captured using a sCMOS camera. High exposure (3500 ms) ROI images showed fluorescence intensities in two of the flight tubes (regions 1 and 2) indicating the presence of oligonucleotides in these flight tubes (see intensity line graphs shown in Figure 3.11-C). The intensity in regions (1) and (2) shows the grey scale value of 2000 and 1000 respectively. The presence of oligonucleotides at the terminal end of the nanometer flight tubes with the absence of fluorescence in the area between the flight tubes indicated that electrokinetic pumping preferably shuttled the DNA into the nanometer flight tube. The preferential transport of the oligonucleotides into the flight tube compared to the microchannels was a direct result of the large electric field drop in the nanochannel with respect to that found in the microchannels. Thus, high efficiency transfer of spLDR products generated in the pixel arrays can be accomplished using electrokinetic pumping.

3.5 Conclusions

We have developed a nanosensor device that was made in a thermoplastic via NIL. Unique to this device is the ability to perform sample preparation directly on-chip followed by nanofluidic detection and identification of the products formed as a result of a spLDR reaction, which can be used to detect point mutations that possess high diagnostic value for a number of diseases. In addition, the spLDR can quantify the expression of certain gene fragments (*i.e.*, mRNA) following reverse transcription. The spLDRs are carried out in 8 separate pixel arrays, which were comprised of 268 1-µm pillars, which were positioned adjacent to the nanometer flight tubes to detect and identify successfully formed spLDR products. While

several operational steps are required for the assay carried out using the nanosensor device, we were able to show that using a combination of hydrodynamic and electrokinetic pumping, passive valving was possible using dimensional features associated with different domains of the nanosensor device. For example, during target loading and reagent introduction necessary to carry out spLDRs, hydrodynamic pumping could be used to eliminate introduction of these reagents form entering the nanometer flight tubes, which may cause failure of the nanometer tubes due to clogging or non-specific adsorption creating bio-fouling. Conversely, following the spLDRs, successfully formed ligation products, which has a unique length associated with the mutation/mRNA being queried, can be selectively injected into the nanometer flight tube for interrogation using electrokinetic pumping due to the fact that the majority of the potential drop occurs in the nanometer flight tube. Once placed in the nanometer flight tube, nanoscale electrophoresis can identify the length of the spLDR product. We have already demonstrated the performance of LDR for analysing single point mutations using microfluidics[36] and also, utilizing single molecule nanoscale electrophoresis for identifying oligonucleotides based on differences in their size.[24]

Our future work will include incorporating spLDR on nanoscale and combining the simultaneous read out of the products of LDR. Some design modifications will be adapted to facilitate the ease of spLDR performance, such as increasing the size (to 2 μm) and spacing of the pillars (to 500 nm) in pixel arrays to avoid the formation of air bubbles during the injection of reagents. Further, the reservoirs at the end of the flight tubes are of 60 μm. This size makes it difficult to establish ohmic contact with individual flight tubes. In this paper, we used a three-dimensional stage with a magnifying camera to use Pt electrodes (40 μm wire) to establish direct contact of the electrodes with reservoirs. Increasing the size of the reservoirs in the next iteration would make the application of DC bias much easier.

3.6 References

1. Feigin, V. L.; Forouzanfar, M. H.; Krishnamurthi, R.; Mensah, G. A.; Connor, M.; Bennett, D. A.; Moran, A. E.; Sacco, R. L.; Anderson, L.; Truelsen, T.; O'Donnell, M.; Venketasubramanian, N.; Barker-Collo, S.; Lawes, C. M.; Wang, W.; Shinohara, Y.; Witt, E.; Ezzati, M.; Naghavi, M.; Murray, C., Global and regional burden of stroke during 1990-2010: findings from the Global Burden of Disease Study 2010. *Lancet (London, England)* **2014,** *383* (9913), 245-54.

2. Baird, A. E., Blood biologic markers of stroke: Improved management, reduced cost? *Current Atherosclerosis Reports* **2006,** *8* (4), 267-275.
3. Theofilatos, K.; Korfiati, A.; Mavroudi, S.; Cowperthwaite, M. C.; Shpak, M., Discovery of stroke-related blood biomarkers from gene expression network models. *BMC Medical Genomics* **2019,** *12* (1), 118.
4. Wijerathne, H.; Witek, M. A.; Jackson, J. M.; Brown, V.; Hupert, M. L.; Herrera, K.; Kramer, C.; Davidow, A. E.; Li, Y.; Baird, A. E.; Murphy, M. C.; Soper, S. A., Affinity enrichment of extracellular vesicles from plasma reveals mRNA changes associated with acute ischemic stroke. *Nature Communications Biology* **2020,** *3*, 613.
5. Vashist, S. K., Point-of-Care Diagnostics: Recent Advances and Trends. *Biosensors (Basel)* **2017,** *7* (4).
6. Levit, L.; Balogh, E.; Nass, S.; Ganz, P. A.; Population, C. o. I. t. Q. o. C. C. A. t. C. o. a. A.; Services, B. o. H. C.; Medicine, I. o., *Accessible and Affordable Cancer Care*. National Academies Press (US): 2013.
7. Shaw, J., Practical Challenges Related to Point of Care Testing. *Practical Laboratory Medicine* **2015,** *4*.
8. Current and Future Challenges in Point-of-Care Technologies: A Paradigm-Shift in Affordable Global Healthcare With Personalized and Preventive Medicine. *IEEE J Transl Eng Health Med* **2015,** *3*.
9. Sivanesan, P.; Okamoto, K.; English, D.; Lee, C. S.; DeVoe, D. L., Polymer Nanochannels Fabricated by Thermomechanical Deformation for Single-Molecule Analysis. *Analytical Chemistry* **2005,** *77* (7), 2252-2258.
10. Tas, N. R.; Berenschot, J. W.; Mela, P.; Jansen, H. V.; Elwenspoek, M.; van den Berg, A., 2D-Confined Nanochannels Fabricated by Conventional Micromachining. *Nano Letters* **2002,** *2* (9), 1031-1032.
11. Ruiz, C.; Huang, J.; Giardina, S. F.; Feinberg, P. B.; Mirza, A. H.; Bacolod, M. D.; Soper, S. A.; Barany, F., Single-molecule detection of cancer mutations using a novel PCR-LDR-qPCR assay. *Human Mutation* **2020,** *41* (5), 1051-1068.
12. Wabuyele, M. B.; Farquar, H.; Stryjewski, W.; Hammer, R. P.; Soper, S. A.; Cheng, Y. W.; Barany, F., Approaching real-time molecular diagnostics: single-pair fluorescence resonance energy transfer (spFRET) detection for the analysis of low abundant point mutations in K-ras oncogenes. *Journal of the American Chemical Society* **2003,** *125* (23), 6937-45.
13. Barany, F., Genetic disease detection and DNA amplification using cloned thermostable ligase. *Proc Natl Acad Sci U S A* **1991,** *88* (1), 189-193.
14. Lofton-Day, C.; Model, F.; Devos, T.; Tetzner, R.; Distler, J.; Schuster, M.; Song, X.; Lesche, R.; Liebenberg, V.; Ebert, M.; Molnar, B.; Grutzmann, R.; Pilarsky, C.; Sledziewski, A., DNA methylation biomarkers for blood-based colorectal cancer screening. *Clin Chem* **2008,** *54* (2), 414-23.
15. Tong, J.; Cao, W.; Barany, F., Biochemical properties of a high fidelity DNA ligase from Thermus species AK16D. *Nucleic Acids Res* **1999,** *27* (3), 788-94.
16. Volckmar, A. L.; Sultmann, H.; Riediger, A.; Fioretos, T.; Schirmacher, P.; Endris, V.; Stenzinger, A.; Dietz, S., A field guide for cancer diagnostics using cell-free DNA: From principles to practice and clinical applications. *Genes, chromosomes & cancer* **2018,** *57* (3), 123-139.
17. Wabuyele, M. B.; Farquar, H.; Stryjewski, W.; Hammer, R. P.; Soper, S. A.; Cheng, Y. W.; Barany, F., Approaching real-time molecular diagnostics: Single-pair fluorescence resonance energy transfer (spFRET) detection for the analysis of low abundant point mutations in K-ras oncogenes. *J. Am. Chem. Soc.* **2003,** *125* (23), 6937-6945.
18. Peng, Z. Y.; Young, B.; Baird, A. E.; Soper, S. A., Single-Pair Fluorescence Resonance Energy Transfer Analysis of mRNA Transcripts for Highly Sensitive Gene Expression Profiling in Near Real Time. *Anal. Chem.* **2013,** *85* (16), 7851-7858.

19. Piruska, A.; Gong, M.; Sweedler, J. V.; Bohn, P. W., Nanofluidics in chemical analysis. *Chemical Society Reviews* **2010,** *39* (3), 1060-1072.
20. Yuan, Z.; Garcia, A. L.; Lopez, G. P.; Petsev, D. N., Electrokinetic transport and separations in fluidic nanochannels. *Electrophoresis* **2007,** *28* (4), 595-610.
21. Pennathur, S.; Santiago, J., Electrokinetic transport in nanochannels. 1. Theory. *Anal Chem* **2005,** *77* (21), 6772 - 6781.
22. Pennathur, S.; Santiago, J. G., Electrokinetic Transport in Nanochannels. 2. Experiments. *Analytical Chemistry* **2005,** *77*, 6782-6789.
23. Movahed, S.; Li, D., Electrokinetic transport through nanochannels. *Electrophoresis* **2011,** *32* (11), 1259-1267.
24. Amarasekara, C. A.; Athapattu, U. S.; Rathnayaka, C.; Choi, J.; Park, S.; Soper, S. A., Open-tubular nanoelectrochromatography (OT-NEC): gel-free separation of single stranded DNAs (ssDNAs) in thermoplastic nanochannels. *ELECTROPHORESIS* **2020,** *41* (18-19), 1627-1640.
25. Reisner, W.; Morton, K. J.; Riehn, R.; Wang, Y. M.; Yu, Z.; Rosen, M.; Sturm, J. C.; Chou, S. Y.; Frey, E.; Austin, R. H., Statics and dynamics of single DNA molecules confined in nanochannels. *Physical Review Letters* **2005,** *94* (19), 196101.
26. Weerakoon-Ratnayake, K. M.; Vaidyanathan, S.; Amarasekara, C. A.; Johnson, C. K.; Soper, S. A., Chapter 7 - Single molecule analysis in nanofluidic devices. In *Spectroscopy and Dynamics of Single Molecules*, Johnson, C. K., Ed. Elsevier: 2019; pp 335-377.
27. I. Uba, F.; Hu, B.; Weerakoon-Ratnayake, K.; Oliver-Calixte, N.; A. Soper, S., High process yield rates of thermoplastic nanofluidic devices using a hybrid thermal assembly technique. *Lab on a Chip* **2015,** *15* (4), 1038-1049.
28. Uba, F. I.; Pullagurla, S. R.; Sirasunthorn, N.; Wu, J.; Park, S.; Chantiwas, R.; Cho, Y. K.; Shin, H.; Soper, S. A., Surface charge, electroosmotic flow and DNA extension in chemically modified thermoplastic nanoslits and nanochannels. *The Analyst* **2015,** *140* (1), 113-26.
29. Vaidya, B.; Soper, S. A.; McCarley, R. L., Surface modification and characterization of microfabricated poly(carbonate) devices: manipulation of electroosmotic flow. *The Analyst* **2002,** *127* (10), 1289-1292.
30. Matschuk, M.; Larsen, N., Injection molding of high aspect ratio sub-100 nm nanostructures. *Journal of Micromechanics and Microengineering* **2012,** *23*, 025003.
31. Uba, F. I.; Hu, B.; Weerakoon-Ratnayake, K.; Oliver-Calixte, N.; Soper, S. A., High Process Yield Rates of Thermoplastic Nanofluidic Devices using a Hybrid Thermal Assembly Technique. *Lab Chip* **2014,** *15*, 1038-1049.
32. Tsao, C.-W.; DeVoe, D. L., Bonding of thermoplastic polymer microfluidics. *Microfluidics and Nanofluidics* **2009,** *6* (1), 1-16.
33. Weerakoon-Ratnayake, K. M.; O'Neil, C. E.; Uba, F. I.; Soper, S. A., Thermoplastic nanofluidic devices for biomedical applications. *Lab on a Chip* **2017,** *17* (3), 362-381.
34. Kooy, N.; Mohamed, K.; Pin, L. T.; Guan, O. S., A review of roll-to-roll nanoimprint lithography. In *Nanoscale Res Lett*, 2014; Vol. 9, p 320.
35. Vaidyanathan, S.; Weerakoon-Ratnayake, K. M.; Uba, F. I.; Hu, B.; Kaufman, D.; Choi, J.; Park, S.; Soper, S. A., Thermoplastic nanofluidic devices for identifying abasic sites in single DNA molecules. *Lab on a Chip* **2021**.
36. Sinville, R.; Coyne, J.; Meagher, R. J.; Cheng, Y.-W.; Barany, F.; Barron, A.; Soper, S. A., Ligase detection reaction for the analysis of point mutations using free-solution conjugate electrophoresis in a polymer microfluidic device. *Electrophoresis* **2008,** *29* (23), 4751-4760.

Chapter 4: Tailoring Thermoplastic In-Plane Nanopore Size by Thermal Fusion Bonding

4.1 Abstract

We report a simple method for tailoring the size of in-plane nanopores fabricated in thermoplastics for single-molecule sensing. The in-plane pores were fabricated via nanoimprint lithography (NIL) from resin stamps, which were generated from FIB-milled Si masters. We could reduce the size of the in-plane nanopores from 30 to ~10 nm during the thermal fusion bonding (TFB) process, which places a cover plate over the imprinted polymer substrate under a controlled pressure and temperature to form nanofluidic devices. Increased pressures during TFB caused the cross-sectional area of the in-plane pore to be reduced. The in-plane nanopores prepared with different TFB pressures were utilized to detect single λ-DNA and oligonucleotide molecules via resistive pulse sensing, which showed a higher current amplitude in devices bonded at higher pressures. The ability to control the nanopore size negates the need for a new FIB-milled master to alter the pore size to suite the application need.

4.2 Introduction

Pores with nanometer dimensions are typically fabricated in a thin membrane separating two fluid chambers.[1] When an electrical bias is applied across the membrane, the resulting electric field can transport charged molecules through the pore, producing signals in the trans-membrane ionic current that can be used to sense single molecules. Among single-molecule sensors, nanopores have garnered significant interest because they allow the detection of single molecules without requiring fluorescent labeling of the target and the need for sophisticated optical equipment for transduction.[2-5] These and other attractive properties have led to the development of many nanopore-based applications including detection of DNA-protein interactions,[6-9] measurement of molecular forces,[10-11] and nucleic acid sequencing.[12-13] Although biological pores, such as α-hemolysin[14] and MspA,[15] have proven to be useful sensors, several disadvantages remain primarily due to their fixed size and limited stability under extreme conditions of salt, pH, temperature, and mechanical stress. As an alternative, solid-state nanopores[3, 16] have captured attention to address challenges

associated with biological pores. Moreover, solid-state nanopores can be integrated with other micro- and nanofluidic components to form lab-on-a-chip systems.

Most solid-state nanopores have been fabricated on inorganic thin-film membranes.[3, 17-19] Several approaches have been demonstrated to produce small nanopores in these substrates through charged particle beams[17-18, 20-21] or electrical breakdown[22] and to control the size of the pores *ex post facto* via exposure with a defocused beam of electrons,[17] ions,[23] direct thermal heating,[24] or focused ion beam (FIB) deposition of materials such as gold.[25] Even though these methods have proven successful in the fabrication of small-diameter pores, they are generally not conducive to production at a scale and cost that will ultimately enable them to be translated for clinical applications that require disposable devices.

Solid-state nanopores have also been fabricated in planar substrates ("in-plane" nanopores) embedded within a fluidic network rather than suspended on a thin membrane.[26] FIB has been used to fabricate monolithic channels with micro- and nanoscale components, including in-plane nanopores.[26-28] In-plane pores can also be produced in series so that other measurement modalities can be realized. For example, Kondylis *et al*. used glass nanopore devices with 2, 4, and 8 pores (width: 60 nm, depth: 70 nm) in series for real-time, resistive pulse analysis of virus capsids. They showed that the standard deviation of the pulse amplitude distributions of individual molecules decreases with the increasing number of pores in series leading to increased measurement precision[29] while the electrophoretic mobility of virus particles have been determined using two in-plane pores.[30-32]

Thermoplastics provide the means for high-throughput manufacturing at low production costs even at the nanoscale due to a plethora of fabrication technologies available, such as nanoimprint lithography (NIL) and injection molding.[33-34] Additionally, due to the diverse physiochemical properties of different thermoplastics, the appropriate material can be selected according to measurement requirements.[35-36] However, it has been a challenge to achieve sub-20 nm structures using thermoplastics due to challenges associated with bonding a cover plate to the nanofluidic network, which can result in deformation of the patterned nanostructures. The cover plate bonding process in thermoplastic devices typically involves the use of thermal fusion bonding (TFB), which bonds a thin cover plate to the nano-patterned substrate under

a controlled pressure at temperatures near the glass transition temperature, T_g, of the substrate or cover plate. The TFB process involves motion of polymer chains between the cover plate and the substrate, which inevitably alters the dimensions of the nanostructures in the enclosed nanofluidic devices from those in the imprinted substrate. We have shown that high process yield rates of thermoplastic nanofluidic devices with minimal deformation of nanostructures can be realized using a hybrid bonding process, in which a lower T_g cover plate is thermally fusion bonded to a higher T_g substrate.[37]

The ability to control the size of in-plane nanopores imprinted from the same mold will allow for reduction in the development and production costs by obviating the need for FIB-milled Si masters to accommodate a particular application, for example reducing in-plane nanopore size to sense molecules of various sizes. Several reports have demonstrated reduction of nanostructure dimensions after initial fabrication by applying pressure to the patterned polymer substrate at an elevated temperature.[38] For example, Choi *et al.* reduced the size of micropores in a perforated SU-8 membrane produced by NIL from 3 μm to 300 nm.[39] The same group utilized polymer reflow, which consists of applying an elevated temperature without any external pressure, to reduce nanopore size from 12 nm to 6 nm.[40] In another report, Chou *et al.* described the use of a method called pressed self-perfection by liquefaction (P-SPEL), where the transiently molten thermoplastic nanostructures were pressed using a blank Si plate to achieve sub-20 nm structures.[38] However, these methods have not been demonstrated to reduce in-plane nanopore size for nanofluidic devices. Moreover, these methods have been employed as an additional process step beyond the original production pipeline, which increases production time and cost.

In this study, we demonstrate a post fabrication method to tailor the dimensions of in-plane nanopores in enclosed nanofluidic devices using TFB, a process step needed to produce enclosed nanofluidic devices. The thermoplastic dual in-plane nanopore devices were fabricated on PMMA substrate and the O_2 plasma activated imprinted substrates and cover plates were subjected to different bonding pressures to vary the size of the in-plane nanopores. The change in depth and width of the nanopores with bonding pressure was measured by AFM and SEM, respectively. The COMSOL simulations and the experimental conductance measurements further demonstrated the pore closing behavior of the nanopores with higher bonding

pressures. The devices bonded at different pressures were used to analyze λ-DNA and showed improved signal-to-noise ratio with lower nanopore size. Furthermore, the use of nanopore devices with different pore sizes fabricated by changing the bonding pressure to analyze different types of molecules with varying diameters was demonstrated using the dual in-plane nanopores bonded at 170 psi for the analysis of oligonucleotides of 50 mer and 70 mer. The differences in TOF were seen when translocating the Oligo 50 and 70 mer which shows a promising application for the detection of mutated products from wild-type ssDNA generated from the spLDR discussed in the previous chapter 3.

4.3 Materials and Methods

4.3.1 Reagents and Materials

Chemicals and materials were obtained from the following sources and used without further purification: S1813 photoresist (MicroChem); MF319 developer (MicroChem); potassium hydroxide (KOH) pellets (Fisher Scientific); isopropyl alcohol (IPA) (Sigma-Aldrich); hydrofluoric acid (HF) (Sigma-Aldrich); Tri(propylene glycol) diacrylate (TPGDA) (Sigma-Aldrich); Trimethylolpropane triacrylate (TMPTA) (Sigma-Aldrich); 2,2-Dimethoxy-2-phenylacetophenone (photoinitiator, Sigma-Aldrich); NOA72 (Norland Products); Si wafers (P/B, resistivity 5-10 Ωcm, orientation of (100), and 525 ± 25 μm thickness) (WaferPro); polyethylene terephthalate (PET) with 250 μm thickness (Goodfellow). Silicon (Si) 〈100〉 wafers were purchased from University Wafers (Boston, MA). PMMA was received from ePlastics (San Diego, CA). Cyclic olefin copolymer (COC 8007) was purchased from TOPAS Advanced Polymers (Florence, KY). COP sheets were obtained from STRATEC SE (Birkenfeld, Germany). UV curable polyurethane resin was purchased from Chansang Co. Guanosine 5'-monophosphate disodium salt was obtained from Sigma-Aldrich (St. Louis, MO). Molecular biology grade water was secured from Thermo Fisher (Waltham, MA). SYTO82 dye was purchased from Life Technologies (Eugene, OR, USA).

4.3.2 Device fabrication and assembly

A Si master mold was prepared by using a combination of photolithography, wet-chemical etching, and focused ion beam (FIB) milling. Si wafers with a 100 nm thick silicon nitride (Si_3N_4) layer on each side were used for fabricating the master mold. Microchannels were fabricated using a combination of photolithography and wet-chemical etching. First, a 1.3 µm thick S1813 photoresist layer was spin-coated at 4,000 rpm for 60 s on the Si wafer and then baked at 115°C for 60 s. Photolithography was performed using a designed photomask in a UV exposure station (Quintel) in a class 100 cleanroom. UV exposure was conducted at 130-140 mJ/cm^2, with post-exposure baking at 95°C for 60 s. Then, the wafer was developed with a MF319 developer for 90 s, followed by washing with deionized water. The exposed Si_3N_4 layer was etched to open a window using an ICP-DRIE system (Plasmalab System 100, Oxford). Subsequently, the wafer was transferred to a 40 wt% KOH solution with IPA (5 % v/v) at 70°C. The KOH solution was prepared by dissolving KOH pellets in deionized water. After 25 min etching to form 10 µm deep microchannels, the wafer was removed from the etchant, rinsed in water, and dried with N_2 gas. Prior to FIB milling, the Si_3N_4 layer was completely removed using a dilute HF solution. The nanochannel flight tube combined with in-plane nanopores was fabricated using FIB milling (Quanta 3D Dual Beam system, FEI). The milling was performed at a beam voltage and current of 30 kV and 10 pA, respectively, in a bitmap mode.

The Si master mold was used to produce a resin stamp by using a UV resin solution (70 wt% TPGDA, 28 wt% TMPTA, and 2 wt% photoinitiator). Drops of the UV-resin were dispensed against the Si master mold. A flexible PET sheet coated with an adhesive layer (NOA72) was then slightly pressed against the liquid drop and used as a backbone substrate. Residual resin solution and air bubbles were gently squeezed out. During the curing process, the sample was exposed to flash-type UV light (250-400 nm) for 20 s at an intensity of ~1.8 W/cm^2 by using a nanoimprinter (Eitre6, Obducat). After UV-curing, the molded UV-resin/PET substrate was demolded from the Si master along the nanochannel direction.

Nanopores were imprinted into a plastic substrate using nanoimprint lithography ,NIL (Nanonex 2500 engine for nanotechnology)[41]. The optimized imprinting conditions for PMMA devices were 145°C, 300

psi, and 5 min and 130°C, 300 psi, and 5 mins for COP devices. Imprinted nanofluidic devices were then characterized using scanning electron microscope, SEM, and atomic force microscopy, AFM.

The nanopore device was sealed after thermal imprinting using a COC 8007 cover plate. Thermal fusion bonding with NIL was used for sealing nanopore devices. Bonding of PMMA/COC devices were done following the method described by Uba *et al.* [37] with 1 min O_2 plasma treatment for both the substrate and cover plate at 50 W.

4.3.3 Atomic Force Microscopy

To determine the depth of the nanopores with increasing pressure an AFM (SPM HT-9700, Shimadzu corporation, Japan) analysis carried out. The tip used for imaging was a Super Sharp Silicon tip (Nanosensors, Switzerland) with a frequency of 300 kHz, a tip radius <2 nm, a half cone angle of 10^o and an aspect ratio of 4:1 at 200 nm from the tip apex. Dynamic scanning mode was used for imaging with a scanning frequency of 0.5 Hz. The acquired images were analyzed using SPM Manager v4.76.1 software (Shimadzu corporation, Japan).

4.3.4 Scanning Electron Microscopy

SEMs of the nanopore devices were acquired using a FEI VERSA 3D Dualbeam field emission/ low vacuum SEM. A 2 nm thin conductive Iridium layer was sputter coated onto thermoplastic devices using an EMS 150ES sputter coater before SEM Imaging. All images were acquired using 5.0 kV accelerating voltage and 8.7 mm working distance. The SEM images of the Si mold masters were acquired using a Quanta™ 3D DualBeam™ FEG FIB-SEM. The acquired images were analyzed using instrument softwares and Image J.

4.3.5 COMSOL

Simulations are performed in COMSOL v5.5 for the dual nanopores of different widths. The length of both the nanopore was kept at 30 nm, but the width was varied from 10-50 nm to calculate the corresponding conductance. The electrolyte used was 1M KCl and a DC field of 1V at 293 K was applied

in the electrostatics module to calculate the electric potential, the current density, and the corresponding conductance across the nanopores.

4.3.6 Conductance Measurements

Experimental conductance measurements were performed using the dual in-plane nanopore devices made in PMMA and cyclic olefin polymer (COP) devices bonded at different pressures using 1 M KCl as the electrolyte. software. Assembled devices were filled with 50% v/v methanol/water and allowed to incubate for 15 min. The 50% methanol solution was then replaced with 1 M KCl and allowed to equilibrate for 15 min. The device was placed in a faraday cage and Pt electrodes were placed on the reservoir filled with liquid to make an ohmic contact with the device. The current was measured from -1 to 1 V with steps of 0.2 V. Current data were acquired using an Axopatch Digidata 1440B instrument and analyzed using Clampfit 11.1. The current measurements corresponding to the voltages were measured for different devices ($n \geq 3$) at each bonding pressure and the conductance was calculated.

4.3.7 λ- DNA and Oligonucleotides Translocation

Translocation experiments were performed for λ- DNA in PMMA dual nanopore devices bonded at 110,170 and 200 psi to confirm the reduction in pore size by seeing an increase in peak amplitudes at higher bonding pressures. Briefly, 100 nM of λ- DNA in 1M KCl in 1X TBE was injected into the microchannels of the device connecting the dual nanopores. The devices were allowed to equilibrate with 50% v/v methanol/water for 15 mins and then filled with λ- DNA. The devices were placed in the faraday cage and Pt electrodes were immersed in the reservoirs of the device filled with liquid. A potential of 1V was applied and the data was acquired using Axopatch Digidata 1440B, analyzed using Clampfit 11.1 software. The peak amplitude data ($n \geq 120$) was collected and was plotted. Wilcoxon p-test was used to calculate the statistical significance of peak amplitudes between each pressure.

500 nM of Oligos of 50 and 70 mer (random sequence) in 1M KCl in 1X TBE were used to estimate the differences in TOF between the dual nanopores. The experiments were performed under similar

conditions as described above. Wilcoxon p-test was used to calculate the statistical significance between the TOF of oligo 50 and 70 and as well between the peak amplitudes of oligo 70.

4.3.8 Statistical analysis

All reported data sets were compared by a two-sided t-test using R Studio v1.0.153 and R v3.5.1 software.

4.4 Results and discussion

4.4.1 Device fabrication and assembly

Nanofluidic devices were fabricated in a thermoplastic using a method we have reported, which consists of making microstructures and nanostructures in Si masters followed by producing resin stamps via UV-NIL then production of the final device using thermal NIL into the appropriate plastic.[42-43] The Si master containing the in-plane nanopores and fluidic network was fabricated using a combination of photolithography and FIB milling. The in-plane nanopores were positioned at either end of a nanochannel, which was 5 μm in length and 50 nm x 50 nm in width and depth (Figure 4.1 A). The nanochannel containing the in-plane nanopores was connected on both ends to access microchannels fabricated via photolithography and wet etching of Si. The structures on the Si master were transferred to a UV curable Tri(propylene glycol) diacrylate (TPGDA) resin situated on a NOA72 coated thin poly(ethyl terephthalate), PET, sheet (250 μm thick) serving as a back plate by exposing to UV light for 3 min (Figure 4.1 B).[44] Next, the TPGDA resin stamp was used to pattern the PMMA substrate at 145°C and 300 psi for 5 min using thermal NIL (Figure 4.1 C). The average height of the in-plane nanopores on the resin stamp were 30.3 ±2.0 nm (n = 4) and the depth of the nanopores in the imprinted substrate were 29.6 ±1.7 nm (n = 3).

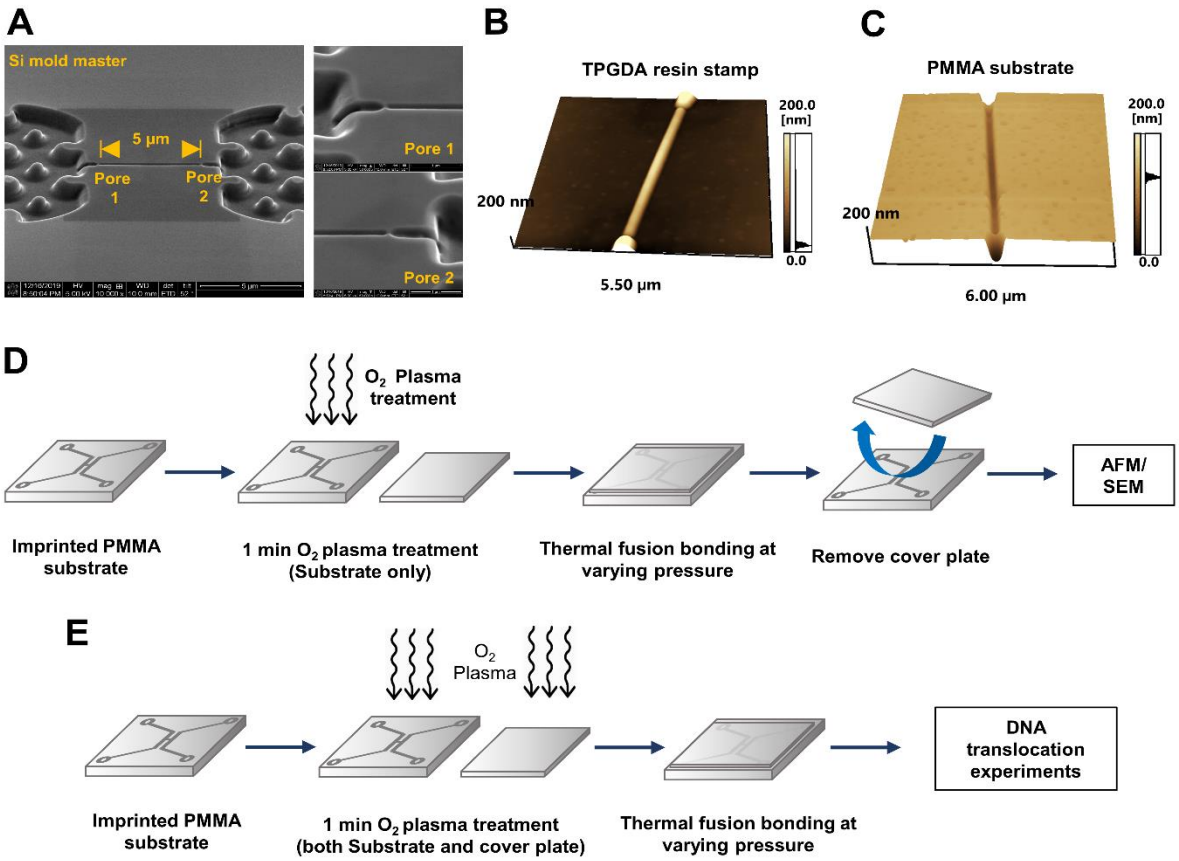

Figure 4.1 Dual in-plane nanopore device. (**A**) SEM image of the Si mold master. The two in-plane nanopores are 5 µm apart from each other. AFM scans of the (**B**) TPGDA resin stamp and (**C**) imprinted PMMA substrate. Tapping mode AFM scans (Shimadzu SPM) were acquired at 0.5 Hz scanning frequency using a high aspect ratio tip with a radius <2 nm. (**C**) Schematic representation of experimental procedure for determining depth and width of dual in-plane nanopores. (**D**) Schematic representation of device assembly for DNA translocation studies.

Following fabrication, the ability to control the size of the in-plane nanopores via TFB was examined by subjecting O_2 plasma activated (50 W, 1 min) NIL imprinted devices to different bonding pressures at 70°C for 15 min and measuring the depth and width of the in-plane nanopores using AFM and SEM. For this purpose, we only treated the imprinted PMMA substrate with O_2 plasma and not the COC cover plate prior to TFB to reduce the bonding strength so that the cover plate and substrate could be pulled apart without damaging the underlying structures (Figure 4.1-D) for metrology. Bonding temperature of 70°C was used as it was closer to the T_g of the COC 8007 coverplate. For λ-DNA translocation studies, the dual in-plane nanopore devices were assembled by O_2 plasma treatment of both the substrate and cover plate

before TFB at varying pressures (Figure 4.1-E) so that the bonding strength was sufficient to sustain fluidic/translocation experiments.

The PMMA substrate was exposed to O_2 plasma to form O-containing groups.[35, 41, 45-47] In TFB, these O-containing species are involved in strong bond formation between the substrate and cover plate.[35] In addition, polymer chain scissoring can result in photo-fragments that are more thermally mobile due to their lower molecular weight. This leads to a lowering of the T_g of the polymer on the surface, making it easier for the polymer chains to fuse into the mating substrate.[41] Depending on the type of polymer and the O_2

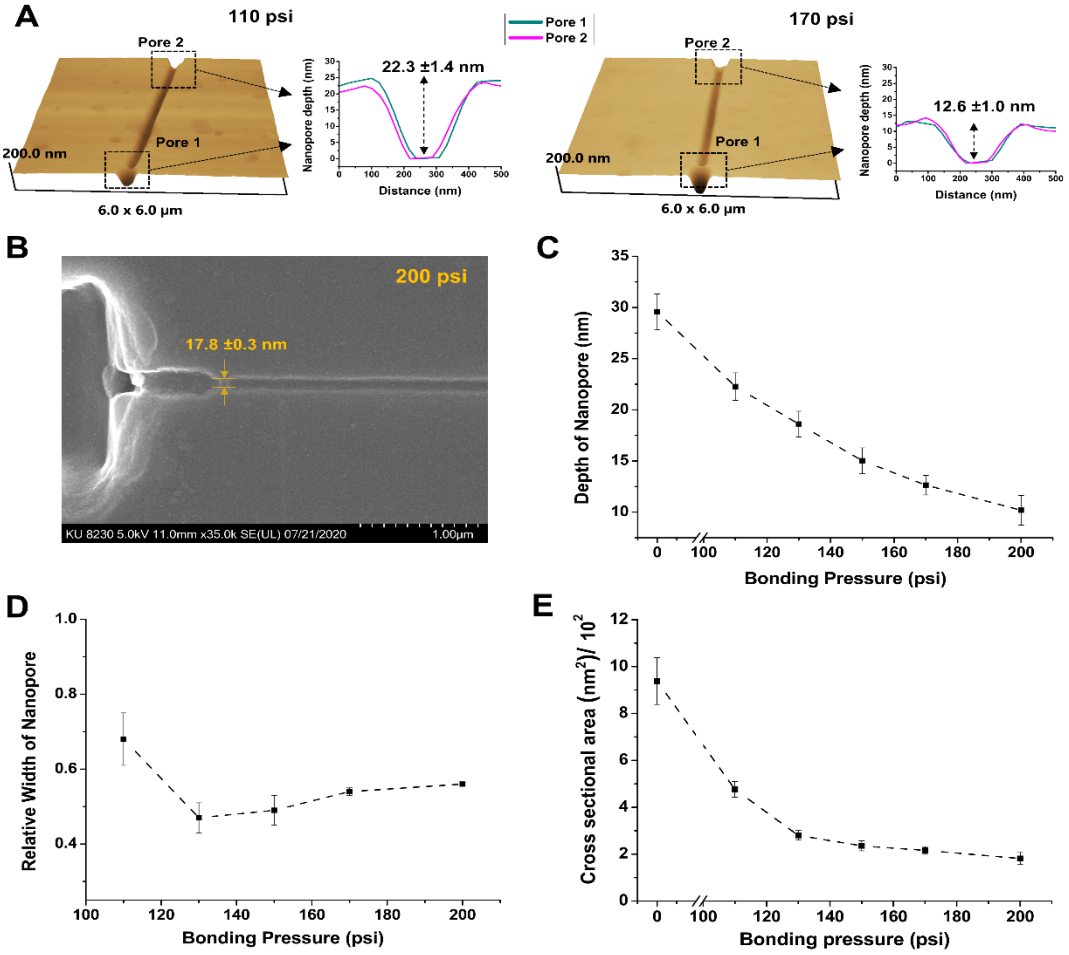

Figure 4.2 Nanopore depth and width with varying thermal fusion bonding pressure. (**A**) AFM scans of PMMA devices at 110 psi and 170 psi bonding pressures. (**B**) SEM image of PMMA device at 200 psi bonding pressure. A 2 nm thin conductive Iridium layer was sputter coated onto the PMMA device using an EMS 150ES sputter coater before SEM Imaging. (**C**) Change in the depth of the in-plane nanopores with bonding pressure. (**D**) Relative width of the in-plane nanopores after bonding at different pressures relative to the width of the nanopore before bonding (0 psi). There was no statistical difference in relative width from 130-200 psi at the 95% confidence interval ($p > 0.05$). (**E**) Cross sectional area of the in-plane nanopore with thermal fusion bonding pressure.

plasma power used as well as exposure time, polymer chain scission can occur up to several molecular layers into the bulk of the polymer. Therefore, during TFB of the cover plate to the substrate, the O_2 plasma activated polymer surfaces can rearrange leading to a change in nanostructure dimensions.

4.4.2 Nanopore Size analysis

The depth of the in-plane nanopores were measured by dynamic mode AFM (Shimadzu Corporation) at a 0.5 Hz scanning rate (Figure 4.2-A). For AFM, a high aspect-ratio tip with a radius <2 nm and a half cone angle of ~10^o was used. To measure the width of the in-plane nanopores following TFB, SEM was performed (Figure 4.2-B). The depth of the in-plane nanopores reduced from 22.3 ±1.4 nm (110 psi, n = 6) to 10.2 ±1.5 nm (200 psi, n = 4) with increasing bonding pressure (Figure 4.2-C). The relative width of the in-plane nanopores decreased initially with bonding pressure to 0.47 ±0.04 (n = 4) at 130 psi compared to the width of the imprinted device but showed no statistically different widths at higher pressures (130-200 psi, p >0.05, see Figure 4.2-D).

4.4.3 COMSOL simulations

We carried out COMSOL simulations for the dual in-plane nanopore sensor to estimate the change in the conductance with change in pore size. The length of the nanopore was maintained at 30 nm, but the width was changed from 10 nm to 50 nm (Figure 4.3-A). A DC bias of 1 V was applied across the ends of the device and 1 M KCl was used as the electrolyte. From Figure 4.3-B, it can be seen that the majority of the potential drop occurred across the two in-plane nanopores (0.03 V in each pore) and the 5 μm long nanochannel. A current density graph was plotted that showed a sharp increase in current density at the nanopores due to the smaller dimensions (Figure 4.3-C). The current density was integrated over the area of the nanopore to calculate the current. The conductance for the pores was then calculated using Ohm's law and was plotted to estimate the conductance at different pore sizes. As shown in Figure 4.3-D, a linear increase in conductance was seen as the size of the nanopore increased. The conductance values obtained

from simulations and depths and widths from AFM and SEM respectively were used to estimate the size of the nanopore with the values of conductance obtained experimentally.

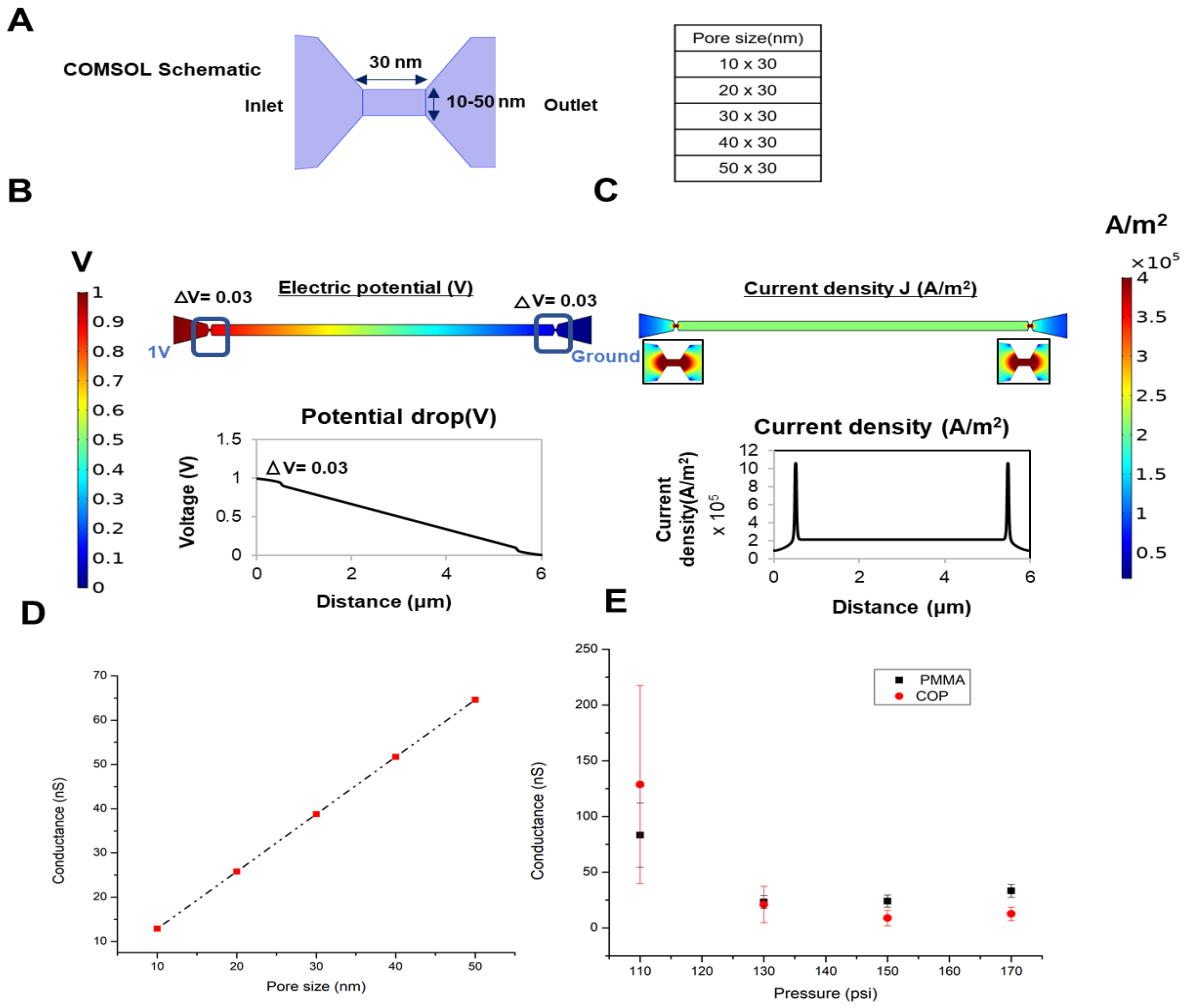

Figure 4.3 Simulated and experimental analysis of the electrical behavior of the dual in-plane nanopores connected by a 5 μm length flight tube at different bonding pressures. (A) The 2D design of the dual in-plane nanopores used for COMSOL simulations. The pore and intervening 5 μm long nanochannel were assumed to be cylindrical. In order to understand if a change of in-plane nanopore size (diameter) would cause an increase in conductance, the pore diameter was varied from 10-50 nm while the length was kept constant at 30 nm. (B) The electric potential data from COMSOL simulations shows that the majority of the potential drop appears across the two nanopores and the nanochannel implying that the overall conductance is contributed by the two nanopores and the nanochannel. (C) The current density was plotted from which the current and the subsequent conductance was calculated (I/V). (D) Conductance (nS) calculated from COMSOL for varying pore size in 1 M KCl. There is a linear increase in conductance with increasing pore width. (E) Variation of measured conductance through the dual in plane nanopore PMMA and COP devices at different bonding conditions using an electrolyte of 1M KCl ($n \geq 3$). There was a decrease in conductance with increase in bonding pressure, but with no statistical differences at pressures above 130 psi ($p>0.05$). The conductance results agree with the pore size determined using AFM and SEM correlated to the results from COMSOL. The y-axis scales of graphs for figures D and E are adjusted according to their corresponding x-axis and hence the range might be different.

4.4.4 Conductance measurements

Experimental conductance measurements were then performed using the dual in-plane nanopore devices made in PMMA and cyclic olefin polymer (COP) devices bonded at different pressures using 1 M KCl as the electrolyte. Current data were acquired using an Axopatch Digidata 1440B instrument and analyzed using Clampfit 11.1 software. Assembled devices were filled with 50% v/v methanol/water and allowed to incubate for 15 min. The 50% methanol solution was then replaced with 1 M KCl and allowed to equilibrate for 15 min. The current was measured from -1 to 1 V with steps of 0.2 V. The conductance was calculated from the slope of the curve for all bonding pressures used and is shown in Figure 4.3-E. The average conductance at 110 psi for PMMA and COP devices were 83 ± 29 nS (RSD 34%) and 128 ± 89 nS (RSD 69%) respectively. However, at 130 psi the average conductance of the PMMA and COP dual in-plane nanopores was 23 nS ± 6 nS (RSD 26%) and 21 ± 16 nS (RSD 76%) respectively. This value correlates well with the conductance (~ 23 nS) obtained from COMSOL for an 18 nm pore, which is the size of the pore obtained from AFM and SEM images when using 130 psi TFB pressure. The conductance values showed a slight increase from 24 ± 5 nS (RSD 22%) to 33 ± 6 nS (RSD 18%) for PMMA devices bonded at 150 and 170 psi, respectively, but there was no statistical difference in the conductance values at bonding pressures >130 psi ($p > 0.05$). Similarly, in the case of COP devices, the conductance values decreased at 150 psi to 9 ± 7 nS (RSD 77%) but showed a statistically insignificant increase at 170 psi to 12 ± 6 (RSD 48%) nS. This small increase in conductance can be correlated to the results from SEM and COMSOL that showed <5 nm increase in pore width. Overall, both PMMA and COP devices followed a similar trend of decrease in conductance at 130 and 150 psi respectively, followed by a slight increase at 170 psi showing the reproducibility of our approach with different materials.

The results of the pore depth and width versus the bonding pressure provided a hint on the pore closing behavior. Our in-plane nanopore in the imprinted PMMA is a V-shaped constriction formed in a nanochannel, attributed to the nature of FIB milling of the Si master. The decrease in both the pore depth and width in the low bonding pressure range can be attributed to the fusion of polymer chains between the two mating polymers, primarily in the thin layer of polymer subjected to O_2 plasma or UV/O_3 prior to

bonding, and to the squeeze flow toward the nanopores. As the bonding pressure increases, the lateral squeeze flow will preferentially flow along the border of nanopores as was observed during the squeeze flow into hydrophilic nanostructures,[48-49] and thus further reduce the pore depth while limiting the decrease

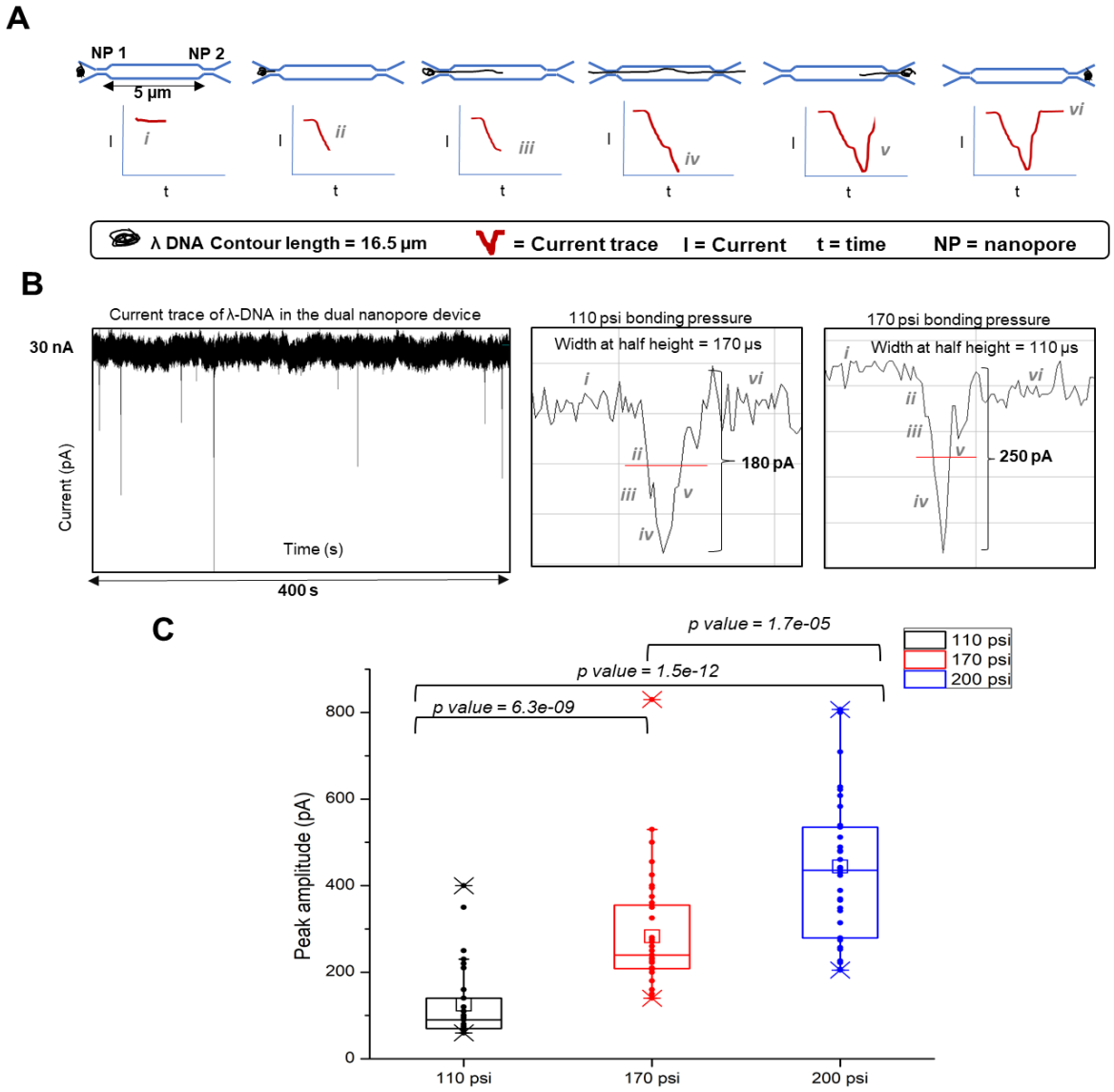

Figure 4.4 λ-DNA translocation through the dual in-plane PMMA nanopores and the ramifications of the size of the nanopore on peak amplitude. **(A)** Schematic of the λ-DNA translocation through the in plane dual nanopore device that gives rise to a negative peak as the DNA enters the first pore. Since the contour length of the DNA is longer than both the pores, there is a second subsequent peak when the DNA co-resides in both the pores. The DNA then leaves the pores very quickly which makes the current return to the baseline. **(B)** A detected current transient trace typically observed in a time interval of 400 s as a result of λ-DNA translocation and magnified images of individual peak shapes at various translocation stages of the DNA through the dual nanopore at 110 and 170 psi pressure respectively. **(C)** Distribution of peak amplitudes of λ-DNA at 110, 170 and 200 psi bonding pressures. The average peak amplitude increases with the increasing bonding pressure. p values calculated between each bonding pressure condition (Wilcoxon signed rank test) show statistically significant difference at 95% confidence interval ($p < 0.05$).

in the pore width. Consequently, the nanopore bonded at higher pressures became a shallower V shape. At the same time, the decrease in the thickness of the surface modified thermoplastic layer will further limit the squeeze flow because of increases in the T_g for polymers in the vicinity of a hydrophilic surface due to the alignment of polymer chains along the surface.[50] This may account for the slight increase in the pore width at higher bonding pressures. Further increases in the bonding pressure beyond 200 psi ultimately led to collapse of the nanopores as evidenced by the cessation of the open pore current.

4.4.5 λ-DNA translocation through the dual in-plane nanopore

Assembled dual in-plane nanopore PMMA devices could be used to electrophoretically drive charged single molecules through the nanopores for single molecule sensing by monitoring the electrical current as a function of time. Figure 4 shows the use of a dual in-plane nanopore device as a sensing platform for the detection of non-labeled 48.5-Kbp λ-DNA that has a contour length of 16.5 μm. When the electrophoretically driven molecule entered the first nanopore, there is a partial current blockage creating a transient increase in the electrical resistance, which is manifested as a negative peak (current drop) in the measured current trace as shown in the schematic of Figure 4.4-A. Because the contour length of λ-DNA is longer than the distance between the two in-plane nanopores (5 μm), the initial drop of current is accompanied by a subsequent drop in current when the DNA co-resides in the first and second in-plane nanopores. Further, when the DNA exits the first nanopore, it resides only in the second nanopore causing a subsequent small shoulder in the current trace, and eventually returning to baseline. A current trace showing multiple current transient signals over a time interval of 400 s for λ-DNA is shown in Figure 4.4-B demonstrating the characteristic shape of the peaks at 110 psi and 170 psi. The various stages of the translocation are marked in both traces to show how the shape of the current transients agree with the aforementioned descriptions. Although the average amplitude increased 2-fold with every increase in bonding pressure, the shape of the peaks remained similar to that shown in Figure 4.3-B indicating that the

size of the nanopore did not alter the translocation dynamics rather changes only the S/N ratio in the resistive pulse sensing.

Peak height measurements (n ≥40) of the current transient amplitudes of λ-DNA in devices bonded at different pressures showed differences between each bonding pressure as determined by the Wilcoxon signed rank test (Figure 4.4-C). The average peak amplitude of λ-DNA in devices bonded at 110 psi for 15 min was 130 pA, while for devices bonded at 170 psi, it was 280 pA, and for 200 psi it was 437 pA. Devices bonded at 200 psi for 15 min served as the upper limit because the nanopore became unusable as the cover plate collapsed into the nanopore. However, for 200 psi bonding pressure the TFB time had to be reduced to 5 min to generate functional devices.

We calculated the apparent mobility (μ_{app}) of λ-DNA based on the time interval between peaks (Δt) at time points (i) and (iv) (see Figure 4.4-A). These time points were used because one end of λ-DNA is entering the first in-plane nanopore and that same end is then entering the second nanopore corresponding to a length of 5 μm (l) at the applied electric field strength (*E*); the apparent mobility was calculated from:

Equation 4.1. $$\mu_{app} = v_{app}/E$$

Equation 4.2. $$v_{app} = l/\Delta t$$

The average apparent mobility for **λ**-DNA was determined to be 2.57×10^{-7} $\pm 9.4 \times 10^{-8}$ m^2/Vs.

4.4.6 Translocation of Oligonucleotides through the Dual in-plane Nanopore

Following translocation with λ-DNA, we used the dual-in plane nanopore devices to distinguish between oligo nucleotides of different sizes based on their TOF between the two nanopores placed in series. The nanopore depth from the Si mold was estimated to be ~30 nm. At this pore depth it is difficult to distinguish oligonucleotides having a radius of gyration (R_g) of 5.9 nm (50 mer) and 7.1 nm (70 mer). Hence, we used the TFB to reduce the size of the nanopore to ~15 nm, which was obtained by bonding at 170 psi and also gives a higher S/N ratio (Figure 4.2, 4.3 and 4.4). Previously, λ-DNA showed a single peak which had "shoulders" on either side as the DNA resides in one of the two pores. But in case of oligonucleotides of 35, 50 and 70 mer lengths, two distinct current drops or "peaks" will be obtained as the

contour length of the molecules are much shorter that it does not co-reside. Previous work from our group has shown that the mobility of the labelled oligonucleotides depend on the length of mer as they translocate through nanofluidic channels [51]. Here, we are approaching a label-less technique utilizing the same dual inplane nanopore PMMA device to distinguish between ssDNA of different lengths. This is particularly useful as the dual nanopore can be integrated into the nanosensor device used previously (Chapter 3), where the products of the spLDR reaction can be distinguished for the presence of the mutation based on the TOF (mobility) obtained as the oligonucleotides (the products that have the mutation and those that doesn't have the mutations have different lengths) translocate through the pore.

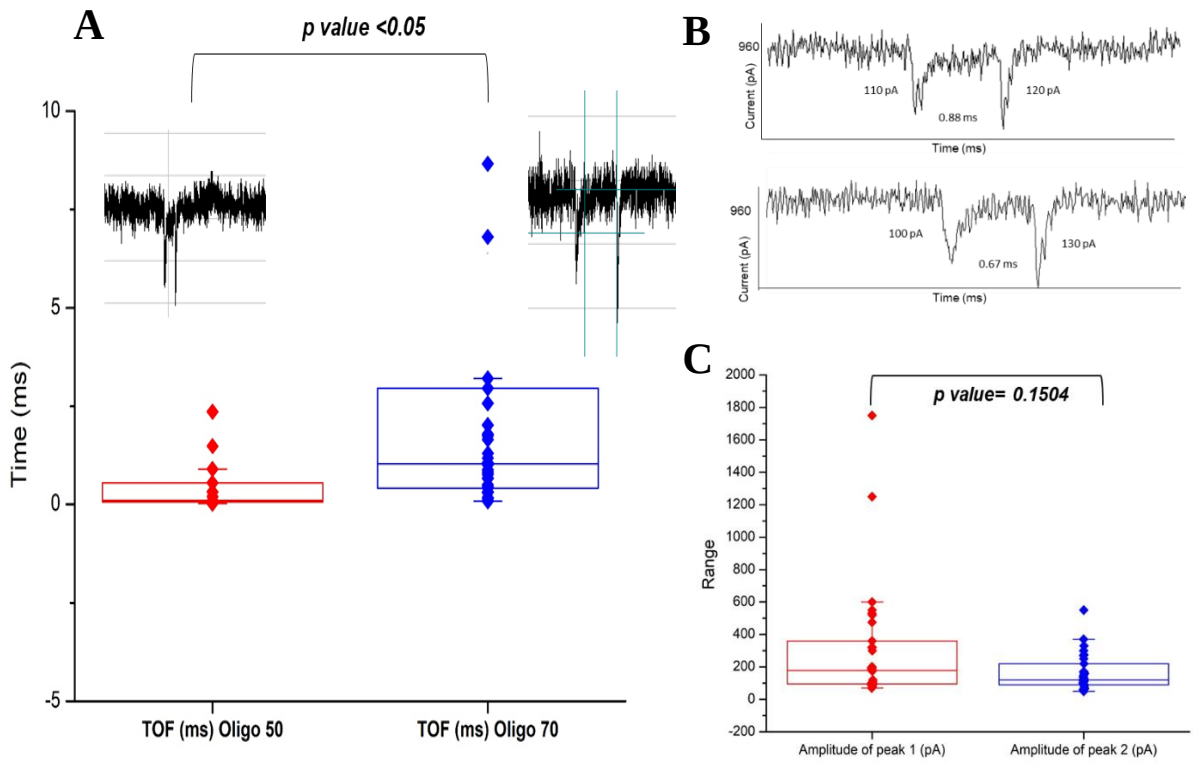

Figure 4.5 A) Different in time of flights between oligo 50 and oligo 70 as they translocate through the PMMA device. The mean TOF of the oligo 50 is 0.43 ms, while for oligo 70 the TOF is higher, i.e 1.48 ms. B) Representative traces of oligo 70 showing two peaks as they pass through the two nanopores placed in series, having TOF of 0.88 ms and 0.67 ms. C) The pulse amplitudes comparison of oligo 70 of peak 1 corresponding to the oligos as they pass through pore 1 and peak 2 corresponding to pore 2 show that there are no statistically significant differences between the amplitudes.

Oligo 50 and 70 were run through the dual nanopore PMMA devices driven at 1V DC bias by placing Pt electrodes on the reservoirs such that they make an ohmic contact. From figure 4.5-A it can be seen that there is statically significant difference between the time of flights (TOF) of both oligo 50 (0.43 ms) and 70, with oligo 70 having a higher TOF (1.48 ms). This means that the migration time is higher for when the length of ssDNA increases. The thermoplastic devices used here has been treated with O_2/plasma thus inducing a negative charge to the surface (-40.5 mC/m^2). We are using 1X TBE as the buffer, which has a pH of 8.3, which causes the carboxylic groups to deprotonate thus inducing an EOF, which makes the oligo travels towards the cathode. The oligos are ssDNA that expose their phosphodiester backbone or their nucleobases to the surface and interact via electrostatic interaction, Vander Waals force, hydrogen bonding and/or hydrophobic interactions. In the above case, the latter forces are assumed to be dominant that they overcome the electrostatic interactions arising from the negative charges in the wall and the solute and allow for hydrophobic interactions thus increasing the TOF as the length of the oligo increases.[52] Previous studies have proved that when the pH of the electrolyte is higher than the pK of the solution, the silanol (wall) /phosphate (DNA backbone) interactions are higher than the electrostatic interactions thus supporting the argument made above.[37] Figure 4.5-B shows representative traces of the current drops between the two in-plane pores having a TOF of 0.88 ms and 0.67 ms. The amplitudes of the peaks are in the range of 100-130 pA. Figure 4.5-C shows that there is no statistical difference in peak amplitudes between pore 1 and pore 2 for Oligo 70. This means that the TFB method to reduce the size of the pores have caused a consistent reduction in the size of the pores.

4.5 Conclusion

In this paper we have shown that the size of an in-plane nanopore can be controlled by TFB at different pressures using an assembly step already required for thermoplastic nanofluidic chip production. We noticed that the original size and shape of the in-plane nanopore changes with different bonding pressures as measured using AFM and SEM. Further, COMSOL simulations with varying pore widths gave the approximate conductance observed in the PMMA and COP dual in-plane nanopore devices connected using

a 5 μm long nanochannel. Further, λ-DNA was electrophoretically driven by a DC voltage through the dual nanopore devices bonded at 110, 170 and 200 psi. The transient current amplitudes were seen to increase with higher TFB pressures. Therefore, thermoplastic nanofluidic devices allow for tuning nanostructure size to accommodate a given application by simply altering device assembly conditions without requiring direct FIB milling of a new Si master. This was further demonstrated using oligonucleotides of 50 and 70 mer in length bonded at 170 psi. The difference in TOF between the oligonucleotides prove that they can be integrated along with the nanosensor motherboard to identify products of spLDR which is indicative of the presence of the mutation. Furthermore, the similarities in amplitudes of oligo 70 between the pores show that there is a uniform reduction in pore size by the TFB. It should be also noted that we could produce >20 resin stamps from a single Si master and from each resin stamp, >20 nanofluidic devices could be produced with a success rate in producing functional devices following TFB of the COC cover plate to the PMMA and/or COP substrates >90%.[37, 42-43]

4.6 References

1. Branton, D.; Deamer, D.; Marziali, A.; Bayley, H.; Benner, S.; Butler, T.; Di Ventra, M.; Garaj, S.; Hibbs, A.; Huang, X., Xinsheng Sean. *L., Mastrangelo, CH, Meller, A., Oliver, JS, Pershin, YV, Ramsey, JM, Riehn, R., Soni, GV, Tabard-Cossa, V., Wanunu, M., Wiggin, M., Schloss, JA: The potential and challenges of nanopore sequencing. Nat. Biotechnol* **2008,** *26* (10), 1146-1153.
2. Wanunu, M.; Sutin, J.; McNally, B.; Chow, A.; Meller, A., DNA translocation governed by interactions with solid-state nanopores. *Biophysical journal* **2008,** *95* (10), 4716-4725.
3. Dekker, C., Solid-state nanopores. *Nature nanotechnology* **2007,** *2* (4), 209-215.
4. Venkatesan, B. M.; Bashir, R., Nanopore sensors for nucleic acid analysis. *Nature nanotechnology* **2011,** *6* (10), 615-624.
5. Smeets, R. M.; Keyser, U. F.; Krapf, D.; Wu, M.-Y.; Dekker, N. H.; Dekker, C., Salt dependence of ion transport and DNA translocation through solid-state nanopores. *Nano letters* **2006,** *6* (1), 89-95.
6. Carlsen, A. T.; Zahid, O. K.; Ruzicka, J. A.; Taylor, E. W.; Hall, A. R., Selective detection and quantification of modified DNA with solid-state nanopores. *Nano letters* **2014,** *14* (10), 5488-5492.
7. Kowalczyk, S. W.; Hall, A. R.; Dekker, C., Detection of local protein structures along DNA using solid-state nanopores. *Nano letters* **2010,** *10* (1), 324-328.
8. Plesa, C.; Ruitenberg, J. W.; Witteveen, M. J.; Dekker, C., Detection of individual proteins bound along DNA using solid-state nanopores. *Nano letters* **2015,** *15* (5), 3153-3158.
9. Smeets, R.; Kowalczyk, S. W.; Hall, A.; Dekker, N.; Dekker, C., Translocation of RecA-coated double-stranded DNA through solid-state nanopores. *Nano letters* **2009,** *9* (9), 3089-3095.

10. Hornblower, B.; Coombs, A.; Whitaker, R. D.; Kolomeisky, A.; Picone, S. J.; Meller, A.; Akeson, M., Single-molecule analysis of DNA-protein complexes using nanopores. *Nature Methods* **2007,** *4* (4), 315-317.
11. Tabard-Cossa, V.; Wiggin, M.; Trivedi, D.; Jetha, N. N.; Dwyer, J. R.; Marziali, A., Single-molecule bonds characterized by solid-state nanopore force spectroscopy. *ACS nano* **2009,** *3* (10), 3009-3014.
12. Cherf, G. M.; Lieberman, K. R.; Rashid, H.; Lam, C. E.; Karplus, K.; Akeson, M., Automated forward and reverse ratcheting of DNA in a nanopore at 5-Å precision. *Nature biotechnology* **2012,** *30* (4), 344-348.
13. Ricroch, A. E., Assessment of GE food safety using '-omics' techniques and long-term animal feeding studies. *New biotechnology* **2013,** *30* (4), 349-354.
14. Song, L.; Hobaugh, M. R.; Shustak, C.; Cheley, S.; Bayley, H.; Gouaux, J. E., Structure of staphylococcal α-hemolysin, a heptameric transmembrane pore. *Science* **1996,** *274* (5294), 1859-1865.
15. Faller, M.; Niederweis, M.; Schulz, G. E., The structure of a mycobacterial outer-membrane channel. *Science* **2004,** *303* (5661), 1189-1192.
16. ávan Loo, N., DNA nanopore translocation in glutamate solutions. *Nanoscale* **2015,** *7* (32), 13605-13609.
17. Storm, A.; Chen, J.; Ling, X.; Zandbergen, H.; Dekker, C., Fabrication of solid-state nanopores with single-nanometre precision. *Nature materials* **2003,** *2* (8), 537-540.
18. Li, J.; Stein, D.; McMullan, C.; Branton, D.; Aziz, M. J.; Golovchenko, J. A., Ion-beam sculpting at nanometre length scales. *Nature* **2001,** *412* (6843), 166-169.
19. Wanunu, M.; Meller, A., Chemically modified solid-state nanopores. *Nano letters* **2007,** *7* (6), 1580-1585.
20. Gierak, J.; Madouri, A.; Biance, A.; Bourhis, E.; Patriarche, G.; Ulysse, C.; Lucot, D.; Lafosse, X.; Auvray, L.; Bruchhaus, L., Sub-5 nm FIB direct patterning of nanodevices. *Microelectronic engineering* **2007,** *84* (5-8), 779-783.
21. Yang, J.; Ferranti, D. C.; Stern, L. A.; Sanford, C. A.; Huang, J.; Ren, Z.; Qin, L.-C.; Hall, A. R., Rapid and precise scanning helium ion microscope milling of solid-state nanopores for biomolecule detection. *Nanotechnology* **2011,** *22* (28), 285310.
22. Kwok, H.; Briggs, K.; Tabard-Cossa, V., Nanopore fabrication by controlled dielectric breakdown. *PloS one* **2014,** *9* (3), e92880.
23. Stein, D. M.; McMullan, C. J.; Li, J.; Golovchenko, J. A., Feedback-controlled ion beam sculpting apparatus. *Review of Scientific Instruments* **2004,** *75* (4), 900-905.
24. Asghar, W.; Ilyas, A.; Billo, J. A.; Iqbal, S. M., Shrinking of solid-state nanopores by direct thermal heating. *Nanoscale research letters* **2011,** *6* (1), 372.
25. Schiedt, B.; Auvray, L.; Bacri, L.; Oukhaled, G.; Madouri, A.; Bourhis, E.; Patriarche, G.; Pelta, J.; Jede, R.; Gierak, J., Direct FIB fabrication and integration of "single nanopore devices" for the manipulation of macromolecules. *Microelectronic engineering* **2010,** *87* (5-8), 1300-1303.
26. Harms, Z. D.; Haywood, D. G.; Kneller, A. R.; Selzer, L.; Zlotnick, A.; Jacobson, S. C., Single-particle electrophoresis in nanochannels. *Analytical chemistry* **2015,** *87* (1), 699-705.
27. Henley, W. H.; Dennis, P. J.; Ramsey, J. M., Fabrication of microfluidic devices containing patterned microwell arrays. *Analytical chemistry* **2012,** *84* (3), 1776-1780.
28. Menard, L. D.; Ramsey, J. M., Fabrication of sub-5 nm nanochannels in insulating substrates using focused ion beam milling. *Nano letters* **2011,** *11* (2), 512-517.
29. Kondylis, P.; Zhou, J.; Harms, Z. D.; Kneller, A. R.; Lee, L. S.; Zlotnick, A.; Jacobson, S. C., Nanofluidic Devices with 8 Pores in Series for Real-Time, Resistive-Pulse Analysis of Hepatitis B Virus Capsid Assembly. *Analytical Chemistry* **2017,** *89*, 4855-4862.
30. Harms, Z. D.; Mogensen, K. B.; Nunes, P. S.; Zhou, K.; Hildenbrand, B. W.; Mitra, I.; Tan, Z.; Zlotnick, A.; Kutter, J. P.; Jacobson, S. C., Nanofluidic Devices with Two Pores in Series for Resistive-Pulse Sensing of Single Virus Capsids. *Analytical Chemistry* **2011,** *83*, 9573-9578.

31. Harms, Z. D.; Selzer, L.; Zlotnick, A.; Jacobson, S. C., Monitoring Assembly of Virus Capsids with Nanofluidic Devices. *ACS Nano* **2015,** *9*, 9087-9096.
32. Zhou, K.; Li, L.; Tan, Z.; Zlotnick, A.; Jacobson, S. C., Characterization of Hepatitis B Virus Capsids by Resistive-Pulse Sensing. *Journal of the American Chemical Society* **2011,** *133*, 1618-1621.
33. Chantiwas, R.; Park, S.; Soper, S. A.; Kim, B. C.; Takayama, S.; Sunkara, V.; Hwang, H.; Cho, Y.-K., Flexible fabrication and applications of polymer nanochannels and nanoslits. *Chemical Society Reviews* **2011,** *40* (7), 3677-3702.
34. Choi, J.; Lee, C. C.; Park, S., Scalable fabrication of sub-10 nm polymer nanopores for DNA analysis. *Microsystems & nanoengineering* **2019,** *5* (1), 1-10.
35. O'Neil, C. E.; Taylor, S.; Ratnayake, K.; Pullagurla, S.; Singh, V.; Soper, S. A., Characterization of activated cyclic olefin copolymer: effects of ethylene/norbornene content on the physiochemical properties. *Analyst* **2016,** *141* (24), 6521-6532.
36. Jia, Z.; Choi, J.; Park, S., Surface Charge Density-Dependent DNA Capture through Polymer Planar Nanopores. *ACS applied materials & interfaces* **2018,** *10* (47), 40927-40937.
37. Uba, F. I.; Hu, B.; Weerakoon-Ratnayake, K.; Oliver-Calixte, N.; Soper, S. A., High process yield rates of thermoplastic nanofluidic devices using a hybrid thermal assembly technique. *Lab on a Chip* **2015,** *15* (4), 1038-1049.
38. Wang, Y.; Liang, X.; Liang, Y.; Chou, S. Y., Sub-10-nm wide trench, line, and hole fabrication using pressed self-perfection. *Nano letters* **2008,** *8* (7), 1986-1990.
39. Choi, J.; Farshchian, B.; Kim, J.; Park, S., Fabrication of perforated micro/nanopore membranes via a combination of nanoimprint lithography and pressed self-perfection process for size reduction. *Journal of Nanoscience and Nanotechnology* **2013,** *13* (6), 4129-4133.
40. Choi, J.; Lee, C. C.; Park, S., Scalable fabrication of sub-10 nm polymer nanopores for DNA analysis. *Microsystems & Nanoengineering* **2019,** *5* (1), 12.
41. Jackson, J. M.; Witek, M. A.; Hupert, M. L.; Brady, C.; Pullagurla, S.; Kamande, J.; Aufforth, R. D.; Tignanelli, C. J.; Torphy, R. J.; Yeh, J. J., UV activation of polymeric high aspect ratio microstructures: ramifications in antibody surface loading for circulating tumor cell selection. *Lab on a Chip* **2014,** *14* (1), 106-117.
42. Chantiwas, R.; Park, S.; Soper, S. A.; Kim, B. C.; Takayama, S.; Sunkara, V.; Hwang, H.; Cho, Y. K., Flexible fabrication and applications of polymer nanochannels and nanoslits. *Chemical Society Reviews* **2011,** *40* (7), 3677-3702.
43. Wu, J. H.; Chantiwas, R.; Amirsadeghi, A.; Soper, S. A.; Park, S., Complete plastic nanofluidic devices for DNA analysis via direct imprinting with polymer stamps. *Lab on a Chip* **2011,** *11* (17), 2984-2989.
44. Jia, Z.; Choi, J.; Park, S., Selection of UV-resins for nanostructured molds for thermal-NIL. *Nanotechnology* **2018,** *29* (36), 365302.
45. Miller, A.; Lawton, E.; Balwit, J., Effect of chemical structure of vinyl polymers on crosslinking and degradation by ionizing radiation. *JPoSc* **1954,** *14* (77), 503-504.
46. Mahmood Raouf, R.; Abdul Wahab, Z.; Azowa Ibrahim, N.; Abidin Talib, Z.; Chieng, B. W., Transparent blend of poly (methylmethacrylate)/cellulose acetate butyrate for the protection from ultraviolet. *Polymers* **2016,** *8* (4), 128.
47. Dole, M., *The Radiation Chemistry of Macromolecules: Volume II*. Elsevier: 2013; Vol. 2.
48. Jeong, J. H.; Choi, Y. S.; Shin, Y. J.; Lee, J. J.; Park, K. T.; Lee, E. S.; Lee, S. R., Flow behavior at the embossing stage of nanoimprint lithography. *Fibers and Polymers* **2002,** *3* (3), 113-119.
49. Heyderman, L. J.; Schift, H.; David, C.; Gobrecht, J.; Schweizer, T., Flow behaviour of thin polymer films used for hot embossing lithography. *Microelectronic Engineering* **2000,** *54* (3-4), 229-245.

50. Fryer, D. S.; Peters, R. D.; Kim, E. J.; Tomaszewski, J. E.; de Pablo, J. J.; Nealey, P. F.; White, C. C.; Wu, W.-l., Dependence of the Glass Transition Temperature of Polymer Films on Interfacial Energy and Thickness. *Macromolecules* **2001,** *34* (16), 5627-5634.
51. Ramakers, C.; Ruijter, J. M.; Deprez, R. H.; Moorman, A. F., Assumption-free analysis of quantitative real-time polymerase chain reaction (PCR) data. *Neuroscience letters* **2003,** *339* (1), 62-6.
52. Wu, J.; Wang, H.; Zhu, A.; Long, F., Adsorption Kinetics of Single-Stranded DNA on Functional Silica Surfaces and Its Influence Factors: An Evanescent-Wave Biosensor Study. *ACS Omega* **2018,** *3* (5), 5605-5614.

Chapter 5: Nano-coulter counter for detection of SARS CoV-2 Viral Particles

5.1 Abstract

Coronavirus disease 2019 (COVID-19) arises from the SARS-CoV-2 virus and has been found to be highly contagious. To mitigate spreading, testing has been deemed an important asset. Testing has predominately utilized RT-qPCR or serological-based methods. While new machines are rolling out for point-of-care testing (POCT), issues are present with the aforementioned technologies, for example the need for reagents (e.g. enzymes, fluorescent reporters, antibodies), workflows that sometimes require specialized operators, and the inability to distinguish between infectious and non-infectious individuals, which is important in determining the time for quarantining. We report an innovative COVID-19 technology that directly addresses the aforementioned issues. The technology specifically selects active SARS-CoV-2 particles from a clinical sample using surface-immobilized DNA aptamers targeting the spike protein, releases photolytically the selected viral particles (VPs), and counts the number of SARS-CoV-2 particles using a label-free approach; resistive pulse sensing (RPS). The workflow is simple and fully automated and also, no reagents are required once the technology is deployed. Sample processing is carried out using microfluidic chips made from a plastic that are injection molded to allow for high scale production at low cost. The VP selection chip consists of 1.5 million pillars that allows for affinity loading ~10^{10} SARS-CoV-2 particles at a recovery of 94.3%. Following selection, the VPs are released from the capture surface using a photocleavable linker by a blue-light LED (89% release efficiency) and subsequently counted using a nano-Coulter Counter (nCC) via RPS. In this chapter, we will specifically discuss the nCC, which is used to detect the presence of SARS CoV-2 viral particles after isolation. For high throughput single VP counting, 5 nCCs were placed in parallel and offered high detection efficiency for single VPs travelling through 350 nm pores. Multiple iterations of the nCC design will be discussed along with COMSOL simulations and fabrication of the nCC design used for counting VPs from SARS CoV-2 standards. The entire nCC sample processing could be completed in <10 min. A calibration curve based on clinically relevant concentrations was built to correlate the number of events observed to the concentration of the

viral load, which gave us a limit of detection (LOD) of 2,500 particles/mL. This will help us determine the viral load in clinical samples thus proving its capability as a preliminary diagnostic tool to diagnose COVID-19.

5.2 Introduction

The severe acute respiratory syndrome coronavirus 2 (SARS-CoV-2) causing coronavirus disease of 2019 (COVID-19) has been found to be highly contagious resulting in community-based quarantines. Since its discovery in late 2019, COVID-19 has resulted in >59 M cases globally (daily reporting rate of new cases ~809 in January 27, 2020 and ~671,885 on November 27, 2020) and ~1.5 M deaths in a span of 12 months (https://coronavirus.jhu.edu/map.html). For comparison, in 2002-2003, the severe acute respiratory syndrome (SARS-CoV; beta-CoV subtype) resulted in ~8,000 infections with 774 deaths, and the Middle East respiratory syndrome (MERS-CoV) in 2012 produced 2,494 cases with 858 deaths.[2] Other human coronaviruses (HCoVs), such as HCoV-NL63, HCoV-229E, HCoV-OC43, HCoV-HKU1, SARS-CoV and MERS-CoV,[3] have been implicated in 5-10% of acute respiratory infections globally with an estimated 2% of the population classified as being carriers of these viruses,[4] but cause only mild respiratory infections.[5]

HCoVs are a family of enveloped viruses with a size of ~150 nm in diameter[6-8] and consist of a single, positive strand RNA genome.[9-10] These viruses were discovered in the 1960s and their genome ranges in size from 27 – 34 kb and phylogenetic clustering has determined various subtypes.[11] SARS-CoV-2 is the seventh coronavirus known to cause infections in humans and its RNA genome encodes 10 genes that produce 26 proteins,[12] including: (i) Spike (S); (ii) nucleocapsid (N); (iii) envelope (E); and (iv) membrane (M) proteins.[13] The S protein plays an important role in binding to ACE2 (angiotensin converting enzyme 2) receptors and subsequent viral entry into a host cell. The N protein is important for RNA synthesis, and the E and M proteins are transmembrane proteins necessary for the assembly, budding, and envelope formation of the virus.[14-15]

Testing has been viewed as an important tool for the control of disease spreading. Common tests for COVID-19 include molecular tests that interrogate the RNA genome of SARS-CoV-2, which requires RNA

extraction and purification, reverse transcription (RT) to generate complementary DNA (cDNA) from target genes (viral N, E, and S with human RNA dependent RNA polymerase (RdRp) as a control), amplification by the polymerase chain reaction (PCR), and reading a fluorescent signal. In fact, the first reported case of COVID-19 in the U.S. appeared in Snohomish County in Washington state and was diagnosed using RT-qPCR on January 20, 2020 after the patient had returned to the U.S. on January 15, 2020 from Wuhan, China.[16] However, it was not until approximately March 1, 2020 that large scale testing in the U.S. commenced with the challenge for scale up associated with securing sufficient supplies required for RT-qPCR such as swabs and sensitive reagents (*i.e.*, enzymes, primers, and fluorescent reporters). RT-qPCR requires sensitive and in some cases costly reagents, such as enzymes and fluorescent reporters.[17] Other challenges include errors in sample collection, variability between different commercially-available extraction kits of RNA, and PCR inhibitors in the sample.[17]

To address some of the challenges associated with RT-qPCR, rapid serological tests, either antibody- or antigen-based, have appeared. These tests can target the S or N proteins.[18-20] Cartridge-based lateral flow assays have received FDA approval through an EUA.[17, 21-23] As of November 13, 2020, FDA has approved more than 50 antibody tests.[24] However, antibody tests have inferior limits-of-detection compared to RT-qPCR and increased false negative results.[25-26] In addition, these tests do require sensitive reagents, such as antibodies and/or fluorescent reporters.

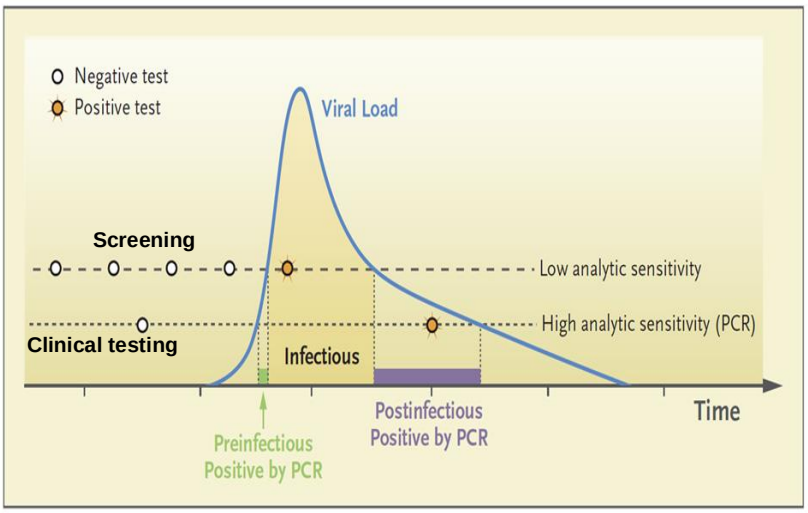

Figure 5.1 Hypothetical viral load as a function of disease progression and different testing strategies. Taken from Ref. (18).

The identification of infected individuals, even those that are asymptomatic, is necessary to prevent disease spreading, especially within vulnerable

populations.[27] Different types of testing needs (*i.e.*, screening versus clinical) are being recognized for monitoring COVID-19 in communities. A screening test, especially those that are simple enough to be carried out at home, would allow for early detection of individuals so that prompt quarantine procedures could be implemented to facilitate containment (Figure 5.1). Whether screening or clinical testing, no test currently available can distinguish between infectious and non-infectious individuals. Those that are infectious are considered to be "active" spreaders of viral particles (VPs). As seen in Figure 5.1, there are certain times during the viral load profile where individuals are infectious and PCR-based tests may provide a positive result on even post-infectious individuals because it cannot distinguish between genomic RNA encapsulated within the VP and free RNA resulting from RNA shedding. In addition, serological tests only inform the individual that infection did occur. To provide some numbers with the temporal dynamics of viral load for SARS-CoV-2, He *et al.* determined that in 94 patients, infectivity started 12.3 days (mean) before symptom onset, but declined rapidly 7 days after symptom onset and peaked 2 days before and 1 day after symptom onset.[28]

Affinity selection of biologicals offer attractive operational characteristics including the ability to specifically select targets with high purity from a variety of biological samples. Monoclonal antibodies are most often used for affinity selection of targets. However, some antibodies generated for SARS-CoV (*i.e.*, mAb CR3022 and pAb) bind SARS-CoV-2 with moderate affinity resulting in low specificity.[29] Other antibody clones directed against the SARS-CoV receptor-binding domain (RBD) do not bind SARS-CoV-2 at all, despite relatively high degrees of structural RBD homology.[30] Aptamers are viewed as an attractive alternative to antibodies due to their ease of selection, high stability even at room temperature, and the ability to place functional groups within their structures for surface attachment. A DNA aptamer targeting the S protein in the SARS-CoV-2 viral envelope has been reported (K_d = 5.8 nM).[31]

In this chapter, we report a technology for COVID-19 testing that is rapid, reagent-free, low cost, and label free. The technology is highly innovative and is based on the affinity-selection of VPs directly from a clinical sample followed by the label-free counting of the selected VPs. The technology uses a microfluidic to: (i) Specifically select SARS-CoV-2 VPs from a clinical sample using a surface-bound

aptamer directed against the ACE2 receptor binding domain of the S protein poised within a plastic chip containing 1.5 M pillars (VP selection chip); (ii) photo-release of the selected VPs using blue light;[32] and (iii) counting the selected VPs using an on-chip nCC. The nCC consists of a narrow constriction (~350 nm) that could electrically detect single VPs passing through an in-plane pore via RPS.[33-34] Unique to this device was the ability to place 5 pores in parallel to increase sampling throughput to reduce processing time. The chips were fabricated in thermoplastics so that they could be produced in a high production mode and at low-cost using replication-based techniques, such as injection molding. They can detect particles even under extremely low concentrations (~ 10^3 particles/ml) in a short time span of 5 mins, and based on the number of peaks detected, the concentration of the viral load can be detected. However, this label-free detection technique cannot distinguish between the types of particles; rather it detects every component that passes through the pore. Hence, an affinity based selection method is required to isolate the specific type of particles/cells that are required to be detected. Collectively, the technology was used to determine the presence of SARS-CoV-2 in a sample in <20 min. Because the technology results were based on detecting VPs possessing an intact S protein, our technology can provide information on patients with *active disease* and with frequent testing, provide early containment minimizing community spread of COVID-19. Finally, the selected and released SARS-CoV-2 VPs could also be subjected to RT-qPCR for confirm the results from the nCC particle enumeration. Since this chapter focused specifically on nCC using the RPS technology, in the subsequent section we will focus on how RPS technology has been used for other applications such as nucleic acid and protein sensing, nanoparticle characterization and so on.

5.3 Evolution of resistive pulse sensing

Resistive Pulse Sensing (RPS) dates back to the 1940's and was used primarily to count biological cells. RPS is based on the principle that a conductive solution filled in two reservoirs separated by a narrow pore with a DC potential applied to drive the particles into through pore will result in a transient perturbation of the conductance of the pore.[35-37] The transient perturbation results in an ionic current blockage event, which generates a detectable "peak". In some cases, the particle may be more conductive than the medium causing

the current to increase, thus forming positive peaks. The magnitude and width of the peak is used to determine the size of the particle, while the number of events in a specific interval of time is used to determine the concentration of the sample.[38-40] The size of the pore can be manipulated to determine the range of particle size that can be transduced and can range from particle size of micrometers to a few tens of nanometers.[41]

In the 1990's, this technique was revolutionized by using biological nanopores including α-haemolysin to detect single DNA molecules.[42] The ultrasmall size of the pore, which was 1.4 nm, allowed for the detection of individual molecules. Further, solid state nanopores such as PDMS, silicon, glass, and graphene have been used to fabricate pores of different sizes (Figure 5.2). In this chapter, we used thermoplastics to fabricate nanopores of ~350 nm in effective diameter to detect single viral particles (VPs) with an average size of ~150 nm.

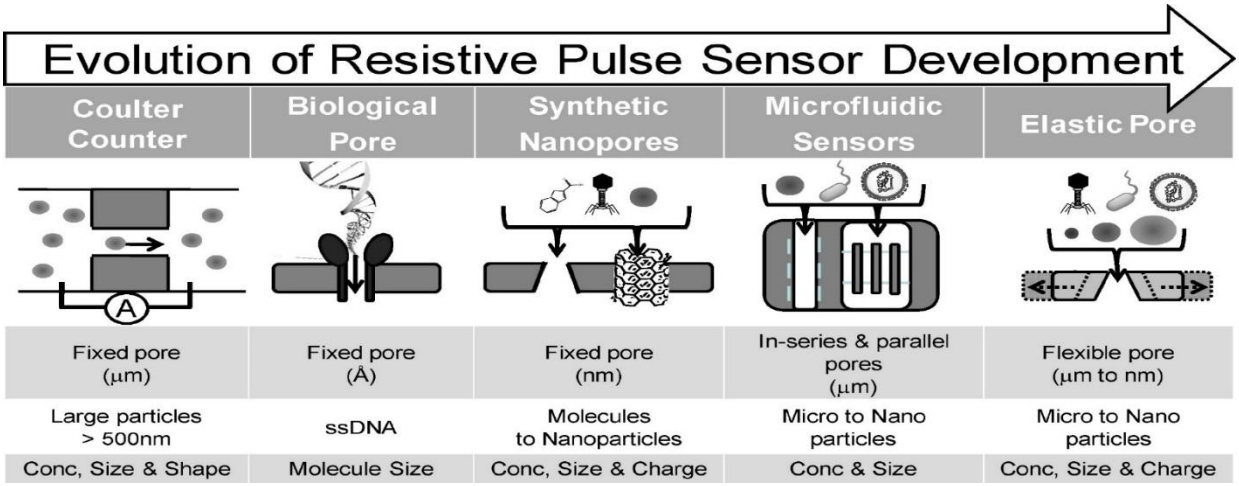

Figure 5.2 The evolution of the RPS development through the years is described. The RPS technology started off with detecting microparticles, eventually leading to single molecule detection. Biological nanopores such as α-hemolysin nanopores to detect ssDNA. Synthetic nanopores having a fixed pore size were used to detect nanoparticles and estimate the concentration, size and even the charge. Microfluidic sensors offer electrical, hydrodynamic focusing to detect particles. Elastic nanopores offer tunable pores that can be stretched to suit the detection conditions [1].

Apart from viral particles, some important applications of RPS include the detection of DNA, proteins, and characterization of nanoparticles. As an example, a report used a nanopore to evaluate the binding of thrombin to DNA coated magnetic beads.[43-44] Further, amplification was adopted by Yang[45] and Kuhnemund[46] to increase the differences in small DNA's by adsorption. The target DNA, padlock probes,

and oligonucleotides were captured by magnetic particles and RPS was utilized to measure the signal. Traversi *et al.* used graphene and SiNx nanopores to measure the electrokinetic behavior of λ-DNA and pNEB DNA.[47] The thickness of graphene can be as small as 0.0335 nm, which is comparable to the distance between two nucleotides in DNA thus showing a promising ability for DNA sequencing.

Detection of proteins have been possible using RPS as well. Rodriguez-Trujilloa *et al.*[48] measured protein concentrations in a suspension using a microfluidic device. IgG serum and polystyrene beads were mixed to form functionalized bead oligomers. The target proteins could be detected when the beads were functionalized, which generated a larger current drop. Furthermore, a cancer biomarker,[49] human ferritin,[50] and other single molecules[51] were also detected using RPS.

Sensing of nanoparticles using nano-RPS is very useful for determining the size, concentration, surface charge, and even the translocation behavior of those particles. An RPS sensing device was fabricated by placing a tunable elastomeric membrane made of polyurethane on a q-Nano device.[52] This way, different pore sizes were obtained by stretching the membrane, which showed that particles of different sizes, such as adenovirus and polystyrene beads, could be evaluated. This was extended to evaluate the concentrations of marine photosynthetic cyanobacterium Prochlorococcus, which has a size of ~600 nm.[53] PDMS sensors were utilized to estimate the concentration of bacteriophage T7 and a nanoparticle suspension of mouse plasma, which gave high throughput sensing of 50,000 particles per second.[54] This led the authors to conclude the presence of some naturally occurring nanoparticles in blood plasma.

Apart from nanoparticle sensing, some researchers have determined the zeta potential of nanoparticles using the RPS technique.[55-57] The critical pressure at which all forces, namely the pressure driven drag force, the electroosmotic force, and the electrokinetic force acting on the particle become balanced so the frequency of the signal was minimized and estimated to calculate the electrophoretic mobility. Using this principle, Eldridge *et al.* calculated the zeta potential of polystyrene particles[58] and Somerville *et al.* calculated the zeta potential of a water-in-oil emulsion.[59] Recently, researchers have also investigated the zeta potential of DNA modified particles, changes in base lengths in ssDNA and dsDNA with high resolution and sensitivity.[60]

5.4 Analysis of viral particles using RPS techniques

Viruses have become popular in recent years as their role in virology, clinical diagnosis, immunology, and therapeutics continues to increase. Hence quantification of viral particles by their size and concentration load has become important to determine their infectivity and for subsequently developing suitable therapeutics.[61] Various limitations of traditional enumeration techniques such as electron microscopy, immunological, and infectious titer assays have made enumeration challenging.[62] For example, viruses have been quantified using antigen-antibody assays, RT-qPCR to determine viral copy numbers, and flow cytometry to identify viral particles via stained proteins unique to a particular particle type. Despite offering high specificity, the aforementioned techniques can be time consuming with complicated workflows. Current nanoparticle sensing can be performed visually with techniques such as TEM that can determine the particle size, shape, and concentration. But, TEM is expensive, labor intensive with extensive sample preparation, and the requirement of highly trained operators.[63] Techniques such as dynamic light scattering (DLS)[64] and nanoparticle tracking analysis (NTA)[65] measure particle size through light scattering or Stokes-Einstein radius of particles undergoing Brownian motion, respectively. But, these techniques have low resolution and sensitivity generated by ensemble detection and overestimation of the size and concentration of particles compared to TEM. The development of nanotechnology and nanostructured electrical sensors have emerged as a real-time platform for sensitive bioanalyte detection. Viral particles dimensionally range from tens to hundreds of nanometers in size. Hence, RPS techniques can be used to enumerate and size single nanoparticles.

RPS uses an electrolyte filled in the apparatus with electrodes placed on either side of the pore. On application of a potential across the pore, an electric current is generated due to the flux of ions moving through the pore where the electrical resistance is high and the large electric field drop across the pore. When an analyte moves through the pore, it causes a transient increase in resistance which causes a drop in current. Depending on the size of the particle the change in resistance as a spherical particle passes through a cylindrical orifice is given by the following equations:[31]

Equation 5.1 Infinitely small diameter particle: $\frac{\Delta R}{R} = \frac{d^3}{D^2 L}$

Equation 5.2 Small diameter: $\frac{\Delta R}{R} = \frac{d^3}{D^2 L}\left[\frac{D^2}{2L^2} + \frac{1}{\sqrt{\left(1+\left(\frac{D}{L}\right)^2\right)}}\right] F\left(\frac{d^3}{D^3}\right)$

Equation 5.3 Medium diameter: $\frac{\Delta R}{R} = \frac{d^3}{D^2 L} \cdot \frac{1}{1-0.8\left(\frac{d}{D}\right)^3}$

Equation 5.4 Large diameter: $\frac{\Delta R}{R} = \frac{D}{L}\left[\frac{\arcsin\left(\frac{d}{D}\right)}{\sqrt{\left(1-\left(\frac{d}{D}\right)^2\right)}} - \frac{d}{D}\right]$

where D and L are the diameter and length of the sensing orifice, d is the diameter of the particle, and $F(x) = 1 + 1.264x + 1.347x^2 + 0.648x^3 + 4.167x^4$. The equations mentioned above use particles and sensing orifices of different sizes. The small diameter equation represents d ranging from 60 nm-357 nm with a D of 490 nm. The D*, which is defined as (d/D) ranges from 0.122-0.728 in this case.[66] In case of the medium diameter, the particles typically used were 91nm and 109 nm in orifices of 324 nm and 252 nm giving a D* of 0.34 and 0.36 respectively.[67-68] However, the larger diameter equations were developed when 2.5 cm disks were sensed using 5 cm orifice (D* = 0.5). The lowest size they could detect was 0.15 cm latex beads in the 5 cm orifice. [67]

5.4.1 Types of RPS Detectors

The circuitry required for RPS detectors include Ag/AgCl electrodes, a current amplifier, filter system, and data acquisition software. Nanopores can vary by size, shape, material, and geometry. Biological nanopores typically consist of proteins embedded in a lipid bilayer but are restricted in size (<5 nm) and lack robustness making them unsuitable for viral particle detection.[69-70] Synthetic nanopores are an attractive alternative because their size, shape, and material can be carefully controlled to create either a cylindrical shape generating a symmetrical pulse or conical shaped pores that generate asymmetrical pulses.[71] There are two main types of synthetic nanopores: (1) Out-of-plane and in-plane RPS sensors. Out-of-plane nanopores are typically configured perpendicular to the surface. In plane sensors are parallel to the surface and are inbuilt with the fluidic chamber.

Nanopores for viral particle detection were initiated in 1977 using polycarbonate pores with sub-micron diameters to measure the size of type C coronaviruses[72]. Further, Uram *et al*. used a conical nanopore of 650 nm fabricated in a glass substrate to investigate the interactions between Paramecium bursaria chlorella virus (diameter ~190 nm) and specific antibody.[73] Zhou *et al*. used a 40 nm conical nanopore (surface was modified with triethylene glycol to reduce non-specific adsorption and electroosmotic flow (EOF)) track-etched in a poly(ethylene terephthalate) membrane to identify hepatitis B virus (HBV).[74] Arjmandi *et al*.[57, 75] fabricated 20-500 nm pores on a silicon membrane to detect human immunodeficiency virus and Epstein-Barr virus. McMullen *et al*. used TEM drilled nanopores of 12-50 nm to identify rod shaped viruses[76] and Wu *et al.* used similar nanopores to monitor translocation of tobacco mosaic virus.[77] These solid state pores discussed above were all single nanopores fabricated in glass, silicon or silicon nitride with fixed dimensions and consisted of out-of-plane senssors.

Tunable resistive-pulse sensing (TRPS) gained some popularity due to their ability to detect polydispersed samples by adjusting the size. These were first developed and commercialized by Izon Science Ltd. (Christchurch, New Zealand), where pores were fabricated using polyurethane membranes that could be stretched in a reversible and biaxial manner. qNano and qViro-X are the commercially-available variants that are integrated with support electronics. Additionally, qNano has a pressure sensor that can push or hinder the particle from moving across the pore to optimize the rate of translocation. qNano pores were used by Vogel *et al.* to determine the size of adenoviruses (70-90 nm)[56], Farkas *et al.* counted rotavirus (75 nm)[78] and Akpinar and Yin enumerated vesicular stomatitis virus (70 × 200 nm) using a combination of a plaque assay and TRPS.[79] These pores are out-of-plane sensors as well.

In-plane nanopores are advantageous over out-of-plane formats of these sensors as the nanopores are integrated into the fluid network facilitating the ease of fabrication, lower sample volume consumption, enhanced portability, and increased sample transfer of analytes to the pores. Harms *et al.* fabricated two nanopores in series on silicon and evaluated the electrophoretic mobility of HBV capsids based on the time of translocation between the two pores.[80] Fraikin *et al.* reported on a nanoparticle analyzer to detect T7 bacteriophage and utilized hydraulic flow to direct the sample into the nano-constriction. The device was

made in a PDMS substrate sealed with a glass plate with patterned gold electrodes.[54] Jiang Zhe *et al.* fabricated 4 microchannels in parallel in PDMS connected by a common inlet possessing an electrode as well as 4 central electrodes specific to each microchannel patterned on a glass cover plate to enumerate polymethylmethacrylate (PMMA) and juniper pollen particles in a high throughput fashion.[81] However, the number of studies focused on the use of parallel and series nanopores are sparse and no study to the author's knowledge used thermoplastics to fabricate in-plane nanopores. The techniques utilized to sense various viral particles using the different type of sensors that were mentioned above are summarized in a table below to provide a comparison of how our in-plane nCC compares to the existing approaches (Table 5.1).

Table 5.1 Figures-of-merit for RPS sensors for the detection of nanoparticles, including virus particles.

Example	Type of Sensor	Material	Fabrication Method	Pore Size	Limit-of-detection	Number of Sensing Pores	Size Range of Particles Detected
Arjmandi et al. [57, 75]	Out of plane	Silicon	Electron beam lithography (EBL)	20–500 nm	10^9 to 10^{10}/mL; 1mM to 3 mM (ionic concentration)	1	20-200 nm
Uram et al. [73]	Out of plane	Borosilicate cover glass	Femtosecond-pulsed laser	650 nm	5×10^7/mL	1	190 nm
Zhou et al. [74]	Out of plane	Poly (ethylene terephthalate) (PET)	Track etching	40 nm	N/A	1	31-36 nm
McMullen et al. [76]	Out of plane	Si_3N_4	TEM-drilled	12–50 nm	0.02 mg/ml (ionic concentration)	1	Rod shaped virus- 880 nm long and 6.6 nm in dia
Fraikin et al. [54] (spectradyne)	In-plane	PDMS	Optical Lithography, micromoulding	200-500 nm	1×10^8 /ml	1	40-130 nm
Harms et al. [80]	In-plane	Silicon	EBL, Reactive Ion Etching	50 nm	N/A	2 pores in series	36 nm
Our Design	**In-plane**	***COP***	***NIL***	***350 nm***	***2,500 /mL***	***5***	***40 – 350 nm***

In our study, we have used 5 nanopores (~350 nm effective diameter each) in parallel fabricated in-plane using cyclic olefin polymer (COP). We utilized photolithography to fabricate the inlet/outlet microchannels and the nanopores (nCC) connected to the microchannels were fabricated using focused ion beam milling (FIB). These structures were fabricated into Si, which as used as a mold master. The features

from the Si mold master were then transferred to COP using nanoimprint lithography (NIL). The fabrication technique is simple, cheap and the use of thermoplastics facilitates high throughput production.

Our goal was to detect SARS CoV-2 viral particles having a diameter of ~150 nm using a nCC. We initially started by using a single nanopore, but due to its poor limit-of-detection and sampling efficiency, we opted for a nCC that possessed 5 nanopores in parallel to increase the sampling efficiency to allow for detection of particles even at low concentrations that are typically not possible using existing RPS techniques. We tested the performance and fluid dynamics of various iterative designs using COMSOL simulations and conducted measurements using polystyrene beads to verify our simulation results. Furthermore, a calibration curve was built for the optimal design iteration by electrically sensing the number of signals (or peaks) versus concentration of the viral particles. These parameters were correlated to the results obtained from nanoparticle tracking analysis (NTA) for the SARS CoV-2 particles.

5.5 Materials and Methods

5.5.1 Overall experimental set up with current amplifier circuitry

Iterations 1-3: About 5 µl of sample is filled on the inlet microchannel and a drop of sample is placed on either ends of the reservoir. The outlet channel is filled with 1X PBS as the buffer. One end of the outlet is sealed with epoxy, while the other end is connected to a syringe pump that withdraws fluid at 20 µl/min. A potential of -1V using Ag/AgCl electrodes is placed on the sample side, while the outlet is placed at earth ground. A sampling frequency of 100 KHz is set and the Axopatch 200 B is used to apply the DC bias, and data is recorded using Clampfit 10.6.

Iteration 4: Approximately 5 µl of sample was placed in the inlet microchannel. The outlets were filled with 1X PBS. The outlets were also connected using a T-shaped connector that led to a vacuum pump used for withdrawal. A syringe pump was used to inject sample at a specified flow rate to one end of the inlets, while a small drop of solution was placed at the other inlet. The current trace recordings from the nCC were carried out with a custom made current amplifier, which consisted of a transimpedance amplifier (TIA) that was battery powered with a gain of 100 nA/V and a single-pole -3db and a bandwidth of 10 kHz. The

output of the TIA was digitized by a National Instruments model NI PXIe-6341 DAQ system at a sample rate of 250 ksps by running WinEDR software (Strathclyde Electrophysiology Software; http://spider.science.strath.ac.uk/sipbs/software_ses.htm).

5.5.2 COMSOL simulations

The nCC design was built in AutoCAD and imported into COMSOL v5.5. The physics used was Electric currents to model the potential, field strength, and current density across the nanopores. Laminar flow in the microfluidic chip was used to estimate the velocity and pressure. The buffer used was 1X PBS. The inlet/outlet conditions vary through different iterations; atmospheric pressure (1 atm) was set at the inlet for iterations 1-3 and a 3 μL/min was used for iteration 4. The outlet was set to 97000 Pa in iteration 3 and 50000 Pa for iteration 4. The simulation was run in a stationary mode and the results were evaluated. Line plots were used to determine the velocity, pressure, potential, electric field strength, and the current density profiles. The effective pore length was calculated from the current density at the full width half-maximum.

5.5.3 Fabrication of the nCC

The access microchannels were fabricated in a Si wafer using conventional photolithography. Briefly, AZ1518 resist was spin coated onto a Si wafer using a spin coater at 3,000 rpm for 30 s. The wafer was soft baked at 100°C for 10 min and allowed to cool until the wafer reached room temperature. A dark-field mask was placed on a mask aligner and the wafer was exposed to UV light (365 nm) for 4 s through the mask. The wafer was then developed in MIF 300 for 20 s, rinsed with DI water, and dried with nitrogen. The wafer was inspected using an optical microscope to ensure that the patterns were completely transferred. Wet etching of the Si wafer was done using 40% KOH with 5% IPA v/v at 70°C until the required depth (5 – 6 μm) was achieved. Then, the chromium layer was etched using a chromium etchant. The cross channels and in-plane pores of the nCC were fabricated in the Si wafer using focused ion beam (FIB) milling with Ga ions. The structures were milled using a 48 pA beam current and a dwell time of 1 μs to achieve a 200 nm x 200 nm x 100 nm (w x d x l) in-plane nanopore (Figure 5.3-A). Resin stamps were

produced from the Si master by UV curing of a polyurethane acrylate (PUA) resin for 3 min placed on a polyethylene terephthalate (PET) plate coated with a NOA72 adhesive. Next, the structures on the resin stamp were thermally imprinted into PMMA or COP substrates using NIL (nanoimprint lithography; Nanonex 2500), which consisted of an air cushion thermal imprinting process. nCC devices were thermally imprinted at 130°C and 300 psi for 5 min. A COC 8007 cover plate and the substrate were treated with O_2 plasma for 2 min (50 W) and then thermal fusion bonded using NIL at 72°C and 110 psi for 15 min (Figure 5.3-B). Following nCC assembly, randomly selected devices were subjected to a sealing test using Rhodamine B seeding into 1X PBS buffer.

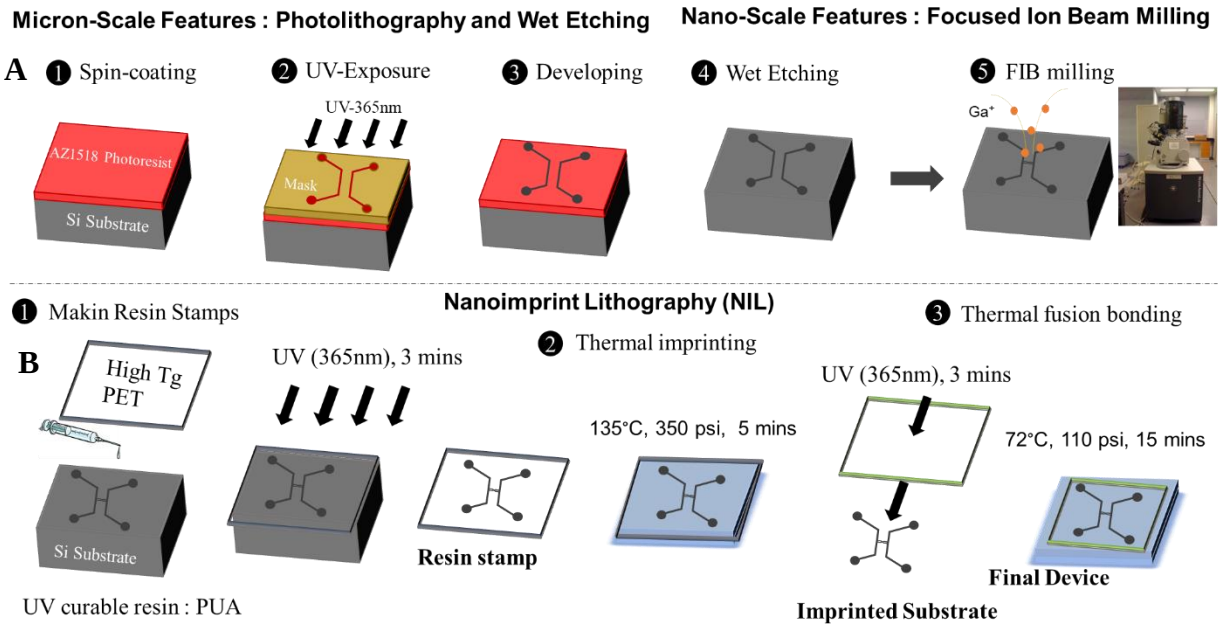

Figure 5.3 A) The steps depicting the process of positive photolithography and wet etching used to fabricate micron scale features are shown; briefly 4 major steps are involved where the Si wafter is spin coated (1) with AZ1518 resist, exposed to UV for 4 s via chrome coated masks that has the features (2). The features were developed using MIF 300 for 20 s (3) and wet etching on Si is performed using 40% KOH to achieve the required depths. The nanoscale features were fabricated using FIB milling using Ga^+ ions rastered on to the Si substrate. B) The features from the Si substate were transferred to the COP/PMMA substrate using NIL. A polymeric resin stamp was made by applying PUA resin on the Si substate and placing PET sheet over it and exposing it to UV for 365 mins (1). The patterns on the stamp are imprinted on the COP/PMMA substrate (2) and finally bonded using a COC 8007 coverplate to seal the devices (3).

5.5.4 Scanning Electron Microscopy

SEMs of the thermoplastic microfluidic/nanofluidic devices and PUA resin stamps were acquired using a Hitachi FlexSEM 1000 II SEM (Hitachi). The thermoplastics were sputter coated with a 10 nm

conductive Au layer prior to SEM using a Denton Desk II Sputter Coater. SEM images of the Si mold master was acquired using a Quanta™ 3D DualBeam™ FEG FIB-SEM (FEI).

5.5.5 Nanoparticle tracking analysis (NTA)

VPs were analyzed via NTA (Nanosight NT 2.3). The SARS stock samples were diluted 30× and vortexed prior to analysis. The instrument parameters used for the analysis consisted of: (i) Camera shutter 1206; (ii) camera gain 366; and (iii) capture duration 90 s. Five videos were taken for each sample at 25°C. The flow cell of the Nanosight instrument was washed 5 times with PBS in between sample analyses. During the final wash with PBS, a video was monitored to check if there were any particles left in the flow cell. If particles were detected, washing was continued until no particles were seen.

5.5.6 Calibration curve for viral particle counting

SARS CoV-2 particles that were pre-heat inactivated were purchased from ATCC having a stock concentration of 4×10^8 particles/ ml. Two different calibration curves were performed: In case of iteration 1, the samples for the calibration curve were prepared by serially diluting the stock in 1X PBS with concentrations ranging from 10^6 to 10^8 (please refer to Table 5.1). About 5 µl of the prepared samples were filled into the inlet reservoir side of the nCC chip's microchannel. The buffer side was filled with 1X PBS and a syringe pump was connected to the buffer side set to withdrawal at 20 µl/min. The sample and the buffer sides were electrically connected by placing Ag/AgCl electrodes into them to establish ohmic contact and a DC bias of -1 V was applied. Data was recorded using an Axopatch 200B with the data analyzed using Clampfit 10.1. Three sets of data were collected.

Table 5.2 Dilution factors of the SARS CoV-2 stock solution used for the calibration curve **(Iteration 1)**

Dilution ID	Concentration (VP/mL)
Stock	3×10^8
A	6×10^7
B	12×10^6
C	2.4×10^6
D	1.2×10^6

In the case of iteration 4, the dilutions from the stock solution of SARS-CoV-2 were serially diluted to establish clinically relevant concentrations with the concentrations verified using NTA (Table 5.2) [82] (The seeding levels varied between 1 x 10^3 copies/mL and 1 x 10^6 copies/mL to represent VP load in clinical samples). About 5 µl of the samples were used to fill one reservoir of the input microchannel while the outlet was filled with 1X PBS. A forward flow of sample was used to inject sample into the device at 3 µl/min and directed from the inlet reservoir and to the outlet reservoir with the outlet channel set to vacuum withdrawal. The TIA was used to apply a voltage of -5 V using Ag/AgCl electrodes and the entire set up was placed in a custom made Faraday cage. A minimum of 3 sets of data were collected.

Table 5.3 The dilution factors of the SARS CoV-2 stock solution with clinically relevant concentration based on the results from NTA **(Iteration 4)**

Dilution ID	Concentration (VPs/mL)
A	520,000
B	104,000
C	52,000
D	10,000
E	5,200

5.5.7 Pressure sensing at the withdrawal end

The withdrawal rate was determined by a pressure drop across the in-plane pores obtained using a flow rate of 20 µl/min. The vacuum withdrawal was estimated by connecting the outlet reservoirs to a T-shaped connector with a pressure sensor connected to it. One end of the pressure sensor was connected to a multimeter from which readings were recorded, while the other end extended into the withdrawal system. The withdrawal was turned on and the reading from the pressure sensor connected to a multimeter was recorded for a period of 720 s. The data was registered in terms of mV, which was then converted into pressure. The drop in pressure with respect to the atmospheric pressure was noted.

5.5.8 Fluorescence measurements

Rhodamine-B (Ex/Em: 534/570) was used as a tracer to check if the devices were sealed well. About 5 μL of 100 nM dye was used to fill the inlet and the dye was tracked as it passed through the nCC using a 532 nm Nd:YAG laser equipped with a 100X oil immersion objective (NA: 1.4). Nile red beads (Ex/Em 552/636) of 40 nm and 100 nm were diluted to 10^7 particles/mL in 1 M NaCl and 1X PBS, which was filled at the inlet side of the nano-Coulter Counter device's fluidic network. The outlet end was connected to a syringe pump withdrawing liquid at 20 μL/min. The single-molecule fluorescence microscope was equipped with a 60X/100X objective and was used to track the particles moving through the nCC. The microscope system was fitted with a sCMOS camera that recorded the data in Metamorph software at an exposure of 10 ms, a binning of 1x1, and analysed using Fiji.

5.6 Results and Discussion

5.6.1 Design Iteration 1

5.6.1.1 Initial Design Schematic and Operational Characteristics

The first design of the nCC featured a single pore of 100 X 200 X 200 nm (l x w x d), which was connected to microchannels on either side with reservoirs where a DC potential was applied. Figure 5.4-A shows the principle of how the in-plane nanopores (RPS) generate signal when a viral particle passes through the pore. When the particle resides within the microchannel, no signal is generated. But, as the particle moves into the pore, a signal is generated because it occupies a part of the pore that causes reduction in the flux of ions passing through the pore. This subsequently reduces the current, which causes a peak (signal) to be generated. The experimental set up is shown in Figure 5.4-B. The sample was applied to one side of the microchannel while the other channel was filled with buffer (Figure 5.4-B (1)) and was connected to a syringe pump set to generate a withdrawing flow of 20 μl/min (Figure 5.4-B (2)). The other reservoir of this microchannel was sealed with epoxy to make sure the particles were primarily withdrawn from the sample microchannel and into the pore. The entire set up was connected to an amplifier circuit and a DC potential of -1V was applied (Figure 5.4-B (3)). The dimensions of the nanochannel and the nanopore

connected to the microchannel is shown in the schematic and the corresponding SEM images shows the shape of the pore and nanochannel as fabricated in the Si master (Figure 5.5). The schematic and dimensions of the nanochannel with the nCC is shown in Figure 5.5-A. The dimensions of the nanochannels were 500 nm x 500 nm x 15 µm (w x d x l) and the nCC was 200 nm x 200 nm x 100 nm (w x d x l). Both ends of this nanochannel were connected to a microchannel with a ~6 µm depth and leading to reservoirs of 1.5 mm in diameter through which the fluid was filled and Ohmic contact was made. Figure 5.5-B shows the nCC connected via the nanochannel to the microchannel and a magnified image showing the actual dimensions of the Si master after FIB milling (Figure 5.5-C). The final dimensions of the nanochannel were 514 nm wide and the nCC was 185 nm x 200 nm (w x d).

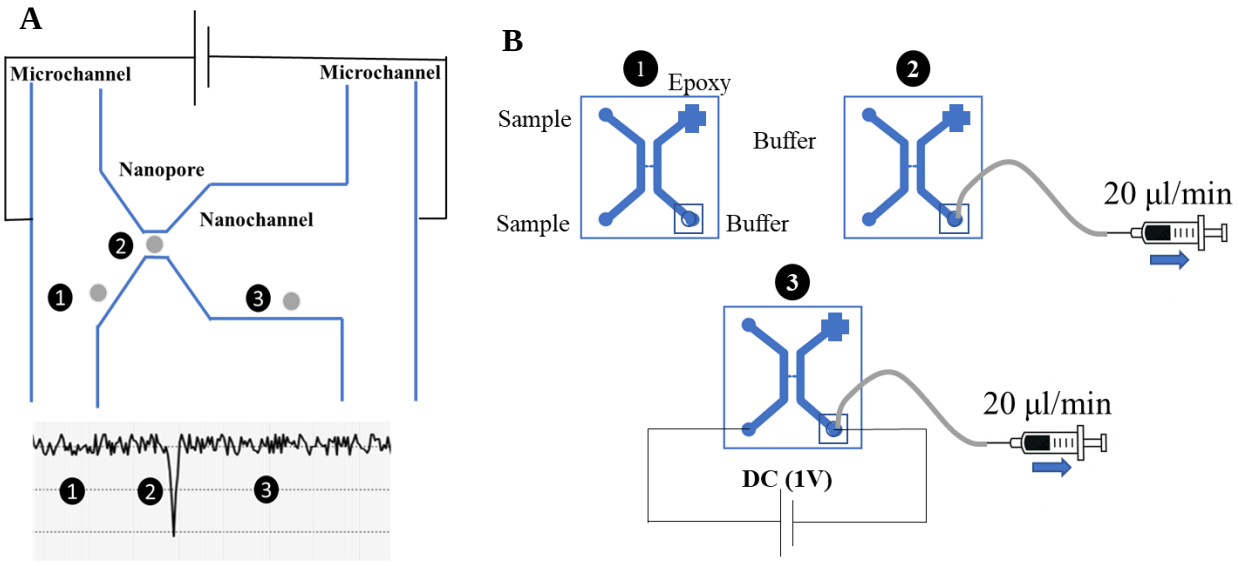

Figure 5.4 Overall concept of RPS and experimental set up of nCC for detecting viral particles. A) The concept of RPS where two access microchannels are connected by a nanopore, which is connected to an electrical circuit. When the viral particles are in microchannel, there is a constant current produced expressed by region 1 in the trace. When the particle moves into the nCC, a drop in current is generated due to the blockage of current produced by viral particle (region 2). The current resumes to the baseline when the viral particle moves from the nCC to the microchannel (region 3). B) The experimental setup is performed in 3 stages; stage 1, where one microchannel is filled with the sample and the other one with the buffer. A ferrule is fixed to connect the syringe pump that withdraws at 20 µl/min on the buffer side, while the other end of the buffer is sealed. The setup is connected to an electrical circuit to measure the current.

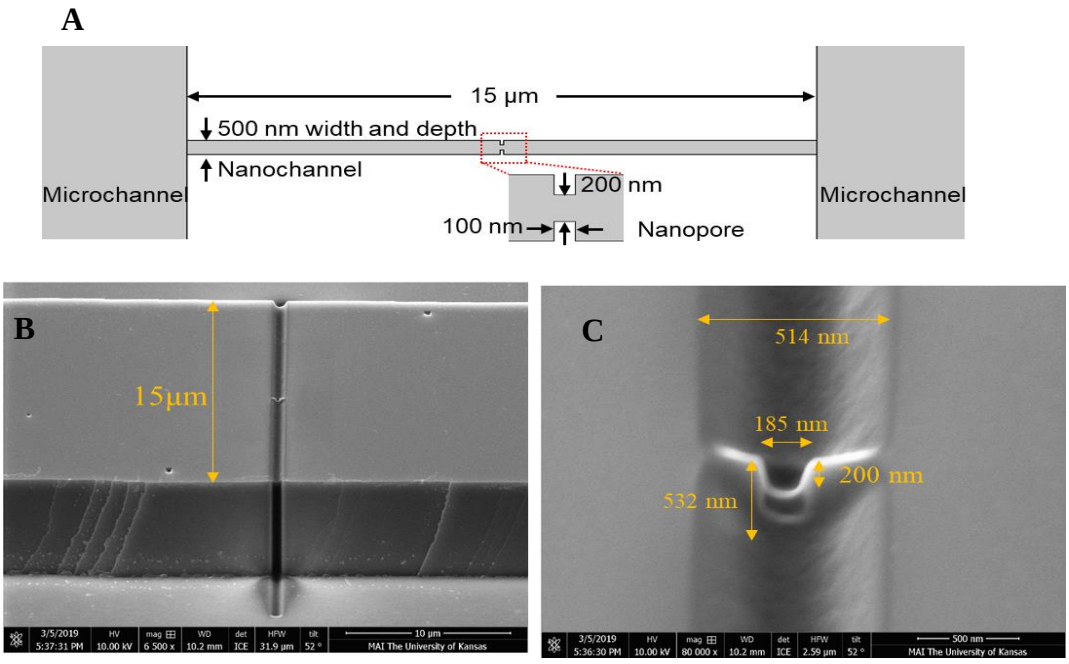

Figure 5.5 A) The overall schematic of the first design of the nCC is shown. The two microchannels (~6 µm deep) is connected to a nanochannel of 500 nm in width and depth, having a nanopore in the center of the channel of 200 nm X 200 nm width and depth and 100 nm long. B) The SEM images of the microchannels, the nanochannel having the nanopore is shown. The distance between the two microchannels is 15 µm. C) The magnified SEM image of the nCC is shown where the actual dimensions of the pore and the nanochannel are shown.

5.6.1.2 COMSOL simulations of nCC and its fabrication

The in-plane nCC device (Figure 5.6-A) utilized some unique characteristics that made it appropriate for high throughput counting of single VPs. The device was fabricated in a plastic using a top-down replication process making each pore of the sensor adopt an in-plane configuration (*i.e.*, the pore was in the same plane as the fluidic network of the chip). In addition, RPS was used for label-free counting of the selected and released VPs. Figure 5.6-B shows the equivalent RPS circuit for a single nCC sensor, where R_{mc} is the resistance of the access microchannel, R_{cc} is the resistance of the connecting nanochannel, R_{np} is the resistance of the in-plane nanopore, and R_{np} is the resistance of the nanoparticle. The resistance of the electrolyte in the device was considered as a series connection in the circuit. Whenever the VP is traveling through the in-plane nanopore, the particle forms a parallel resistor with the nanopore resistance. We modeled via COMSOL an in-nanopore as a fluidic constriction through which VPs can pass and produce unique electrical signatures. When a VP occupies the nanopore, buffer ions are displaced; the nanopore's resistivity transiently changes and causes a detectable current transient event.[83-85] Simulations

aimed to gauge the feasibility (SNR) for enumerating 30-150 nm VPs within 50-200 nm nanopores were carried out. Detectable current transient events were generated for all VPs if nanopores were appropriately sized, and current spikes scaled cubically with VP size (Figure 5.6-C). Recorded peak amplitudes and widths can be used to determine the transit time of the VPs within the sensing element. The pore size (~224 nm effective diameter) was predicated on optimizing the amplitude of the RPS signal with respect to the SARS-CoV-2 particle size as determined using nanoparticle tracking analysis (NTA), which indicated an average diameter of ~143 nm (see Figure 5.17-A for NTA analysis). The line graph of the voltage shows that the majority of the potential drops across the nanochannel and nanopore with a sharp drop of 0.04 V

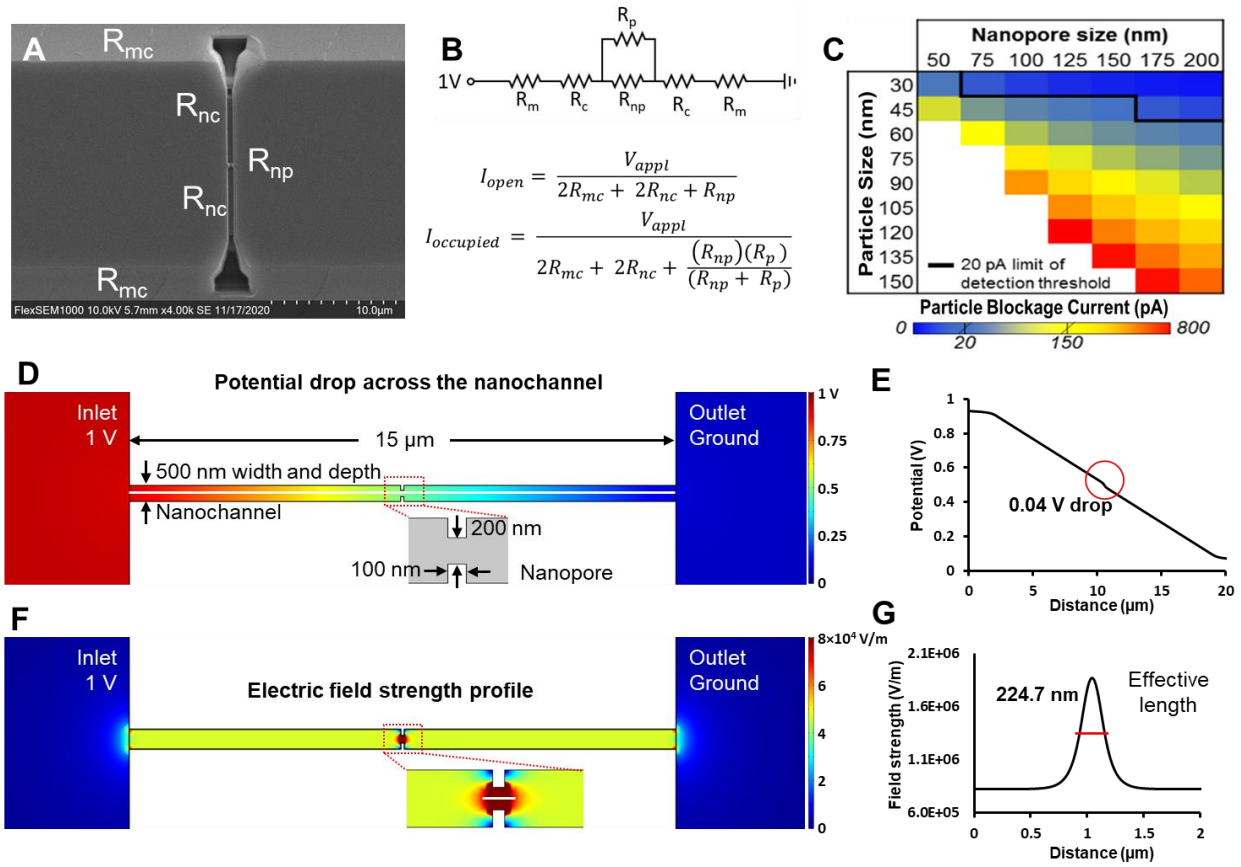

Figure 5.6 Nanopores for resistive pulse sensing of VPs**.** A) SEM image of the nCC (200 nm effective diameter. B) Equivalent sensing circuit for the nano-coulter counter, where Rmc is the resistance of the microchannel, Rnc is the resistance of nanochannel, R_{np} is the resistance of the in-plane nanopore, and R_{np} is the resistance of the nanoparticle. C) Simulations of nanopore-based VPs sensing showing the relation between the size of the particle and the size of the pore and the current drop that is expected D) COMSOL simulations of the voltage potential drop across the nanochannel. E) The plot of potential drop vs. distance of nanochannel. The potential drop across the nanopore is only 4% in the 2D dimension. By involving the depth to the 3D factor, the nanopore only shares the potential by 10%. F) Electric field strength profile showing the nCC having a higher field strength extending out to the nanochannel. G) The 50% of full strength was taken as the effective nanopore length, which is 224.7 nm.

across the pore, when a 1V DC bias was applied across the fluidic circuit (Figure 5.6 D-E). The corresponding field strength graph shows a higher field strength at the nanopore due to its smaller dimensions with respect to the nanochannel and microchannels. However, the field strength extended out from the physical dimensions of the nanopore, thus increasing the effective length of the nanopore from 100 nm to a 224 nm (Figure 5.6 F-G).

5.6.1.3 Calibration curve

We further evaluated the correlation of the number of peaks observed to the load concentration to establish a calibration curve from which the LOD could be determined (Figure 5.7). Figure 5.7-A shows the blank (1X PBS) trace where we did not observe any events in a 30 s time interval. From this blank, set a discriminator threshold condition so that no observable events would be registered in the blank to minimize false positive events when running the SARS CoV-2 samples. At a concentration of 3 x 10^8 particels per mL we observed ~371 particles/µl (Figure 5.7-B). When the sample was diluted by 100 fold, we observed 21 particles/µl (Figure 5.7-C). We proceeded to build a calibration curve and subsequently

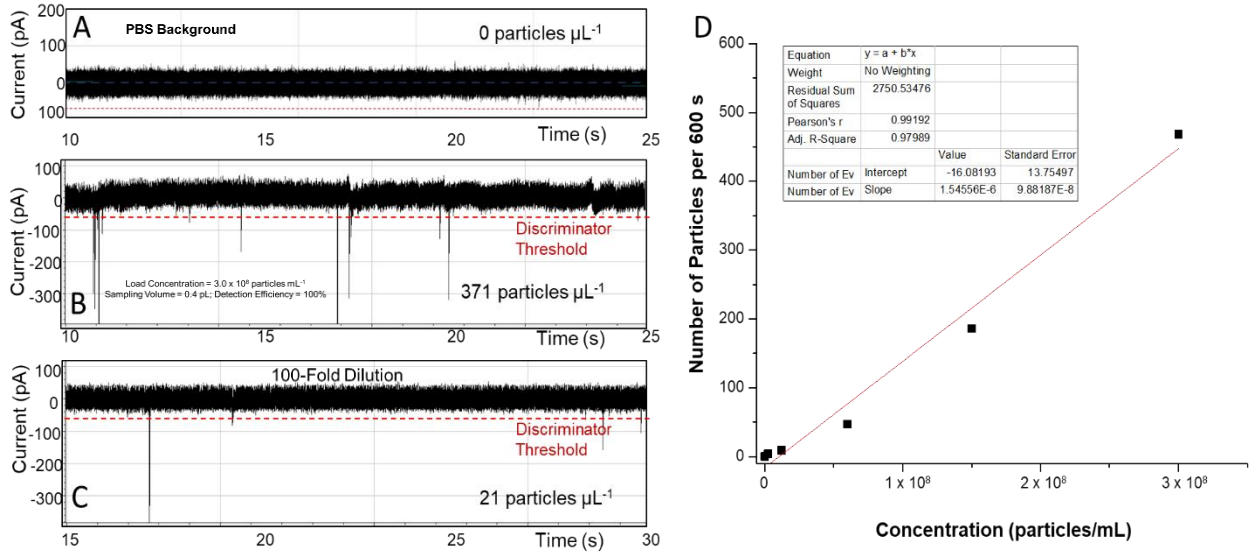

Figure 5.7 Representative traces of the Calibration curve that are background subtracted and filtered built for SARS CoV-2 VPs. A) The blank of 1X PBS showing no peaks that are observed above the discriminator threshold. B) The SARS stock having a concentration of 3 x 10^8 particles/mL showing 371 particles/µL. C) 100 fold dilution of SARS CoV-2 showing only 21 particles/µL. A 30 s time trace is shown for all the three data sets. D) Calibration curve built for 6 different concentrations (represented in the table 5.1) showing a LOD in the range of 6 x 10^5 particles mL^{-1} for a 600 s counting interval.

determined the limit of detection (LOD); the LOD is the lowest amount of sample that can be detected by an analytical procedure. In other words, LOD is estimated to be 3 times the standard deviation (SD) of the lowest concentration divided the slope (m) of the calibration curve (LOD = 3*SD/m)[86]. Based on the above criteria, the calibration curve showed that the concentration LOD was 6 x 10^5 particles mL^{-1} (600 s counting time) with a sampling efficiency, which is defined as the number of particles going through the single pore with respect to the number of particles traving through the fluidic device, of 4.5 x 10^{-4} % (Figure 5.7-D). The challenge with the existing design was that we had poor sampling efficiency resulting in a poor LOD. Hence, we embarked upon a design change to the nCC to improve the sampling efficiency. This was done by placing 5 pores in parallel to increase the sampling efficiency and thus, reduce the LOD.

5.6.2 Design Modifications: Iteration 2

5.6.2.1 Schematic and SEM of Iteration 2 design

In the subsequent design we made some design modifications by FIB milling 5 pores in parallel of the exact same design (iteration 1). We have 3 other iterations (2,3 and 4) in this chapter having 5 pores in parallel. The rationale behind choosing 5 pores in parallel is explained in detail further in the chapter in the final design section (iteration 4). Figure 5.8-A shows a schematic and SEM of the 5 nanopore design in the Si master. The SEM images of the microchannel and the placement of the 5 pores in the design are represented in Figure 5.8-B. One nanochannel and the corresponding nCC are magnified to clearly show the shape of the nCC (Figure 5.8-C). The depth profiles of the nCC with respect to the connecting nanochannel are shown as well (Figure 5.8-D). The individual pores were fabricated with the same dimensions as compared to the previous single nanopore design and hence, the potential drop (0.04 V) as estimated for the single pore system, and as such, the effective pore length estimated from the electric field strength (~224.7 nm) in the individual pores remain the same (Refer to Figure 5.6 D-G). Although this design offered a higher sampling efficiency, the potential drop across the pore was only 0.04 V. Increasing a potential drop is an important factor as it subsequently increases the current density, which determines the effective pore length. Hence, we proceeded to the third iteration to increase the voltage drop across the

nanopore to effectively increase the effective pore length and as well as increase the influx of particles into the nanopore region.

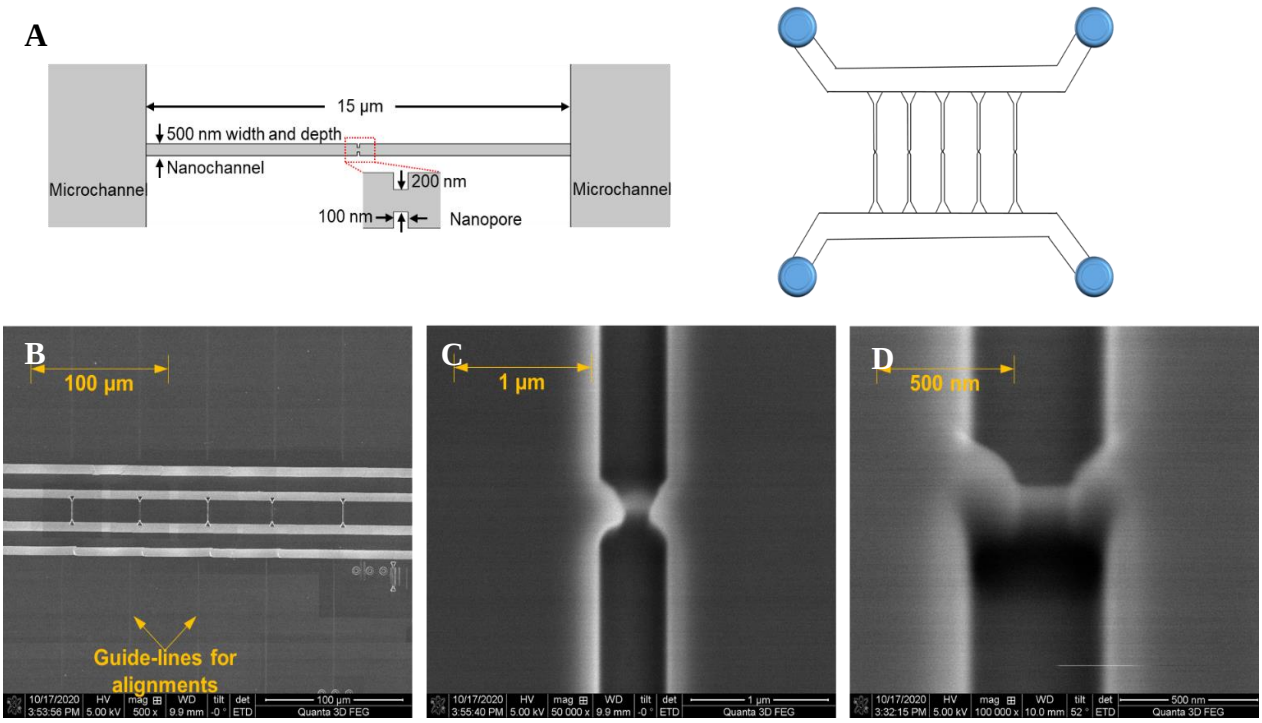

Figure 5.8 A) Schematic of a single nanochannel with nCC in the second iteration. B) SEM images of the nCC device showing the overall view of the 5 nanochannels with the nCC. C-D) Magnified image of a single nanochannel with nCC in the 5 channel design. The dimensions of the individual nCC and the connecting nanochannels have been fabricated similar to iteration.

5.6.3 Design Modifications: Iteration 3

5.6.3.1 Schematic and SEM images of Iteration 3 design

The next iteration focused on increasing the potential drop across the nanopore. From our previous simulations it was seen that the potential drop occurs across the narrowest dimension in the device. Subsequently, we increased the width of the connecting nanochannels from 500 nm to 2 µm (Figure 5.9-A). Increasing the width of the nanochannel would give a 10-fold increase in dimensions between the nCC and the nanochannel. The microchannel/nanochannel interface was connected by an input funnel of ~6 µm. The funnel structure not only offered a more gradual increase in electric field strength, but also offered a higher injection rate (Refer to Chapter 2, Figure 2.5). The SEM of the overall design of the Si master and the magnified images showing the nanopore and the connecting microchannels is shown in Figure 5.9 B-

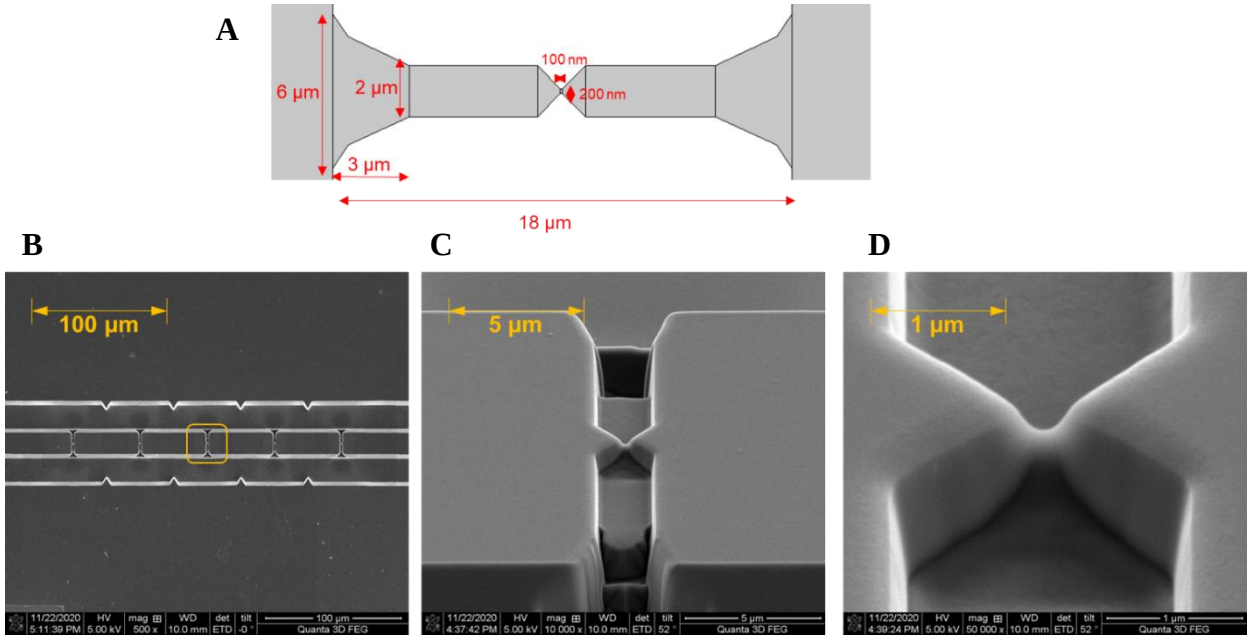

Figure 5.9 A) Overall Schematic showing the modified design having the connecting nanochannel increased from 200 nm to 2 µm. B) Overall SEM image showing the 5 channels. C-D) Magnified image of the modified nanochannel and the nCC, showing the depth profiles. The size of the nanochannel has been increased 20 fold, but the size of the nCC nanopores have been retained similar to previous iterations.

D. The schematic of the nCC with the new dimensions is shown. The SEM image (Figure 5.9-B shows the section of the device showing the 5 nCC, along with the inlet structures and the connecting microchannels. The magnified image of the connecting nanochannel and the pore can be seen in Figure 5.9-C. The depth profiles can be clearly seen where the pore is seen having a much smaller depth compared to the nanochannel. The connecting nanochannel converges to the pore of the nCC and can be clearly seen in Figure 5.9 D.

5.6.3.2 COMSOL Simulations

The simulations for this device iteration were modified based on the results from the pressure drop experiment performed at a withdrawal of 20 µL/min resulting in a 3,000-4,000 Pa pressure drop across the pores. Hence, the pressure at the inlet was set to atmospheric pressure (101,325 Pa), while the outlets were set to 97,000 Pa for the hydrodynamic withdrawal. COMSOL simulations of the velocity profile showed that there was fluid passing through all of the pores. The velocity in the microchannels was found to be 1.5 mm/s and in the pore regions the velocity increased to ~5 mm/s at this pressure difference (Figure 5.10-A).

With the increased size of the connecting nanochannels, the potential drop in the pore increased from 0.04 V (iteration 1 design had 500 nm wide connecting nanochannel) to 0.2 V (iteration 3 design has 2 µm connecting nanochannels) when 1V DC bias was applied, thus increasing the probability of a larger amplitude current drop as the VPs pass through the pore (Figure 5.10-B). The larger drop also increased the current density in the pore, where it can be seen extending out to the nanochannels on either side. Consequently, the effective length of the nanopore increased from 100 nm, to ~407 nm, which was determined by the physical length of the pore as defined during fabrication, increased the effective sampling volume (Figure 5.10 C-D). The pressure drop profile, however, showed that the majority of the drop occurred only across the nanochannel and the nanopore region.

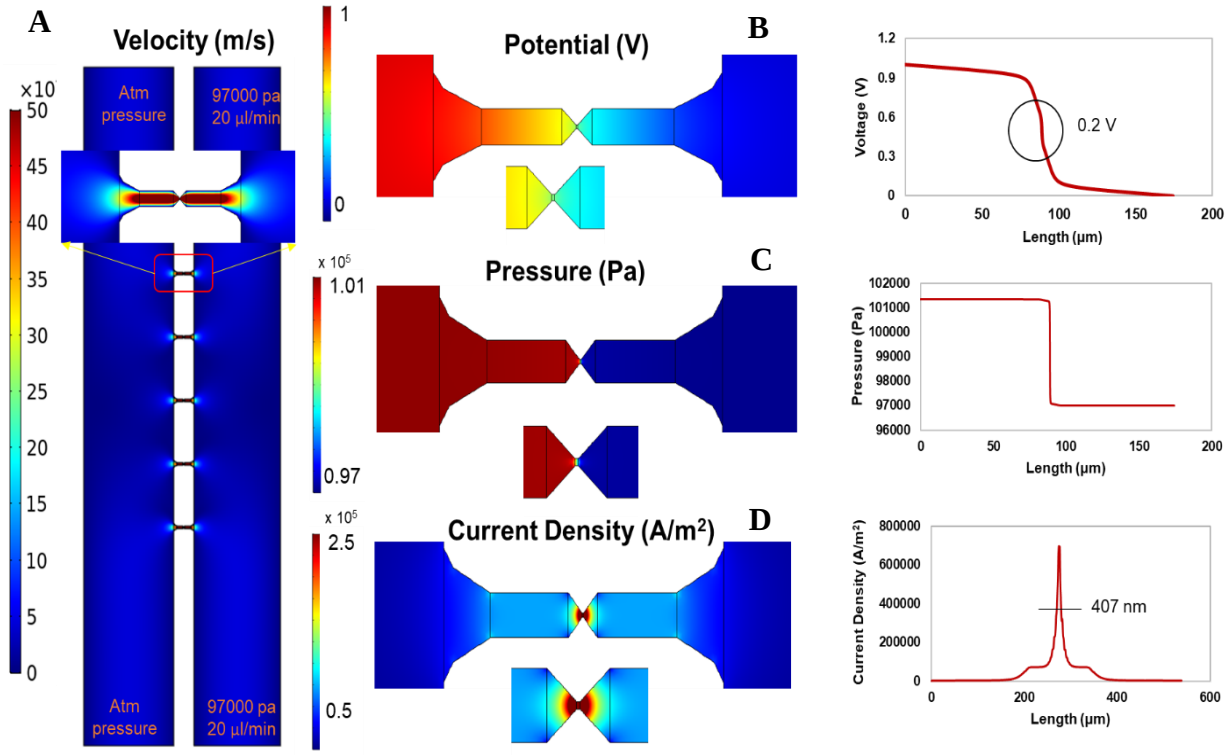

Figure 5.10 COMSOL simulation of iteration 3 design. A) The velocity profile with the inlets set to atmospheric pressure on both the same inlets and the outlets set to the pressure 97000 Pa (estimated from the pressure sensor set to 20 µL/min. The fluid from the inlet side are seen entering the outlet side due to the difference in pressure drop. The magnified image showing the higher velocity in the nCC. B) The pressure profile and the line graph showing a sharp decrease in the pressure at the pore region. It is evident the pressure drop does not occur in the access microchannels. C) The potential drop profile and the line graph showing the voltage drop at the pore (0.2 V) with the rest of the voltage drop across the nanochannel. D) The current density profile plotted from the voltage profile to estimate the effective length of the pore at FWHM, which is ~407 nm. This happens due to the field strength extending out of the pore and into the nanochannel contributing to the current drop.

5.6.3.3 Estimation of the pressure drop at 20 µL/min withdrawal rate

While we have been using a withdrawal flow rate of 20 µL/min in our previous iterations, we went ahead to determine the pressure it induces across the pores. The experimental set up was similar to the previous iterations, where the sample was filled on one of the microchannels and buffer (1X PBS) was filled on the other side. One reservoir on the buffer side was connected to a syringe pump withdrawing fluid at 20 µl/min, while the other end was sealed using epoxy. A pressure sensor was connected to the withdrawal end and pressure values were recorded for a period of 12 min. We decided to run the experiment for 12 min as we used a 600 s counting interval to establish the number of events that were produced when

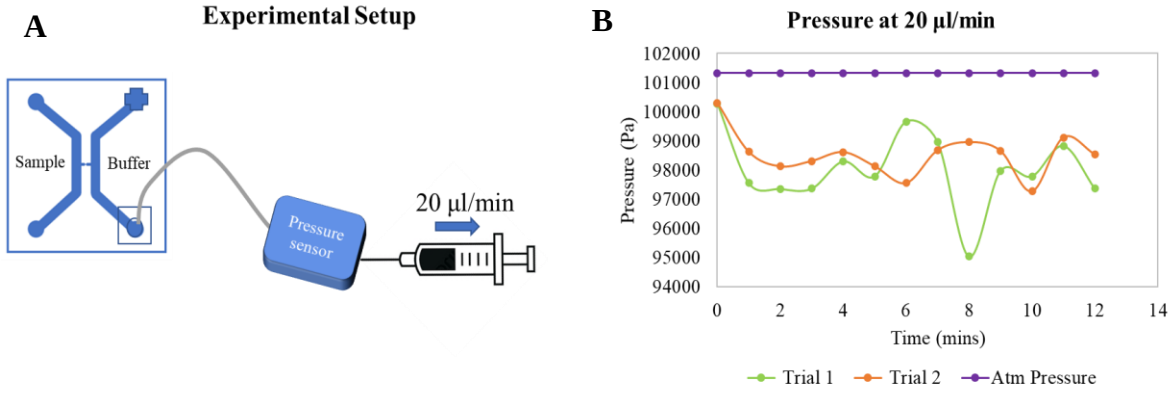

Figure 5.11 The experimental setup modified from iteration 1 to have a pressure sensor fixed before the withdrawal pump to estimate the pressure drop at the buffer side at a flow rate of 20 µL/min. B) The pressure drop across the sample and the buffer side at this flow rate was evaluated across the nCC for a period of 12 mins. The purple line represents the atmospheric pressure (101325 Pa) in the absence of any flow rate. The orange and green lines represent the pressure at buffer side from 2 different trails averaging to approximately 97000 Pa. The differential pressure drop across the nCC is about 4000 Pa.

running the SARS CoV-2 sample. The pressure induced by the flow rate was recorded over 2 trails and it can be seen that the pressure drop was in the range of 97,000 to 98,000 Pa (*i.e.*, ~3000-4000 Pa pressure drop) across the nCC pores (Figure 5.11 A-B). In order to estimate the approximate velocity and the distribution of pressure in the device, we used the pressure values obtained from the experiments to perform 2D COMSOL simulations. The inlet was maintained at atmospheric pressure, while the other side of the microchannel was placed at 97000 Pa (see Figure 5.10).

5.6.4 Some important considerations for optimizing the results of the nCC

Based on the results from our previous iterations, we considered some important design factors to further optimize the figures-of-merit of the nCC to detect SARS CoV-2 particles with favorable limits-of-detection. The design considerations included: 1) Selection of the correct thermoplastic (PMMA vs COP) to minimize non-specific adsorption, but still providing the ability to replicate the desired structures. 2) Fluorescence experiments. Two different fluorescent experiments were performed; (i) sealing test to check if the device completely filled with no leaking; and (ii) tracking beads to ensure that the nCC was capable of translocating viral particles (VPs). 3) Electrical considerations; selection of the correct low pass filter to optimize SNR and selection of proper sampling frequency to eliminate signal aliasing. 4) Optimizing the pressure drop across the nCC to induce efficient hydrodynamic flow across the device and adequate inflow of sample to the nCC. 5) Rationale behind 5 nCCs in parallel, rather than a single nCC of dimensions equivalent to 5 nCCs. A theoretical comparison of the current (I) and resistance (R) and the corresponding S/N ratio of the two designs with the accompanying simulations were used to compare the current density, which was used to determine the effective sampling length, was performed to establish why we selected 5 nCCs in parallel as opposed to a single larger nCC with the same effective diameter.

5.6.4.1 Selecting the correct material for the nCC

We fabricated the nCC in two different materials; (i) polymethyl methacrylate (PMMA) and (ii) cyclic olefin polymer (COP) to evaluate if nanoparticles adsorbed/stick to the microchannel channel wall. Polystyrene Nile red beads (40 and 100 nm) at a concentration of 10^6 particles/mL in 1 M NaCl in 1X PBS were introduced into the sample channel, while 1X PBS only was filled on the buffer side and was withdrawn at a flow rate of 20 μL/min. The device was filled and placed on a wide-field epifluorescence microscope having a 532 nm laser equipped with a 60X and 100X oil immersion objective and a sCMOS camera to record fluorescence videos. Figure 5.12-A shows Nile red beads stuck on the surface of PMMA device, while in the case of COP (Figure 5.12-B), the beads did not seem to stick. Some beads were also seen to move across the nCC when withdrawn under a 20 μL/min flow rate. This result demonstrated that

COP was a more ideal thermoplastic for a RPS device. Going forward, all experiments were performed in COP devices.

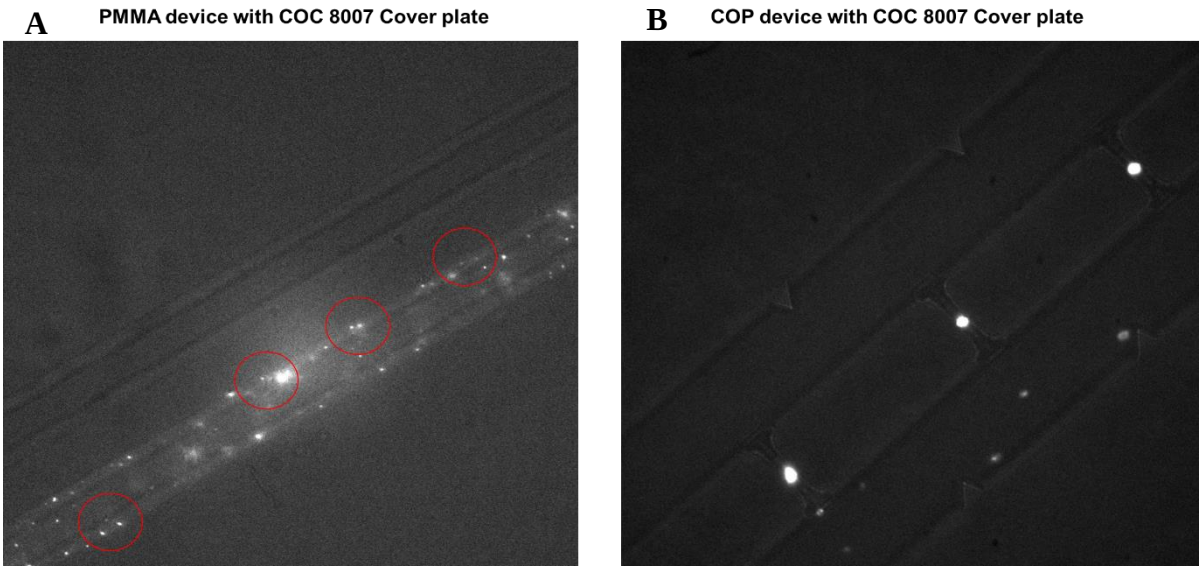

Figure 5.12 A) Polystyrene beads stuck on the microchannel walls on the PMMA device, represented by red circles. B) COP device showing no beads stuck on the microchannel wall and some beads are observed moving across the nCC from the sample to the buffer side.

5.6.4.2 Testing the translocation of polystyrene beads though the COP devices

We imprinted COP devices at 135°C, 300 psi for 5 min and performed thermal fusion bonding at 72°C and 110 psi at 5 min using a COC 8007 cover plate (Tg = 87°C). Rhodamine B was used to fill devices to make sure all 5 nCCs were open and fluid could flow through the constrictions. From Figure 5.13 A-B, it can be seen that there was fluorescence observed in all of the connecting nanochannels and the nCCs. A line plot across three nCCs showed fluorescence represented in gray values for both the background and the pore area. It was evident that there was higher fluorescence in the nCC pore area indicative of proper device filling and there was no fluorescence observable outside the pore area thus showing that the device was sealed properly, even around the nanopores.

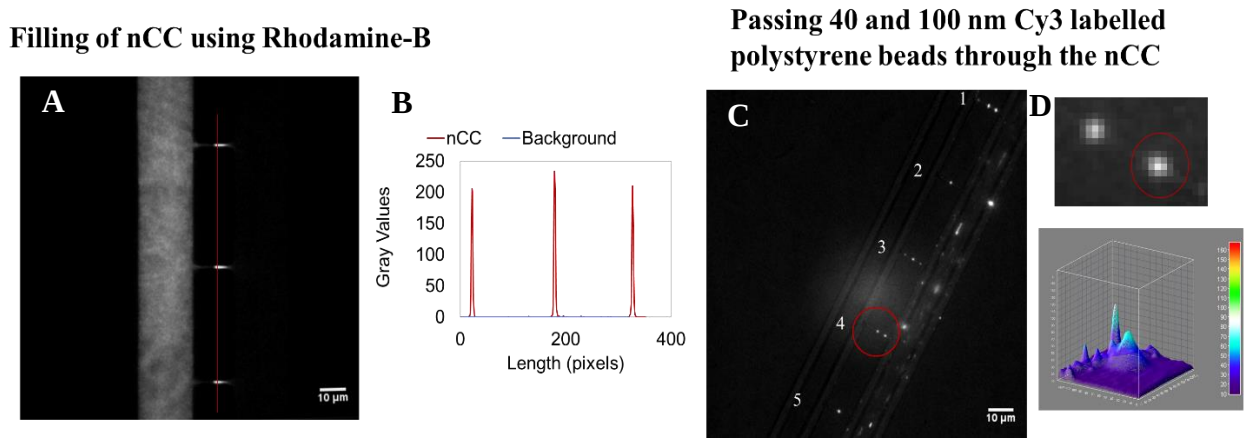

Figure 5.13 A) Fluorescence image of the nCC device which is filled with Rhodamine-B, showing the fluorescence in the microchannel and the 3 nCC that is in the field of view. B) The line plot showing the fluorescence intensity values in the 3 nCC compared to the background. C) 40 and 100 nm Polystyrene beads mixed that were filled on the sample side of the nCC and were drawn into the nCC using 20 µL/min withdrawal rate. The 5 nCC shown in the field of view have beads in the nCC region. C) The magnified image of the beads in one of the nCC shows that there are single molecules occupying a 3X3 pixel array D) A 3D plot of a single molecule shows the intensity spread across the 3X3 pixel array.

Polystyrene nile red beads of 40 and 100 nm diameter were mixed and diluted to a final concentration of ~10^7 particles/mL in 1 M NaCl placed in 1X PBS. The beads were then filled into the sample microchannel, while the other side was filled with buffer (1 M NaCl in 1X PBS) and connected to a syringe pump that withdrew the fluid through the nCC (volume withdrawal rate was 20 µL/min). Figure 5.13-C shows the polystyrene beads that were in the microchannel near the nCC region and some beads that were seen entering the nCC when the withdrawal was started. In some pores, multiple beads were seen entering the nCC. A magnified image of beads in pore 4 showed that these were indeed single beads as represented by the 3 X 3 pixel area (Figure 5.13-D). A 3D plot shows the higher fluorescence intensity distribution across the pixel area within the pores indicating single particles (Figure 5.13-E).

However, at this volume withdrawal rate only a few particles were seen entering the pore, and it appeared that the pressure drop was not sufficient to draw the particles through the pores with high efficiency. Furthermore, only the particles near the entrance of the microchannel/nanochannel interface had a higher probability of entering the nCCs compared to the ones away from them and this would affect the sampling efficiency. Therefore, the concentration limit-of-detection would be poor. As such, we made some

changes to the design of the nCC as well as the experimental set up to improve sampling efficiency, which will be discussed in design iteration 4.

5.6.4.3 Selecting the correct low pass filter for electronic signals

Low pass filters are designed to modify, reject unwanted high frequency noise, and allow only frequencies up to the cut off frequency. For example, a 100 kHz low pass filter allows frequencies up to 100 kHz to be included into the data trace and cuts off frequencies above it. In the case of a 10 kHz low pass filter, only frequencies up to 10 kHz are allowed. For low pass filter 100 kHz filters, the filters are made using a simple resistor-capacitor (RC) network, while 100 kHz high pass filters are constructed using a resistor-inductor-capacitor (RLC) network.[87] Choosing the correct low pass filter is important because they define the bandwidth of the system. Also, as the frequency of the filter increases, there is a corresponding increase in the noise level. While it may appear that higher frequency filters are beneficial in extracting signals from trace data, there is a possibility of the analytical signals being masked by noise. Hence, we tested three different low pass filters: 5 kHz, 10 kHz, and 100 kHz filters and evaluated the standard deviation (SD) noise levels using 1X PBS as a carrier buffer using for the 5-nCC COP devices. A voltage of -1 V was applied and an open pore current of 22.2 nA was recorded. Our instrument allowed a sampling frequency up to 500 kHz, but recording at such a high sampling frequency increased the size of the data files acquired thus limiting the recording time. Therefore, we used a sampling frequency of 100 kHz. According to the Nyquist theorem, the sampling frequency must be at least two times greater than the frequency of the low pass filter (This establishes the bandwidth) . For our current transient peaks that occur when a nanoparticle is passing through the nCC pore, we found the FWHM of the peak to be 31 µs under optimal conditions. Therefore, our 100 kHz sampling frequency was 3-fold larger than the inverse peak FWHM value and we would not expect signal aliasing based on the Nyquist theorem. We adopted a criteria for the amplitude of the events to be SD*5 open pore baseline to be considered true events as this would eliminate false positive results. A 10 kHz filter had a SD of ~11 pA and a 5 kHz filter had a SD of ~ 6 pA. With the SD noise levels at 10 kHz being reasonable (event threshold of 55 pA at 10 kHz, and 30 pA at 5

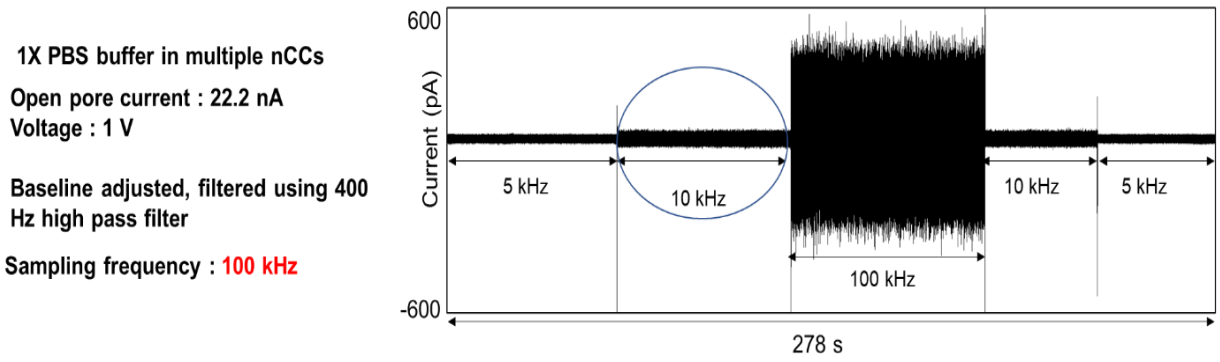

Figure 5.14 The baseline noise levels at three different low pass filters : 5,10 and 100 kHz. The data was recorded at 5 kHz, subsequently increased to 10 and 100 kHz, followed by gradually reducing the frequencies, all acquired in a time duration of ~278 s. A voltage of 1V was applied and an open pore current of 22.2 nA in 1X PBS was recorded on multiple pore nCC device. The data shown above is baseline subtracted and filtered using a 400 Hz high pass filter. The sampling frequency was set to 100 kHz.

kHz), we selected 10 kHz as our filter (Figure 5.14), to optimize the SNR in the measurement and minimizing event distortions from using a lower frequency filter.

5.6.5 Design Modifications: Iteration 4

The above iterations based on COMSOL simulations and experimental results provided to us some insights to the design type that would be required to satisfy the following conditions; **1)** Increased sampling efficiency by utilizing 5 pores in parallel; **2)** reducing the width of the microchannel near the pores and also placing the pores close to the sample microchannel so that there would be a higher probability of particles entering the nCC pores; **3)** higher pressure drop across the pores so that the particles from the inlet side are pulled more efficiently to the other side; and **4)** utilizing a forward flow so more particles are brought into the region around the nCC for sampling.

5.6.5.1 Rationale behind choosing 5 pores in parallel

The rationale behind choosing 5 pores was to improve the sampling efficiency by providing more area for the particles to be sampled from the access microchannels while being able to preserve the signal to noise ratio of single particles. The final design had a pore of 350 nm (width) and hence the calculations were based on this dimension. There are two ways to achieve this; 1) Having a single pore of 1.75 μm wide or 2) fabricating 5 pores in parallel with each pore having a width of 350 nm.

From our experiments, the current at 1 V potential across the 5 pores in parallel is 14 nA;

$$V = IR$$

$$\mathrm{R} = \frac{\mathrm{V}}{\mathrm{I}} = \frac{1\mathrm{V}}{14}\mathrm{nA} \; = \; 71.4\ \mathrm{M\Omega}\ \text{(For a single 350 nm pore)}$$

$$\frac{1}{R_T} = \frac{1}{R} + \frac{1}{R} + \frac{1}{R} + \frac{1}{R} + \frac{1}{R} = \frac{5}{R}$$

$$R_T = \frac{R}{5} \quad R = 5R_T$$

R= 357.1 MΩ (Total for a single 1.75 μm pore)

Case 1: Single 1.75 μm pore

$$R_T = 357.1\ \mathrm{M\Omega}$$

I =14 nA x 5 = 70 nA

Pore diameter = 1750 nm; Assume virus diameter = 150 nm;

Occlusion Ratio = (150 nm/1750 nm) x 100% = 8.6%

ΔI = (8.6/100) x 70 nA = 6.02 nA in 70 nA

Case 2: 5 pores in parallel

R = 71.4 MΩ (Single 350 nm pore)

Pore diameter = 350 nm; Assume virus diameter = 150 nm;

Occlusion Ratio = (150 nm/350 nm) x 100% = 42.86%

I_T = 14 nA x 5 = 70 nA

ΔI = (42.86/100) x 14 nA = 6.02 nA in 70 nA

Electronically, both methods yielded the same result, which was evident from the ΔI calculation. However, we estimated the effective length by calculating the FWHM from the current density plot from COMSOL simulations.[54] This was designed to have a pore width of 1.75 μm and a length of 100 nm. The connecting nanochannels were designed to have a width 4 μm having a total length of 20 μm between the

microchannels. A potential of -5 V was applied to the inlet microchannel and the outlet was placed at earth ground.

Figure 5.15A shows the electric potential distribution across the single pore device. The potential drop occurs across the nCC and the connecting nanochannel (~4.8 V to 0 V). The connecting nanochannel is only about 2.9 times greater than that of the nCC. Hence, the potential drop is distributed throughout the nCC and the connecting nanochannels unlike having 5 pores in parallel where a 0.5 V drop occurs across

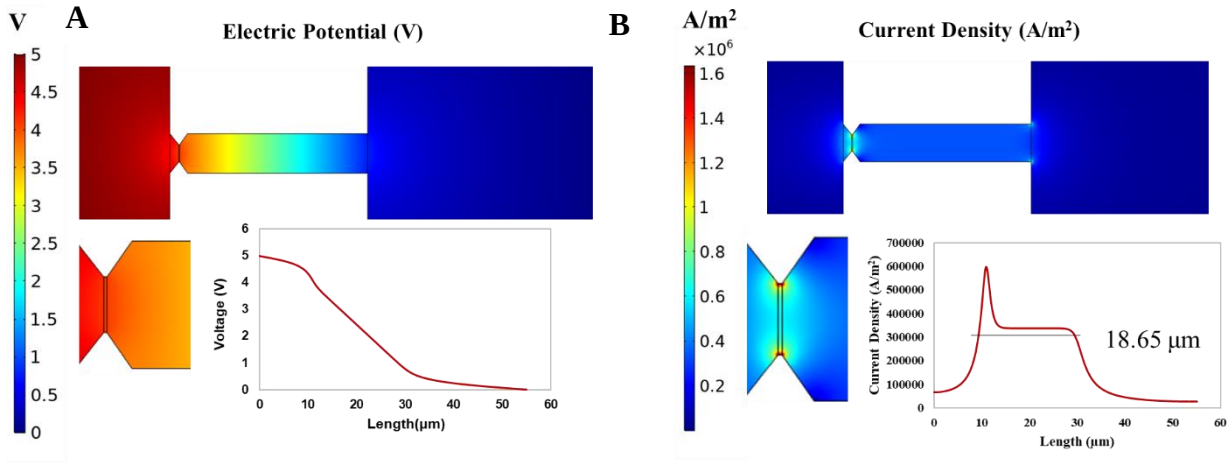

Figure 5.15 COMSOL simulations of the 1.75 μm pore ; A) Electric potential (-5V) applied in the microchannel inlet showing a drop in potential through the nCC and the connecting nanochannels. A magnified image of the nCC and the corresponding line plot showing the drop from 5V to the ground is shown. B) The current density corresponding to the potential drop is shown with the regions in the nCC having a higher current density. A magnified image of the nCC with the corresponding line plot showing the current density across the microchannels, nCC and the connecting nanochannels. The current density in the nCC reaches the highest of 600000 A/m^2, giving rise to an effective length of 18.65 μm.

each nCC (see Figure 5.17-D); the connecting microchannel (2 μm) is 5.7 times greater in size than the 350 nm pore (see Figure 5.16). Figure 5.15-B shows the corresponding current density giving an effective length of 18.65 μm, as opposed to the design having 5 pores in parallel giving an effective length of 667 nm (Figure 5.17-E). The corresponding probe volume for the single 1.75 μm nCC is 57 fL, while for the 5 channel nCC, the overall probe volume is 405 aL (85 aL x 5). This difference in probe volume size for the single 1.75 μm nCC increases the probability of occupancy of multiple VPs in the nCC at a given time, which decreases the analytical sensitivity. Analytical sensitivity determines the ability of the nCC to determine differences between very close concentrations of a target (slope of the calibration curve).[88] In

addition, fabricating a single 1.75 µm pore with a 100 nm length and connecting channels of 4 µm becomes challenging; FIB milling takes much longer to write 4 µm channels having a length of 20 µm, but these dimensions are well in the range of photolithography.[89] But, because the nCC has one dimension in the nanometer range (length of 100 nm), it can only be done using FIB milling. Due to these reasons, we fabricated 5 pores in parallel of 350 nm each as opposed to a single pore of 1.75 µm in effective diameter.

5.6.5.2 Design schematic and SEM images

The nCC having 5 pores placed in parallel was designed to have similar dimensions for each pore as discussed is the previous iteration (Figure 5.16-A), but during FIB milling the width and depth of the pore was increased to 350 nm and 336 nm, respectively (Figure 5.16-D); this was done to accommodate the size range of SARS-CoV-2 VPs as determined by NTA (see Figure 5.22-A). The width of the microchannels were reduced to 25 µm overall and in the region near the 5 pores, the width of the

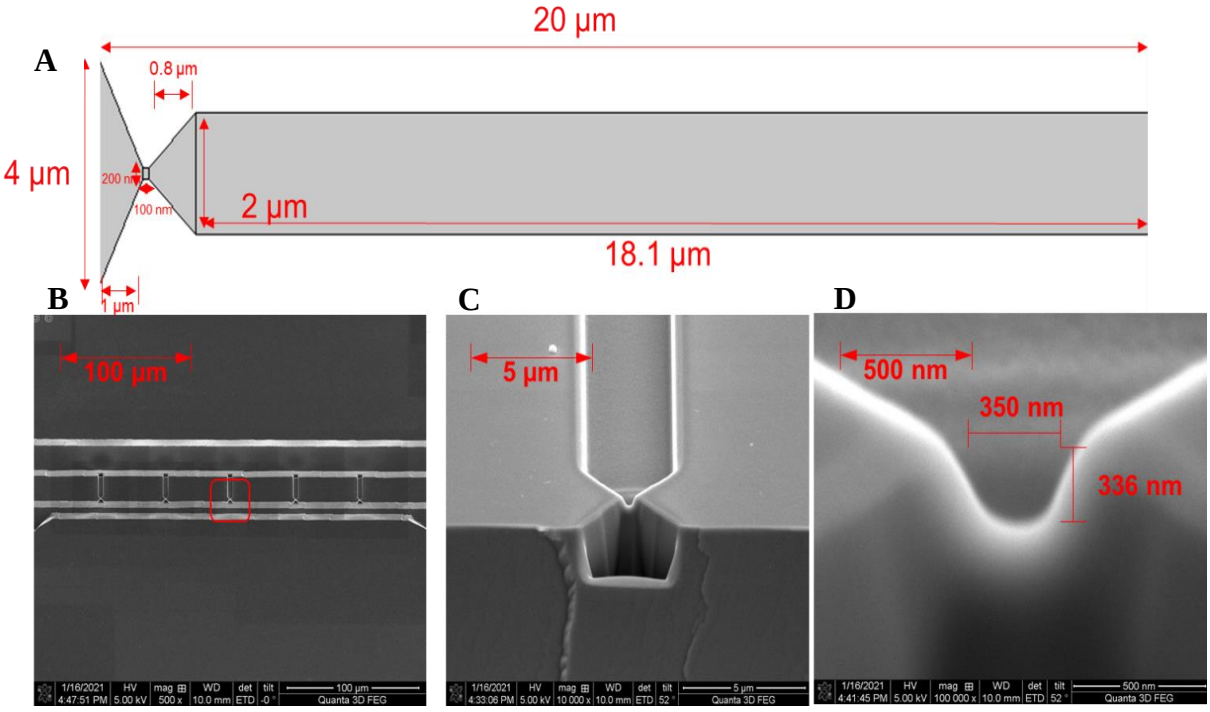

Figure 5.16 A) Gray-scale diagram of a single in-plane nanopore associated with the final nCC iteration. The nCC in this design was placed adjacent to the access microchannel and the funnel structure near the pore was increased to 4 µm and the nanochannels to 2 µm to have a higher injection efficiency of the VPs into the nCC. B) SEM of the 5 in-plane nanopores FIB milled in the Si wafer. The width of the access microchannels on the sample side was reduced from 25 µm to 10 µm only in the region having the nCC pores. C) SEM showing the bridge channels flanking the access microchannels. D) The final nCC dimensions after FIB milling was 350 nm X 336 nm (w x d).

microchannel was further reduced to 10 μm (Figure 5.16-B) to increase the sampling efficiency. The nCC in the previous iterations were placed in the center of the connecting nanochannels, however, in this iteration we positioned the nanopore next to the funnel connecting to the microchannel to also increase sampling efficiency.

A 4 μm funnel at the microchannel and placed immediately in front of the nCC funnel was used to assure that during the imprinting phase, the structures would not collapse. A SEM image of the funnel and the nCC can be seen in Figure 5.16-C.

5.6.5.3 COMSOL simulations

COMSOL simulations were performed on the modified nCC design having a pore of 350 nm x 100 nm, w x l) with conditions at the inlet having a 3 μL/min flow rate for pumping the sample and the other reservoir at the inlet held at atmospheric pressure. The outlet side was held at 50,000 Pa (refer to Figure 5.18-B). The velocity profile showed that the sample from the inlet side entered into the nCC and to the buffer side, but now with a higher velocity due to an increase in pressure drop compared to the previous iteration. The velocity in the microchannel ranged from 0.1 m/s in the wider part of the microchannel (near the inlets) and increased to 0.25 m/s in the narrower region, which was placed in front of the pores (Figure 5.17-A). The simulated velocity in the 5 nCCs were magnified and it can be seen that they were very uniform reaching a velocity of 1.5 m/s (Figure 5.17-B), which would give a pulse duration of 0.45 μs. The pressure profile (Figure 5.17-C) showed a drop in pressure between the inlet microchannel (i) and the outlet microchannel (ii). Figure 5.17-C(i) shows the pressure drop across the inlet microchannel. The inlet microchannel had a 3 μl/min inflow rate, which drove the particles from the inlet microchannel to the sampling zone, which is the narrow region (10 μm) in the microchannel adjacent to the 5 nCCs. However, the majority of the pressure drop (~40,000 Pa) occurred across the nCC and about 10,000 Pa in the nanochannel following the nCC was observed (Figure 5.17-C(ii)). To determine the potential drop and the corresponding current density, we used a higher voltage in this case, which was -5 V. The inlet side of the microchannel was placed at -5 V (absolute potential values are used in the simulations), while the outlet

side was placed at earth ground. The majority of the potential drop was seen to occur across the nCC pore (~0.5 V) and the connecting nanochannel (~3.7 V; Figure 5.17-D). The current density at this potential showed an effective pore length of 667 nm at its FWHM (Figure 5.17-E).

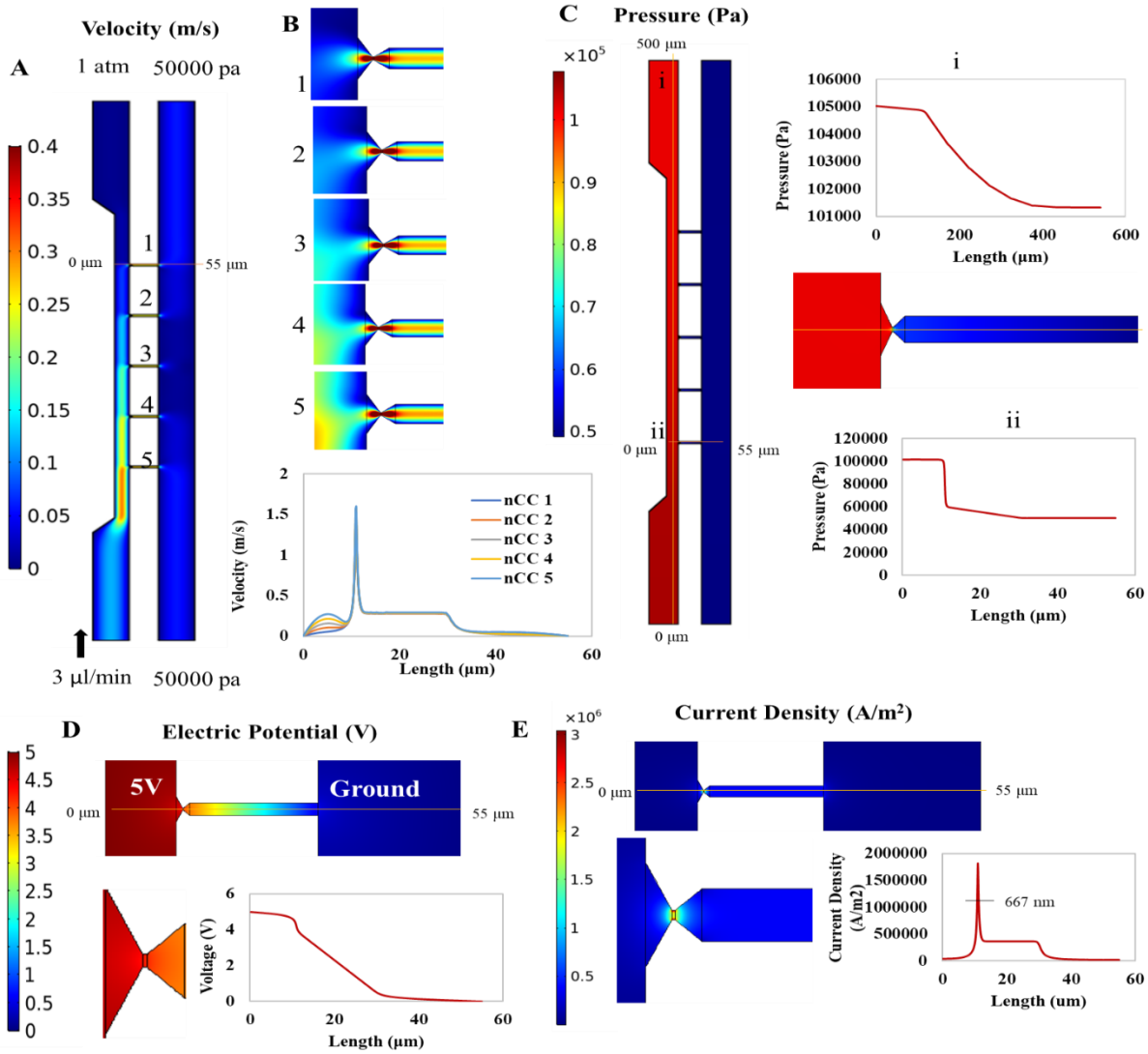

Figure 5.17 COMSOL simulation of iteration 4 design. A) The velocity profile with the inlets set to atmospheric pressure on one side of the inlet and the other side at a flow rate of 3 µL/min. The outlets were set to a pressure 50000 Pa (estimated from the pressure sensor). The fluid from the inlet side are seen entering the outlet side due to the difference in pressure drop. B) The magnified image showing the higher velocity in the nCC and the line graph shows the velocity profiles across all the 5 nCCs. C) Pressure drops across the 5 in-plane nCC; i) The pressure drop in the inlet microchannel showing a small pressure drop of 3500 Pa; ii) The pressure drop across the nCC showing the majority of the pressure drop occurring across the nCC. D) Potential drop across the 5 nCC in-plane nanopore sensors. A 2-dimensional line plot of potential drop versus distance across one of the nCC in-plane nanopore sensors. The potential drop across the nCC represents 10% of the total voltage drop across the sensor (5.0 V). E) The current density profile plotted from the voltage profile to estimate the effective length of the pore at FWHM, which is ~667 nm for a pore width of 350 nm.

5.6.5.4 Estimation of pressure at outlet channel under vacuum withdrawal

While the first two conditions mentioned above were satisfied by making changes to the design, increasing the pressure drop across the nCC was achieved by utilizing a vacuum pump to withdraw the sample. The working principle and new schematic of our final design is shown in Figure 5.18. The modified

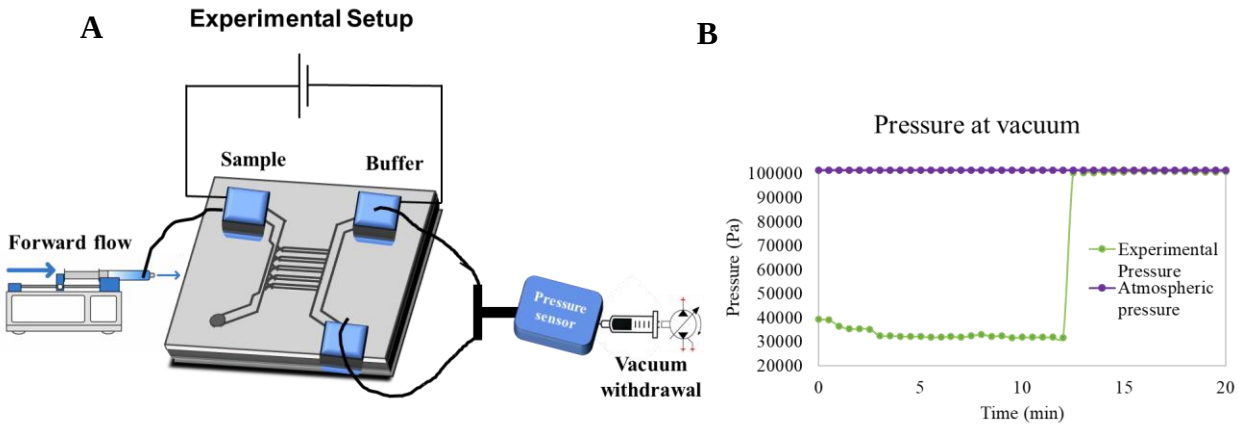

Figure 5.18 A) Final design experimental setup that features a forward flow for the sample to be injected at ~ 3 µL/min. The buffer ends are connected to a vacuum pump to increase the pressure drop across the nCC. The pressure sensor is inserted to quantitatively measure the increase in pressure drop. B) The pressure sensor was connected to the buffer ends using a T shaped connector and reading was recorded for 12 min with the pump on. The pressure drop reportedly increased from ~4000 Pa to ~60,000 Pa for the time the pump was on. Once the vacuum was disconnected the pressure increased to the atmospheric level for the next 8 min of the recorded time interval.

experimental set up had a pump for the forward flow, which delivers the sampling region of the device. The two outlets on the buffer side were connected via a T-shaped connector to a vacuum pump (Figure 5.18-A). Simulations and experiments performed in the previous iteration with a withdrawal flow rate of 20 µL/min gave a pressure drop of ~4000 Pa. This pressure drop was minimally sufficient to withdraw fluid from the sample microchannel and through the nanopores. Therefore, the withdrawal was performed using a vacuum pump to increase the pressure drop. In this iteration, the withdrawal line was connected to both reservoirs flanking the output microchannel and the pressure sensor was connected to the withdrawal line to determine the pressure drop induced by the vacuum pump; the measurement proceeded for a period of 12 min followed by switching off the vacuum to see if the vacuum held (Figure 5.18-A). Figure 5.18-B shows the pressure drop generated across the nCC by the vacuum pump. As can be seen, the pressure level was quite stable (~40,000 Pa) when the vacuum was ON. Once the withdrawal vacuum was terminated, the

pressure returned to atmospheric pressure indicating that the withdrawal was only effective when the vacuum pump was running. The pressure drop was increased from 4,000 Pa to 60,000 Pa using the vacuum pump.

5.6.5.5 Effect of forward flow rate on the number of current transient events

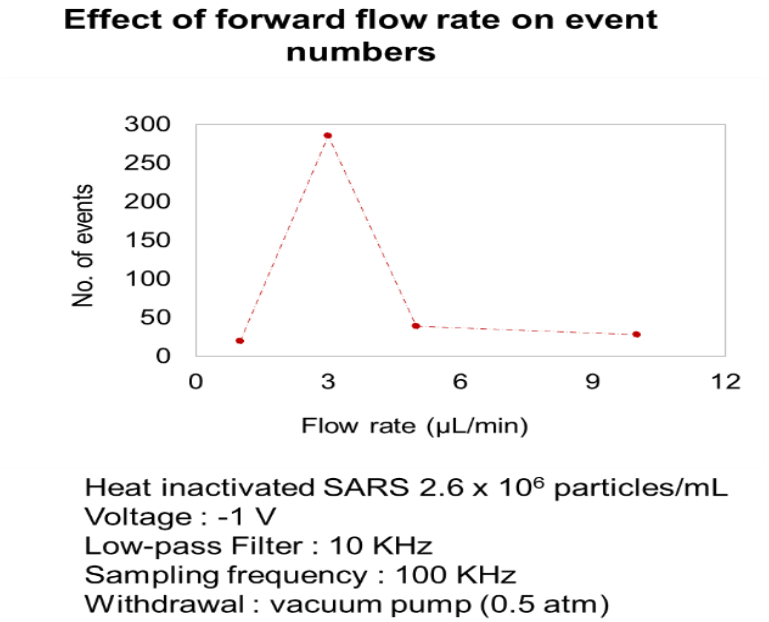

Figure 5.19 Graph showing the effect of varying the forward flow to the number of peaks obtained. The device was set up to simultaneously have a withdrawal using a vacuum pump. The data was recorded for a period of 300 s.

Over the course of the nCC measurements, it was necessary to have a continuous supply of sample to the microchannel sampling region of the nCC device. Therefore, we ran a SARS CoV-2 particle suspension (2.6 x 10^6 particles/mL) through the nCC chip at various volume flow rates to deliver particles to the sampling region. A potential of -1 V was applied at the sample end and the outlet was connected to the vacuum pump withdrawing fluid at 0.5 atm. The inlet flow rate ranged from 1 µL/min to 10 µL/min to test the effects on the number of events detected. The inlet of the sampling microchannel was set up to have a forward flow. The outlet ends were connected to the vacuum pump to continuously withdraw the sample. Figure 5.19-A shows the event number for a counting period of 300 s as a function of volume flow rate. It can be seen that the number of events at 3 µL/min was higher (285) compared to the other flow rates, with 1 µl/min being the lowest. The reason for these results could be due to the fact that at 1 µl/min there is not

enough sample brought into the region near the microchannel/nanochannel interface. However, at flow rates higher than 3 μl/min, the velocity at which the sample flows become increasing high such that fewer particles have the opportunity to be drawn into the pores. The pressure drop in the sample inlet microchannel and across the nCC at 3 μl/min inflow and the outlet held at 50,000 Pa is shown in simulations (Figure 5.17). For our experiments, we therefore decided to use 3 μl/min as the forward flow while simultaneously using vacuum withdrawal. The data traces shown are baseline subtracted and filtered using 400 Hz high pass filter.

5.6.5.6 Determining event width at full width half-maximum (FWHM) and amplitude at 3 μl/min in-flow rate and -1 V

From the experiment above, we chose SARS CoV-2 particle nCC detection using a forward flow rate of 3 μL/min and a vacuum pump simultaneously withdrawing fluid to evaluate the performance of the nCC possessing an ~350 nm effective diameter and 5 pores placed in parallel. We determined the average width of the current transient events at half-height and the average event amplitude distributions. The inlet and the buffer side were connected to an Axopatch 200B using Ag/AgCl electrodes for recording electrical signals when a potential of -1 V was applied to the inlet side and grounded at the outlet side of the device. Figure 5.20-A shows representative trace events distributed over a 1 s time interval. Magnified images of two random peaks are shown with their respective amplitudes of 250 pA and 300 pA. A threshold level was set to 65 pA, which was set with respect to background (*i.e.*, open pore current) and reduce the false positive rate to 0 over the 300 s counting interval. The peak amplitude histogram showed that there was a range of amplitudes for the events collected under the aforementioned conditions, which ranged from 66 pA to 1000 pA; Figure 5.20-B), with an average amplitude of 204 pA. The half-width distribution shows the width of the peaks at FWHM, which ranged from 0.02 ms to 3 ms.(Figure 5.20-C). The sampling frequency was 100,000 Hz, which translated into data collected every 0.01 ms. A peak was considered an event only if it had more than one data point per peak; multiple peaks having an amplitude greater than the threshold but having a half-width less than 0.02 ms were not considered true events. The average half width of the peaks

was found to be 0.6 ms and the average width of the events at the base was 1.27 ms. The numbers show that the sampling frequency is sufficient (60 data points for a 0.6 ms half-width and 127 data points for a 1.27 ms event) and that the shape of the events is not distorted. (signal aliasing).

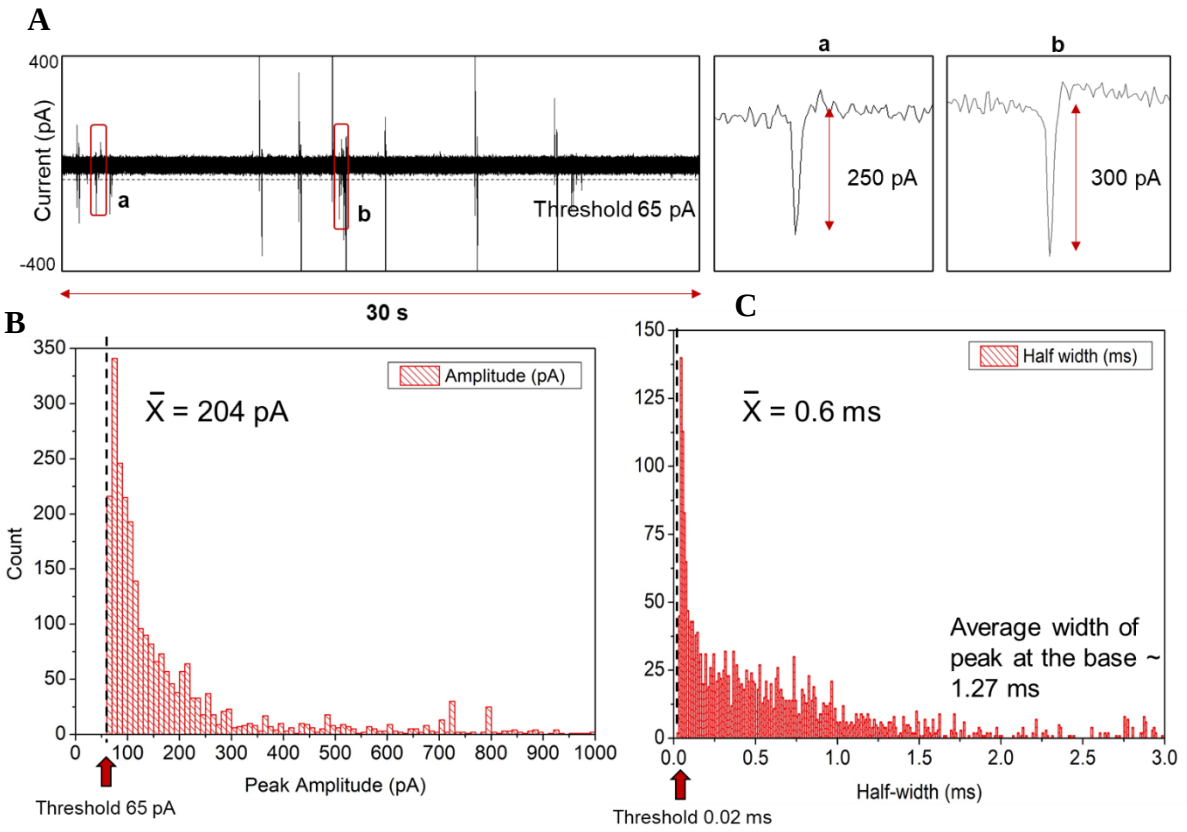

Figure 5.20 A) Representative data trace showing the SARS stock diluted 100 X times. The events are shown as peaks showing a drop in the current amplitude. The threshold is set to 65 pA, beyond which the peaks are considered as events. Two random events (a) and (b) are magnified showing the peak amplitudes of 250 and 300 pA respectively. B) The peak amplitude histogram showing the distribution of the event amplitudes is shown. The amplitudes range from 66 pA to 1000 pA, with an average amplitude of 204 pA. C) The half-width of the peaks showing the width at FWHM corresponding to the events obtained in the peak amplitude graph. The half-width in ms ranges from 0.02 to 3 ms, with an average half-width of 0.6 ms.

5.6.5.7 Determining event width at FWHM and amplitude at 3 µl/min in-flow rate and -5 V

Because SARS CoV-2 particles have a negative zeta potential,[90] the applied DC bias voltage was increased from -1 V to -5 V on the inlet side and the corresponding event half-width and amplitude were evaluated at 3 µl/min inflow rate to test if the applied potential had any effect on the translocation of VPs through the nCC. A representative trace (Figure 5.21-A) shows the data recorded for a period of 30 s for SARS CoV-2 VPs having a concentration of 520,000 VPs/mL. The sampling frequency was set to 100 KHz

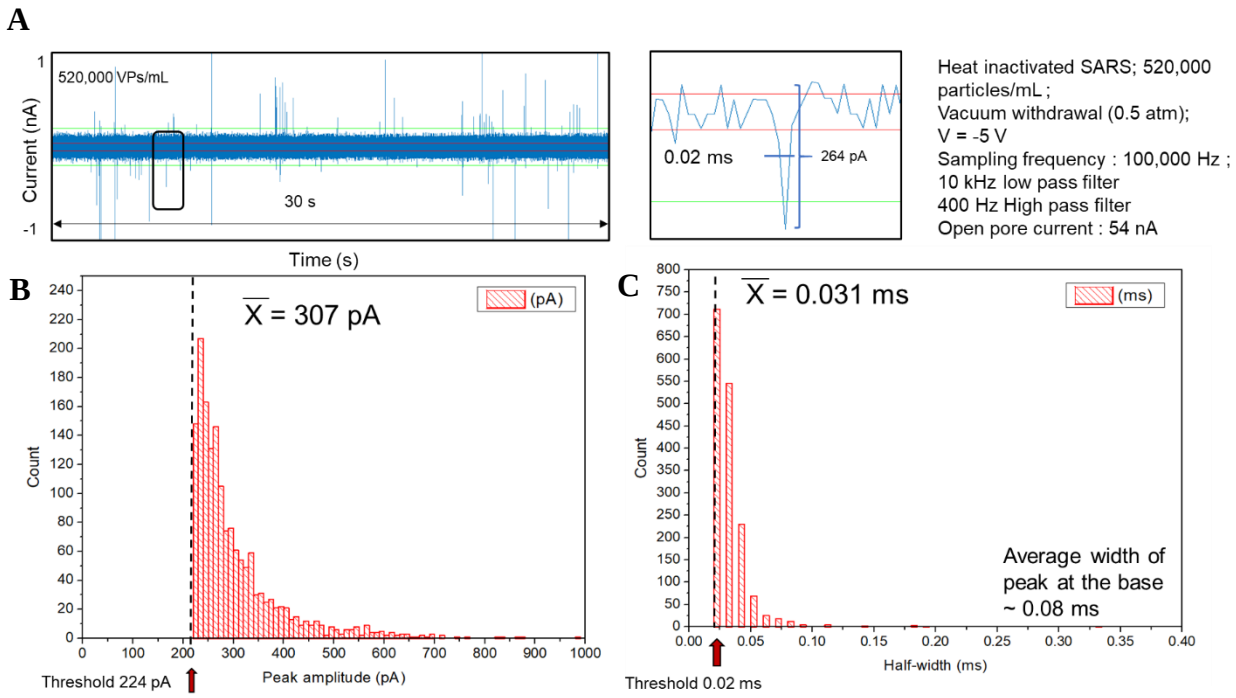

Figure 5.21 A) Processed representative data trace of dilution A (520,000 VPs/mL) with events spanned over a 30 s time interval. The peak shape of one event in magnified that shows a peak amplitude of 264 pA and a half-width of 0.02 ms. B) Histogram showing the distribution of peak amplitudes with an average peak amplitude of 307 pA. The SD threshold was set to 224 pA, only beyond which the peaks were counted as events. C) The half width distribution of the events is shown with events ranging from 0.02 ms to 0.10 ms, having an average half-width of 0.031 ms.

and the peaks were considered events only if they had a minimum of two data points (0.02 ms). An expanded view of a single peak is shown having a half-width of 20 µs (0.02 ms) and an event amplitude of 264 pA. The average peak amplitude was estimated to be 307 pA (Figure 5.21-B) with an average half-width of 0.031 ms (Figure 5.21-C). The average width of the peaks at the base was calculated to be 0.08 ms. There was an increase in baseline due to an increase in the applied voltage (from -1 V to -5 V), which increased the threshold value (65 pA to 224 pA) and correspondingly the average event amplitude increased from 204 pA to 307 pA. Compared to the -1 V data, there was a reduction in the average half-width of events from 0.8 ms to 0.031 ms (Figure 5.21-D). This could be attributed to the higher bias voltage, which induced a higher electrophoretic force that influenced the SARS particles (negatively charged) to translocate faster through the nCC.[90] However, the pulse duration calculated from COMSOL simulations was 0.45 µs. There appears to be a 100 fold difference in the simulated pulse duration versus the experimental result (0.031ms). This result could be attributed to the following reasons: The simulations

include an electric current component to determine the current density; but however, the electroosmotic component has not been included. The thermoplastic material, COP was activated with UV/O_3 before thermal fusion bonding to include carboxylic groups (-COOH), which impart a negative charge to the plastic thus introducing an electroosmotic flow.[91] The charge of the SARS CoV-2 particles is known to have a negative zeta potential (~ -25 mV) and are seen to migrate electrophoretically, which was evident from the reduction of the half-width (0.6 ms to 0.031 ms) of the events when the applied potential was increased from -1V to -5V. While the hydrodynamic flow is not influenced by the electroosmotic effects (the hydrodynamic and electrophoretic flow are in the same direction), the electrophoretic and the electroosmotic flow are said to be in the opposite directions, thus reducing the overall translocation velocity of the SARS CoV-2 particles experimentally. Furthermore, 2D COMSOL simulations do not account for the asymmetry in the pore that is attributed by the Z-direction (depth) of the pore, which gives rise to the possibility of the particles blocking various parts of the nCC while translocating. This can impact both amplitude and half-width differences on the particles translocating through the nCC.

5.6.5.8 Calibration curve for VP counting using iteration 4

To determine if the changes enveloped into iteration 4 significantly improved the concentration limit-of-detection compared to the single pore device shown in Figure 5.7, we generated a calibration plot using standard SARS-CoV-2 solutions. The concentration of the SARS-CoV-2 stock was estimated using nanoparticle tracking analysis (NTA) from which the concentration was calculated to be 7.8 x 10^9 particles/mL (Figure 5.22-A). From the NTA trace, the average size of the SARS CoV-2 particles was estimated to be 143.7 nm ±5 nm. The standard solutions and the corresponding concentrations (VPs/mL) are given in the table found in Figure 5.22-B. The experimental setup for the calibration curve collection was as follows: We used a custom-made Transimpedance Amplifier (TIA) for nanoparticle counting that delivered a DC voltage up to -5 V. The device was placed inside a custom made Faraday cage and each

dilution was performed from the lowest to the highest concentration using an nCC chip. The sample was filled at the inlet channel and 1X PBS was filled in the other microchannel. One end of the sample microchannel was connected to a syringe pump that infused the sample at 3 µL/min, while the other end

A

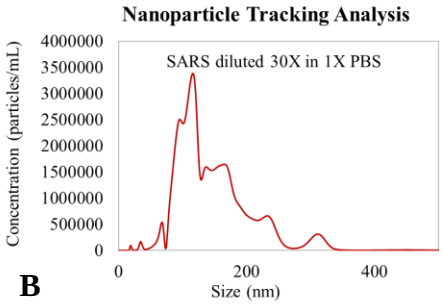

B

Concentration of original stock : 7.8 x 10^9 particles/mL

Average particle size : 143.7 +/- 4.9 nm

Dilution ID	Concentration (VP/mL)
A	520,000
B	104,000
C	52,000
D	10,000
E	5,200

C

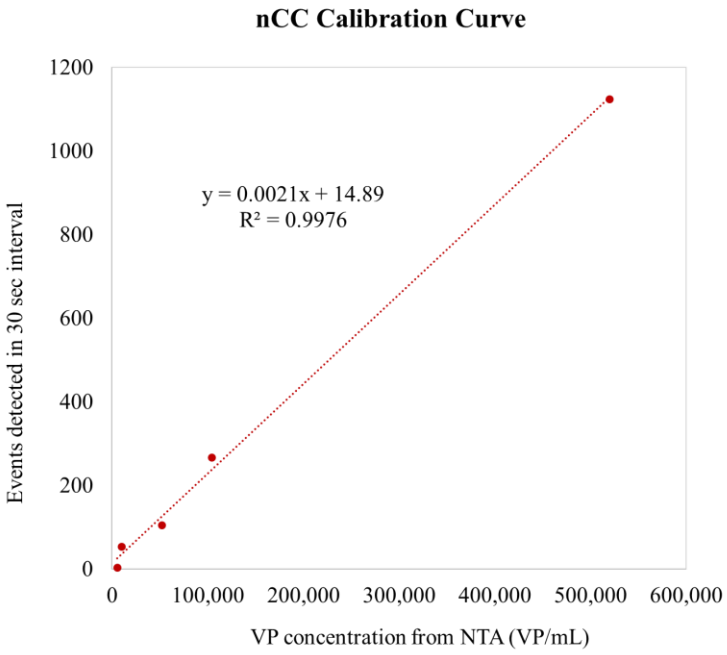

Figure 5.22 A) NTA results of SARS CoV-2 VPs diluted 30X showing the size distribution of the particles (average ~43 nm) and the concentration, from which he concentration of the original stock is estimated to be 7.8 x 10^9 particles/mL. B) The dilution ID with the corresponding concentration of VPs/mL used for the calibration curve. C) Results of the calibration curve calculated from nCC showing the VPs concentration/mL and the events detected in a 30 s time interval for various dilutions.

was placed at atmospheric pressure. Both buffer or outlet reservoirs were connected to a T-shaped connector leading to the vacuum pump for withdrawal and the pressure sensor to track the pressure drop in the system. The electrodes were placed within reservoirs on both microchannels such that a potential of -5 V was applied across the nCC. The calibration curve was built from each standard solution based on the average number of events observed over a defined counting interval with respect to the concentration of VPs for the corresponding dilution estimated from the NTA (Figure 5.22-C).

As can be seen from the calibration plot, we saw that there was a direct correlation to the number of events observed and the concentration, where the number of events decreased as the concentration of

VPs in the standard solutions decreased. A highly linear curve with an R^2 of 0.9976, and a slope 0.0021 was calculated. (see Figure 5.22-C). In the case of dilution E, 4 events were observed over a 30 s interval with a SD of 1.7 (RSD = 43%). The LOD obtained from the calibration curve was estimated to be 2.43 x 10^3 particles/mL with a sampling efficiency of 1.6 x 10^{-2} % and the lower limit of quantification (LOQ) was 8.10 x 10^3 particles/mL (The LOQ of an analytical procedure is measured by the lowest amount sample that can be quantitatively determined with precision and accuracy).[86] The LOD improved from 10^5 particles/mL in iteration 1 to 10^3 particles/mL and the sampling efficiency increased from 4.5 x 10^{-4} % to 1.6 x 10^{-2} % with the modified final design and the experimental set up that resulted from extensive simulation results and experimentation. Overall, there was a 100-fold improvement in both the LOD and sampling efficiency with our final design iteration compared to the single pore device (iteration 1).

A representative trace showing the events recorded for 100 s for a negative control of 1X PBS, where no peaks were seen crossing the threshold (131 pA; green line, Figure 5.23-A). A magnified view of the PBS data showing the data trace for a time interval of 10 ms is shown. Figure 5.23-B shows the data recorded for a 100 s duration for SARS CoV-2 particles having a concentration of 52,000 VPs/mL. Events having both a positive and negative polarity were observed. Magnified events in the dilution are shown: (a) a negative event having an amplitude of 255 pA with a half-width of 0.03 ms; (b) a negative event having an amplitude of 420 pA with a half-width of 0.02 ms. However, this event also showed a small shoulder (positive polarity). These types of events are called biphasic pulses, which are a typical observation in particles that have a higher surface charge, which caused the particles to temporarily become more conductive than the electrolyte thus generating a positive pulse.[92] This is subsequently followed by volume exclusion of the particle causing the generation of a negative pulse.[92-93] In this case, only the negative pulse was scored as an event. (c) Negative and positive events occurring at close intervals of time (0.29 s). These events appear as two discrete events and are not biphasic. The first pulse is a positive event that has an amplitude of 229 nA and a half-width of 0.03 ms, while the second pulse has an amplitude and half-width of 230 pA and 0.02 ms respectively. The reason for generation of positive pulses is due to the local modulation of the ionic concentration, where the surface charge of the particle adds to the existing ionic

concentration that causes an increase in conductivity in the nCC when the particle translocates.[92-93] Moreover, there is a possibility that particles could be porous causing it to become more conductive than the carrier electrolyte, which in this case was 1X PBS that has a relatively low ionic concentration of ~162.7 mM. The result would be positive polarity peaks. In the case of negative polarity peaks, a volume exclusion process induced by a lower conductivity particle compared to the carrier electrolyte would create such events. We suspect that the positive polarity peaks could be due to exosomes present in the SARS-CoV-2 suspension, which were secured from cell culture medium and thus, contain exosomes as well. The negative

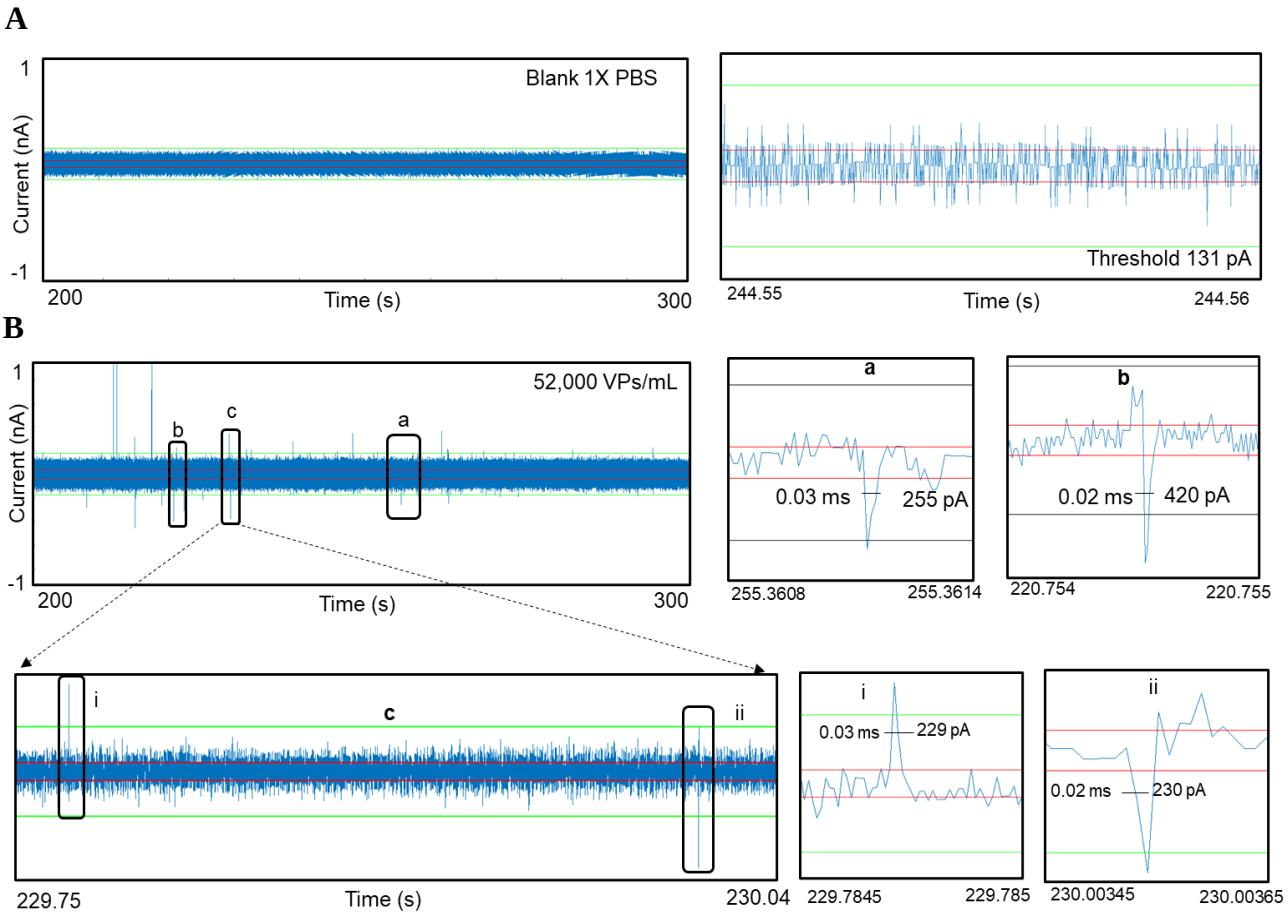

Figure 5.23 A) Processed data showing the negative control, blank 1X PBS for a period of 100 s, with no apparent events crossing the threshold. The magnified image of the 1X PBS for a duration of 0.01 s is correspondingly shown. B) Representative data trace of dilution A (52,000 VPs/mL) with events spanned over the same 100 s time interval. (a) The peak shape of a negative event is magnified that shows a peak amplitude of 255 pA and a half-width of 0.02 ms. (b) shows a negative event with a positive shoulder (biphasic pulse) having an amplitude of 420 pA and a half-width of 0.02 ms. (c) shows a negative and positive event occurring in a close interval (0.29 ms). Magnified images of the event are shown where the positive pulse has an amplitude of 229 pA and a half-width of 0.03 ms, followed by the negative event having an amplitude of 230 pA and a half-width of 0.02 ms

polarity peaks are due to the SARS-CoV-2 VPs. We are carrying out further experiments to prove/disprove these suppositions.

5.7 Conclusions

Highly accessible screening tests for SARS-CoV-2 infections can be an essential tool for effective containment of COVID-19 because it allows for more frequent testing and provides rapid results as opposed to clinical testing that is performed less frequently because it requires a centralized laboratory (see Figure 5.1). While new at-home technologies for screening that are based on PCR or antibodies are evolving, there are some challenges such as the need for cold storage due to the use of sensitive reagents. An additional challenge with PCR and antibody-based technologies is that they detect those that have COVID-19, but most likely will not report on the active state of the disease causing excessive isolation and/or quarantines.

To address these challenges, we presented a technology to identify those that have been infected with SARS-CoV-2. Unique to our technology is the ability to select intact SARS-CoV-2 VPs from the sample and perform label-free counting of the VPs following selection and blue-light release of the intact VPs. We envision our technology for immediate use by first-contact healthcare professionals at the POC and then, due to the simplicity of the instrumentation and ease of use, home-based testing. The nCC devices, which were made from thermoplastics, can be fabricated by injection molding that is conducive to high-scale production at low cost appropriate for large-scale screening tests.

We started from a single nCC device that was capable of enumerating viral particles having a concentration of 10^5 particles/mL and above. Because this concentration limit may not be fully relevant to clinical viral load, we fabricated a 5 nCC device to improve the sampling efficiency and the LOD. The nCC device went through multiple iterations (1-4) before we arrived at an optimal design that enabled us to reach the analytical figures-of-merit that were competitive to PCR-based testing, which suggested that we could rapidly detect single VPs using a nCC that possessed 5 counters in parallel, but could be further scaled by adding additional parallel pores. The calibration plot can be utilized to test clinical samples to establish the concentration/severity of the disease in patients by monitoring the number of events obtained from the nCC.

The peak amplitude histogram data suggested that the SARS CoV-2 particles having a size of ~150 nm gives rise to events of ~307 pA with an average transit time of 0.031 ms (-5V).

Following testing of clinical samples using our technology platform, we envision packaging the assay into a small footprint (handheld) for potential at-home testing using our SARS-CoV-2 assay. The chip operation and supporting equipment need to be packaged into a handheld instrument with full sample processing automation. To realize this, our team is currently working on a new integrated chip design and handheld instrument. The chip measures 38 x 42 mm in size and consists of 3 layers including a cover plate with electrical connects for the nCC, a layer containing the VP selection step, and the final layer consisting of the fluidic network for nCC enumeration of selected and subsequently released via blue light VPs. The integrated chip, which is made entirely from plastics to allow for injection molding, fits into the handheld instrument and contains a port that allows for sample introduction, which in this case consists of saliva. However, other samples can be inserted into the instrument as well.

5.8 References

1. Kozak, D.; Anderson, W.; Vogel, R.; Trau, M., Advances in resistive pulse sensors: Devices bridging the void between molecular and microscopic detection. *Nano Today* **2011,** *6* (5), 531-545.
2. Peeri, N. C.; Shrestha, N.; Rahman, M. S.; Zaki, R.; Tan, Z.; Bibi, S.; Baghbanzadeh, M.; Aghamohammadi, N.; Zhang, W.; Haque, U., The SARS, MERS and novel coronavirus (COVID-19) epidemics, the newest and biggest global health threats: what lessons have we learned? *Int J Epidemiol* **2020,** *49* (3), 717-726.
3. Ye, Z.-W.; Yuan, S.; Yuen, K.-S.; Fung, S.-Y.; Chan, C.-P.; Jin, D.-Y., Zoonotic origins of human coronaviruses. *International journal of biological sciences* **2020,** *16* (10), 1686.
4. Chen, Y.; Liu, Q.; Guo, D., Emerging Coronaviruses: Genome Structure, Replication, and Pathogenesis. *Journal of Medical Virology* **2020,** *92*, 418-423.
5. Vabret, A.; Dina, J.; Brison, E.; Brouard, J.; Freymuth, F., Coronavirus humains (HCoV). *Pathologie Biologie* **2009,** *57* (2), 149-160.
6. Cui, J.; Li, F.; Shi, Z. L., Origin and evolution of pathogenic coronaviruses. *Nat Rev Microbiol* **2019,** *17* (3), 181-192.
7. Bárcena, M.; Oostergetel, G. T.; Bartelink, W.; Faas, F. G.; Verkleij, A.; Rottier, P. J.; Koster, A. J.; Bosch, B. J., Cryo-electron tomography of mouse hepatitis virus: insights into the structure of the coronavirion. *Proceedings of the National Academy of Sciences* **2009,** *106* (2), 582-587.
8. Neuman, B. W.; Adair, B. D.; Yoshioka, C.; Quispe, J. D.; Orca, G.; Kuhn, P.; Milligan, R. A.; Yeager, M.; Buchmeier, M. J., Supramolecular architecture of severe acute respiratory syndrome coronavirus revealed by electron cryomicroscopy. *Journal of virology* **2006,** *80* (16), 7918-7928.

9. Wang, Y.; Sun, J.; Zhu, A.; Zhao, J.; Zhao, J., Current understanding of middle east respiratory syndrome coronavirus infection in human and animal models. *Journal of thoracic disease* **2018,** *10* (Suppl 19), S2260.
10. Chen, B.; Tian, E. K.; He, B.; Tian, L.; Han, R.; Wang, S.; Xiang, Q.; Zhang, S.; El Arnaout, T.; Cheng, W., Overview of lethal human coronaviruses. *Signal Transduct Target Ther* **2020,** *5* (1), 89.
11. Lu, R.; Zhao, X.; Li, J.; al., e., Genome Characterization and epidemiology of the 2019 novel coronavirus: Implications for Virus Origins and Receptor Binding. *Lancet* **2020,** *395*, 565-574.
12. Cheng, M. P.; Papenburg, J.; Desjardins, M.; Kanjilal, S.; Quach, C.; Libman, M.; Dittrich, S.; Yansouni, C. P., Diagnostic testing for severe acute respiratory syndrome–related coronavirus-2: A narrative review. *Annals of internal medicine* **2020**.
13. Malik, Y. A., Properties of Coronavirus and SARS-CoV-2. *The Malaysian Journal of Pathology* **2020,** *42* (1), 3-11.
14. Weiss, S. R.; Leibowitz, J. L., Coronavirus pathogenesis. In *Advances in virus research*, Elsevier: 2011; Vol. 81, pp 85-164.
15. Schoeman, D.; Fielding, B. C., Coronavirus envelope protein: current knowledge. *Virology journal* **2019,** *16* (1), 1-22.
16. Holshue, M. L.; DeBolt, C.; Lindquist, S.; Lofy, K. H.; Wiesman, J.; Bruce, H.; Spitters, C.; Ericson, K.; Wilkerson, S.; Tural, A.; Diaz, G.; Cohn, A.; Fox, L.; Patel, A.; Gerber, S. I.; Kim, L.; Tong, S.; Lu, X.; Lindstrom, S.; Pallansch, M. A.; Weldon, W. C.; Biggs, H. M.; Uyeki, T. M.; Pillai, S. K., First Case of 2019 Novel Coronavirus in the United States. *New England Journal of Medicine* **2020,** *382*, 929-936.
17. Hosseini, A.; Pandey, R.; Osman, E.; Victorious, A.; Li, F.; Didar, T.; Soleymani, L., Roadmap to the Bioanalytical Testing of COVID-19: From Sample Collection to Disease Surveillance. *ACS sensors* **2020**.
18. Lambert-Niclot, S.; Cuffel, A.; Le Pape, S.; Vauloup-Fellous, C.; Morand-Joubert, L.; Roque-Afonso, A.-M.; Le Goff, J.; Delaugerre, C., Evaluation of a rapid diagnostic assay for detection of SARS CoV-2 antigen in nasopharyngeal swab. *Journal of clinical microbiology* **2020**.
19. Nagura-Ikeda, M.; Imai, K.; Tabata, S.; Miyoshi, K.; Murahara, N.; Mizuno, T.; Horiuchi, M.; Kato, K.; Imoto, Y.; Iwata, M., Clinical evaluation of self-collected saliva by RT-qPCR, direct RT-qPCR, RT-LAMP, and a rapid antigen test to diagnose COVID-19. *Journal of Clinical Microbiology* **2020**.
20. Grant, B. D.; Anderson, C. E.; Williford, J. R.; Alonzo, L. F.; Glukhova, V. A.; Boyle, D. S.; Weigl, B. H.; Nichols, K. P., SARS-CoV-2 coronavirus nucleocapsid antigen-detecting half-strip lateral flow assay toward the development of point of care tests using commercially available reagents. *Analytical chemistry* **2020,** *92* (16), 11305-11309.
21. Matthews, Q.; da Silva, S. J. R.; Norouzi, M.; Pena, L. J.; Pardee, K., Adaptive, diverse and de-centralized diagnostics are key to the future of outbreak response. *BMC biology* **2020,** *18* (1), 1-5.
22. Liu, Y.; Liu, Y.; Diao, B.; Ren, F.; Wang, Y.; Ding, J.; Huang, Q., Diagnostic Indexes of a Rapid IgG/IgM Combined Antibody Test for SARS-CoV-2. *medRxiv* **2020**.
23. Chen, Z.; Zhang, Z.; Zhai, X.; Li, Y.; Lin, L.; Zhao, H.; Bian, L.; Li, P.; Yu, L.; Wu, Y., Rapid and Sensitive Detection of anti-SARS-CoV-2 IgG, Using Lanthanide-Doped Nanoparticles-Based Lateral Flow Immunoassay. *Analytical chemistry* **2020,** *92* (10), 7226-7231.
24. https://www.fda.gov/medical-devices/coronavirus-disease-2019-covid-19-emergency-use-authorizations-medical-devices/vitro-diagnostics-euas#individual-serological (accessed 11.15.20).
25. Mertens, P.; De Vos, N.; Martiny, D.; Jassoy, C.; Mirazimi, A.; Cuypers, L.; Van den Wijngaert, S.; Monteil, V.; Melin, P.; Stoffels, K., Development and potential usefulness of the

COVID-19 Ag Respi-Strip diagnostic assay in a pandemic context. *Frontiers in Medicine* **2020,** *7*, 225.
26. Mak, G. C.; Cheng, P. K.; Lau, S. S.; Wong, K. K.; Lau, C.; Lam, E. T.; Chan, R. C.; Tsang, D. N., Evaluation of rapid antigen test for detection of SARS-CoV-2 virus. *Journal of Clinical Virology* **2020**, 104500.
27. Mina, M. J.; Parker, R.; Larremore, D. B., Perspective: Rethinking Covid-19 Test Sensitivity — A Strategy for Containment. *New England Journal of Medicine* **2020,** *382*, 1-3.
28. He, X.; Lau, E. H. Y.; Wu, P.; Deng, X.; Wang, J.; Hao, X.; Lau, Y. C.; Wong, J. Y.; Guan, Y.; Tan, X.; Mo, X.; Chen, Y.; Liao, B.; Chen, W.; Hu, F.; Zhang, Q.; Zhong, M.; Wu, Y.; Zhao, L.; Zhang, F.; Cowling, B. J.; Li, F.; Leung, G. M., Temporal dynamics in viral shedding and transmissibility of COVID-19. *Nature Medicine* **2020,** *26*, 672-675.
29. Jiang, S.; Hillyer, C.; Du, L., Neutralizing Antibodies against SARS-CoV-2 and Other Human Coronaviruses. *Trends in Immunology* **2020**.
30. Wrapp, D.; Wang, N.; Corbett, K. S.; Goldsmith, J. A.; Hsieh, C.-L.; Abiona, O.; Graham, B. S.; McLellan, J. S., Cryo-EM structure of the 2019-nCoV spike in the prefusion conformation. *Science* **2020,** *367* (6483), 1260-1263.
31. Song, Y.; Song, J.; Wei, X.; Huang, M.; Sun, M.; Zhu, L.; Lin, B.; Shen, H.; Zhu, Z.; Yang, C., Discovery of Aptamers Targeting Receptor-Binding Domain of the SARS-CoV-2 Spike Glycoprotein. **2020**.
32. Pahattuge, T. N.; Jackson, J. M.; Digamber, R.; Wijerathne, H.; Brown, V.; Witek, M. A.; Perera, C.; Givens, R. S.; Peterson, B. R.; Soper, S. A., Visible photorelease of liquid biopsy markers following microfluidic affinity-enrichment. *Chemical Communications* **2020,** *56* (29), 4098-4101.
33. Maas, S. L.; Broekman, M. L.; de Vrij, J., Tunable resistive pulse sensing for the characterization of extracellular vesicles. In *Exosomes and Microvesicles*, Springer: 2017; pp 21-33.
34. Anderson, W.; Lane, R.; Korbie, D.; Trau, M., Observations of tunable resistive pulse sensing for exosome analysis: improving system sensitivity and stability. *Langmuir* **2015,** *31* (23), 6577-6587.
35. Shapiro, H. M., The evolution of cytometers. *Cytometry. Part A : the journal of the International Society for Analytical Cytology* **2004,** *58* (1), 13-20.
36. Davey, H. M.; Kell, D. B., Flow cytometry and cell sorting of heterogeneous microbial populations: the importance of single-cell analyses. *Microbiological Reviews* **1996,** *60* (4), 641-696.
37. Javanmard, M.; Davis, R. W., A microfluidic platform for electrical detection of DNA hybridization. *Sensors and Actuators B: Chemical* **2011,** *154* (1), 22-27.
38. Javanmard, M.; Emaminejad, S.; Dutton, R. W.; Davis, R. W., Use of Negative Dielectrophoresis for Selective Elution of Protein-Bound Particles. *Analytical Chemistry* **2012,** *84* (3), 1432-1438.
39. Emaminejad, S.; Javanmard, M.; Dutton, R. W.; Davis, R. W., Microfluidic diagnostic tool for the developing world: contactless impedance flow cytometry. *Lab on a Chip* **2012,** *12* (21), 4499-4507.
40. Emaminejad, S.; Javanmard, M.; Dutton, R. W.; Davis, R. W., Smart Surface for Elution of Protein–Protein Bound Particles: Nanonewton Dielectrophoretic Forces Using Atomic Layer Deposited Oxides. *Analytical Chemistry* **2012,** *84* (24), 10793-10801.
41. Song, Y.; Zhang, J.; Li, D., Microfluidic and Nanofluidic Resistive Pulse Sensing: A Review. *Micromachines* **2017,** *8* (7), 204.
42. Kasianowicz, J. J.; Brandin, E.; Branton, D.; Deamer, D. W., Characterization of individual polynucleotide molecules using a membrane channel. *Proceedings of the National Academy of Sciences* **1996,** *93* (24), 13770-13773.

43. Billinge, E. R.; Broom, M.; Platt, M., Monitoring Aptamer–Protein Interactions Using Tunable Resistive Pulse Sensing. *Analytical Chemistry* **2014,** *86* (2), 1030-1037.
44. Huang, S. T.; Yang, L. F.; Li, N. B.; Luo, H. Q., An ultrasensitive and selective fluorescence assay for Sudan I and III against the influence of Sudan II andIV. *Biosensors and Bioelectronics* **2013,** *42*, 136-140.
45. Yang, J.; Ferranti, D. C.; Stern, L. A.; Sanford, C. A.; Huang, J.; Ren, Z.; Qin, L.-C.; Hall, A. R., Rapid and precise scanning helium ion microscope milling of solid-state nanopores for biomolecule detection. *Nanotechnology* **2011,** *22*, 285310.
46. Kühnemund, M.; Nilsson, M., Digital quantification of rolling circle amplified single DNA molecules in a resistive pulse sensing nanopore. *Biosensors and Bioelectronics* **2015,** *67*, 11-17.
47. Traversi, F.; Raillon, C.; Benameur, S. M.; Liu, K.; Khlybov, S.; Tosun, M.; Krasnozhon, D.; Kis, A.; Radenovic, A., Detecting the translocation of DNA through a nanopore using graphene nanoribbons. *Nature Nanotechnology* **2013,** *8* (12), 939-945.
48. Rodriguez-Trujillo, R.; Ajine, M. A.; Orzan, A.; Mar, M. D.; Larsen, F.; Clausen, C. H.; Svendsen, W. E., Label-free protein detection using a microfluidic Coulter-counter device. *Sensors and Actuators B: Chemical* **2014,** *190*, 922-927.
49. Cai, H.; Wang, Y.; Yu, Y.; Mirkin, M. V.; Bhakta, S.; Bishop, G. W.; Joshi, A. A.; Rusling, J. F., Resistive-Pulse Measurements with Nanopipettes: Detection of Vascular Endothelial Growth Factor C (VEGF-C) Using Antibody-Decorated Nanoparticles. *Analytical Chemistry* **2015,** *87* (12), 6403-6410.
50. Han, Y.; Wu, H.; Liu, F.; Cheng, G.; Zhe, J., Label-Free Biomarker Assay in a Microresistive Pulse Sensor via Immunoaggregation. *Analytical Chemistry* **2014,** *86* (19), 9717-9722.
51. Takakura, T.; Yanagi, I.; Goto, Y.; Ishige, Y.; Kohara, Y., Single-molecule detection of proteins with antigen-antibody interaction using resistive-pulse sensing of submicron latex particles. *Applied Physics Letters* **2016,** *108* (12), 123701.
52. Vogel, R.; Willmott, G.; Kozak, D.; Roberts, G. S.; Anderson, W.; Groenewegen, L.; Glossop, B.; Barnett, A.; Turner, A.; Trau, M., Quantitative Sizing of Nano/Microparticles with a Tunable Elastomeric Pore Sensor. *Analytical Chemistry* **2011,** *83* (9), 3499-3506.
53. Roberts, G. S.; Yu, S.; Zeng, Q.; Chan, L. C. L.; Anderson, W.; Colby, A. H.; Grinstaff, M. W.; Reid, S.; Vogel, R., Tunable pores for measuring concentrations of synthetic and biological nanoparticle dispersions. *Biosensors and Bioelectronics* **2012,** *31* (1), 17-25.
54. Fraikin, J.-L.; Teesalu, T.; McKenney, C. M.; Ruoslahti, E.; Cleland, A. N., A high-throughput label-free nanoparticle analyser. *Nature Nanotechnology* **2011,** *6* (5), 308-313.
55. Kozak, D.; Anderson, W.; Vogel, R.; Chen, S.; Antaw, F.; Trau, M., Simultaneous Size and ζ-Potential Measurements of Individual Nanoparticles in Dispersion Using Size-Tunable Pore Sensors. *ACS Nano* **2012,** *6* (8), 6990-6997.
56. Vogel, R.; Anderson, W.; Eldridge, J.; Glossop, B.; Willmott, G., A Variable Pressure Method for Characterizing Nanoparticle Surface Charge Using Pore Sensors. *Analytical Chemistry* **2012,** *84* (7), 3125-3131.
57. Arjmandi, N.; Van Roy, W.; Lagae, L.; Borghs, G., Measuring the Electric Charge and Zeta Potential of Nanometer-Sized Objects Using Pyramidal-Shaped Nanopores. *Analytical Chemistry* **2012,** *84* (20), 8490-8496.
58. Eldridge, J. A.; Willmott, G. R.; Anderson, W.; Vogel, R., Nanoparticle ζ-potential measurements using tunable resistive pulse sensing with variable pressure. *Journal of Colloid and Interface Science* **2014,** *429*, 45-52.
59. Somerville, J. A.; Willmott, G. R.; Eldridge, J.; Griffiths, M.; McGrath, K. M., Size and charge characterisation of a submicrometre oil-in-water emulsion using resistive pulse sensing with tunable pores. *Journal of Colloid and Interface Science* **2013,** *394*, 243-251.

60. Blundell, E. L. C. J.; Vogel, R.; Platt, M., Particle-by-Particle Charge Analysis of DNA-Modified Nanoparticles Using Tunable Resistive Pulse Sensing. *Langmuir* **2016,** *32* (4), 1082-1090.
61. Yang, Y.; Sebra, R.; Pullman, B. S.; Qiao, W. Q.; Peter, I.; Desnick, R. J.; Geyer, C. R.; DeCoteau, J. F.; Scott, S. A., Quantitative and multiplexed DNA methylation analysis using long-read single-molecule real-time bisulfite sequencing (SMRT-BS). *Bmc Genomics* **2015,** *16*.
62. Heider, S.; Metzner, C., Quantitative real-time single particle analysis of virions. *Virology* **2014,** *462-463*, 199-206.
63. Schatten, H., Low voltage high-resolution SEM (LVHRSEM) for biological structural and molecular analysis. *Micron* **2011,** *42* (2), 175-185.
64. Driskell, J. D.; Jones, C. A.; Tompkins, S. M.; Tripp, R. A., One-step assay for detecting influenza virus using dynamic light scattering and gold nanoparticles. *Analyst* **2011,** *136* (15), 3083-90.
65. Nikitin, N.; Trifonova, E.; Evtushenko, E.; Kirpichnikov, M.; Atabekov, J.; Karpova, O., Comparative Study of Non-Enveloped Icosahedral Viruses Size. *PloS one* **2015,** *10* (11), e0142415.
66. DeBlois, R. W.; Bean, C. P., Counting and Sizing of Submicron Particles by the Resistive Pulse Technique. *Review of Scientific Instruments* **1970,** *41* (7), 909-916.
67. Gregg, E. C.; Steidley, K. D., Electrical counting and sizing of mammalian cells in suspension. *Biophys J* **1965,** *5* (4), 393-405.
68. Smythe, W. R., Flow Around a Spheroid in a Circular Tube. *The Physics of Fluids* **1964,** *7* (5), 633-638.
69. Haque, F.; Li, J.; Wu, H.-C.; Liang, X.-J.; Guo, P., Solid-state and biological nanopore for real-time sensing of single chemical and sequencing of DNA. *Nano Today* **2013,** *8* (1), 56-74.
70. Ying, Y.-L.; Cao, C.; Long, Y.-T., Single molecule analysis by biological nanopore sensors. *Analyst* **2014,** *139* (16), 3826-3835.
71. Davenport, M. W.; Healy, K.; Pevarnik, M.; Teslich, N.; Cabrini, S.; Morrison, A.; Siwy, Z. S.; Létant, S. E., The Role of Pore Geometry in Single Particle Detection. *Biophysical Journal* **2013,** *104* (2, Supplement 1), 521a.
72. DeBlois, R. W.; Wesley, R. K., Sizes and concentrations of several type C oncornaviruses and bacteriophage T2 by the resistive-pulse technique. *Journal of virology* **1977,** *23* (2), 227-33.
73. Uram, J. D.; Ke, K.; Hunt, A. J.; Mayer, M., Submicrometer Pore-Based Characterization and Quantification of Antibody–Virus Interactions. *Small* **2006,** *2* (8-9), 967-972.
74. Zhou, K.; Li, L.; Tan, Z.; Zlotnick, A.; Jacobson, S. C., Characterization of Hepatitis B Virus Capsids by Resistive-Pulse Sensing. *Journal of the American Chemical Society* **2011,** *133* (6), 1618-1621.
75. Arjmandi, N.; Van Roy, W.; Lagae, L., Measuring Mass of Nanoparticles and Viruses in Liquids with Nanometer-Scale Pores. *Analytical Chemistry* **2014,** *86* (10), 4637-4641.
76. McMullen, A.; de Haan, H. W.; Tang, J. X.; Stein, D., Stiff filamentous virus translocations through solid-state nanopores. *Nature Communications* **2014,** *5* (1), 4171.
77. Wu, H.; Chen, Y.; Zhou, Q.; Wang, R.; Xia, B.; Ma, D.; Luo, K.; Liu, Q., Translocation of Rigid Rod-Shaped Virus through Various Solid-State Nanopores. *Analytical Chemistry* **2016,** *88* (4), 2502-2510.
78. Farkas, K.; Pang, L.; Lin, S.; Williamson, W.; Easingwood, R.; Fredericks, R.; Jaffer, M. A.; Varsani, A., A Gel Filtration-Based Method for the Purification of Infectious Rotavirus Particles for Environmental Research Applications. *Food and Environmental Virology* **2013,** *5* (4), 231-235.
79. Akpinar, F.; Yin, J., Characterization of vesicular stomatitis virus populations by tunable resistive pulse sensing. *Journal of Virological Methods* **2015,** *218*, 71-76.
80. Harms, Z. D.; Mogensen, K. B.; Nunes, P. S.; Zhou, K.; Hildenbrand, B. W.; Mitra, I.; Tan, Z.; Zlotnick, A.; Kutter, J. P.; Jacobson, S. C., Nanofluidic Devices with Two Pores in Series for Resistive-Pulse Sensing of Single Virus Capsids. *Analytical Chemistry* **2011,** *83* (24), 9573-9578.

81. Zhe, J.; Jagtiani, A.; Dutta, P.; Hu, J.; Carletta, J., A micromachined high throughput Coulter counter for bioparticle detection and counting. *Journal of Micromechanics and Microengineering* **2007,** *17*, 304-313.
82. Pan, Y.; Zhang, D.; Yang, P.; Poon, L. L. M.; Wang, Q., Viral load of SARS-CoV-2 in clinical samples. *The Lancet Infectious Diseases* **2020,** *20* (4), 411-412.
83. Anderson, W.; Lane, R.; Korbie, D.; Trau, M., Observations of Tunable Resistive Pulse Sensing for Exosome Analysis: Improving System Sensitivity and Stability. *Langmuir : the ACS journal of surfaces and colloids* **2015,** *31* (23), 6577-87.
84. Zhou, K.; Li, L.; Tan, Z.; Zlotnick, A.; Jacobson, S. C., Characterization of hepatitis B virus capsids by resistive-pulse sensing. *J Am Chem Soc* **2011,** *133* (6), 1618-21.
85. Yang, L.; Yamamoto, T., Quantification of Virus Particles Using Nanopore-Based Resistive-Pulse Sensing Techniques. *Frontiers in Microbiology* **2016,** *7* (1500).
86. Armbruster, D. A.; Pry, T., Limit of blank, limit of detection and limit of quantitation. *Clin Biochem Rev* **2008,** *29 Suppl 1* (Suppl 1), S49-S52.
87. Low Pass Filter - Passive RC Filter Tutorial. In *Basic Electronics Tutorials*, 2013.
88. Lozano, D.; Cantero, M., Difference Between Analytical Sensitivity and Detection Limit. *American Journal of Clinical Pathology* **1997,** *107* (5), 619-619.
89. Okazaki, S., Resolution limits of optical lithography. *Journal of Vacuum Science & Technology B: Microelectronics and Nanometer Structures Processing, Measurement, and Phenomena* **1991,** *9* (6), 2829-2833.
90. Abhishek, S.; Dolly, K.; Subhadip, G.; Vinoj, G.; Kenneth, C.; Sashwati, R.; Savita, K.; Chandan, S., *Electroceutical Fabric Lowers Zeta Potential and Eradicates Coronavirus Infectivity upon Contact*. 2020.
91. Uba, F. I.; Pullagurla, S.; Sirasunthorn, N.; Wu, J.; Park, S.; Chantiwas, R.; Cho, Y.-K.; Shin, H.; Soper, S. A., Surface charge, electroosmotic flow and DNA extension in chemically modified thermoplastic nanoslits and nanochannels. *Analyst* **2014,** *139*.
92. Menestrina, J.; Yang, C.; Schiel, M.; Vlassiouk, I.; Siwy, Z. S., Charged Particles Modulate Local Ionic Concentrations and Cause Formation of Positive Peaks in Resistive-Pulse-Based Detection. *The Journal of Physical Chemistry C* **2014,** *118* (5), 2391-2398.
93. Weatherall, E.; Willmott, G. R., Conductive and Biphasic Pulses in Tunable Resistive Pulse Sensing. *The Journal of Physical Chemistry B* **2015,** *119* (16), 5328-5335.

Chapter 6: Conclusions and Future Directions: Simulations of Single Molecule Sequencing using X-TOF

6.1 Conclusions

In this dissertation, we carefully examined the use of nanofluidic devices for various diagnostic applications. In chapter 1, we cited extensive literature where researchers have used nanochannels for different applications, from identifying methylation sites to optical and genomic mapping for uncovering sequence variations using nanofluidic devices made in Si and other inorganic materials. The challenge with the use of these materials is that sophisticated equipment and complicated fabrication methods must be employed to deliver the device for the intended application. This is problematic for diagnostic applications because the device must be used a single time and then discarded to eliminate sample carryover artifacts.

Thermoplastics is our choice of material for the myriad of applications and the devices used for clinical applications because they offer significant advantages compared to the other materials in terms of the ease of fabrication, high throughput manufacturing and inexpensive devices making them appropriate for *in vitro* diagnostics. In chapter 2, we investigated the use of nanofluidic channels fabricated in PMMA via NIL with dimensions near the persistence length of double-stranded DNA molecules (~50 nm) to search for abasic sites in DNA molecules and used as an indicator of treatment efficacy for breast cancer patients undergoing chemotherapy with drugs such as Doxorubicin. Fluorescent detection was utilized to identify both the DNA backbone using an intercalating dye and detection of the abasic sites that were labelled with another dye. The use of the nanofluidic network with nanotraps to store the DNA and having 20 nanochannels facilitated simultaneous high throughput detection of the DNA and their abasic sites.

A nanosensor device was built in a subsequent project to specifically identify single nucleotide polymorphisms for major life threatening diseases such as cancer and stroke. This device, which consisted of mixed-scale structures, was developed to perform Ligase Detection Reactions on a solid phase (spLDR) to identify mutations at the single nucleotide level to facilitate precision medicine. In addition, the spLDR with appropriate primers could be used to expression profile mRNAs that were converted to cDNA using a

reverse transcription reaction. Unique to the spLDR for mRNA expression profiling was that NO PCR was required; the mRNA copy number was read following primer ligation if recognizing through Watson/Crick base pairing rules resulting in a unique length spLDR that identified a specific mRNA transcript via single-molecule nanoscale electrophoresis. After spLDR, the products could be electrophoretically driven into a nanochannel electrophoresis tube for identifying for the presence of mutations or certain mRNAs using a molecular dependent time-of-flight (TOF) mechanism. The nanosensor components and their functionality were extensively discussed followed by simulations to guide device design and establishing device operation. Finally, the operational characteristics were demonstrated experimentally, and were in close agreement with the results from the simulations. Further developments are being made to transition the spLDR chemistry onto the nanopillars poised within this device.

An extension of the nanosensor device is the dual in-plane nanopore sensors, which are utilized to identify the products of spLDR based on differences in ssDNA length through the use of a label-free electrical detection protocol coupled to TOF (*i.e.*, nanoscale electrophoresis). The dual nanopores have a size of ~30 nm; at this size, larger molecules such as λ-DNA and T4 DNA can be identified. However, smaller DNA's have smaller radius of gyration and as such, the signal can be lost in the background. So, we developed a simple thermal fusion bonding (TFB) technique to reduce the size of the pore by bonding the imprinted devices at selected pressures. We saw an effective reduction in the depth of the nanopores, which consecutively increased the S/N ratio (Chapter 4) of λ-DNA molecules that were being electrophoretically driven through the dual ini-plane nanopore sensor. We were also able to identify small oligonucleotides having 50 and 70 nucleotides by their molecular-dependent mobility. Thus, the products of the spLDR have similar sizes of ssDNA (35-70mers) and can be detected and identified by electrophoretically driving them into the dual nanopore sensors.

While the previous research have dealt primarily with nucleic acids (mainly DNA/RNA), we have extended the use of label-free detection to identify viral particles (SARS CoV-2) from patients potentially having COVID-19 and using the capability as a rapid turnaround method to detect extremely low viral loads in <15 min. With this technique we have reported a high sensitivity resistive pulse sensor having 5

nanopores (~350 nm × 350 nm, width and depth) in parallel where affinity selected viral particles from saliva samples using a microfluidic device were directly injected into a nano-Coulter counter (nCC) and the concentration of the particles in the samples was determined based on the number of peaks identified. We used a vacuum pump for withdrawing the particles while simultaneously having an inlet flow (3 µl/min) to bring new particles to the sampling area. We established a direct correlation to the number of events identified and the concentration of the VPs. Extensive COMSOL simulations were carried out to help guide the design and operation of the nCC. From an iterative method of development, the final design of the nCC was able to achieve a concentration limit of detection of 2.4×10^3 viral particles mL^{-1}, which was a 100-fold compared to a single pore device.

Resulting from the work reported in this document, we have successfully provided a knowledge base and developed methods supported by simulations on how to use thermoplastics for engineering nanochannels, nanopores, and developed a system for processing and identifying single point mutations as well as expression profiling mRNA that may serve as biomarkers to diagnose major life threatening diseases. Apart from nucleic acids which were our primary focus, we extended the applications of these devices to allow for integration with other lab-on-chip platforms to automate the isolation and diagnosis for detection of viral particles causing COVID-19. Furthermore, we are applying this knowledge set into the development of a single-nucleotide sequencing platform using thermoplastic nanopores, which could bring down the costs of sequencing tremendously,[1-7] while increasing the read accuracy even for single-molecule processing with extremely long read lengths. This will be discussed below in Future Directions.

6.2 Future Directions

Analyzing blood-based biomarkers can identify early stage disease due to their signaling mechanism, and looking at nucleic acids like DNA and RNA can help identify specific subpopulations of diseases that can guide treatment decisions.[8] PCR or RT-PCR is usually used for amplification and detection of specific nucleic acid sequences, especially related to cancer and other diseases. As long as the sequence is known, PCR can be used to either amplify collected DNA or reverse transcribed RNA from blood-based

biomarkers, such as circulating tumor cells, cell free DNA, or exosomes, for use in providing the mutational status of the DNA or expression profiling the RNA. Next generation sequencing (NGS) is the second-generation sequencing platform that followed Sanger sequencing and is used for identifying the exact nucleotide sequence of DNA and RNA in which millions of DNA fragments are sequenced simultaneously following their amplification. With rare biomarkers, it may be difficult to distinguish between the background and a true positive. Often, standard kits and processes require at least 50 copies of the target DNA per sample in a concentration of at least 1% mutant-to-wild type to provide quality results. The past decade has seen massive improvement in the development of different techniques in NGS like pyrosequencing, sequencing by ligation and so on, which are now being used to enable precision medicine.[9]

Figure 6.1 shows the entire workflow required for NGS, which requires different types of techniques as well as a number of ancillary instruments. However, NGS has disadvantages. In the case of pyrosequencing, the reagent cost is high and has high error rates. With sequencing-by-synthesis, the error

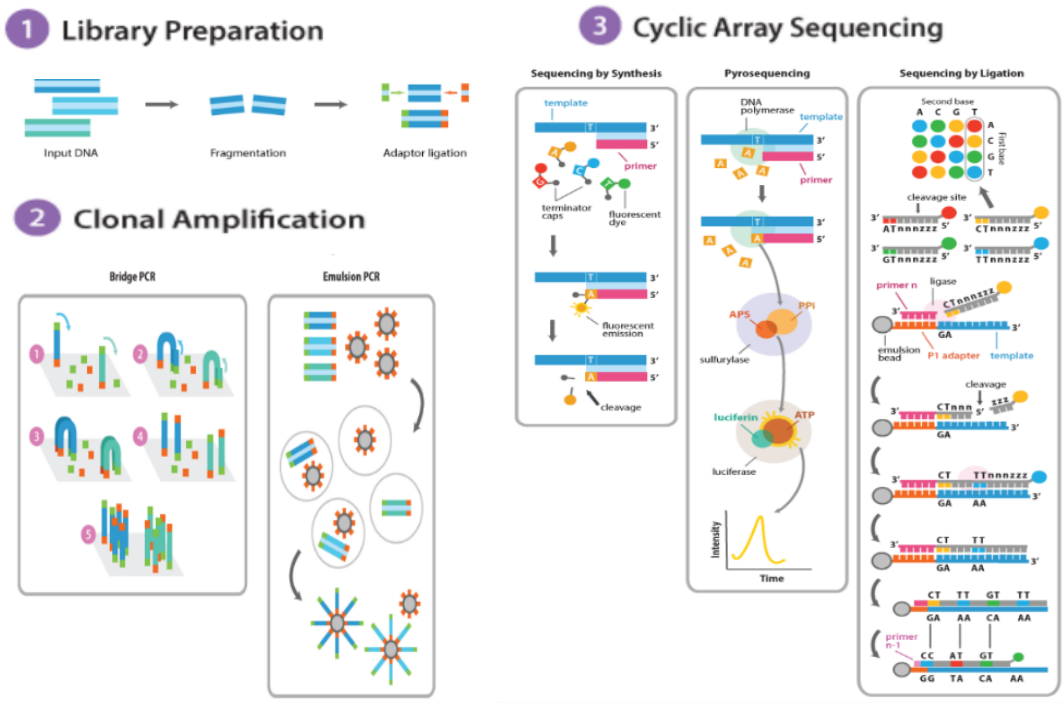

Figure 6.1 Commonly used sample processing techniques used for NGS. Steps 1 and 2 remains common for most NGS techniques, while step 3 shows steps specific for each type of NGS technique chosen. The figure explains sequencing by synthesis, pyrosequencing, and sequencing by ligation. **Adapted from https://www.abmgood.com/marketing/knowledge_base/next_generation_sequencing_introduction.php**

rates typically are much lower than pyrosequencing, they have very short sequencing read lengths.[10] The main technologies involved in identifying mutations have their own disadvantages. Currently, NGS is not being extensively used for mutation detection due to the error rates and the high costs associated with them, which creates a major clinical need to accurately identify diseases at the genetic level. Consequently, the need to accurately identify single mutations responsible for diseases is a major requirement for the advancement towards precision medicine.

Single-molecule sequencing (SMS) was initially proposed by the Keller group in the 1980's[11] which addressed the limitations in terms of library preparation and the ability to read out 10's of kbps.[12-34] Further many commercially available ventures such as Helicos,[35] Pacific Biosciences,[36-37] Genia,[38-39] and Oxford Nanopore[40-45] have made significant progress towards sequencing of DNA at the single-molecule level. We are particularly interested in Oxford Nanopore as they are using nanopores to identify single bases using electrical readout, which offers a simplistic platform compared to others. Furthermore, our group has made tremendous progress using nanopores to detect large DNA's like λ-DNA and T4 DNA and using TFB to reduce the size of nanopores to identify smaller oligonucleotides in the range of 35-100mers (Chapter 4).

However, there are some challenges associated with nanopore sequencing; 1) The shorter translocation times as the nucleotides pass through the pore. This issue has been addressed by the use of polymerase racheting action.[46-48] 2) The resolution of the nucleotide readout, which is limited by the pore thickness, which is larger than the ~0.34 nm to accommodate a single base during readout. Traditional α-hemolysin and synthetic nanopores are thicker (5-15 nm), which causes multiple bases to co-reside within the pore at the same time. Evolution of Msp nanopores have addressed this to a reasonable extent.[49-50] Even if the nanopores are fabricated with the required thickness, the electric field applied extends out of the nanopore[51] on either side effectively reducing the accuracy of the base readout compared to conventional sequencing platforms.[19]

We have developed a SMS platform that uses exonuclease combined with time-of-flight (TOF) called X-TOF which uses sequencing-by-subtraction (Figure 6.2). The X-TOF utilizes a nanofluidic device made in thermoplastics and contains three essential components: 1) The inlet/outlet channel network of ~50-100 nm, which contains two in-plane pore placed sequentially in the network which the DNA/RNA can be translocated through to signal a successful single-molecule injection event. The inlet region also has an entropic trap (~600 nm), which serves as a storage chamber where DNA/RNA can be momentarily stored and ejected on an application of voltage. 2) A solid-phase bioreactor consisting of a single pillar (~1,000 nm diameter) where an exonuclease enzyme that has a high processivity is surface immobilized. The enzyme can be activated with a Mg^{2+} co-factor, which starts clipping the target DNA/RNA and generates

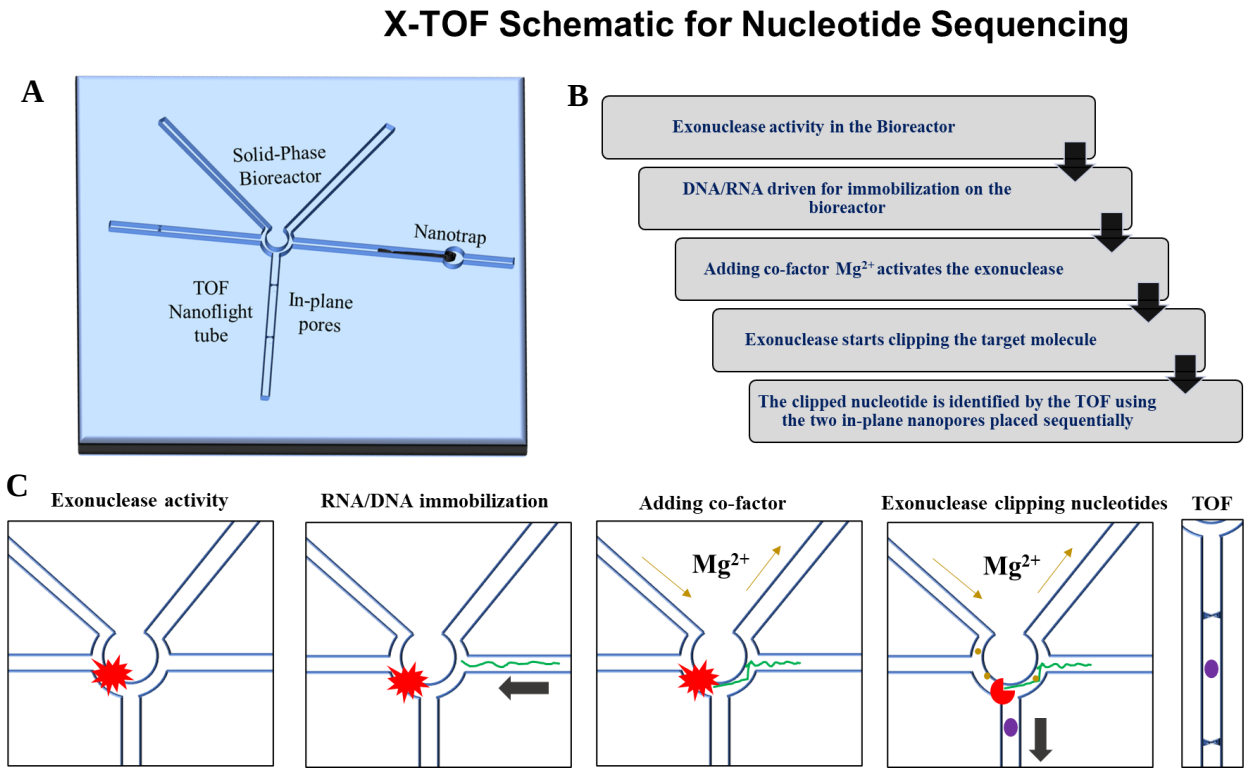

Figure 6.2 A) Schematic showing the overall X-TOF sensor that features the nanotrap for storing the nucleic acids, the solid phase bioreactor for immobilizing the target, and the TOF nanochannel that features two in-plane pores. B-C) The entire process of the SM sequencing in X-TOF takes place in 5 steps and is represented in a flow chart in (B) and a schematic in (C); 1) The XRN1 enzyme is immobilized to the bioreactor; 2) The DNA/RNA molecule is driven for immobilization in the bioreactor containing the XRN1 enzyme. 3) The Mg^{2+} cofactor is added to activate the enzyme. 4) The XRNI that is activated, starts clipping the nucleotides one by one. 5) The clipped nucleotides are electrokinetically driven into the flight tube and is identified by the current drop and the TOF.

single nucleotides. 3) TOF nanochannel (~50 nm x 50 nm) that contains two in-plane pores (~10 nm), which is placed sequentially and separated by a distance >10 μm. Once the target DNA/RNA is clipped, the nucleotides can be electrokinetically driven into the flight tube and based on differences in electrophoretic mobility between the 4 nucleotides, they can be identified.[52-53] Figure 6.2 shows a schematic of X-TOF design showing the entropic trap, the bioreactor and the TOF nanochannel having two in-plane pores.

In order to evaluate the X-TOF design, we tested some operational conditions using COMSOL simulations prior to fabrication to ensure the feasibility of the design to facilitate SMS. For the COMSOL simulations, we used 100 mM NaCl as the electrolyte as this is typically used as the buffer for the experiments. We used human Duchenne muscular dystrophy gene (DMD) RNA of 70 nm, having an arbitrary negative charge as the target molecule for sequencing. rAMP molecules of 1 nm, having a -2 charge were the nucleotide molecules generated after exoribonuclease enzyme such XRN1 that cleaves nucleic acid molecules[54].

We started off by testing the effects of the inlet structures, such as the iinterface that connects the microchannels to the inlet nanochannel of X-TOF. When having a blunt interface, there was an abrupt change in the electric field strength in the microchannel with respect to the nanochannel (Figure 6.3A-B (i)). This could cause the DNA/RNA molecules to accumulate at the microchannel-nanochannel interface due to entropic effects. Additionally, there could be also be dielectrophoretic trapping that could prevent the DNA/RNA molecules from entering into the nanochannel. Hence, we tested two alternate designs: (1) A narrow inlet with depths gradually tapering from the microchannel towards the nanochannels (Figure 6.3 A-B (ii)). As seen in Chapter 2, the effects of having tapered inlets lead to higher injection efficiency of the nucleic acid molecules into the nanofluidic network. (2) Placing pillars in the tapered input with the pillars having ~1 μm spacing between them. In this way, the nucleic acid molecules would pre-stretch before entering the nanochannels, thus reducing entropic barriers. In Figure 6.3-B (iii), we can see that there is a more stepwise and gradual increase of the electric field strength in the taper inlet with pillars compared to the blunt interface.

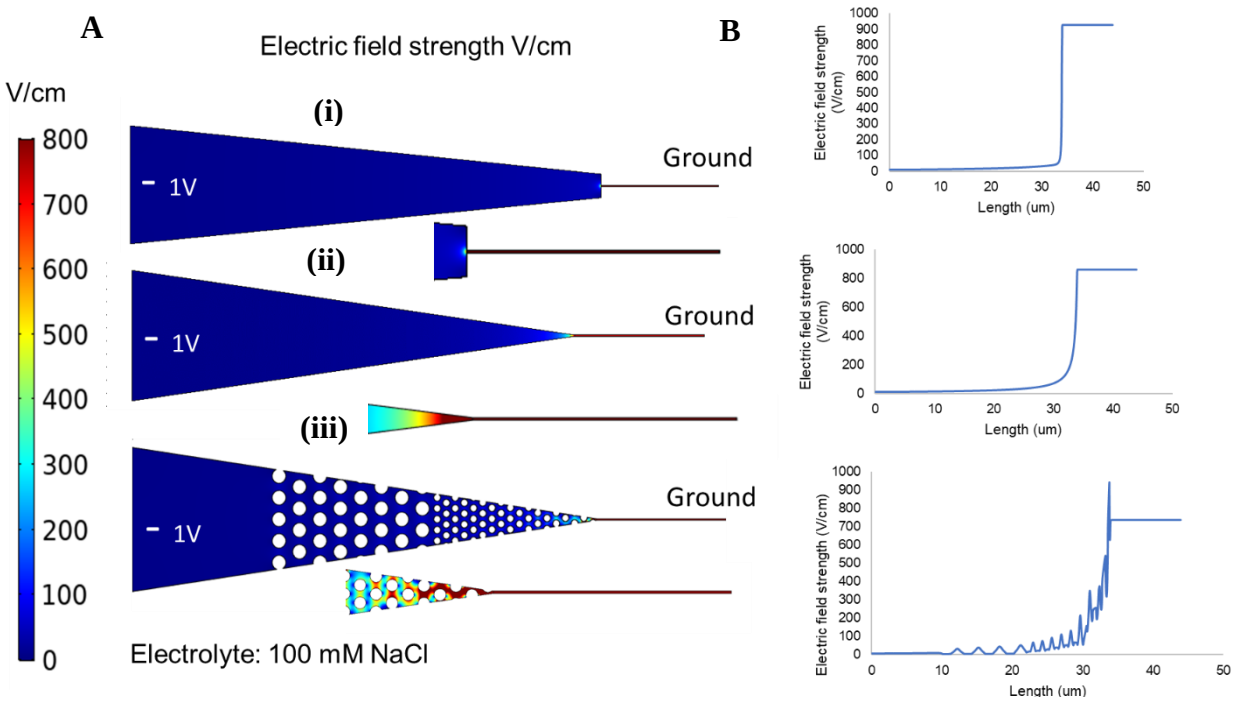

Figure 6.3 A) COMSOL simulations of the electric field strength profiles of the 3 inlet designs (i,ii,iii) is represented with their corresponding line graphs (B). A-B) The design (i) inlet has an abrupt increase in field strength right at the entrance of the nanochannel. The design (ii) has a narrower inlet where the entrance to the nanochannel is more gradual and the electric field is seen extending out of the nanochannel. The design (iii) has pillars that only helps to unravel the DNA/RNA molecules before entering, but also helps in reducing the entropic barrier. The field strength extends further towards the pillars, which shows a step wise increase in field strength.

We further investigated the effects of having an offset in the inlet/outlet nanochannels connecting to the bioreactor. The position of these channels will determine the region in the bioreactor where the target molecules can be immobilized to be cleaved by the XRN1 enzyme. In a regular design, the inlet/outlet nanochannels are positioned in the line with the diameter of the bioreactor (center); however when a channel is placed at an offset, it means that there is a shift of the channels from the diameter of the bioreactor by 75 nm (in this case). Figure 6.4-A shows the inlet/outlet nanochannels (150 nm in width) showing a shift in the nanochannel with respect to the diameter (center of bioreactor, which is the 0% offset). A 25% offset means that there is 75 nm shift in the nanochannel from the center of the bioreactor. Subsequently, a 50% offset means that there is a 150 nm shift in nanochannel from the center. With every increasing offset percentage, the target DNA translocating through the inlet/outlet channels have accessibility to a lesser region in the bioreactor. However, with a -25% offset, the channels are positioned above the center of the bioreactor, meaning, there is a larger region that is accessible for the target molecule to be immobilized in

the bioreactor. Having an offset is vital because we want the target nucleotides to be attached in regions closer to the flight tube placement. Hence, once the molecule is cleaved by the XRN1 enzyme, they will be released as single nucleotides that would be directed into the flight tube under the influence of electric field. Having a larger immobilization area would be problematic to drive the cleaved nucleotides into the flight tube with 100% efficiency. Hence choosing an optimal offset condition is vital to have an adequate area for nucleic acid immobilization while also being able to drive the cleaved nucleotides into the flight tube without them escaping into the connecting channels. The velocity profiles (Figure 6.4-B) clearly shows the area of the bioreactor suitable for enzyme and DNA/RNA interaction under different offset conditions. COMSOL simulations were done to showing the fluid flowing through the XTOF device when 100 mM NaCl was injected at a voltage of -1V. It can be seen that as for a 50% offset design, the area of the bioreactor that has the fluid flow is much larger than the 100% offset design which has velocity in a smaller region.

The electric field strength profiles (at -1 V) corresponding to the offsets showed a similar trend. The field strength was highly focused in the area where the inlet/outlet channel was placed (Figure 6.4-C).

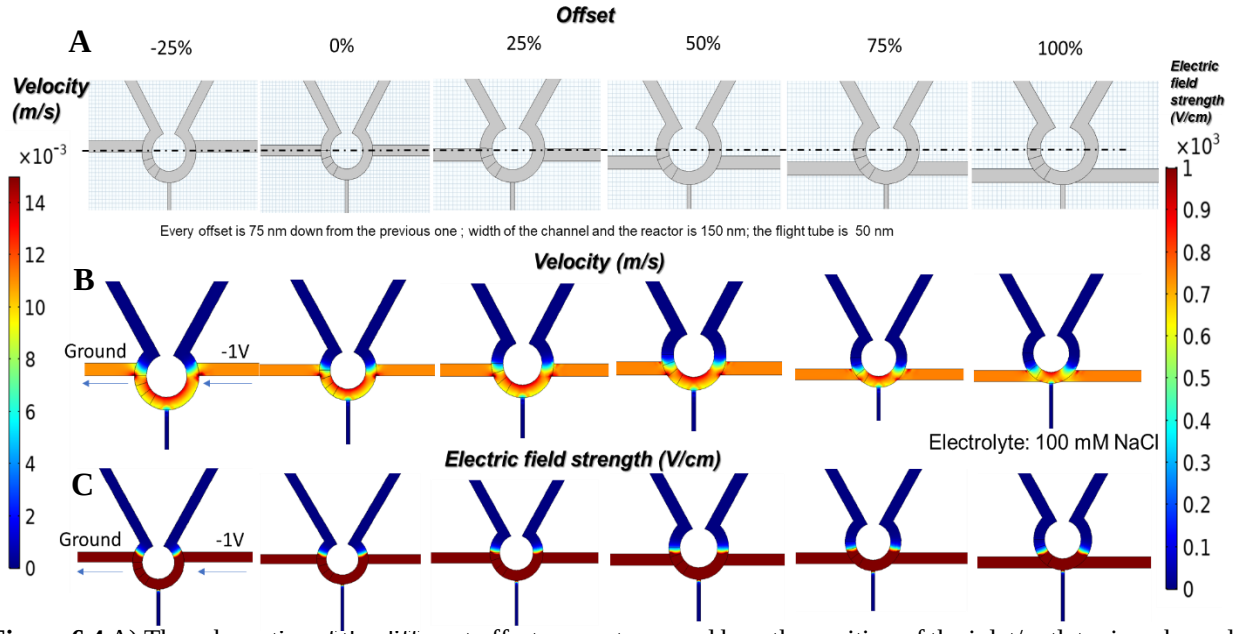

Figure 6.4 A) The schematics of the different offset percentages and how the position of the inlet/outlet microchannel varies with respect to the bioreactor. B) The velocity profiles of the different offset conditions show the areas in the bioreactor that would be accessible to the DNA that is introduced. As the offset percentage is increased, the accessibility area decreases. C) The corresponding electric field strength profile showing the field strength in the areas of the bioreactor corresponding to the offset conditions.

We decided to opt for the 50% offset design as it offered a reasonable area for the target DNA to interact with the surface immobilized enzyme as well as reducing the probability of the cleaved single nucleotides to efficiently be electrophoretically shuttled into the TOF nanochannel.

We next evaluated the use of different voltages to increase/decrease the rate at which the target molecule (DMD RNA) translocates and reaches the bioreactor. From Figure 6.5 it can be seen that the velocity increased with increase in voltage. At 1 V, the velocity in the input/output channels and the bioreactor was around 0.002 mm/s, while at 3 V and 5 V they were 0.0055 mm/s and 0.008 mm/s, respectively (Figure 6.5 A-C). This difference in velocity would impact the rate at which the target molecules translocate through the nanochannel and bioreactor; lower resident times of the target molecule in the bioreactor limits the time for association between the target and the surface immobilized exonuclease enzyme. The target molecule was assumed to be a spherical having a size of 70 nm and a negative charge.

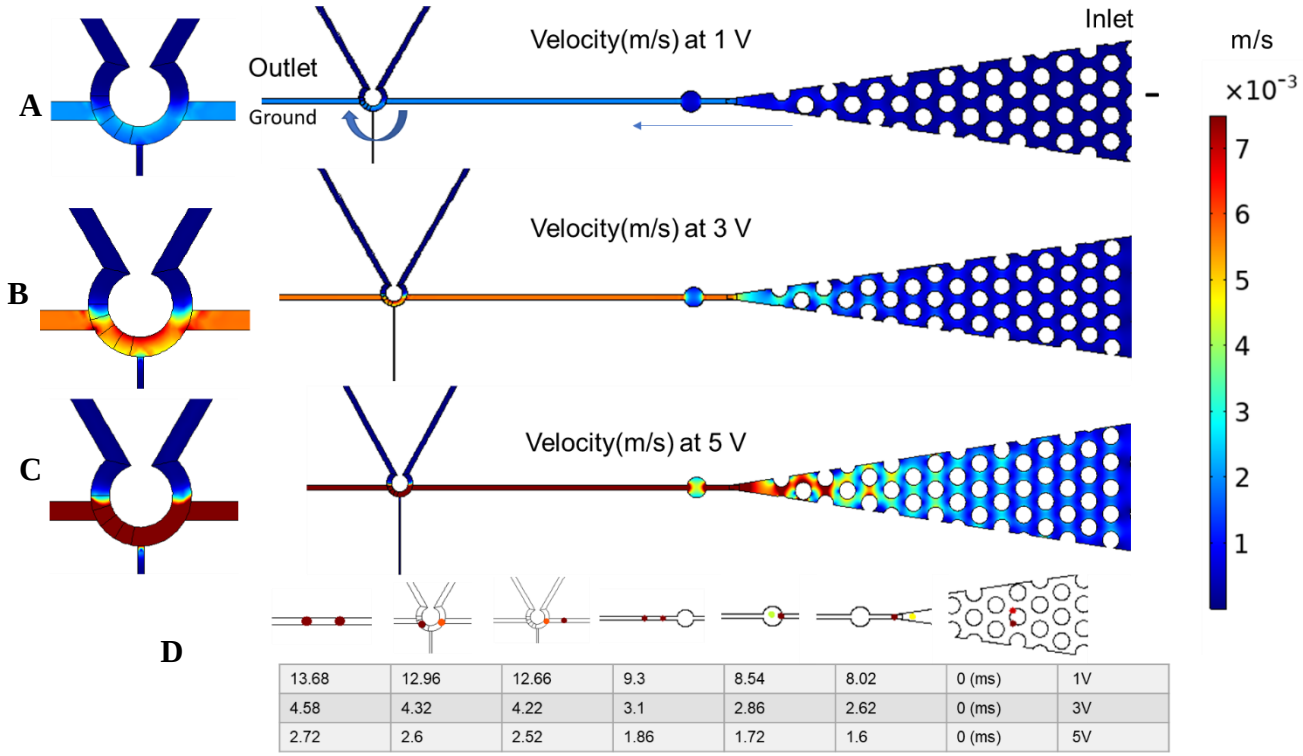

13.68	12.96	12.66	9.3	8.54	8.02	0 (ms)	1V
4.58	4.32	4.22	3.1	2.86	2.62	0 (ms)	3V
2.72	2.6	2.52	1.86	1.72	1.6	0 (ms)	5V

Figure 6.5 Effects of voltage on DMD RNA translocation velocity. A) The velocity of the translocating nucleic acids was evaluated a voltage of 1V. It takes 12.96 ms for the DMD RNA to reach the bioreactor; B) At 3V, the RNA translocates much faster, where it takes only 4.32 ms for the reactor. A higher velocity is seen from the scale bar. C) At 5V, RNA translocates even faster, where it takes only 2.6 ms to reach the bioreactor. D) The simulated particles at different regions in the X-TOF device is shown. The table below corresponds to the time it takes for the particles to reach the designated region at the given voltages.

Under the influence of -1V potential, the DMD RNA took about 5.14 ms to reach the bioreactor from the entrance of the input nanochannel and about 0.62 ms to move across the bioreactor. However, at higher voltages of -3 V and -5 V, they took about 1.74 ms and 1.04 ms to reach the bioreactor, respectively. Similarly, at -3 V and -5 V, they required 0.2 ms and 0.1 ms, respectively, to move across the bioreactor (Figure 6.5-D). Additionally, at voltages less than 0.1 V, the DNA molecules were found to transiently remain in the 600 nm entropic trap until a higher voltage was applied to eject the molecule out (refer to Chapter 2). This information can be utilized to avoid multiple target molecules entering into the bioreactor.

Further, the method of utilizing voltages to control the velocity/rate of translocation has been utilized for the injection of the co-factor Mg^{2+} into the bioreactor to activate the immobilized XRN1 enzyme. The velocity and electric field strength profiles are shown for 1 V, 3 V and 5 V DC bias. At 1 V, the velocity is much lower (0.002 mm/s) that at higher voltages. However, at 3 V and 5 V, there is a much higher

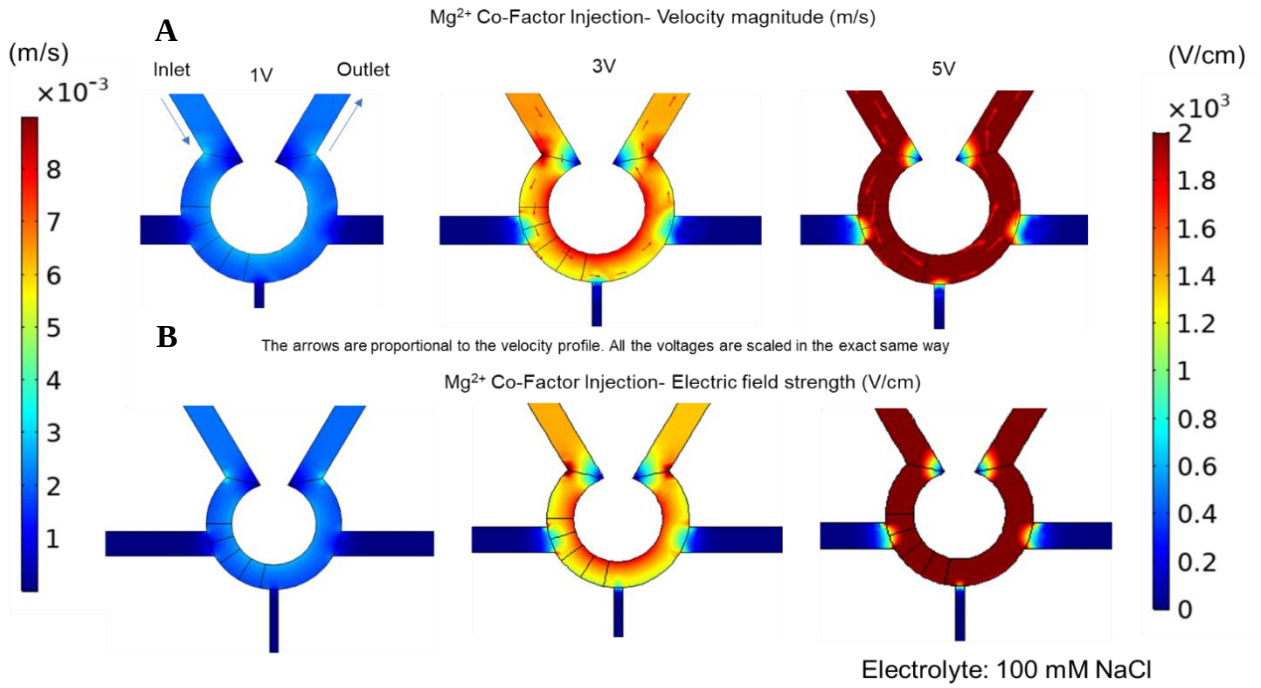

Figure 6.6 Effect of voltage to control the velocity and field strength of introducing Mg^{2+} to the bioreactor. A) The effect of voltages on the velocity of cofactor injection. At higher voltages, there is a significant increase in the velocity at which the Mg^{2+} is introduced. The increase in velocity at higher voltages can be seen in the scale bar. The arrows are proportional to the velocity. At 5V velocity, the arrows are much larger than those at 3V and 1V. The direction of arrows indicates the direction of injection. B) The corresponding increase in field strengths at higher voltages (1,3 and 5V) is seen. The field strength is highly restricted to the bioreactor indicating the possibility of the cofactor to bleed outside. Refer the scale bar for the absolute values corresponding to the scale.

velocity; the velocity at 3V is about 0.006 mm/s, while at 5V, the velocity is about 0.009 mm/s which causes the co-factor to move faster through the bioreactor (refer scale bar for quantitative values, Figure 6.6-A). The arrows show the direction of the movement of the co-factor and is proportional to the velocity magnitude at different voltages. The electric field strength profiles show the corresponding and expected increase in field strength with increase in the applied voltage (Figure 6.6-B).

Finally, the rate of translocation (rAMP molecule, size of ~1 nm^3), which were generated by the XRN1 enzyme from an intact RNA molecule, under different applied voltages was examined. When the

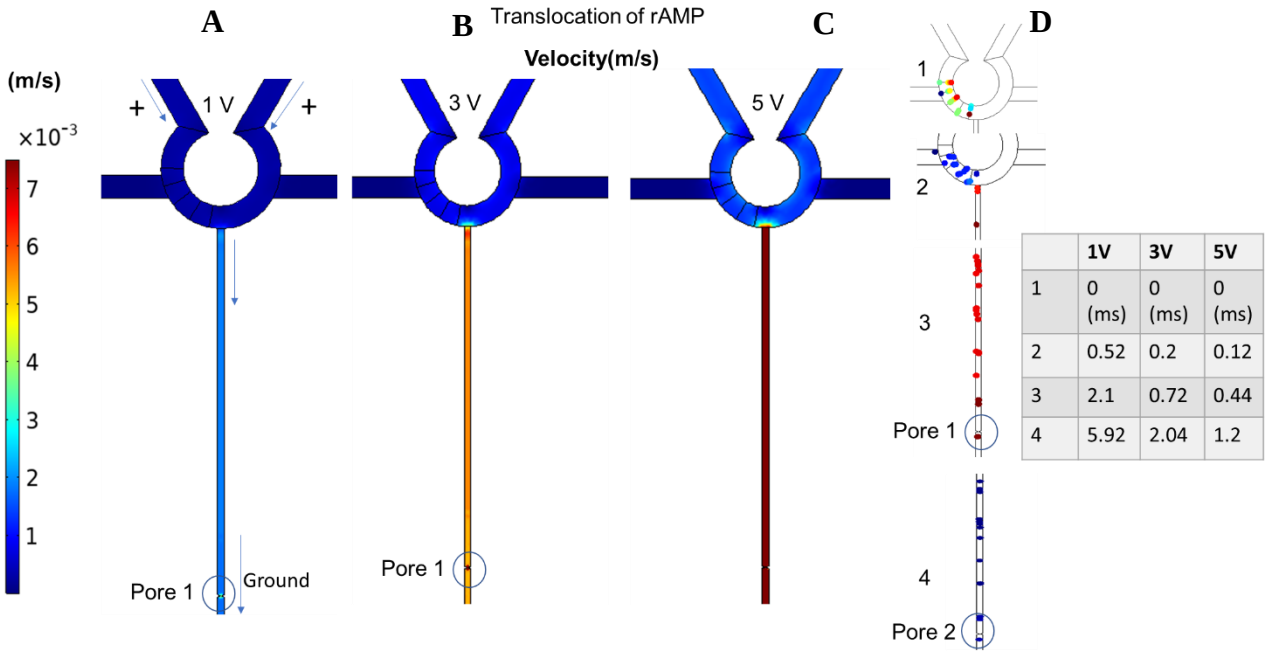

	1V	3V	5V
1	0 (ms)	0 (ms)	0 (ms)
2	0.52	0.2	0.12
3	2.1	0.72	0.44
4	5.92	2.04	1.2

Figure 6.7 Effect of voltage on translocation of rAMP from the bioreactor after it has been cleaved by the XRN1 enzyme. They are driven into the flight tube electrokinetically by applying voltage. A) At 1V, the rAMP molecule simulated takes about 2.1 ms to reach the first pore and 5.92 ms to reach the second pore (see the table). B) At 3V, they take only 0.72 ms to reach the first pore and a 2.04 ms to the second pore, giving a TOF of 1.32 ms. C) At 5V, it takes 0.44 ms and 1.2 ms to reach the first and second pore thus giving a TOF of 0.76 ms. D) The particle tracing results showing the position of the particles at various positions on the device: 1- Bioreactor, 2- When they start moving into the flight tube, 3- first pore, 4-second pore. The time at which the simulated rAMP molecules reach the designated regions at different voltages is given in the table.

nucleotides are cleaved, they are electrokinetically driven into the TOF nanochannel. From simulation, it was found that there was a 100% efficiency of the cleaved nucleotides entering into the TOF nanochannel at applied voltages ranging from 0.1 V to 10 V (figure not shown) at the 50% offset conditions. We observed that at an applied voltage of 1 V, it took about 2.06 ms for a single nucleotide to reach the first pore, and

about 5.88 ms to reach the second pore. This gives a TOF value of 3.82 ms. At a voltage of 3 V, it took only 0.71 ms for the nucleotide to reach the first pore and about 2 ms to reach the second pore, thus giving a TOF of 1.29 ms. At 5 V, this value decreased even further giving a TOF of 0.67 ms (Figure 6.7). It is important to note that XRN1 cleaves nucleotides from a nucleic acid molecule every 38 ms (clipping rate + 26 ±5 nucleotides/s).[54] This means that the estimated TOF values are well below the clipping rate of the enzyme, which eliminates the possibility of multiple nucleotides resident within the TOF nanochannel at any given time.

The results from these simulations will be useful for guiding the experiments with our X-TOF device. Our group has made some progress with the fabrication and operational characteristics of the device, with more experimentation underway to prove the feasibility of the device for SMS.

6.3 References

1. Hattori, S.; Nagato, K.; Hamaguchi, T.; Nakao, M., Rapid injection molding of high-aspect-ratio nanostructures. *Microelectronic Engineering* **2010,** *87* (5-8), 1546-1549.
2. Huang, C. K., Rapid replication of nanostructures made with a polymer using simple injection molding. *Journal of Applied Polymer Science* **2008,** *107* (1), 497-500.
3. Kim, K. H.; Kim, W.; Hong, J. C.; Ko, H. S.; Kim, B. K.; Huh, C.; Sung, G. Y., Fabrication of a Nanosize Pattern Embedded Plastic Chip via an Injection Molding Method for Application to an Optical Biosensor. *International Polymer Processing* **2010,** *25* (5), 341-345.
4. Matschuk, M.; Larsen, N. B., Injection molding of high aspect ratio sub-100 nm nanostructures. *Journal of Micromechanics and Microengineering* **2013,** *23* (2).
5. Matteucci, M.; Christiansen, T. L.; Tanzi, S.; Ostergaard, P. F.; Larsen, S. T.; Taboryski, R., Fabrication and characterization of injection molded multi level nano and microfluidic systems. *Microelectronic Engineering* **2013,** *111*, 294-298.
6. Schift, H.; David, C.; Gabriel, M.; Gobrecht, J.; Heyderman, L. J.; Kaiser, W.; Koppel, S.; Scandella, L., Nanoreplication in polymers using hot embossing and injection molding. *Microelectronic Engineering* **2000,** *53* (1-4), 171-174.
7. Utko, P.; Persson, F.; Kristensen, A.; Larsen, N. B., Injection molded nanofluidic chips: Fabrication method and functional tests using single-molecule DNA experiments. *Lab on a Chip* **2011,** *11* (2), 303-308.
8. Snyder, H. M.; Carrillo, M. C.; Grodstein, F.; Henriksen, K.; Jeromin, A.; Lovestone, S.; Mielke, M. M.; O'Bryant, S.; Sarasa, M.; Sjøgren, M.; Soares, H.; Teeling, J.; Trushina, E.; Ward, M.; West, T.; Bain, L. J.; Shineman, D. W.; Weiner, M.; Fillit, H. M., Developing novel blood-based biomarkers for Alzheimer's disease. *Alzheimer's & Dementia: The Journal of the Alzheimer's Association* **2014,** *10* (1), 109-114.
9. Serratì, S.; De Summa, S.; Pilato, B.; Petriella, D.; Lacalamita, R.; Tommasi, S.; Pinto, R., Next-generation sequencing: advances and applications in cancer diagnosis. In *Onco Targets Ther*, 2016; Vol. 9, pp 7355-65.

10. Hert, D. G.; Fredlake, C. P.; Barron, A. E., Advantages and limitations of next-generation sequencing technologies: a comparison of electrophoresis and non-electrophoresis methods. *Electrophoresis* **2008,** *29* (23), 4618-26.
11. Davis, L. M.; Fairfield, E. R.; Harger, C. A.; Jett, J. H.; Hahn, J. H.; Keller, R. A.; Krakowski, L. A.; Martin, J. C.; Marrone, B. L.; Ratliff, R. L.; Seitzinger, N. K.; Shera, E. B.; Soper, S. A., High-Speed DNA Sequencing - an Approach Based Upon Fluorescence Detection of Single Molecules. *Abstr. Pap. Am. Chem. Soc.* **1990,** *200*, 75-ANYL.
12. Gupta, P. K., Single-molecule DNA sequencing technologies for future genomics research. *Trends in Biotechnology* **2008,** *26* (11), 602-611.
13. Clarke, J.; Wu, H. C.; Jayasinghe, L.; Patel, A.; Reid, S.; Bayley, H., Continuous base identification for single-molecule nanopore DNA sequencing. *Nature Nanotechnology* **2009,** *4* (4), 265-270.
14. Milos, P. M., Emergence of single-molecule sequencing and potential for molecular diagnostic applications. *Expert Review of Molecular Diagnostics* **2009,** *9* (7), 659-666.
15. Pushkarev, D.; Neff, N. F.; Quake, S. R., Single-molecule sequencing of an individual human genome. *Nature Biotechnology* **2009,** *27* (9), 847-U101.
16. Turner, S., Applying single molecule real time DNA sequencing. *Cancer Research* **2009,** *69*.
17. Braslavsky, I., Single Molecule DNA Sequencing: from Demonstration to Application. *Biophysical Journal* **2010,** *98* (3), 208A-209A.
18. Flusberg, B. A.; Webster, D. R.; Lee, J. H.; Travers, K. J.; Olivares, E. C.; Clark, T. A.; Korlach, J.; Turner, S. W., Direct detection of DNA methylation during single-molecule, real-time sequencing. *Nature Methods* **2010,** *7* (6), 461-U72.
19. Sam, L. T.; Lipson, D.; Raz, T.; Cao, X. H.; Thompson, J.; Milos, P. M.; Robinson, D.; Chinnaiyan, A. M.; Kumar-Sinha, C.; Maher, C. A., A Comparison of Single Molecule and Amplification Based Sequencing of Cancer Transcriptomes. *Plos One* **2011,** *6* (3).
20. Thompson, J. F., Single Molecule Sequencing Technology: the Applications and Implications for Biological Research. *In Vitro Cellular & Developmental Biology-Animal* **2011,** *47*, S14-S14.
21. Thompson, J. F.; Milos, P. M., The properties and applications of single-molecule DNA sequencing. *Genome Biology* **2011,** *12* (2).
22. Avent, N. D., Refining Noninvasive Prenatal Diagnosis with Single-Molecule Next-Generation Sequencing. *Clinical Chemistry* **2012,** *58* (4), 657-658.
23. van den Oever, J. M. E.; Balkassmi, S.; Verweij, E. J.; van Iterson, M.; van Scheltema, P. N. A.; Oepkes, D.; van Lith, J. M. M.; Hoffer, M. J. V.; den Dunnen, J. T.; Bakker, E.; Boon, E. M. J., Single Molecule Sequencing of Free DNA from Maternal Plasma for Noninvasive Trisomy 21 Detection. *Clinical Chemistry* **2012,** *58* (4), 699-706.
24. Davis, B. M.; Chao, M. C.; Waldor, M. K., Entering the era of bacterial epigenomics with single molecule real time DNA sequencing. *Current Opinion in Microbiology* **2013,** *16* (2), 192-198.
25. Shin, S. C.; Ahn, D. H.; Kim, S. J.; Lee, H.; Oh, T. J.; Lee, J. E.; Park, H., Advantages of Single-Molecule Real-Time Sequencing in High-GC Content Genomes. *Plos One* **2013,** *8* (7).
26. Patel, A.; Schwab, R.; Liu, Y. T.; Bafna, V., Amplification and thrifty single-molecule sequencing of recurrent somatic structural variations. *Genome Research* **2014,** *24* (2), 318-328.
27. Sakai, H.; Naito, K.; Ogiso-Tanaka, E.; Takahashi, Y.; Iseki, K.; Muto, C.; Satou, K.; Teruya, K.; Shiroma, A.; Shimoji, M.; Hirano, T.; Itoh, T.; Kaga, A.; Tomooka, N., The power of single molecule real-time sequencing technology in the de novo assembly of a eukaryotic genome. *Scientific Reports* **2015,** *5*.
28. Steinig, E. J.; Andersson, P.; Harris, S. R.; Sarovich, D. S.; Manoharan, A.; Coupland, P.; Holden, M. T. G.; Parkhill, J.; Bentley, S. D.; Robinson, D. A.; Tong, S. Y. C., Single-molecule

sequencing reveals the molecular basis of multidrug-resistance in ST772 methicillin-resistant Staphylococcus aureus. *Bmc Genomics* **2015,** *16*.
29. Yang, Y.; Sebra, R.; Pullman, B. S.; Qiao, W. Q.; Peter, I.; Desnick, R. J.; Geyer, C. R.; DeCoteau, J. F.; Scott, S. A., Quantitative and multiplexed DNA methylation analysis using long-read single-molecule real-time bisulfite sequencing (SMRT-BS). *Bmc Genomics* **2015,** *16*.
30. Betz-Stablein, B. D.; Topfer, A.; Littlejohn, M.; Yuen, L.; Colledge, D.; Sozzi, V.; Angus, P.; Thompson, A.; Revill, P.; Beerenwinkel, N.; Warner, N.; Luciani, F., Single-Molecule Sequencing Reveals Complex Genome Variation of Hepatitis B Virus during 15 Years of Chronic Infection following Liver Transplantation. *Journal of Virology* **2016,** *90* (16), 7171-7183.
31. Gao, Y.; Deng, L. W.; Yan, Q.; Gao, Y. Q.; Wu, Z. D.; Cai, J. S.; Ji, D. R.; Li, G. L.; Wu, P.; Jin, H.; Zhao, L. Y.; Liu, S.; Ge, L. J.; Deem, M. W.; He, J. K., Single molecule targeted sequencing for cancer gene mutation detection. *Scientific Reports* **2016,** *6*.
32. Hargreaves, K. R.; Thanki, A. M.; Jose, B. R.; Oggioni, M. R.; Clokie, M. R. J., Use of single molecule sequencing for comparative genomics of an environmental and a clinical isolate of Clostridium difficile ribotype 078. *Bmc Genomics* **2016,** *17*.
33. Kujawa, S.; Sethuraman, A.; Eng, K.; Baybayan, P.; Heyrman, L.; Del Favero, J., Highly sensitive and cost-effective detection of somatic cancer variants using single molecule, real-time sequencing. *Cancer Research* **2016,** *76*.
34. Ozsolak, F., Attomole-level Genomics with Single-molecule Direct DNA, cDNA and RNA Sequencing Technologies. *Current Issues in Molecular Biology* **2016,** *18*, 43-48.
35. Milos, P. M., Helicos single molecule sequencing: unique capabilities and importance for molecular diagnostics. *Genome Biology* **2010,** *11*.
36. McCarthy, A., Third Generation DNA Sequencing: Pacific Biosciences' Single Molecule Real Time Technology. *Chemistry & Biology* **2010,** *17* (7), 675-676.
37. Grohme, M. A.; Soler, R. F.; Wink, M.; Frohme, M., Microsatellite marker discovery using single molecule real-time circular consensus sequencing on the Pacific Biosciences RS. *Biotechniques* **2013,** *55* (5), 255-258.
38. Fuller, C. W.; Kumar, S.; Porel, M.; Chien, M. C.; Bibillo, A.; Stranges, P. B.; Dorwart, M.; Tao, C. J.; Li, Z. M.; Guo, W. J.; Shi, S. D.; Korenblum, D.; Trans, A.; Aguirre, A.; Liu, E.; Harada, E. T.; Pollard, J.; Bhat, A.; Cech, C.; Yang, A.; Arnold, C.; Palla, M.; Hovis, J.; Chen, R.; Morozova, I.; Kalachikov, S.; Russo, J. J.; Kasianowicz, J. J.; Davis, R.; Roever, S.; Church, G. M.; Ju, J. Y., Real-time single-molecule electronic DNA sequencing by synthesis using polymer-tagged nucleotides on a nanopore array. *Proceedings of the National Academy of Sciences of the United States of America* **2016,** *113* (19), 5233-5238.
39. Stranges, P. B.; Palla, M.; Kalachikov, S.; Nivala, J.; Dorwart, M.; Trans, A.; Kumar, S.; Porel, M.; Chien, M. C.; Tao, C. J.; Morozova, I.; Li, Z. M.; Shi, S. D.; Aberra, A.; Arnold, C.; Yang, A.; Aguirre, A.; Harada, E. T.; Korenblum, D.; Pollard, J.; Bhat, A.; Gremyachinskiy, D.; Bibillo, A.; Chen, R.; Davis, R.; Russo, J. J.; Fuller, C. W.; Roever, S.; Ju, J. Y.; Church, G. M., Design and characterization of a nanopore-coupled polymerase for single-molecule DNA sequencing by synthesis on an electrode array. *Proceedings of the National Academy of Sciences of the United States of America* **2016,** *113* (44), E6749-E6756.
40. Eisenstein, M., Oxford Nanopore announcement sets sequencing sector abuzz. *Nature Biotechnology* **2012,** *30* (4), 295-296.
41. Goodwin, S.; Gurtowski, J.; Ethe-Sayers, S.; Deshpande, P.; Schatz, M. C.; McCombie, W. R., Oxford Nanopore sequencing, hybrid error correction, and de novo assembly of a eukaryotic genome. *Genome Research* **2015,** *25* (11), 1750-1756.
42. Hargreaves, A. D.; Mulley, J. F., Assessing the utility of the Oxford Nanopore MinION for snake venom gland cDNA sequencing. *Peerj* **2015,** *3*.
43. Jain, M.; Olsen, H. E.; Paten, B.; Akeson, M., The Oxford Nanopore MinION: delivery of nanopore sequencing to the genomics community (vol 17, 239, 2016). *Genome Biology* **2016,** *17*.

44. Jain, M.; Olsen, H. E.; Paten, B.; Akeson, M., The Oxford Nanopore MinION: delivery of nanopore sequencing to the genomics community. *Genome Biology* **2016,** *17*.
45. Oikonomopoulos, S.; Wang, Y. C.; Djambazian, H.; Badescu, D.; Ragoussis, J., Benchmarking of the Oxford Nanopore MinION sequencing for quantitative and qualitative assessment of cDNA populations. *Scientific Reports* **2016,** *6*.
46. Greenleaf, W. J.; Block, S. M., Single-molecule, motion-based DNA sequencing using RNA polymerase. *Science* **2006,** *313* (5788), 801-801.
47. Larkin, J.; Foquet, M.; Korlach, J.; Wanunu, M., Nanopore immobilization of DNA polymerase enhances single-molecule sequencing. *Journal of Biomolecular Structure & Dynamics* **2013,** *31*, 134-135.
48. Cherf, G. M.; Lieberman, K. R.; Rashid, H.; Lam, C. E.; Karplus, K.; Akeson, M., Automated forward and reverse ratcheting of DNA in a nanopore at 5-Å precision. *Nature Biotechnology* **2012,** *30*, 344-348.
49. Brinkerhoff, H., Improving DNA Sequencing with Nanopore MSPA. *Biophysical Journal* **2016,** *110* (3), 531A-531A.
50. Manara, R. M. A.; Wallace, E. J.; Khalid, S., DNA sequencing with MspA: Molecular Dynamics simulations reveal free-energy differences between sequencing and non-sequencing mutants. *Scientific Reports* **2015,** *5*.
51. Liu, H.; Qian, S.; Bau, H. H., The effect of translocating cylindrical particles on the ionic current through a nanopore. *Biophysical Journal* **2007,** *92*, 1164-1177.
52. Novak, B. R.; Moldovan, D.; Nikitopoulos, D. E.; Soper, S. A., Distinguishing Single DNA Nucleotides Based on Their Times of Flight Through Nanoslits: A Molecular Dynamics Simulation Study. *Journal of Physical Chemistry B* **2013,** *117* (12), 3271-3279.
53. Xia, K.; Novak, B. R.; Weerakoon-Ratnayake, K. M.; Soper, S. A.; Nikitopoulos, D. E.; Moldovan, D., Electrophoretic Transport of Single DNA Nucleotides through Nanoslits: A Molecular Dynamics Simulation Study. *Journal of Physical Chemistry B* **2015,** *119*, 11443-11448.
54. Athapattu, U. S.; Amarasekara, C. A.; Immel, J. R.; Bloom, S.; Barany, F.; Nagel, A. C.; Soper, S. A., Solid-phase XRN1 reactions for RNA cleavage: application in single-molecule sequencing. *Nucleic Acids Research* **2021**.